Ph.D. Thesis

An Innovative Positron Spectrometer
to Search for the Lepton Flavour Violating Muon Decay
with a Sensitivity of 10^{-13}

By

Hajime Nishiguchi

March 2008

Department of Physics, School of Science

THE UNIVERSITY OF TOKYO

Abstract

An innovative positron spectrometer has been developed for the MEG experiment at the Paul Scherrer Institute (PSI) in Switzerland. The MEG experiment searches for lepton flavour violating decays $\mu \rightarrow e\gamma$ with a sensitivity of 10^{-13} in order to explore physics beyond the Standard Model, in particular, the Grand Unified Theories.

In order to achieve such an excellent sensitivity, the MEG positron spectrometer has been designed to consist of a superconducting solenoidal magnet with a specially graded magnetic field which eases handling of high rate positrons up to $3 \times 10^7 \text{ sec}^{-1}$, low-mass drift chamber system that minimizes multiple scatterings and annihilations of positrons, and a precise timing counter system which determines the positron timing with a precision of 50 psec. In 2007, we completed construction of the spectrometer and carried out a successful engineering run toward the end of the year. The positron spectrometer was operated successfully with a high muon stopping rate (up to $3 \times 10^7 \text{ sec}^{-1}$), and the detector calibration procedures have been established to achieve the necessary detector performance.

A momentum resolution of 0.9 % and an angular resolution of 6 mrad (both in σ) for 52.8MeV/c positron at a muon stopping rate of $3 \times 10^7 \text{ sec}^{-1}$ have been achieved in the engineering run. A precise Monte Calro simulation incorporating the actual detector conditions has been carried out to verify that the measured and extrapolated performance of the positron spectrometer is sufficient for the MEG experiment to reach a sensitivity below 10^{-12} in the physics run planned in 2008.

Contents

Chapter 1

Introduction

The Standard Model of elementary particle physics is one of the greatest success of modern science. Based on the principles of gauge symmetries and spontaneous symmetry breaking, it seems to describe all known phenomena in Nature and is supported by extensive experimental evidences. Essentially no experimental observation contradicts the Standard Model so far.

The Standard Model successfully explains the observed violation of CP symmetry in the framework of Cabibbo-Kobayashi-Maskawa (CKM) mechanism, the lepton- and baryon-number conservation as accidental global symmetries of its Lagrangian, the quark confinement by the asymptotically free colour force, the natural suppression of the flavour changing neutral currents (FCNC) via the Glashow-Iliopoulos-Maiani (GIM) mechanism, *etc.* Everything had been consistently described until experimental evidence for neutrino oscillation was shown by SuperKamiokande for the first time.

One of the important assumptions is zero neutrino masses which assures lepton flavour conservation. In the Standard Model, renormalizable neutrino mass terms are therefore forbidden by the quantum number assignment. With the matter contents of the Standard Model, the neutrino mass terms can be introduced only by supposing a new mass scale at much higher energy beyond the Standard Model scale and Majorana mass terms. Briefly speaking, neutrino masses can be generated only when we regard the Standard Model as an effective low energy theory of more fundamental theory. In consequence, the existence of non-zero neutrino masses strongly implies the existence of new physics beyond the Standard Model for the first time.

In the past several years, our knowledge about the neutrinos has been drastically improved by the discoveries of neutrino oscillations (*e.g.* by Super-Kamiokande, SNO, K2K, KamLAND, *etc*). Neutrino oscillation is a quantum-mechanical phenomenon where a neutrino created with a specific lepton flavour may later be measured to have a different flavour. It indicates a mismatch between the flavour and mass eigenstates of neutrinos. Observation of neutrino oscillation therefore corresponds to the evidences that neutrinos have finite masses.

To explain the observed neutrino oscillation, theoretical models of lepton flavour mixing have been extensively developed, although there is no standard answer yet. Obviously, a complete understanding of the lepton flavour structure is a very important challenge in particle physics today. While lepton flavour is totally violated in the neutrino sector, lepton flavour violation in the charged lepton sector (electron, muon, tau) has never been observed. An observation of lepton flavour violation in the charged lepton sector, such as the decay processes $\mu \to e\gamma$, $\mu \to 3e$, $\tau \to \mu\gamma$, $\tau \to e\gamma$, $\mu - e$ conversion in a nucleus, *etc.*, therefore, would be a breakthrough that would unambiguously lead to new physics beyond the Standard Model.

The MEG experiment [1] was proposed in 1999 to look for experimental evidence of lepton flavour violation in charged leptons. The ambitious goal of the MEG experiment is to search for a $\mu^+ \to e^+\gamma$ decay with a sensitivity improved by which is two orders of magnitude better than the current best limit on this decay branching ratio, $\mathcal{B}(\mu^+ \to e^+\gamma) < 1.2 \times 10^{-11}$ by the MEGA experiment [2]. The $\mu \to e\gamma$ decay may likely occur with a branching ratio just below the current upper limit, according to many of the promising theories for physics beyond the Standard Model, in particular, the Supersymmetric theories of Grand Unification or Supersymmetric Standard Model with the *seesaw* mechanism. This experiment has therefore a real chance of making a discovery. The observation of the $\mu \to e\gamma$ decays would give us important insights about the new physics which cannot be obtained by the energy frontier experiments such as LHC and ILC. On the other hand, non-observation of the $\mu^+ \to e^+\gamma$ signal in the MEG experiment would give a stringent constraint on these theories and on the general Nature of the new physics beyond the Standard Model which usually cannot avoid significant lepton flavour violation. Recent reviews on flavour physics (see Ref. [3] for example) thus indicate high expectations for the MEG experiment.

The $\mu^+ \to e^+\gamma$ signal is very simple and is characterized by a 2-body final state of the decay positron and γ-ray emitted in opposite directions with the same energy, 52.8 MeV, which corresponds to half the muon mass. The background to the $\mu^+ \to e^+\gamma$ search experiment is dominated by two major contributions; (1) Prompt (or physics) background from radiative muon decays, $\mu \to e\nu\nu\gamma$; (2) Accidental coincidence of positrons coming from normal Michel decays and a γ-ray coming from other sources, *i.e.* radiative muon decay or in-flight annihilation of the Michel positrons. In consequence, suppressing such accidental coincidences is the key for leading MEG to a successful conclusion.

The MEG experiment employs the following three elements to achieve its goal:

- The most intense DC muon beam presently available in the world

- A novel liquid-xenon scintillation γ-ray detector

- A specially designed positron spectrometer with a specially designed magnetic field

A direct current (DC) muon beam is best suited for $\mu \to e\gamma$ search rather than pulsed beam to minimize accidental overlaps. The 590 MeV proton accelerator complex at the Paul Scherrer Institute in Switzerland provides the world's most intense DC muon beams. This makes it possible to search for the rare decays within a reasonably short term ($\sim$ a year).

A novel liquid xenon scintillation γ-ray detector, which is viewed from all sides by $\sim$850 photomultipliers immersed in the liquid xenon, has been newly developed in order to achieve ultimate resolutions of simultaneous measurements of energy, position, and time. of the γ rays.

Last but not least, an innovative positron spectrometer that can cope with a high muon-stopping rate of up to 3×10^7 sec^{-1} is necessary. Moreover, a very-low-mass tracker is required to minimize multiple Coulomb scattering that limits positron measurement resolutions, and positron annihilations in detector material that increases high energy γ-ray background.

A fast, 3D measurement of positron trajectory is also advisable to clearly disentangle a signal positron out of tremendous background tracks. Extremely good timing resolution is also needed to suppress accidental background. In order to fulfill these requirements we designed,

developed and recently completed a new spectrometer consisting of a specially graded magnetic field, ultimately low-mass drift chambers and timing counters with good timing resolution.

In this thesis, the development of the positron spectrometer for the MEG experiment is described and the performance of the completed spectrometer is studied in detail from a point of view of feasible physics sensitivity of the experiment. First of all, the fundamental muon physics is described in Chapter 2. Normal muon decay process in the framework of the Standard Model and possible rare decay processes predicted by several theoretical models beyond the Standard Model are described in this chapter. Chapter 3 gives a brief description of the MEG experiment; the beam and the detectors. In Chapter 4, details of the positron spectrometer are described. One of the most important component of the spectrometer, the drift chamber, is described in Chapter 5. Detailed description of the drift-chamber simulation is given in Chapter 6. In the momentum region of interest ($\sim$50 MeV/c), the track reconstruction must employ an adaptive fitting method that takes into account both multiple scattering and energy loss. Development of the reconstruction algorithm is presented in Chapter 7. Chapter 8 explains in detail the calibration procedure that had been established during the engineering run of the whole experiment conducted in 2007. The data analysis and evaluated spectrometer performances by the engineering run are presented in Chapter 9. Finally, in Chapter 10, we discuss the systematic effects that constrain and determine spectrometer performance and then evaluate a physics sensitivity of the MEG experiment in the planned physics run in 2008.

Chapter 2

$\mu \to e\gamma$ **Decay**

Ever since the discovery of the muon [4], the study of muon properties has contributed to a deeper understanding of physics of electromagnetic and weak interactions, in particular, the "V-A" structure of weak interactions and validity of quantum electrodynamics [5,6]. The muon might not have exhausted its potential yet and more precise understanding of its properties could still provide crucial information on new physics principles that might lie beyond the Standard Model.

While precise measurements of the muon lifetime and Michel parameters provide stringent tests for the theory of electroweak interactions and its possible extensions, one of the main interests in muon physics still lies in the search for processes that violate the lepton flavour conservation. The discovery of decays such as $\mu \to e\gamma$, $\mu \to eee$ or μ-e conversion in nuclei would be an indisputable proof of the existence of new dynamics beyond the Standard Model.

In this chapter, a brief summary of the decay $\mu \to e\gamma$ is given from both theoretical and experimental aspects. The normal muon decay phenomenology is presented in Section 1. In Section 2, we go into the lepton-flavour physics on muon decay. In this Section, physics motivation of the $\mu \to e\gamma$ search experiment is first described. Then, the status of the $\mu \to e\gamma$ search experiments is summarized. Finally, the event signature and the background in the $\mu \to e\gamma$ search are described.

2.1 Muon Decay in the Standard Model

Before working on the $\mu \to e\gamma$ search experiment, it is worth the normal muon decay in order to obtain a better understanding of the experimental environments, especially the experimental background. The Michel decays are also useful for calibration of detectors which will be described in Chapter 8.

As is well known, a muon decays into an electron(a positron) and two neutrinos:

$$\mu^- \to e^- \nu_\mu \bar{\nu}_e, \quad \mu^+ \to e^+ \nu_e \bar{\nu}_\mu. \tag{2.1}$$

It may decay radiatively:

$$\mu^- \to e^- \nu_\mu \bar{\nu}_e \gamma, \quad \mu^+ \to e^+ \nu_e \bar{\nu}_\mu \gamma, \tag{2.2}$$

or with an associated e^+e^- pair:

$$\mu^- \to e^- \nu_\mu \bar{\nu}_e e^+ e^-, \quad \mu^+ \to e^+ \nu_e \bar{\nu}_\mu e^+ e^-, \tag{2.3}$$

but with smaller branching ratios. The branching ratios for these decay modes and the upper limit of some *exotic* decay modes at 90% confidence level are summarized in Table 2.1. (Only negatively charged muons are listed. The corresponding decays of positively charged muons are obvious and not listed.)

Decay mode	Branching ratio	Reference
$\mu^- \to e^- \nu_\mu \bar{\nu}_e$	$\sim 100\%$	
$\mu^- \to e^- \nu_\mu \bar{\nu}_e \gamma$	$1.4 \pm 0.4\%$ *	[7] †
$\mu^- \to e^- \nu_\mu \bar{\nu}_e e^+ e^-$	$(3.4 \pm 0.4) \times 10^{-5}$	[8]
$\mu^- \to e^- \nu_e \bar{\nu}_\mu$	$< 1.2\%$	[9]
$\mu^- \to e^- \gamma$	$< 1.2 \times 10^{-11}$	[2]
$\mu^- \to e^- e^+ e^-$	$< 1.0 \times 10^{-12}$	[10]
$\mu^- \to e^- \gamma\gamma$	$< 7.2 \times 10^{-11}$	[11]

Table 2.1: Decay modes and branching fractions of muon (Listed in PDG table [12])

The dominant process, $\mu^- \to e^- \nu_\mu \bar{\nu}_e$, is usually called as the *"**Michel decay**"* [14]. We will treat this decay and the radiative decay mode later in Section 2.1.1 and Section 2.1.2, respectively.

The matrix element $\mathcal{M}$ of a muon decay is given by

$$\mathcal{M} = -\frac{4G_F}{\sqrt{2}} \sum_{\substack{\gamma=S,V,T \\ \epsilon,\mu=R,L}} g^\gamma_{\epsilon\mu} \langle \bar{e}_\epsilon | \Gamma^\gamma | (\nu_e)_n \rangle \langle (\bar{\nu}_\mu)_m | \Gamma_\gamma | \mu_\mu \rangle, \tag{2.4}$$

where G_F is the Fermi coupling constant and $g^\gamma_{\epsilon\mu}$ are the dimensionless complex coupling constants, $\gamma =$S,V,T indicate a Lorentz Scalar, Vector, or Tensor interaction, and the chirality of the electron or muon (Right- or Left-handed) is labeled by $\epsilon, \mu =$R,L. The chiralities n and m of the ν_e and the $\bar{\nu}_\mu$ are determined by given values of γ, ϵ and μ. All the observables in muon decay (energy spectrum, polarization and angular distributions) may be parameterized in terms of these coupling constants $g^\gamma_{\epsilon\mu}$ and G_F. These coupling constants and G_F constitute 19 independent parameters to be determined experimentally. They are subject to the normalization condition [6]:

$$n_S\left(|g^S_{RR}|^2 + |g^S_{LL}|^2 + |g^S_{RL}|^2 + |g^S_{LR}|^2\right)$$
$$+n_V\left(|g^V_{RR}|^2 + |g^V_{LL}|^2 + |g^V_{RL}|^2 + |g^V_{LR}|^2\right) \tag{2.5}$$
$$+n_T\left(|g^T_{RL}|^2 + |g^T_{LR}|^2\right) = 1,$$

where $n_S = \frac{1}{4}$, $n_V = 1$ and $n_T = 3$. **From the *Physics* point of view, $n_\gamma |g^\gamma_{\epsilon\mu}|^2$ represents the relative probability that a "μ"-handed muon will decay into an "ϵ"-handed electron via the interaction Γ^γ.** All the muon decay parameters, which represents the observables of the muon

---

*This only includes events with $E_\gamma > 10$ MeV. The radiative mode cannot be clearly separated from the normal decay mode in the soft-photon limit.

†Recently, a new result has been reported by the PIBETA experiment [13]. The Particle-Data-Group record will be updated for the first time in almost 40 years. We will discuss it later (Section 2.1.2).

decay and are referred to as the "*Michel parameters*" (see Section 2.1.1), can be described by the bilinear combinations of these coupling constants. Therefore the coupling constants are uniquely determined by measuring the muon decay spectra, asymmetry and polarization precisely, and hence the Lorentz structure of the weak interaction is completely determined. There is no *a priori* reason to expect that some of these couplings vanish. However, all experimental tests are consistent with a weak interaction which has only V coupling between left-handed muons and left-handed electrons. This fact is built into the Standard Model by setting

$$g_{\mathrm{LL}}^{\mathrm{V}} = 1 \tag{2.6}$$

with all the other coupling constants being zero, as they must be according to Equation (2.5). Thus the weak interaction has been completely determined, as "V-A" interaction, by using only data from this purely leptonic interaction.

2.1.1 Michel Decay

Michel decay [14] has been measured precisely to determine features of the weak interaction. From late 1960s to 1980s, many experiments were carried out and all measurements are found to be consistent with the Standard Model. This means that all observables, such as the electron's spectrum, decay asymmetry and polarization vector, can be described by the V-A interaction perfectly.

Beginning from the matrix element (2.4), one can derive the differential decay rate of Michel decay [6];

$$\frac{\mathrm{d}^2\Gamma}{\mathrm{d}x\mathrm{d}(\cos\theta)} = \frac{m_\mu}{4\pi^3}W_{\mathrm{e}\mu}^4 G_F^2 \sqrt{x^2 - x_0^2}\left[\mathcal{F}_{IS}(x) + P_\mu\cos\theta_{\mathrm{e}}\mathcal{F}_{AS}(x)\right]\left[1 + \vec{P}_{\mathrm{e}}(x,\theta_{\mathrm{e}})\cdot\hat{\zeta}\right] \tag{2.7}$$

where $W_{\mathrm{e}\mu} = (m_\mu^2 - m_{\mathrm{e}}^2)/(2m_\mu)$, $x = E_{\mathrm{e}}/W_{\mu\mathrm{e}}$ and $x_0 = m_{\mathrm{e}}/W_{\mu\mathrm{e}}$. Here, E_{e} is the energy of the electron and m_μ and m_{e} are the masses of the muon and electron, respectively. The range of allowed electron energies is $m_{\mathrm{e}} \leq E_{\mathrm{e}} \leq W_{\mu\mathrm{e}}$ or equivalently, $x_0 \leq x \leq 1$. The variable θ_{e} is the angle between the muon polarization $\vec{P}_\mu$ and the electron momentum and $\hat{\zeta}$ is the unit vector in the direction of the electron spin polarization. $\vec{P}_{\mathrm{e}}$ is the polarization of the electron along the direction of its momentum. The function $\mathcal{F}_{IS}$ and $\mathcal{F}_{AS}$ are the isotropic and anisotropic parts of the electron energy spectrum. They are given by

$$\mathcal{F}_{IS} = x(1-x) + \frac{2}{9}\rho(4x^2 - 3x - x_0^2) + \eta x_0(1-x), \tag{2.8}$$

$$\mathcal{F}_{AS} = \frac{1}{3}\xi\sqrt{x^2 - x_0^2}\left[1 - x + \frac{2}{3}\delta\left(4x - 3 - \left(1 - \sqrt{1 - x_0^2}\right)\right)\right]. \tag{2.9}$$

The parameters ρ, η, ξ and δ are called the Michel parameters [14], defined in terms of bilinear combinations of the coupling constants $g_{\epsilon\mu}^\gamma$.

For the MEG experiment, we use a thin plastic target, which does not hold the muon polarization. In such a case, differential decay rate (2.7) can be simplified. Since averaging over the possible polarizations involves integration of $\cos\theta_{\mathrm{e}}$ over the antisymmetric interval $-1 \leq \cos\theta_{\mathrm{e}} \leq 1$, the term involving $\mathcal{F}_{AS}$ in (2.7) vanishes. An analogous argument applies to

the term $\vec{P}_{\rm e}(x, \theta_{\rm e}) \cdot \hat{\xi}$. Then, simplified decay rate explicitly depends on the Michel parameter ρ and η only, and these parameters have been measured ultra-precisely [12] as mentioned above. Consequently, **precisely determined Michel spectrum suits very well the detector calibration, such as absolute energy-scale calibration for the positron spectrometer** (Section 8.7).

2.1.2 Radiative Muon Decay

Approximately 1% of all muon decays is accompanied by a photon with energy $E_\gamma \geq 10$ MeV. The differential branching ratio of the radiative muon decay has been calculated by several authors [15, 16]. In addition, electron and photon energy spectra of the radiative muon decay have been derived as explained in Ref. [17, 18]. Here, the spectra of electron and photon depend not only on the two Michel paramters ρ and δ, but also on the additional parameter, $\bar{\eta}$, which should be zero in the V-A interactoin of the Standard Model. This parameter $\bar{\eta}$ does not appear in the non-radiative Michel spectrum (2.7) and can be determined only by measuring the radiative muon decay spectrum. Like the other Michel parameters, it is described by the bilinear combination of the coupling constant $g^{\gamma}_{\epsilon\mu}$ [16].

As just described, the branching ratio and spectra of the radiative muon decay have been calculated by assuming the V-A interaction of the Standard Model. Several experiments measured the branching ratio and $\bar{\eta}$ parameter, and their results are consistent with the Standard Model predictions. Until recently, the best measurements of $\mathcal{B}(\mu \to e\nu\nu\gamma)$ and $\bar{\eta}$ had not been updated; $\mathcal{B}(\mu \to e\nu\nu\gamma) = (1.4 \pm 0.2) \times 10^{-2}$ [7] was obtained in 1961, and $\bar{\eta} = 0.035 \pm 0.098$ [19] was reported in 1983. However, recently, much more precise measurements were reported by the PIBETA experiment [13];

$$\mathcal{B}(\mu \to e\nu\nu\gamma) = [4.40 \pm 0.02(\text{stat.}) \pm 0.09(\text{syst.})] \times 10^{-3},$$
$$\bar{\eta} = -0.084 \pm 0.050(\text{stat.}) \pm 0.034(\text{syst.}).$$

Both are in excellent agreement with Standard Model predictions.

Consequently, with these accurately determined parameters, we can precisely simulate the electron/photon energy spectra and the differential rate of the radiative muon decay to evaluate the background of the MEG experiment. It is also used to calibrate arrival time measurement of the photon and positron. We will mention this again in the discussion concerning the background estimation (Section 2.4) and the spectrometer calibration (Section 8.7).

2.2 $\mu \to$ eγ Decay

As mentioned above, the standard muon decay is perfectly described by the Standard Model. However, as neutrino experiments report that the lepton flavour conservation is violated in the neutrino sector, we are naturally facing a fundamental question; *"Is the lepton flavour conservation violated also in the charged lepton sector ?"* This issue does need to be addressed, because it might give us a breakthrough in clarifying new physics beyond the Standard Model.

In this Section, physics behind the most popular lepton flavour violating decay, $\mu \to$ eγ , is described in the framework of the Standard Model and the supersymmetric extensions of the Standard Model, respectively.

2.2.1 $\mu \to e\gamma$ **Decay in the Standard Model**

In the Standard Model, lepton flavour is conserved thanks to the global symmetry of Lagrangian. However, in order to describe the neutrino oscillation we have to introduce mass terms of neutrinos. The simplest extension of the Standard Model which accommodates the neutrino masses and mixings is just to introduce finite Dirac mass terms of neutrinos. Such mass terms automatically induce lepton flavour violation (LFV) not only in the neutrino sector but also in the charged lepton sector through a mechanism that is quite similar to the CKM scheme of the quark sector.

For instance, the $\mu \to e\gamma$ decay can be induced via the diagram of Figure 2.1, in which ν_μ oscillates into ν_e. However, the branching ratio of this process is strongly suppressed by the
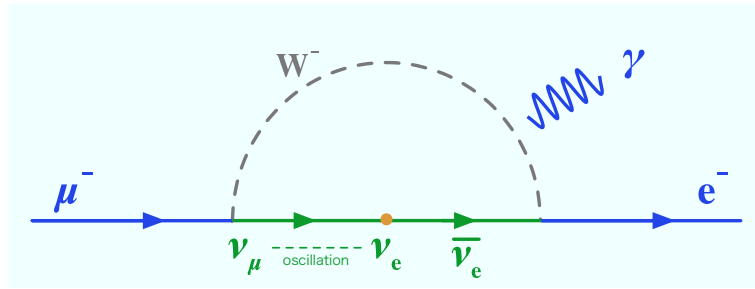
Figure 2.1: An example of Feynman diagrams that contribute to $\mu \to e\gamma$ decay in the Standard Model with finite neutrino masses

fourth power of the ratio of the neutrino masses m_{ν_i} to the W boson mass m_W as

$$\mathcal{B}(\mu \to e\gamma) = \frac{3\alpha}{32\pi} \sum_i \left| U^*_{\mu i} U_{ei} \frac{m^2_{\nu i}}{m^2_W} \right|^2, \tag{2.10}$$

where $U_{\alpha i}(\alpha = e, \mu, \tau)$ is an element of the unitary matrix which diagonalizes the neutrino mass matrix by $\nu_\alpha = U_{\alpha i}\nu_i$ [20]. Because of this suppression (so-called leptonic version of GIM mechanism), the branching ratio of $\mu \to e\gamma$ in this framework is estimated as $\lesssim 10^{-50}$ assuming the neutrino mass of order $\sim$1 eV. Even if we apply the cosmological bound of the neutrino mass of 100 eV [21], the branching ratio can be at most 10^{-40} [22]. It is out of reach of any experiment in the conceivable future to detect such a small branching ratio.

2.2.2 $\mu \to e\gamma$ **Decay in the Physics Beyond the Standard Model**

Many studies indicate that lepton flavour may be significantly violated through TeV-scale physics which the LHC experiments plan to explore in the coming decade. In particular, in the supersymmetric theories, a mismatch in the flavour space between the leptons and their superpartners, sleptons, is known to cause naturally large flavour mixings. The slepton mass matrices generates tree-level transitions between different leptonic generations, both in charged and neutral currents [23, 24].

In this case, using the mixing angle between the first two generations of sleptons, *selectron* ẽ and *smuon* $\tilde{\mu}$, $\theta_{\tilde{e}\tilde{\mu}}$, the branching ratio of $\mu \to e\gamma$ becomes

$$\mathcal{B}(\mu \to e\gamma) \simeq \frac{\alpha^3 \pi \theta_{\tilde{e}\tilde{\mu}}^2}{G_F^2 \tilde{m}^4}, \tag{2.11}$$

where $\tilde{m}^4$ is a typical supersymmetric mass. In general, $\theta_{\tilde{e}\tilde{\mu}}^2$ receives contributions from the flavour mismatches of sleptons and sneutrinos which originate from new physics at much higher energies, such as Grand Unification and *seesaw* mechanism. As is clear from Eq. (2.11), the rates of $\mu \to e\gamma$ can be large, because they are not suppressed by powers of the neutrino masses, unlike Eq. (2.10). An example of supersymmetric $\mu \to e\gamma$ decay processes, for instance, by flavour mixing between $\tilde{\mu}$ and $\tilde{e}$ with a neutralino $\tilde{\chi}^0$ intermediation, is shown in Figure 2.2.
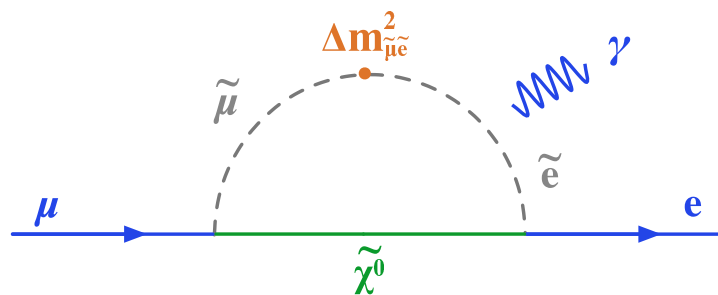
Figure 2.2: A possible example of Feynman diagram for $\mu \to e\gamma$ decay induced by slepton flavour mixing .

Without any huge suppression of $\theta_{\tilde{e}\tilde{\mu}}^2$, the predicted branching ratios for $\mu \to e\gamma$ decays are far larger and, in fact, as large as the experimental results could permit [25, 26, 27, 28, 29, 30].

For example, **a minimal supersymmetric standard model (MSSM) with right-handed neutrinos model**, where lepton flavour is violated by the *seesaw* mechanism with the heavy right-handed neutrinos, predicts a large $\mathcal{B}(\mu \to e\gamma)$ [28] as shown in Figure 2.3. Two examples of Feynman diagram for $\mu \to e\gamma$ decay in this frameworks for the $\mu \to e\gamma$ decays are also shown in Figure 2.3. The assumption here is that the scale of the right-handed neutrino mass $M_R = 10^{13}$ GeV, $\tan\beta = 10$ [*], $M_1 = 100$GeV [†], $A_0 = 0$[‡], $\mu > 0$[§], and that all the neutrino mixings come from the Yukawa couplings. In this plot, two cases, which correspond to $U_{e3} = 0$ (solid line) and $U_{e3} = 0.05$ (dotted line), are shown with three different solutions to the solar-neutrino problem [31, 32], LMA (Large Mixing Angle), SMA (Small Mixising Angle) and LOW (Low Probability/Mass) out of which we now know LMA is the correct answer [¶]. Therefore, this model predicts large values for the branching ratio, $\mathcal{B}(\mu \to e\gamma)$, as large as the current

---

[*]the ratio of the two Higgs vacuum expectation values

[†]Gaugino mass at the GUT scale

[‡]Universal soft SUSY breaking trilinear term

[§]Higgsino mass parameter

[¶]For example, see results from Super-Kamiokande [33], KamLAND [34] and SNO experiment [35]. See also Ref. [36] for a review.
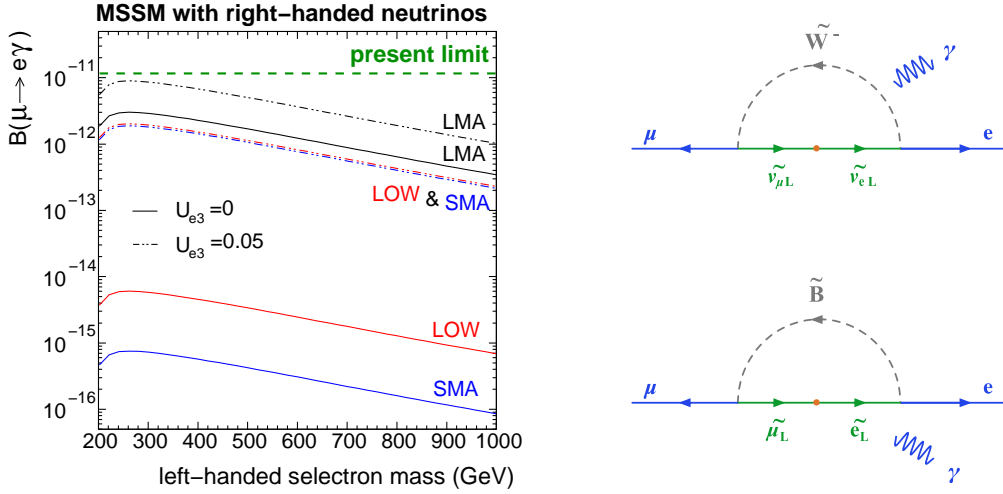
Figure 2.3: (Left) $\mathcal{B}(\mu \rightarrow e\gamma)$ as a function of the left-handed selectron mass for MSSM with heavy right-handed neutrinos. Assumed values for the other parameters are listed in the text. (Right) Examples of the Feynman diagrams for the $\mu \rightarrow e\gamma$ decay in this model. The symbols $\tilde{\nu}_{\ell L}, \tilde{\ell}_L, \tilde{W}^-$, and $\tilde{B}$ represent left-handed sneutrinos, left-handed charged sleptons, charged W-ino, and B-ino, respectively. (W-ino is the superpartner of the W boson, and B-ino is the superpartner of the gauge boson corresponding to weak hypercharge, respectively.)

upper bound, even if the unknown 1-3 neutrino mixing, U_{e3}, is zero.

Although a variety of such models have been considered, recently the most commonly-quoted, well-motivated, and thus most promising among many supersymmetric models are **supersymmetric grand unified theories (SUSY-GUT)**, which unify quarks and leptons into the same representations of the unification gauge group at the GUT scale. Thanks to the quark-lepton unification, the large Yukawa coupling responsible for the top quark mass also appears in LFV couplings. For instance, in **SU(5) SUSY-GUT** models [29, 30], which may be possibly already excluded by the proton decay experiments, $\mathcal{B}(\mu \rightarrow e\gamma)$ is predicted as shown in Figure 2.4 for different values of $\tan\beta$. The assumed values of M_R, M_1, A_0 and sign of μ are same as Figure 2.3. Two of the possible Feynman diagrams of the $\mu \rightarrow e\gamma$ decay in SU(5) SUSY-GUT are also shown in Figure 2.4. $\mathcal{B}(\mu \rightarrow e\gamma)$ may become larger if higher dimensional operators are taken into account [29].

In **SO(10) SUSY-GUT** models [26], all the fermions including the right-handed neutrinos belong to the same irreducible representation, and therefore the large top Yukawa coupling affects not only right-handed sleptons but also left-handed sleptons. Moreover, in the loop diagrams involving the exchange of a third generation slepton, the necessary chiral flip can occur along the $\tilde{\tau}$-line and enhance $\mathcal{B}(\mu \rightarrow e\gamma)$ by a factor $m_{\tilde{\tau}}^2/m_{\mu}^2 (\sim 245)$. Figure 2.5 shows the predicted values of $\mathcal{B}(\mu \rightarrow e\gamma)$ in a SO(10) SUSY-GUT model as a function of the right-handed selectron mass for the different values of $\tan\beta$, together with two examples of the Feynman diagrams. The assumed values of M_R, M_1, A_0 and sign of μ are same as Figure 2.3.

In summary, the supersymmetric extensions of the Standard Model generally induce very

Figure 2.4: (Left) $\mathcal{B}(\mu \to e\gamma)$ as a function of the right-handed selectron mass in SU(5) SUSY-GUT model. (Right) Feynman diagrams for the $\mu \to e\gamma$ decay in SU(5) SUSY-GUT model. The symbol $\tilde{\ell}_R$ represents right-handed slepton.

large lepton flavour violation not only in the neutrino sector but also in the charged lepton sector. Although only three representative models are described here, supersymmetric theories (broken gravitationally) generically predict large values of $\mathcal{B}(\mu \to e\gamma)$ [||].

2.3 History and Status of $\mu \to e\gamma$ Decay Search Experiment

Historically, the $\mu \to e\gamma$ decays were intensively looked for in the 1950s and 1960s, when it was believed that electrons and muons have identical quantum numbers and thus this decay should naturally occur. The main interest was evoked by the postulate of the existence of an intermediate charged vector boson mediating the weak interactions. Using the assumptions of a charged intermediate vector boson, two-component neutrino, and lepton number conservation, the $\mathcal{B}(\mu \to e\gamma)$ had been calculated by several authors [38]. Ever since the first search experiment for $\mu \to e\gamma$ [39] in 1947, however, searches of increasing experimental accuracy over a decade have failed to detect $\mu \to e\gamma$ decay. All the models predicted $\mu \to e\gamma$ proceeds in second order of either the semiweak or the weak coupling constants and hence that the estimates were beset with divergent integrals that could be damped only with artificial cutoffs. Thus one could not be absolutely sure that a fundamental problem existed, although within the framework of these theories no convincing model simultaneously forbidding $\mu \to e\gamma$ could be constructed. It was not before the rates of the unambiguously calculable processes $\nu_\mu N \to N\mu$ and $\nu_\mu N \to eN$ were measured experimentally that people finally realized that muons and electrons are independent entities separated by some fundamental law [40]. In this pioneering experiment, using neutrinos from the decay of positive pions, *i.e.* ν_μ, no electron events were observed. It was now attractive to introduce a new quantum number (**muon number**), so-called *flavour*, different for a muon and an electron. The simple muon number scheme also

---

[||]*cf.* Ref. [37] for a review.
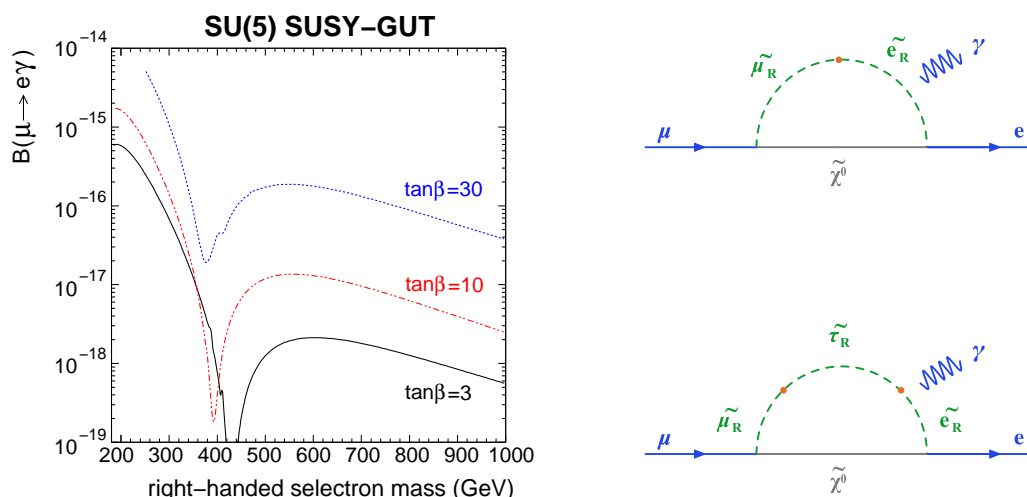
Figure 2.5: (Left) $\mathcal{B}(\mu \rightarrow$ e$\gamma)$ as a function of the right-handed selectron mass in SO(10) SUSY-GUT model. (Right) Feynman diagrams for the $\mu \rightarrow$ eγ decay in SO(10) SUSY-GUT model.

forbade $\mu \rightarrow$ eγ process so that this decay no longer provided a testing ground for weak inter-action theories and in particular for the intermediate vector boson theory. In this way, theories of weak interaction advanced and eventually evolved into the electroweak part of the Standard Model.

When the Standard Model was still at its birth, the search for neutrinoless decay modes of the muon entered a new phase, namely, precise tests of the weak interaction theory and attempts to understand the generations better. A rush of research activities occurred in 1977 when a rumour was circulated that an experiment at the Swiss Institute for Nuclear Research (SIN **) had found $\mu \rightarrow$ eγ decays. Peoples's excitement was based on their realization that the conservation of muon number is only empirical and without a fundamental basis. The rumour was later refuted, but it had motivated various theoretical and experimental researches and lead to a better understanding in the end. Theorists found that the suppression of the branching ratios for lepton flavour violating decays below the experimental upper limits ($\approx 10^{-8}$) was a natural result of the new models. On the experiment side, besides the search at SIN [41], two other experiments were quickly assembled to search with improved sensitivities for $\mu \rightarrow$ eγ . One was at the Tri-University Meson Facility (TRIUMF) [42], and the other was at the Los Alamos Meson Physics Facility (LAMPF) [43]. The results from these experiments showed no evidence at a level of 1.7×10^{-10}.

Figure 2.6 shows the experimental progress of the upper limits on the decay branching ratio of the $\mu \rightarrow$ eγ . Clusters of points in the plot (coloured differently) reflect innovations in muon sources and instrumentation. The first search used muons from cosmic-ray showers and an apparatus consisting of Geiger-Müller tubes and absorbers. The next series of searches, until 1964, used accelerators and stopped pion beams as sources of muons; the detectors were of various types, such as scintillation counters, water Čerenkov counters, spark chambers, a freon bubble chamber, and energy measurements with NaI(Tl) crystals. The recent searches, from the
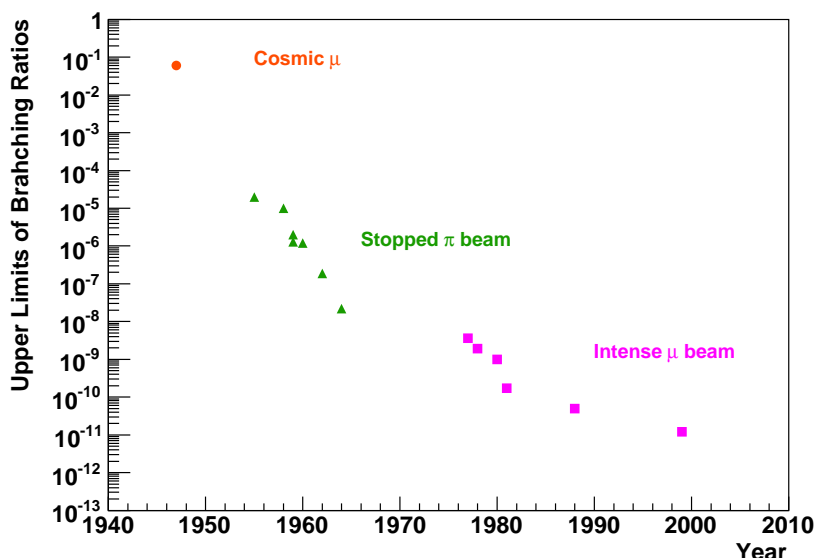

** currently PSI

Figure 2.6: Historical progress of the experimental upper limits for $\mathcal{B}(\mu \to e\gamma)$

mid 1970s until the present, utilized high-intensity muon beams from the meson factories and improved spectrometer designs to search for these rare decays with remarkable sensitivities around that time.

Obviously, the largest steps towards an improvement in the $\mathcal{B}(\mu \to e\gamma)$ determination were due to improvements in the muon source. From the first to the second group, one can see the significant improvement over four order of magnitudes, and further orders of magnitude were gained in the passage from pion to muon beam. The limit improved essentially as the number of observed muons, and within each beam configuration improvements of the detectors were fundamental. The quality of a detector is judged by its capability of discriminating a signal event from the background, which mimic a $\mu \to e\gamma$ decay. With the increased muon rate the background rate also increased, therefore new experiments had to be more cleverly designed to fight the ever increasing background. Thus the $\mu \to e\gamma$ search experiments have gradually improved the detector resolutions of four variables, namely, the positron energy E_e, the γ-ray energy E_γ, the timing between the positron and γ, $\Delta t_{e\gamma}$, and the angle between the positron and γ, $\Delta\theta_{e\gamma}$. Table 2.2 summarizes detector resolutions and the results of the most recent five $\mu^+ \to e^+\gamma$ search experiments.

The MEGA experiment [2], which is the lowest point in Figure 2.6, set the best upper limit on $\mathcal{B}(\mu \to e\gamma)$, 1.2×10^{-11}. As already stated in Section 2.2.2, over the past years, considerable interest in LFV processes, in particular $\mu \to e\gamma$, has arisen based on supersymmetric extensions of the Standard Model. Although the MEGA result is already significant in eliminating a good portion of the theoretical parameter space, the region allowed by the SUSY GUT theories still extends below by another few orders of magnitude in branching ratios. The MEG experiment aims at improving the sensitivity by at least two orders of magnitude over the current best limit to make a discovery.

Institute	Year	ΔE_e	ΔE_γ	$\Delta t_{e\gamma}$	$\Delta\theta_{e\gamma}$	Upper limit	Reference
TRIUMF	1977	10%	8.7%	6.7 ns		$< 3.6 \times 10^{-9}$	[42]
SIN	1980	8.7%	9.3%	1.4 ns		$< 1.0 \times 10^{-9}$	[41]
LAMPF	1982	8.8%	8.0%	1.9 ns	37 mrad	$< 1.7 \times 10^{-10}$	[43]
LAMPF	1988	8.0%	8.0%	1.8 ns	87 mrad	$< 4.9 \times 10^{-11}$	[11]
LAMPF	1999	1.2%	4.5%	1.6 ns	15 mrad	$< 1.2 \times 10^{-11}$	[2]

Table 2.2: Historical progress of the searches for $\mu^+ \to e^+\gamma$ since the era of meson factories with 90% C.L. upper limits in the era of the meson factories. Shown are the 90% C.L. upper limit on the branching ratio. The resolutions quoted are full widths at half maximum (FWHM)

2.4 Signature and Backgrounds

The event signature of $\mu^+ \to e^+\gamma$ is very simple and is characterized by a 2-body final state of the decay positron and γ-ray emitted collinear back-to-back with the same energy, 52.8 MeV, which corresponds to half the muon mass. The searches use positive muons decaying at rest. Negative muons are not used because they form muonic atoms when brought to rest and thus do not exhibit 2-body decay signatures. A $\mu^+ \to e^+\gamma$ event signature is shown here schematically, in Figure 2.7(a).

(a) $\mu \to e\gamma$ event signature (b) Physics Background (c) Accidental Background
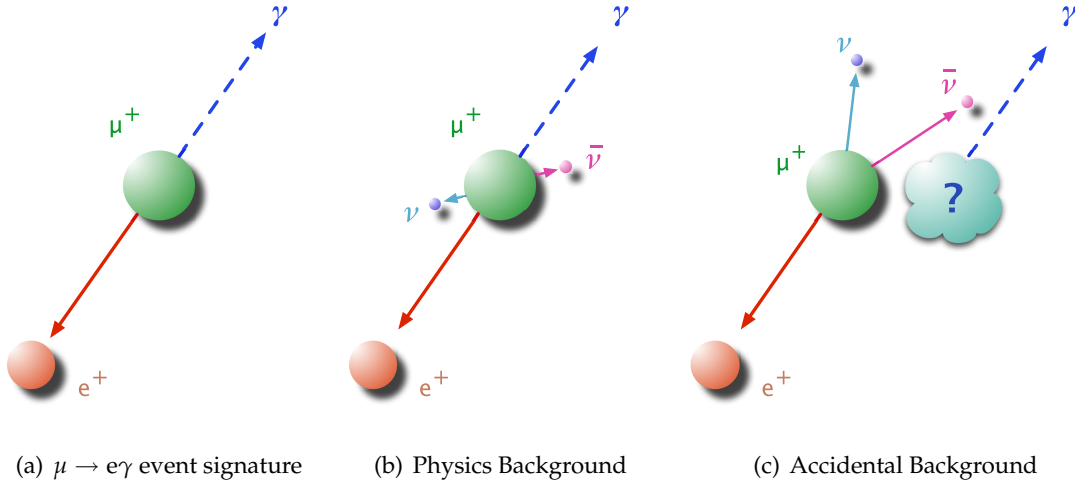
Figure 2.7: Schematic views of $\mu \to e\gamma$ event signature and backgrounds

There are two major backgrounds in the search for $\mu^+ \to e^+\gamma$. One is a physics (prompt) background from a radiative muon decay, $\mu^+ \to e^+\nu_e\bar{\nu}_\mu\gamma$, as shown in Figure 2.7(b). The other background is an accidental coincidence of a positron from a normal Michel decay, $\mu^+ \to e^+\nu_e\bar{\nu}_\mu$, with a high energy photon. The source of high energy γ ray is either a radiative decay $\mu^+ \to e^+\nu_e\bar{\nu}_\mu\gamma$, annihilation-in-flight or external bremsstrahlung of a positron, as shown in Figure 2.7(c).

2.4.1 Physics Background

As shown in Figure 2.7(b), one of the major backgrounds to the search for $\mu^+ \to e^+\gamma$ decay is a radiative muon decay, $\mu^+ \to e^+\nu_e\bar{\nu}_\mu\gamma$, where the positron and the γ-ray are emitted back-to-back with two neutrinos carrying off little energy. The differential decay width of a radiative muon decay was calculated [16, 18] as a function of positron energy (E_e) and γ-ray energy (E_γ) normalized to their maximum energies (of $m_\mu/2$), namely, $x = 2E_e/m_\mu$ and $y = 2E_\gamma/m_\mu$, where x and y range from 0 to 1. It also depends on the angle between the positron and the γ ray, $\theta_{e\gamma}$; here we introduce $z = \pi - \theta_{e\gamma}$. The radiative decays look similar to the $\mu^+ \to e^+\gamma$ decays when $x \approx 1$, $y \approx 1$, and $z \approx 0$.

When $x = 1$ and $y = 1$ exactly, the differential decay width vanishes. However, in a real case, finite detector resolutions introduce background events which would ultimately limit the sensitivity of a search for $\mu^+ \to e^+\gamma$. A further detailed consideration on the physics background will be made in Chapter 10.4.2.

2.4.2 Accidental Background

With a very high rate of muon decays, the accidental background (Figure 2.7(c)) becomes more important than the physics background. This is the case with the recent high rate experiments, including MEG and possible future experiments. The event rate of the accidental background normalized to the total decay rate ($\mathcal{B}_{acc}$) is written as

$$\mathcal{B}_{acc} = \mathcal{R}_\mu \cdot f_e^0 \cdot f_\gamma^0 \cdot \left(\Delta t_{e\gamma}\right) \cdot \left(\frac{\Delta\omega_{e\gamma}}{4\pi}\right), \tag{2.12}$$

where $\mathcal{R}_\mu$ is the instantaneous muon intensity. Here f_e^0 and f_γ^0 are the integrated fractions of the spectrum of the positron and the γ ray in the muon decay within the signal region, respectively. They include the corresponding branching ratios. The terms $\Delta t_{e\gamma}$ and $\Delta\omega_{e\gamma}$ are the full widths of the signal regions for timing coincidence and opening angle of the positron and the γ ray, respectively. A further detailed consideration on the accidental background will be taken later in Chapter 10.4.2.

As the muon rate has increased in the recent search experiments, the accidental background has become much more severe than the physics background which is typically an order of magnitude smaller. Because higher and higher muon rates are needed to achieve a better sensitivity to the branching ratio, *i.e.* **it is critical to make significant improvements in the detector resolutions in order to discriminate the accidental background effectively even with extremely high rate of muon decays.**

Chapter 3

MEG Experiment

In order to fulfill the ambitious goal, the MEG experiment is designed carefully and uniquely. The MEG apparatus consists of the Muon Beam Transport system and the detector system; the Photon Detector and the Positron Spectrometer. A schematic view of the MEG apparatus is shown in Figure 3.1. Provided muon beam is transported by the muon beam transport solenoid
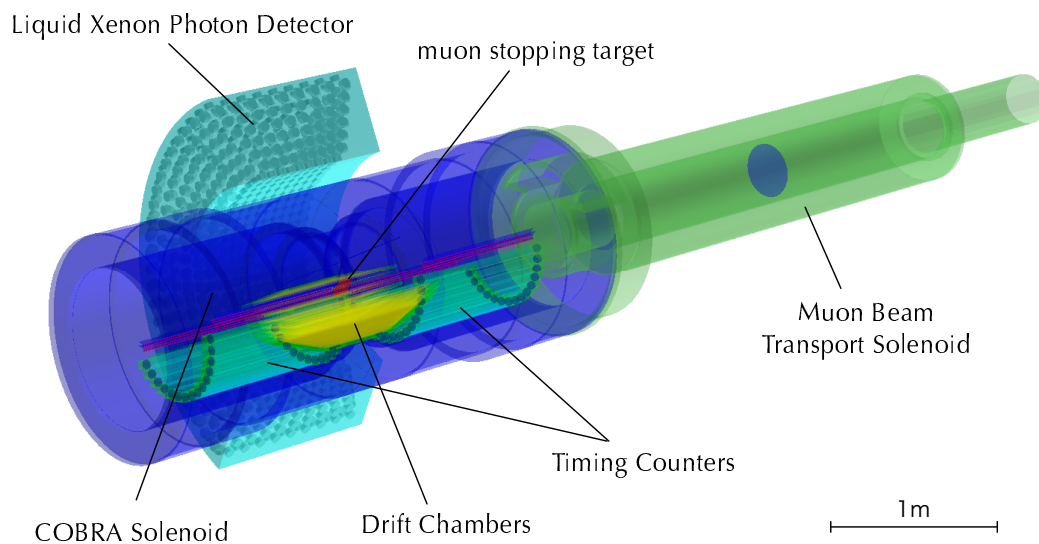
Figure 3.1: A schematic view of the MEG apparatus

towards a thin muon stopping target placed in the centre of the detector system. Emitted γ from the stopped muon decay impinges the Liquid Xenon Photon Detector that measures the energy, position, and timing of the γ simultaneously. Emitted positron to the oposit side is observed by the Positron Spectrometer. In the Positron Spectrometer, positron track is confined by the superconducting solenoidal magnet, called **COBRA** solenoid, and traced by the Drift Chamber system in order to measure the momentum and the direction of the positron. A hodoscope

array of plastic scintillators placed on each side of the spectrometer measures the timing of the positron together with its impact point.

In this chapter, the concept and the design of the MEG experiment are described in detail.

3.1 Beam

As mentioned in Section 2.3, the experimental upper limit of $\mathcal{B}(\mu \to e\gamma)$ had been improved primarily as the number of obserbed muons. In other words, increasing intensity of muon beam has a possibility to improve the sensitivity of the search for $\mu \to e\gamma$. However, it must be noted that increasing intensity of muon beam introduces tremendous amount of unwanted γ-ray production inside the apparatus, then they can easily create accidental coincidences between positron and γ close to the $\mu^+ \to e^+\gamma$ event signature. Consequently, a Direct-Current (DC) muon beam is the best solution for the $\mu^+ \to e^+\gamma$ search in order to minimize accidental overlap, since a pulsed muon beam makes it difficult to distinguish each event inside single bunch. A DC muon beam can suppress the rate of accidental coincidence while it increases the muon intensity.

Paul Scherrer Institut (PSI) runs several particle accelerators. The 590 MeV proton cyclotoron, with its 72 MeV companion preaccelerator, is one of them. It delivers up to 2 mA proton beam, 1.2 MW of beam power, which is the world record for such proton cyclotrons at present (2007). The design is based on criteria that allows operation at very high beam intensity; an open structure of four large and powerful RF-cavities providing a high acceleration voltage, and a flat-top cavity operating at the third harmonic of the accelerating RF-voltage. The resulting strong, phase-independent energy gain per revolution gives good turn separation and hence beam extraction with low beam losses.

This megawatt accelerator has played a role of *progenitor* of the world's most intense DC pion and muon beams and made it possible to measure the rare decays and the search for "classical" forbidden decay modes. The MEG experiment adopts this world's most intense DC muon beam.

3.1.1 Surface Muon

The term **surface muon** referes to the μ^+ formed from pions decaying at rest within a few μm of the surface of a meson production target [44]. Surface muons have a maximum momentum of 29.8 MeV/c and a momenrum spectrum which falls off as $p^{7/2}$ below this maximum. The primary advantages associated with surface muon beams are: (1) the high DC muon beam flux available due to the high pion stopping densities at the production target surface [44], (2) the high luminosity and good optics of the beam [45] due to the direct imaging of the meson production target, (3) the short range (<150 mg/cm^2) and low range straggling (<30 mg/cm^2) [45], allowing to use of very thin targets such as thin foils to stop muons, (4) the high ($\approx 100\%$) longitudinal spin polarization. In particular, (1) and (3) give important benefits to the $\mu^+ \to e^+\gamma$ search experiment. Needless to mention, (1) is the most important benefit increasing the number of obserbed muons. On the other hand, in order to suppress accidental overlaps it is

26

mandatory to reduce an amount of material of the muon stopping target as low as possible [*]. Thanks to (3), one can reduce the material amount of the target dramatically.

3.1.2 πE5 Beam Channel

In the PSI proton cyclotron complex, some of secondary beam channels provide high intensity surface muon beam. One of them, πE5 beam channel, is utilized as a muon driver for the MEG. The πE5 channel extracts low energy pion and muon beams from π/μ production target at an angle of 175° with respect to the primary proton beam as shown in Figure 3.2(a). The πE5 channel can be operated in two modes, called "U-branch" and "Z-branch", leading to different experimental areas, depending on the sign of the current in the second bending magnet AST. The beam-line studies have been performed to obtain the best choice of branch with the muon transportation system; it will be given in Section 3.1.3.

The main characteristics of the πE5 channel are listed in Table 3.1. In the middle of the beam

Beam Channel Length	10.4 m
Solid angle acceptance	150 msr
Momentum acceptance (FWHM)	10 %
Momentum resolution (FWHM)	2 %
Horizontal emittance	15.3 cm·rad
Vertical emittance	3.6 cm·rad
Spot size	4×4 cm^2

Table 3.1: Main characteristics of the πE5 beam channel

channel, where the momentum restricting slit system is located, the aberrations are rather large and therefore the momentum resolution is poor (2%). The situation is better at the final focus since the beam line is built up symmetrically causing some aberrations to vanish at the end. The positron content of the beam at the production is a factor of ten higher than the muon content, mostly because of the low energy positrons coming from the decays of the muons trapped in the target and from the conversion of photons from neutral pion decays.

3.1.3 Muon Beam Transportation to the MEG Detector Apparatus

From the end of πE5 beam channel to the MEG detector apparatus, the muon beam transportation system accompanied with some utilized magnet components is put into place. The beam must be manipulated before reaching the stopping target in order to accomplish two features; (1) Reducing the positron contamination in the muon beam; (2) Reducing the muon momentum in order to stop them in a thin target. The beam-line studies [46,47] converged towards the choice of Z-branch in which some elements are added between the end of last bending magnet ASC (*cf.* Figure 3.2(a)) and the MEG detector apparatus. The muon beam transportation system consists of the four main components: (A) The extraction element, called Triplet I, a quadrupole triplet which couples to the end of πE5 beam channel; (B) The WIEN-filter, an E∧B crossed-field, vertically deflecting separator, neccessary for good beam positron suppression;

---

[*]We will discuss it later in Section 3.2

(C) Triplet II, necessary for good optical focusing at the collimator system placed behind this triplet; (D) Beam Transport Solenoid, which is used as a coupling element to the final solenoid of the MEG detector apparatus, as well as housing the momentum degrader/collimator system.
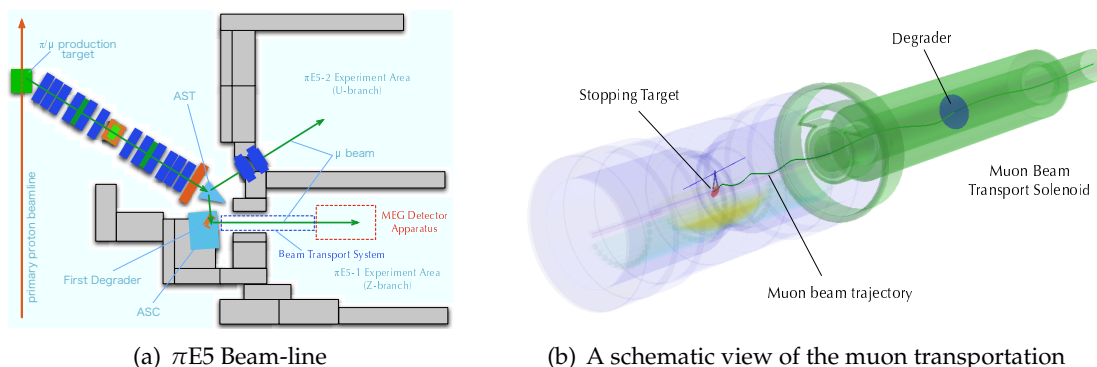

(a) πE5 Beam-line

(b) A schematic view of the muon transportation

Figure 3.2: Muon Beam Line

The WIEN-filter has a 19 cm gap with the horizontal magnetic field (133 Gaus) and the vertical electric field (195 kV) and is used as a velocity selector, thus enabling a spatial separation of muons and electrons. The vertical separation at the output of the filter amounts to 8.1 σ, where σ is the combined Root-Mean-Square (RMS) of the muon and positron beam envelope. A momentum degrader, 300μm thickness polyethylene-terephthalate $(C_5H_4O_2)_n$, is placed in the solenoid intermediate focus, in order to reduce the μ^+ momentum. Here is a schematic view of the muon transportat solenoid after the last quadrupole triplet towards the MEG apparatus and a trajectory of transported muon, Figure 3.2(b). In these conditions up to 1.0×10^8 μ^+/sec can be focused in a ellipsoidal spot, whose axes measure σ_x = 9.5 mm and σ_y = 10.2 mm at the position of the muon stopping target.

3.2 Target

The muon stopping target is placed at centre of the MEG detector, and should be enough thin since the positron tracking acuracy can be affected very easily by target material. As we discussed in Section 2.4, the detector resolution is essential to the $\mu^+ \rightarrow e^+\gamma$ search experiment, and hence the amount of material, which positron passes through, should be minimized. This is also important from the γ detection point of view, because the target material can cause unwanted γ-ray backgrounds for the photon detector by positron annihilation in the target. In order to fulfill such requirements, the muon stopping target is slightly slanted with respect to the beam axis to have enough muon stopping power while it is keeping the amount of material. Figure 3.3 schematically shows slanted muon stopping target[†]. Various materials were considered in the design stage, namely polyethylene $(CH_2)_n$, polyethylene-terephthalate, polyimide $(C_{22}H_{10}N_2O_5)_n$, both for their stopping power and short radiation length. Polyethylene was

---

[†] The incline angle of the target with respect to the beam axis was 12.8° for the MEG Engineering Run 2007. This was determined due to some problems of design work, and this should be optimized in the MEG Physics Run 2008.

found to be the best material mainly because of its longer radiation length.
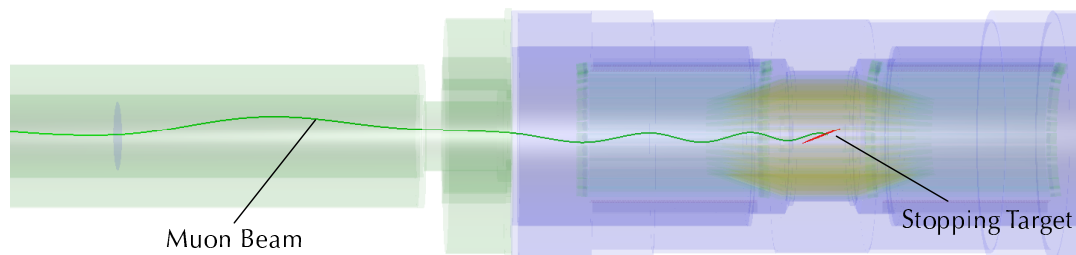
Figure 3.3: slant target and the beam
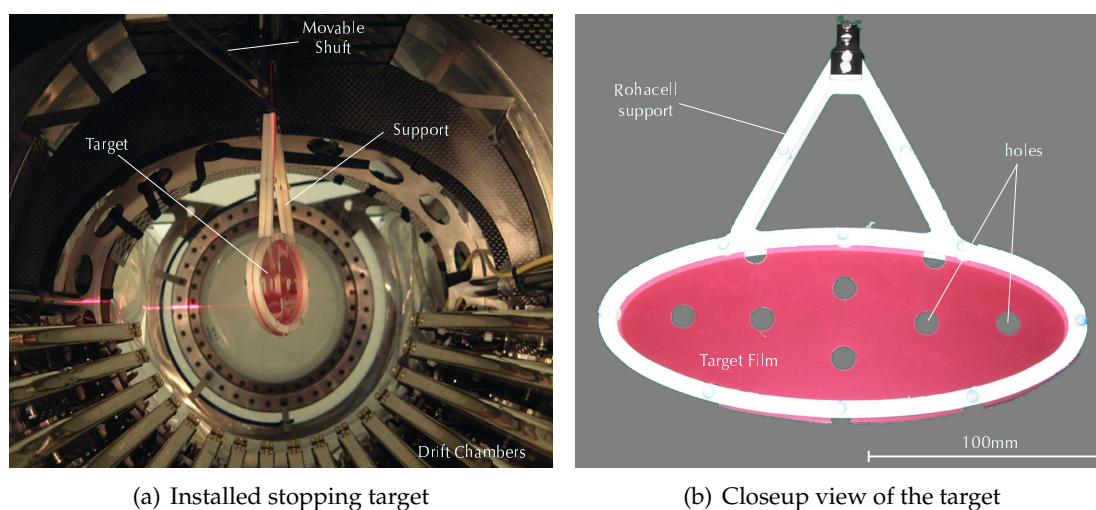
(a) Installed stopping target   (b) Closeup view of the target

Figure 3.4: Target Pictures

Figure 3.4(b) is a closeup view of the target. The target itself is made of thin polyethylene film, 205 μm thickess, and supported by the **Rohacell®** [‡]. **Rohacell®** is a polymethacrylimide hard foam; that is used as a core material for sandwich constructions. It shows outstanding mechanical and thermal properties and it is extremely light material. Its density is 0.05 g/cm^3 and radiation length is 820 cm. The target foil is sandwithced by the **Rohacell®** supporting frame as shown in Figure 3.4(b). In this picture, one can see six holes 10 mm in diameter on the target; these holes are created in order to align the target position by using data itself and to evaluate the performance of the muon decay position reconstruction.

[‡] **Rohacell®** is the proprietary name and developped by Degussa AG, currently Evonik-Degussa GmbH [48].

3.3   Positron Spectrometer

The momentum and direction of emerging positron are measured precisely by a "COnstant-Bending-RAdius (COBRA) spectrometer", which consists of a superconducting solenoidal magnet specially designed to form a highly graded field, an ultimate low-mass drift chamber system, and a precise time measuring counter system. Figure 3.5 is a schematic view of the positron spectrometer. The positron spectrometer holds the key for leading MEG to a suc-
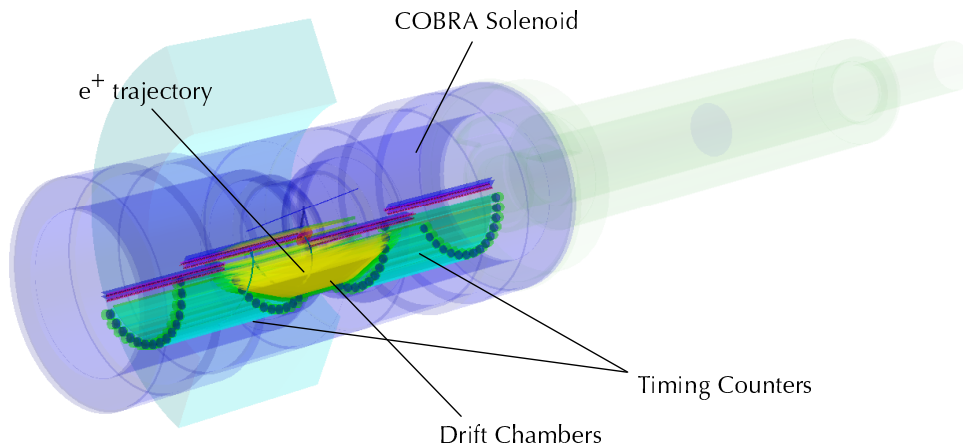
Figure 3.5: A schematic view of the e^+ spectrometer

cessful conclusion and has to satisfy several important requirements. In order to realize such requirements, the MEG positron spectrometer adopts an indeed ambitious design. Details of the spectrometer will be described in chapter 4.

3.4   Photon Detector

While all positron are confined by the bendings, the γ ray pass through the thin superconducting coil of the spectrometer with ≈ 80 % transmission probability, and are detected by a liquid Xenon scintillation detector, which is filled with over 0.8 m^3 of liquid xenon surrounded by 846 photo-multiplier tubes (PMT) [49, 50]. The PMTs are immersed in the liquid xenon to observe scintillation photons without using any transmission window. Figure 3.6 is a schematic view of the liquid xenon schintillation photon detector. As shown in the figure, the photon detector is C-shaped to fit the outer radius of the solenoidal magnet and located next to the positron spectrometer, covering ≈ 10 % of the solid angle viewed from the muon stopping target. In the figure, many PMTs are colored and each color indicates the amount of observed scintillation light. Liquid xenon scintillator has high light yield (≈ 80 % of NaI(Tl)) and fast response, which are the most essential ingredients for precise energy and timing resolutions re-
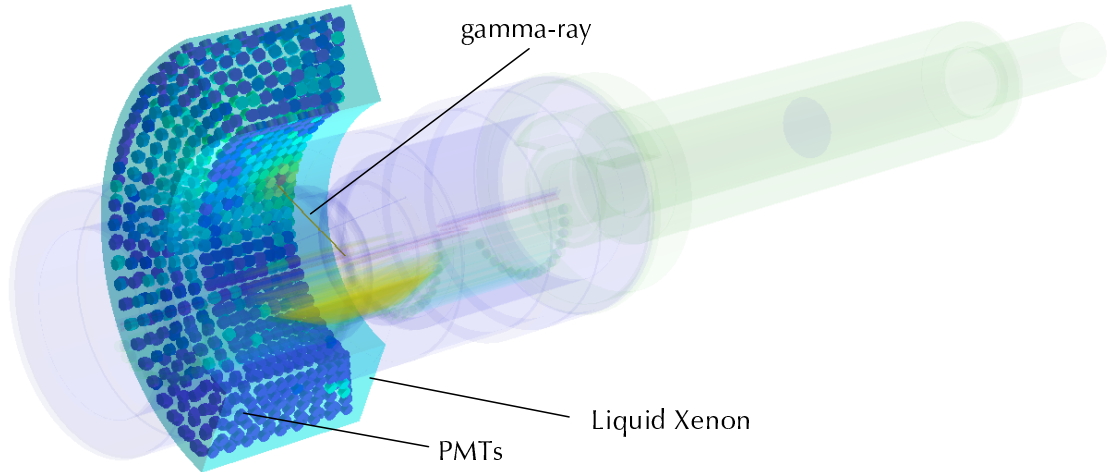
Figure 3.6: A schematic view of the liquid xenon scintillation photon detector

quired for this experiment. The characteristics of xenon are summarize in Table 3.2 with other two noble gases, Ar and Kr, as a comparison. Liquid xenon is the most interesting, having the

	Ar	Kr	Xe
Density ρ (g/cm^3)	1.39	2.45	2.98
Mass number Z	18	36	54
Scintillation light wave length λ_{peak} (nm)	128	147	178
Boiling point (K)	87.3	119.9	167.1
dE/dx for MIP (MeV/cm)	2.11	3.45	3.89
Radiation length X_0 (cm)	14.3	4.76	2.77
Molière radius (cm)	7.3	4.7	4.1
Decay time (fast components) τ_1 (ns)	6	2	4
Decay time (slow components) τ_2 (ns)	1000	91	22
Decay time (recombination) τ_r (ns)	-	-	45

Table 3.2: Characteristics of Ar, Kr and Xe

longest wavelength, the fastest response and the shortest radiation length.

We constructed a prototype liquid xenon detector in order to gain experience with the detector operation and to investigate its performance [51, 52]. The depth of the prototype along the incident γ-ray direction is as long as that of the final detector in order to contain whole showers up to the energy of the $\mu^+ \rightarrow e^+\gamma$ signal, namely, 52.8 MeV. The prototype has a fiducial volume of 70l and is surrounded by 238 PMTs. At the early stages of the prototype detector study it was soon realized that the purity of liquid xenon is crucial for scintillation light

collection. More than one year was needed to fully understand and solve this problem, with the ultimate introduction of a xenon circulation and purification system to guarantee a sufficient transparency of xenon to its scintillation light [53, 54]. Only after this was accomplished we succeeded to start reliable measurements of the detector performance obtained excellent resolutions for each measurements; energy resolution $\sigma_{E_\gamma} = 2\%$ (for 55MeV γ ray); position resolution $\sigma_{x_\gamma} = 4 \sim 5$ mm; timing resolution $\sigma_{t_\gamma} = 65$ps [55].
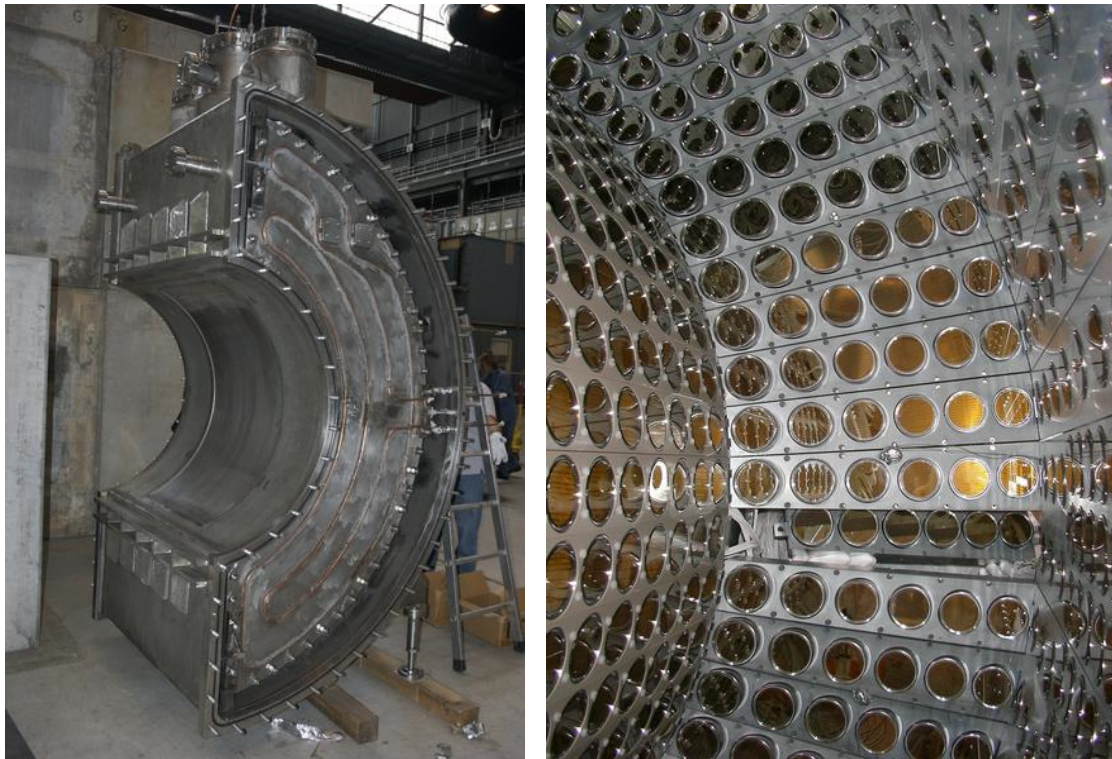
(a) Cryostat of the liquid xenon detector   (b) PMTs viewed from detector inside

Figure 3.7: Construction of the Liquid Xenon Scintillation Photon Detector

After intensive studies using the prototype, we started construction of the final liquid-xenon photon detector. Figure 3.7 show the actual liquid-xenon photon detector.

3.5 Trigger and Data Aquisition

Here we roughly summarize the trigger electronics and the data aquisition system (DAQ) for the MEG experiment. The signature of a $\mu^+ \to e^+\gamma$ is a back-to-back $\gamma - e^+$ pair coincident in time, each carrying half the muon mass of energy. The experiment trigger therefore requires the presence of two high-energy particles with opposite momenta. The information available at trigger level comes from the liquid xenon detector and from the timing counter, the information from the drift chamber is too slow due to the electron drift time. Trigger rates have been

estimated taking into account the main sources of background.

All the signals, PMTs and drift chambers, are individually recorded as digitized waveform by a custom chip, called **Domino Ring Sampler** (**DRS**) [56]. Recording all the waveform may cause difficulties concerning data size, DAQ flow speed *etc.*, however the rewards outweighed the work and difficulties, because waveform digitizing on all channels gives an excellent handle to identify the pile-up event and to suppress noise that can worsen detector resolutions.

3.5.1 Trigger

The trigger system for the MEG experiment is based on the coupled use of Flash Analog to Digital Converters (FADC) and Field Programmable Gate Arrays (FPGA). All the analog-output signals are sampled with FADCs at 100 MHz, and the digitized information is analyzed by means of FPGAs.
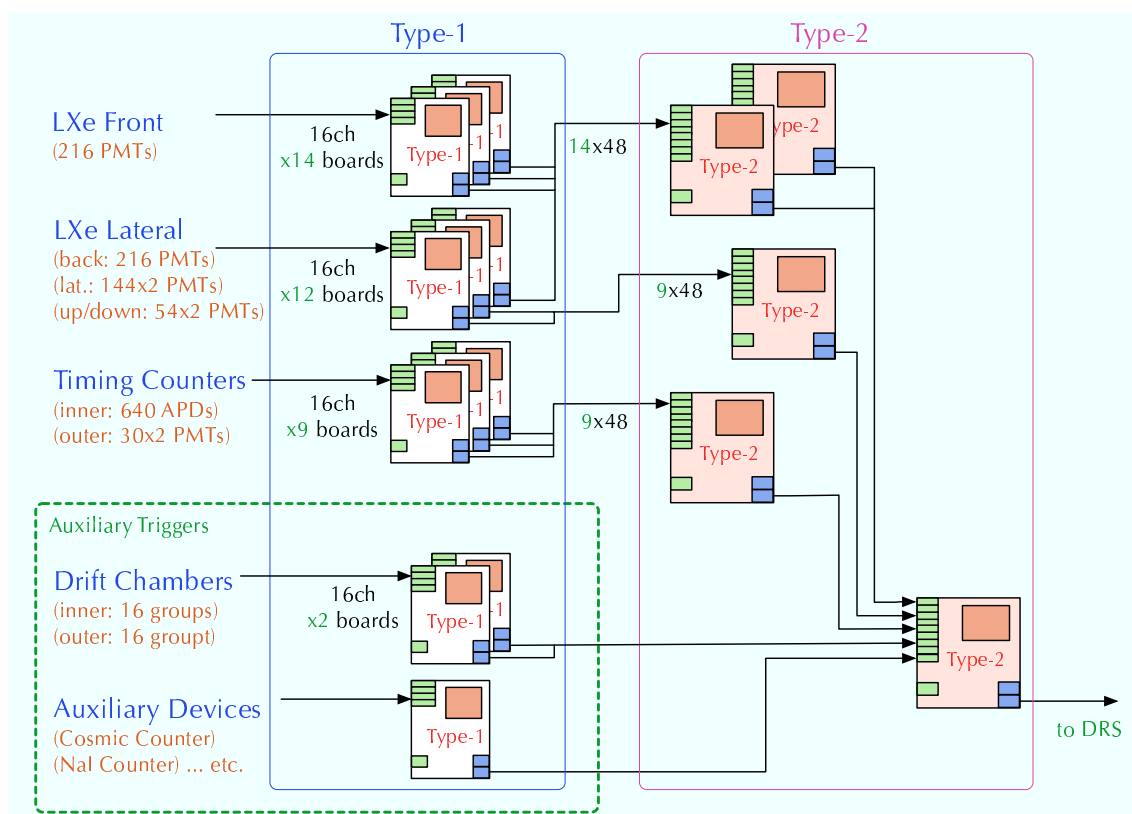
Figure 3.8: A Schematic View of Trigger Flow

The complete system is arranged in a tree structure on three layers with two different types of boads as schematically shown in Figure 3.8. The first layer consists of boards, called Type1. A board Type1 receives and digitizes the PMT analog signals from the liquid xenon detector and the timing counter, implements some reconstruction algorithms on a large size FPGA and sends the reconstructed informations to the successive trigger layer through Low Voltage Differential Signaling (LVDS) serialized connections. The two remaining trigger layers consists of

a second type of boards, named Type2. The reconstruction algorighms are completed on the board Type2, and the trigger signal is generated.

The information provided by the liquid xenon photon detector and the positron timing counter is sufficient to generate the MEG event trigger at an acceptable rate. The photon energy is determined by the sum of the light collected by all PMTs, while its direction is determined by the position of the PMT with the largest signal. The photon conversion time is extracted from the rising edge of this PMT signal. The estimated trigger rate for photons with energy larger than 45 MeV is $\mathcal{R}_\gamma \approx 600$ Hz for a muon stopping rate of $\mathcal{R}_\mu = 3 \times 10^7$ sec^{-1}. On the other hand, the presence of a time-coincident positron is provided by the timing counter; its radial position already excludes most of low momentum positrons. The overall rate on each of the two timing counters due to Michel positrons is estimated to be $\mathcal{R}_{e^+} \approx 6 \times 10^5$ Hz. The azimuthal segmentation of the timing counter allows for a corrrelation of the positron direction with that of the photon, with a rejection factor of $f_\phi \approx 5$. If we adopt a coincidence window of $\Delta T = 10$ ns, the rate of MEG event trigger for a muon stopping rate of $\mathcal{R}_\mu = 3 \times 10^7$ sec^{-1} is

$$\mathcal{R}_{\text{MEG}} = 2\Delta T \mathcal{R}_\gamma \frac{\mathcal{R}_{e^+}}{f_\phi} \approx 6\text{Hz}.$$

In addition to the MEG event trigger, there are several alternative trigger settings for many purposes quoted as "Auxiliary Triggers" in Figure 3.8; pedestal trigger, calibration triggers for each sub-detectors, *etc.* In particular for the drift chambers, three types of trigger are prepared in order to acquire the cosmic-ray muons and Michel positrons to perform several kinds of calibrations effectively. Concerning such special trigger modes, we will discuss it later in another chapter related with the drift chamber calibrations, chapter 8.

3.5.2 Waveform Digitizer

The **DRS** is a high resolution analog signal sampling chip. The DRS chip contains 1024 capacitive sampling cells fabricated in a 0.25 μm CMOS processor. The sampling frequency is generated on the chip itself and variable from 0.5 to 4 GHz. The cells are read out at 40 MHz with an external 12 bit FADC. The chip contains 8 input channels with a voltage limit of 2 Volts.

The analog signal is stored in a switched-capacitor array (SCA) with 1024 cells organized as a ring buffer so that the switched-capacitors are sequentially enabled by an inverter chain, referred to as a **Domino wave**. The speed of the domino wave is controlled by an external voltage such that the domino inverters can be seen as a Voltage-Controlled-Oscillator. The phase and speed of the domino wave are synchronized to an external common reference clock by an on-board Phase-Locked loop. Once an external trigger is received, the sampled signal is frozen in the SCA and read out in a shift register and digitized at high resolution (12 bit), at low frequency (30 MHz) with an external FADC.

In the MEG experimnt, all the detector outputs are individually recorded in DRS; the PMT signals are digitized at 2 GHz (500 ps bin width) in order to be able to obtain a timing resolution of 50 ps by bin interpolation, and the drift chamber signals are digitized at 500 MHz (2 ns bin width) in order to compensate wide drift time distributions. A 500 MHz sampling by 1024 cells is corresponding to 2 μsec time-window, which is enough covering the wide drift time distribution. Figure 3.9 is an example of the DRS waveform of the drift chamber anode signal. Figure 3.9(a) represents a raw waveform that is recorded in 2 μ sec time-window, and Figure

(a) 2 μsec DRS time-window   (b) Closeup view in 700 nsec time-window
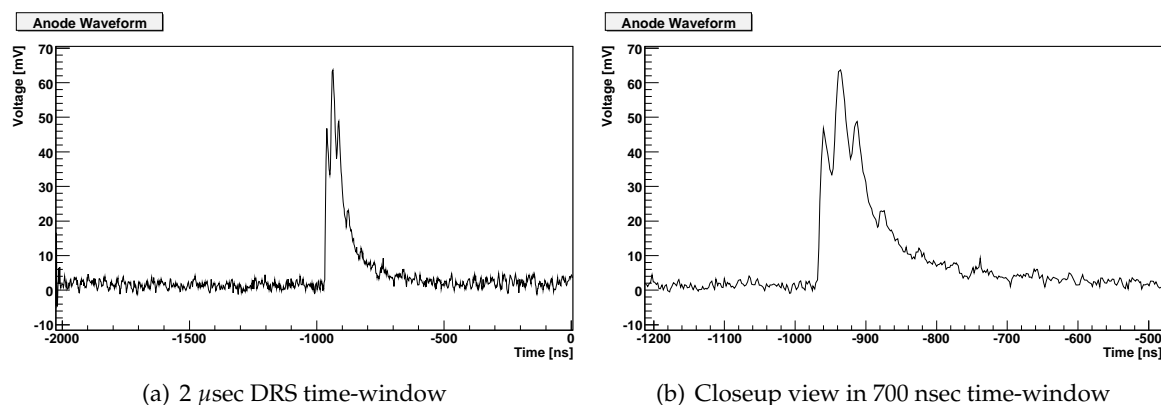
Figure 3.9: An example of the DRS waveform from Drift Chamber

3.9(b) is its closeup view in 700 nsec time-window in order to see a fine structure of recorded pulse, especially leading-edge neighborhood. As described above, all the sampled voltages are frozen in the SCA when an external trigger is fired, and hence the final cell of the domino chain corresponds to the zero-time; all other cells store the sampled voltage going into the past 2 μsec from the zero-time. One can see the negative time axis in Figure 3.9 due to this mechanism.

The flush timing of DRS can be delayed from the external trigger. By using this functionality the trigger latency is arranged so that the triggering pulse appears around the centre of time-window, and thus the additional delay cables are not necessary. Consequently, one can recognize the objective pulse in the DRS-waveform output clearly, and hence, this helps much to eliminate the pile-up pulses in the offline analysis.

A general information of the DRS chip is available in Ref. [56], and detailed calibration method and properties of the current version [§] of the DRS chip, "DRS2", are described in Ref. [58]. Three calibrations, namely *response-*, *offset-*, and *time-*calibration, are necessary for the DRS2. When the DRS2 is heated up, the deviation from the real response increases. In order to avoid this deviation, the response calibration is required to be carried out at frequent intervals. This tememperature dependence also causes a serious deterioration on the detector resolution. This issue is described in Appendix A, and we will discuss this effect as a source of systematic uncertainty to the detector resolution in Section 10.1.4. All such problems are fixed in the DRS4, *i.e.* the MEG *physics* data-taking will not be suffered from this kind of problem.

3.6   Current Status of the MEG Experiment

In the summer 2007, construction of all the main detector components was completed. Then we started the detector operation in a phased manner.

Liquid-xenon γ-ray detector started several studies; the liquefaction test, liquid xenon transfering test, keeping long term monitoring, stability checks, PMT gain calibrations, liquid xenon purification *etc*.

[§] The first version of the DRS chip was developed in 2001 at PSI, and after that, it has been revised continouslly. The next version of the chip is DRS4 (2008). For this thesis, DRS2 [57] has been used for all the data taking.

In parallel with this, positron-spectrometer conditioning was performed; drift chamber gas control test, high-voltage conditioning, wire alignment by using cosmic-rays, position-measurement calibration, relative gain calibration *etc*.

After such fundamental studies and conditionings, the muon-beam commissioning was performed with the final detector apparatus.

After the muon-beam commissioning was completed, we started **the engineering run** in the autumn/winter 2007. We successfully ran the whole program of the engineering run. All the detector components were installed and operated over 4 months; trigger and DAQ electronics were integrated and data-taking worked at expected event rate; a full set of calibration has been performed.

The physics data that has been taken at the engineering run is being analyzed during the winter shutdown 2007-2008, and its results will give a certain feedbacks to the detector maintenances and also the offline-analysis development. One of the most important analysis of engineering run 2007 are to establish the positron-tracking algorithm for the COBRA spectrometer, to evaluate the spectrometer performances, and to estimate the feasible sensitivity of MEG.

Chapter 4

COBRA Spectrometer

In this chapter, the MEG positron spectrometer is explained in detail, its principle, concept and design.

The MEG positron spectrometer, called **COBRA spectrometer**, schematically shown in Figure 4.1, consists of a superconducting solenoidal magnet specially designed to form a highly graded field, an ultimate low-mass drift chamber system, and a precise time measuring counter system.
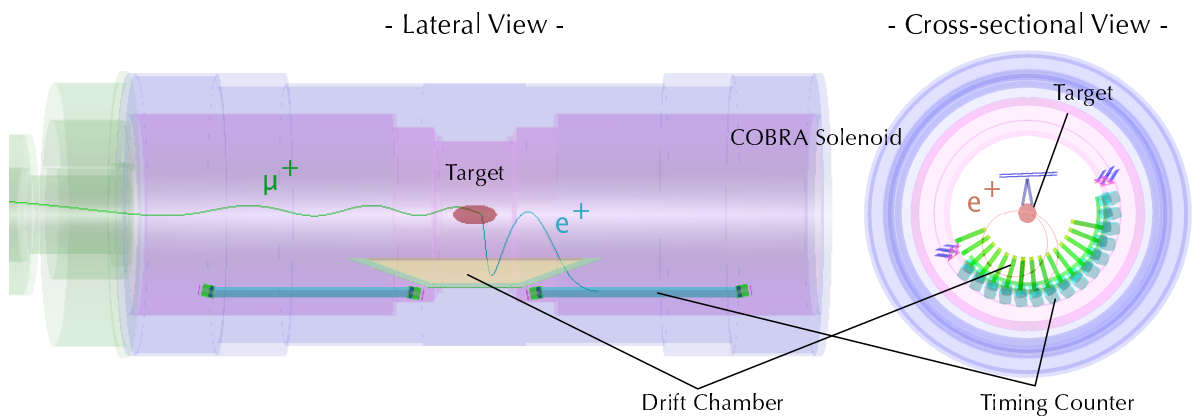
Figure 4.1: A schematic view of the e^+ spectrometer

The positron spectrometer has to satisfy several requirements. First, **the spectrometer must cope in a stable way with a very high muon rate up to** $3 \times 10^7 \text{s}^{-1}$. Second, **a very-low-mass tracker is required** since the momentum resolution is limited primarily by multiple Coulomb scatering. Furthermore, **it is also impotant to minimize the amount of material** from the point of view of background suppression in the γ-ray suppression for the photon detector. Additionally, **excellent bidirectional position resolution is necessary for both the transvers and longitudinal directions.** Finally, **extremely good timing resolution is also needed in order to suppress accidental overlap of events.**

However, it is prohibitively difficult to realize all requirements well. If one try to realize the first requirement, the tracker will get serious difficulties because the muon stopping rate has already achieved extremely high. If we assume that the nominal operation rate of the MEG is $3 \times 10^7 \mu^+ \text{s}^{-1}$, same amount of decay positrons will be generated inside detector immediately. In such a high dose irradiation, no wire chamber can cope. Of course, in the world of high energy physics experiment, there are special wire chambers which are designed to be operational with very high rate. But such a chamber can not have excellent resolutions and also have relatively large amount of material, because effective quenching gas, so-called *fast gas*, has to be used and such gas usually has large Z. Even if one can operate a wire chamber with such a high rate, off-line analysis will confront severe problem concerning the track following, since tremendous trajectories overlapped in a single event. Such a problem may be solved by adopting up-to-date pattern recognition algorithms. In fact, many high rate experiments, *e.g.* hadron collider experiments or heavy ion collision experiments, can handle tremendous trajectories simultaneously by adopting various pattern recognitions. However, it must be noted that such a pattern recognition will require reasonable number of position measurements in order to perfom track finding effectively. This means that we have to increase the number of tracking devices or wire densities and this is not a suitable remedy for the MEG. In consequence, it is extremely difficult to realize all requirements simultaneously by the combination of usual solenoidal field and a tracker based on the wire chamber.

In order to attain such high requirements, we adopted a specially designed solenoidal magnet with a highly graded field. The MEG solenoidal magnet is designed to change its radius between the centre and the outside as schematically shown in Figure 4.2(b). This provides a graded magnetic field (1.27 T at $z = 0$ and decreasing as $|z|$ increases, 0.49 T at z=1.25 m, where z is the coordinate along the beam axis) and allows to solve the problems inevitable in a normal uniform solenoidal field. In a normal uniform solenoidal field, positrons emitted close

(a) Uniform B-field   (b) COBRA field
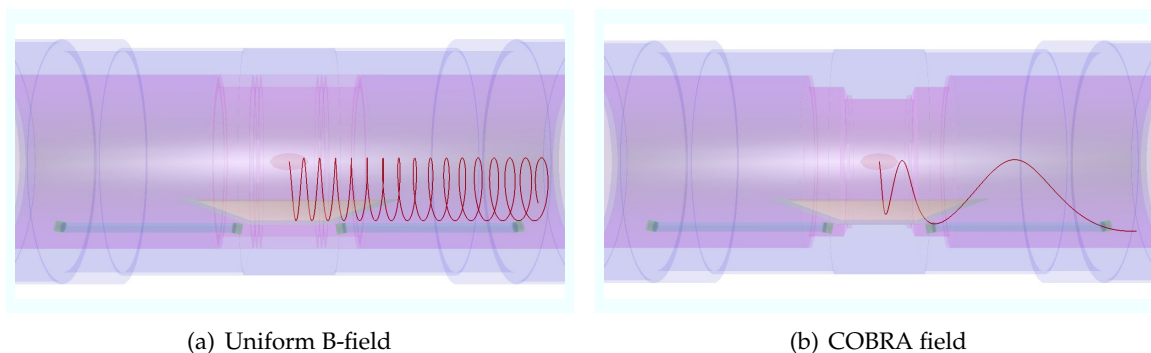
Figure 4.2: Advantage of COBRA (1)

to 90° undergo many turns in the tracker volume, as shown in Figure 4.2(a). However, the MEG solenoidal magnetic field can sweep such positrons out of the fiducial tracking volume effectively, as shown in Figure 4.2(b). In addition, this special magnetic field has yet another advantage. In this specially designed field, positrons with the same absolute momenta follow trajectories with a **CO**nstant projected **B**ending **RA**dius, this is the origin of the name of CO-BRA spectrometer, independent of the emission angles, as shown in Figure 4.3(b), while in a

uniform solenoidal field the radius depends on the emission angle, as shown in Figure 4.3(a). This allows us to sharply discriminate high-momentum signal positrons from the tremendous

(a) Uniform B-field   (b) COBRA B-field
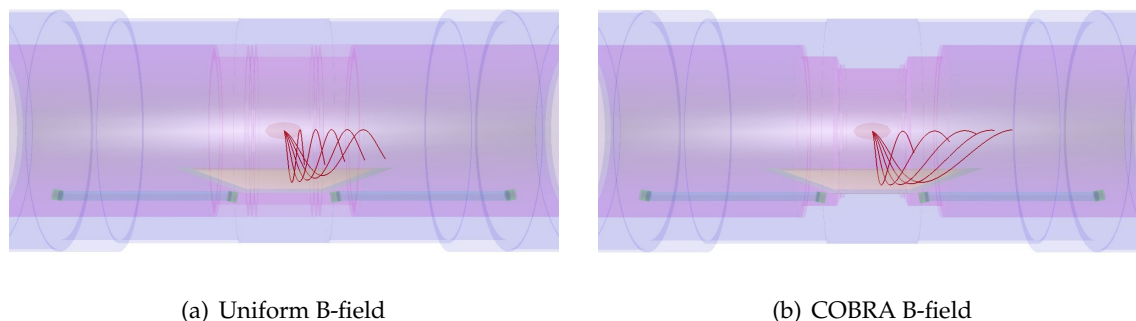
Figure 4.3: Advantage of COBRA (2)

Michel positron background originating from the target. The COBRA spectrometer therefore does not need to measure the positron trajectory in the small-radius region. This does not cause any loss of efficiencies of signal positrons. In other words, **the drift chambers can be sensitive only to higher momentum positrons and blind to most of the Michel positrons that can cause accidental coincidences.** Thanks to this COBRA magnetic field, we can reduce a hit rate for the drift chambers drastically, as shown in Figure 4.4.
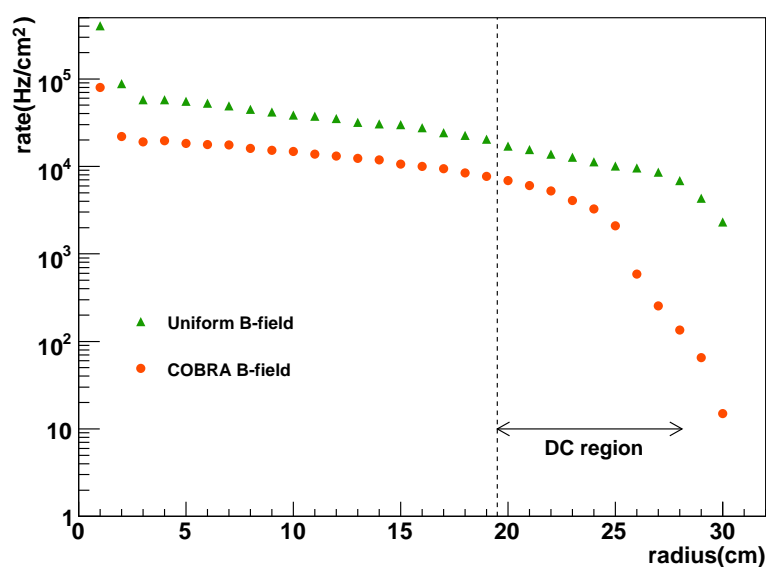
Figure 4.4: Rate of Michel e^+ per cm^2 per second as a function of radius assuming muon decay rate of 3×10^7/sec.

4.1 COBRA Magnet

The superconducting solenoidal magnet for MEG, COBRA magnet [59], is designed to realize such a highly graded magnetic field. The COBRA magnet consists of a main superconducting magnet and a pair of compensation coils in order to reduce stray field around the photon detector to be placed next to the main magnet (see Figure 3.6). The layout and the dimension is shown in Figure 4.5(a) and its completed picture is shown in Figure 4.5(b). The superconduct-

(a) Layout

(b) Completed Picture
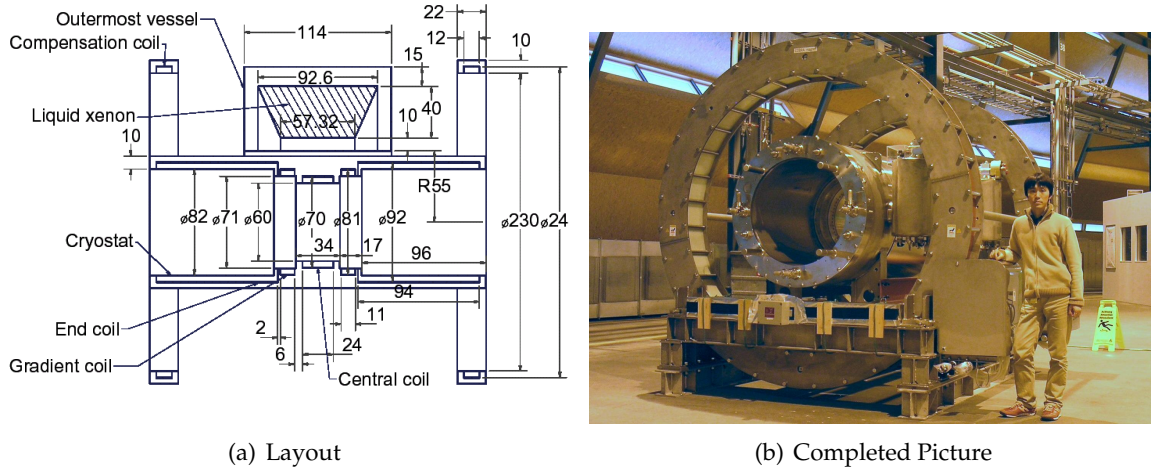
Figure 4.5: The COBRA magnet

ing magnet consists of five coils with three different radii: one central coil, two gradient coils and two end coils. The end coil is separated into inner and outer parts with different current densities. Main parameters of the superconducting magnet are listed in Table 4.1. It is also

| Coil	Central	Gradient	Inner end	Outer end
Inner dia. (mm)	699.1	809.1	919.1	919.1
Outer dia. (mm)	711.6	820.6	929.5	929.5
Length (mm)	240.3	110.4	189.9	749.2
Number of Layers	4	4	3	3
Number of Turns	1068	399	240	1548
Winding density (Turns/m)	4444.4	3614.1	1263.8	2066.2
Current (A)	360	360	360	360
Inductance (H)	1.64	0.62	0.35	2.29
Energy (kJ)	106	40	23	148

Table 4.1: Parameters of the superconducting coil of the COBRA magnet

important to make the coil as transparent as possible, since signal γ-ray from the target passes through the coil. In order to realize such a requirement, a high-strentgh aluminum stabilized conductor is adopted for the superconducting magnet. It allows to minimize the thickness of the support cylinder of the superconducting magnet. A copper matrix NbTi multi filamentary

core wire is clad with aluminum stabilizer. Aluminum stabilizer can be reinforced by adding small amount of metals such as nickel, magnesium, and copper while keeping electrical resistivity as low as possible. Nickel at 5000 ppm is added into the aluminum-stabilizer in the conductor. A cross-sectional view of the conductor is shown in Figure 4.6(a). The field gradient

(a) Cross-section of the conductor (b) Schematic view of the winding
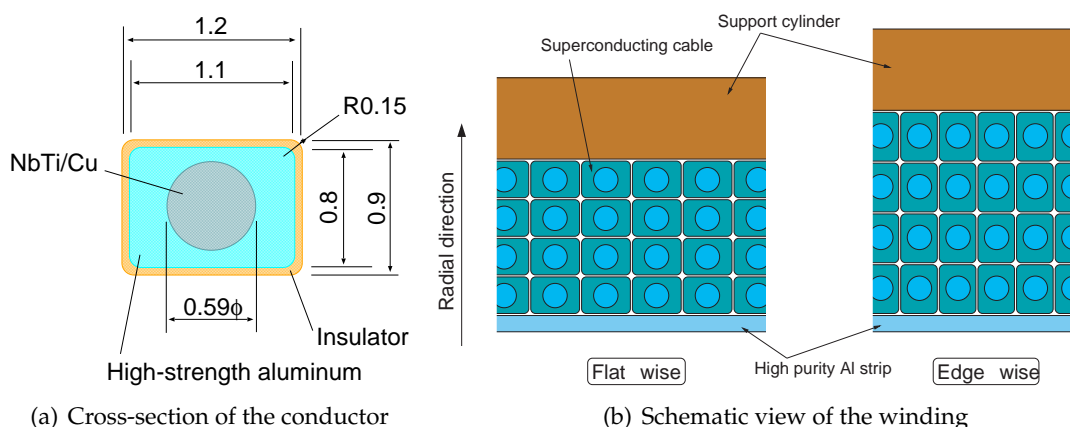
Figure 4.6: Conductor of the COBRA superconducting magnet

is arranged by a step-structure in the coil layout and adjusting winding density in each coil. The layer structure is schematically illustrated in Figure 4.6(b). As listed in Table 4.1, number of layers are different for each part of the coil to realize different current densities. In the central coil the conductor is densely wound "Edge wise" in four layers inside a 2 mm thickness aluminum support cylinder, and end-coil parts are wound "Flat wise", as shown in Figure 4.6(b). Thanks to adopting such a *self-stabilized* conductor and thin support, within the acceptance of the photon detector, the thickness of the magnet could be reduced down to 0.197 X_0 so that the γ-rays can pass through it with $\approx$ 80 % transmission probability.
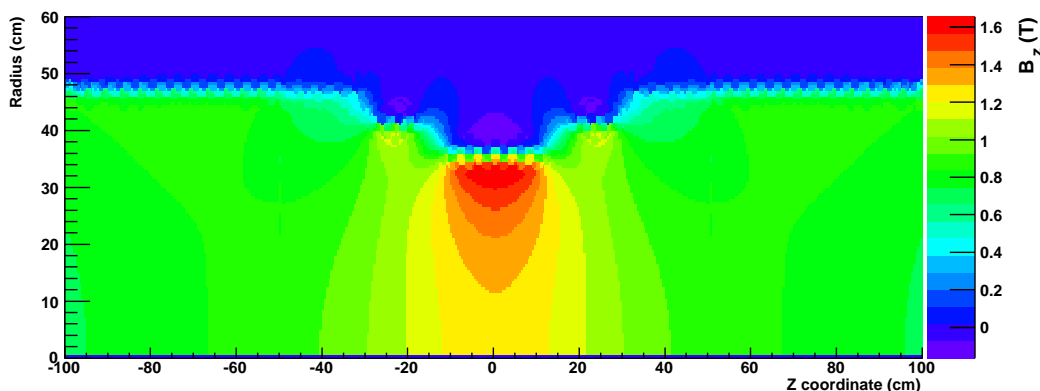
Figure 4.7: Contour plot of the COBRA magnetic field

Figure 4.7 shows a contour view of the COBRA magnetic field strength. "Z" coordinate, which is along the beam axis, is corresponding to the magnet axis, and the origin of this coordinate is the position of the muon stopping target. From the figure, one can see the *sand glass* structure of the COBRA field following the concave coil surface and highly graded field from 0.5 to 1.7 T.

The stray field from the superconducting magnet could degrade the performance of the liquid xenon photon detector because the PMT gain rapidly drops as the strength of applied magnetic field increases. In order to avoid such an effect, one pair compensation coil is integrated with the COBRA superconducting magnet. Figure 4.8 shows the contour plot of the COBRA magnetic field with the compensation coils. It can be seen the residual field is very small (<50 Gaus) over the photon detector region.
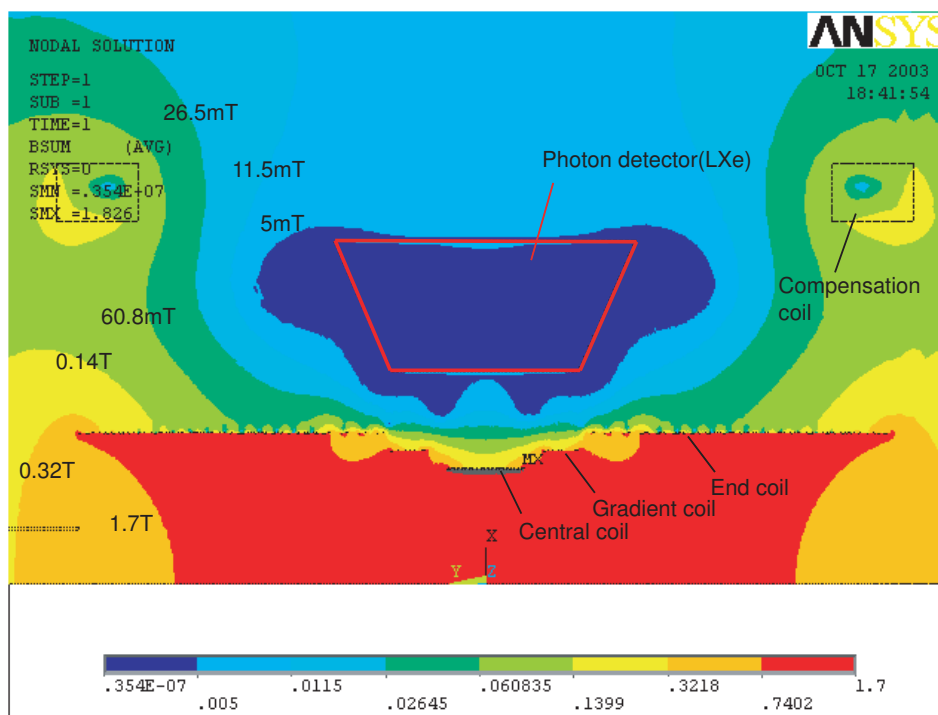
Figure 4.8: Contour plot of the residual magnetic field

4.2 Drift Chamber

Positron tracks are measured by 16 drift chamber modules aligned radially at $10.5°$ intervals in azimuthal angle. For each drift chamber module, two layers of axial sense wires and potential wires stretched by a 4.5 mm pitch, are formed on a carbon fibre frame. Each layer is isolated by a ultra-thin cathode foil and shifted by one-half cell to allow a local resolution of left-right ambiguity. Figure 4.9 shows an schematical view of the drift chamber tracking system and traced positron trajectory. In order to satisfy all requirements for the positron spectrometer
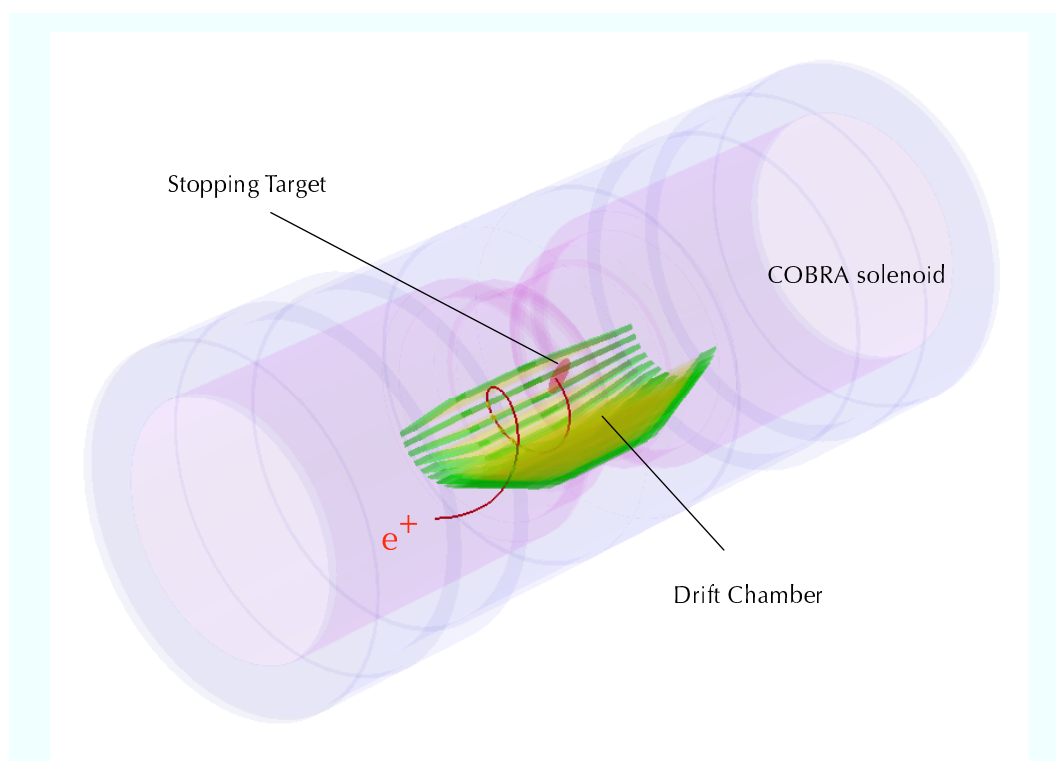
Figure 4.9: A schematical view of the drift chamber system and traced e^+ trajectory

which are listed in the outset of this chapter, an innovative drift chamber has been developed. This development has been carried out by indeed unique approach and this is essential for unprecedented senstivity of the MEG experiment.

The detailed description concerning the drift chamber system is given in the next chapter.

4.3 Timing Counter

Timing information and hence trigger information for the positrons are provided by a set of fast, double-layerd, orthogonally placed hodoscope arrays, positioned at both ends of the spectrometer. The timing counter consists of two sub-detectors; the outer layer counter and the inner layer one. Each sub-detector is optimized for each specific task. The outer layer counter, called $\phi-$counter, is designed to obtain a precise timing of the incident positron as well as a fast estimation of the positron emission angle ϕ. On the other hand, the inner layer counter, called z-counter, is optimized to give a reliable first level trigger, along with the determination of the impact point in z on the timing counter, which is related to the initial positron emission angle [60, 61].

The preliminary determination of the positron trajectory, provided by the timing counter, allows for the fast rejection of more than 95 % of events with unmatched kinematic parameters. Besides, this device will provide a very precise impact position information, *i.e.* allowing

for eventual corrections of the positron timing and giving one more constraint for the track reconstruction.

The timing counter system covers the same solid angle as the drift chamber, corresponding to the acceptance of the liquid xenon photon detector, given the positron trajectories inside COBRA magnet. The timing counter position extends over the region $25 < |z| < 105$ cm along the magnet axis and $220° < \phi < 380°$ in the azimuthal direction. The z-counter module is placed at the radius of 292.4 mm from the COBRA axis, while the ϕ-counter stands at $r = 320$ mm.

Each ϕ-counter consists of 15 plastic scintillation bars ($4 \times 4 \times 90$cm^3, BC404 [62]) with 2″ fine-mesh PMTs (HAMAMATSU R5924 [63]) on both ends. A schematic view is shonw in Figure 4.10(a) with positron trajectory and its completed picture is also presented in Figure 4.10(b). Each bar is stacked with a radial coverage of $10.5°$, *i.e.* the whole ϕ-counter covers over $160°$ in ϕ.

(a) A schematic view   (b) Completed Picture
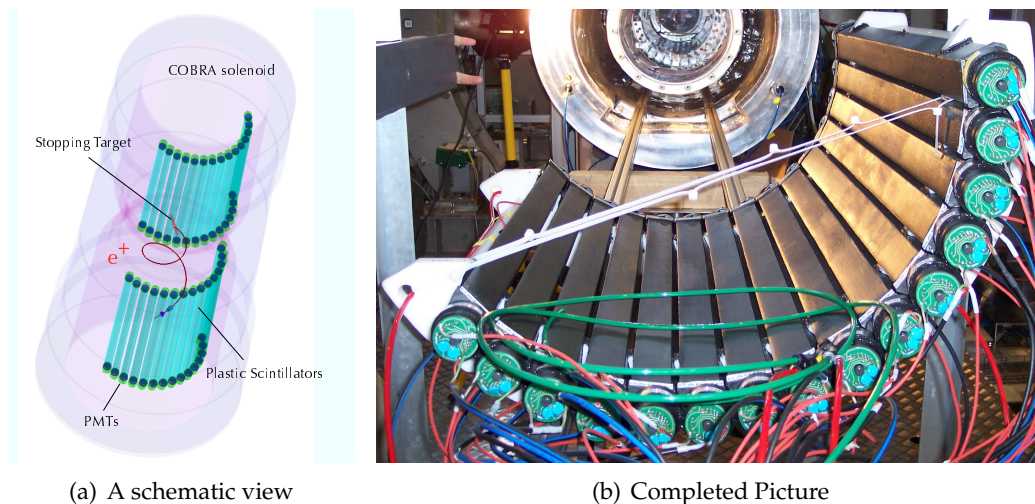
Figure 4.10: Timing Counter (ϕ-counter)

The z-counter is used in the trigger mainly for selecting events by using the z-position information for triggering events. This counter consists of 256 scintillating fibre bundles (6×6mm^2, BCF-20 [62]) read out by 5×5mm^2 Silicon avalanche photo-diodes (APD) (HAMAMATSU S8664-55 [63]) on both ends. Figure 4.11(a) shows a schematical view of the z-counter and Figure 4.11(b) presents the scintillation fibre bundles. Eight APDs are grouped and integrated with a low-noise front-end electronics modules as shown in 4.11(b). The APD readout guarantees that the performances of this counter are quite independent on the magnetic field: due to the orghogonal placement of the fibre slices, PMT read out would be complicated by the large gain loss with respect to normal operation. This is true even for the fine-mesh PMT which can be used successfully up to 1 T of magnetic field and with the axis rotated by a small angle with respect to the direction of the magnetic field, as it can be seen in the longitudinal detector. It should be pointed out that PMTs can be used in such conditions but at the cost of building a detector with suitable light-guides allowing for a better placing of PMT, *i.e.* with a maximum angle between tube axis and magnetic field lines of $30°$ since magnetic field is perpendicular to

44

(a) A schematic view

(b) Photos; Scintillation Fibres and APD front-end circuit board with eight APDs
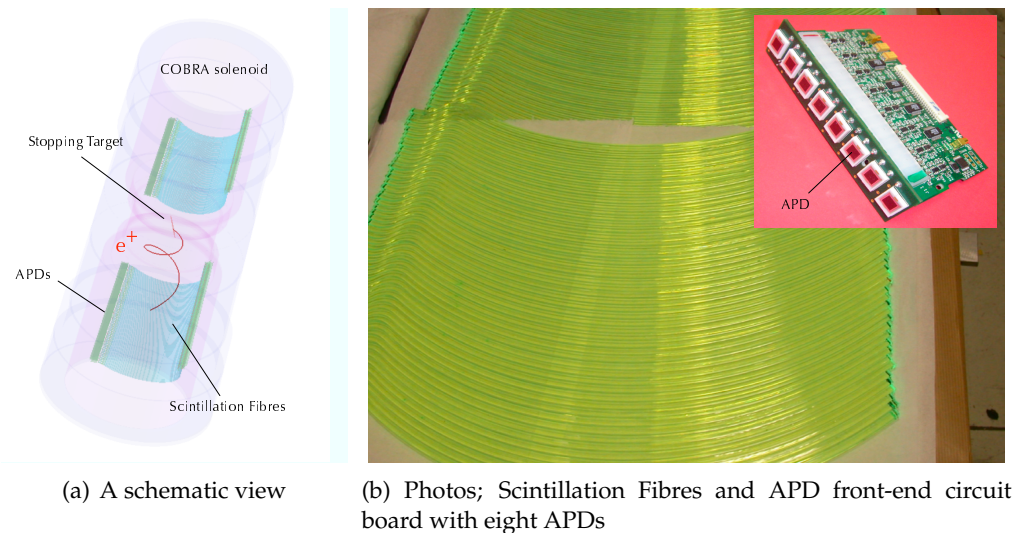
Figure 4.11: Timing Counter (z-counter)

the PMT axis.

In order to achieve the aiming sensitivity, 50 ps timing resolution in σ is necessary. We accomplished successfully an excellent timing resolution by using a prototype, 40 ps in σ, over whole detector acceptance.

The inside of the COBRA magnet is filled with the helium gas in order to reduce the amount of the material in the spectrometer. Thus it is necessary to isolate the timing counter PMTs from the helium atmosphere. The timing counter is surrounded by an ethylene vinyl alcohol copolymer film which offers outstanding helium barrier property. Nitrogen gas is continuously flushed inside this volume in order to assure a long-enough life time of PMTs.

4.4 Coordinate System and Notation for the Spectrometer

We here summarize the global coordinate system and the drift-chamber numbering scheme of the module and cell, plane naming, as shown in Figure 4.12. These notations will be referred commonly over this thesis.

(a) 3-D Coordinate System

(b) 2-D Coordinate and DC numbering
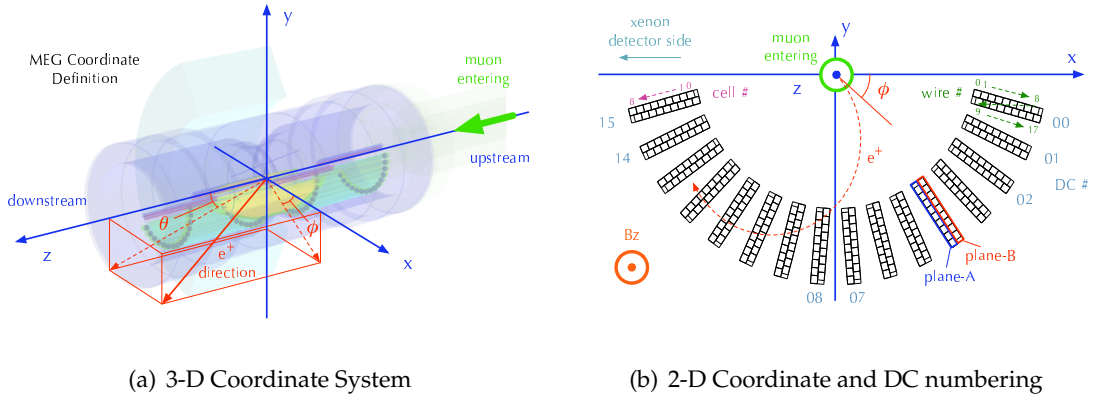
Figure 4.12: Coordinate System of the MEG Positron Spectrometer

Concerning the global coordinate system, z-axis is assigned corresponding to the muon-beam direction; this is also equal to the COBRA axis. Then, the x- and y-axis are determined, as shown in Figure 4.12. Figure 4.12(b) is viewed from the downstream of the muon beam. If not otherwise specified, two-dimensional event display will be shown in this $x - y$ view always in this thesis.

Positron emission angle is determined by this global coordinate system. The azimuthal angle ϕ is determined by the angle between projected momentum onto $x - y$ plane and x-axis, and the polar angle θ is given by the angle between projected momentum onto $y - z$ plane and z-axis; the latter angle, θ, is usually represented by its cosine, $\cos\theta$. Due to geometrical limit, the spectrometer acceptance is determined. In this thesis, the spectrometer acceptance is commonly referred as $|\phi| < 60°$ and $0.08 < |\cos\theta| < 0.35$ so that the positron can be traced by the drift chamber and triggered by the timing counter effectively while the γ ray can be detected by the liquid xenon γ-ray detector on the counter side.

As for the drift chamber, there are four kinds of numbering (or naming) scheme. First, drift-chamber module identification is numbered from 0 to 15 clockwise, as shown in Figure 4.12(b), *i.e.* positron curling direction matchs with this numbering. Each module has two planes, "plane-A" and "plane B", and then, if one need to point each plane individually, this can be denoted by *e.g.* DC02A, DC15B, *etc*. Cell identification is numbered from 0 to 8; 0 is the innermost cell and 8 is the outermost cell. Wire numbering is similar with this, cell-0 of DC00B is numbered as wire-0, and next cell is wire-1, and then, the final cell, cell-8 of DC15A is wire-287. The detailed geometry of drift chamber will be given in next chapter.

46

Chapter 5

Drift Chamber

Details of the MEG positron spectrometer is described in the previous chapter except for the drift chamber system for positron tracking. In this chapter, a detailed account of the MEG drift chamber system is given. At the outset of this chapter, requirements for the MEG drift chamber which should be satisfied in order to achieve excellent sensitivity are compiled. Therefrom a detailed description of the MEG drift chamber is presented; in addition construction procedure of the system will be explained together with the control system and its operation scheme.

5.1 Requirements for the MEG Drift Chamber

As described in chapter 3, each detector has to satisfy many high requirements in MEG. In particular, the drift chamber system is requested to satisfy several critical issues, *i.e.* development of an innovative drift chamber system has been strongly desired.

Requirements for the drift chamber are the following. First, amount of material used in the drift chamber should be minimized since this affects the tracking resolution and the background suppression capability. Second, the MEG drift chamber should be operational under the high counting rate environment, as mentioned frequently. Although the extremely high positron rate could be suppressed thanks to benefit of the COBRA magnetic field, the drift chamber still have a lot of positron hits regularly, especially for the innermost region. Finally, excellent bidirectional position resolution is necessary for both the transverse and longitudinal directions.

5.1.1 Light Material

In general, minimization of the material has been forefront subject in the drift-chamber development for high energy physics experiment since the momentum/tracking resolution is limited primarily by multiple Coulomb scattering. In particular, if the experiment concentrates on the relatively low energy region, *e.g.* below GeV level, a substantially lower-mass chamber is essential. Furthermore, it is crusial for not only the tracking accuracy but also for the background suppression, because amount of generated backgrounds is propotional to amount of material that composes the detector.

For the MEG experiment, the detector resolution and background suppression hold the most important key. Figure 5.1 shows a relative probability density map of the positron annihilation-

(a) $x - y$ view

(b) $z - x$ and $z - y$ view
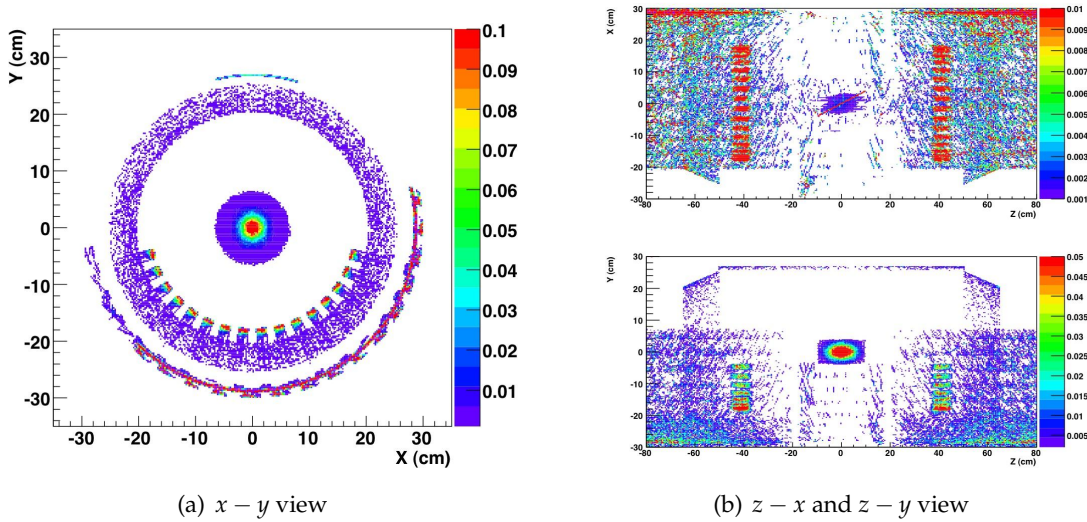
Figure 5.1: Probability density map of the e$^+$ annihilarion-in-flight

in-flight estimated by Monte Carlo (MC) simulation. The color indicator (scales are arbitrary) shows a relative probability of the positron annihilation as projection onto perpendicular direction. As shown in Figure 5.1, many detector components can cause background γ ray, especially the stopping target and the trackers. As discussed in Chapter 3, the thickness of the target has been already minimized, *i.e.* next possible candidate for the material minimization is the drift chamber. One can see from Figure 5.1 the innermost part of the drift chamber is bombarded by much more positron than other part. Therefore if we can reduce the amount of material in such parts, background can be suppressed drastically, resulting in improving the detector sensitivity.

5.1.2 High Rate

For the nominal muon rate, $3 \times 10^7 \mu^+/\text{sec}$, same amount of positron is produced inside detector apparatus because of muon decays. In such a heavily irradiation environment, no wire chamber can cope. If we can use other tracking devices, *e.g.* silicon tracker, this will help so much from the point of view of high rate operation. Of course, however, this can not be a solution, since such a large Z detector must not be used for the MEG. Consequently, we have to adopt wire chamber as a tracking detector. Thanks to a great benefit of the COBRA magnetic field, for outer radii we can reduce the number of positron hit drastically. However the drift chamber still have a lot of positron hit regularly. From Figure 4.4, one can see the innermost region of the drift chamber will have a lot of positron hit, $\sim$10 kHz/cm^2. Thus, the MEG drift chamber should be designed to be operational in such an irradiation environment.

5.1.3   High Resolution

In general, this requirement is already satisfied if the first requirement is fulfilled successfully, since the momentum/tracking resolution is limited primarily by multiple Coulomb scattering. However, if we aim ultimate level of material minimization, the detector readout performance is also limited. For example, in order to minimize material, we should minimize the number of readout channel. Otherwise, the front-end electronics for readout will have a certain amount of material. Consequently, at the ultimate level of material minimization, both of requirements are irreconcilable. Thus the MEG drift chamber should be designed to realize excellent resolutions of transverse and longitudinal directions by employing innovative design using minimum amount of material.

5.2   MEG Drift Chamber

5.2.1   Overview

The drift chamber system is segmented into 16 modules radially with $10.5°$ intervals in the azimuthal angle. By closing both ends of COBRA magnet and filling the volume with helium gas, amount of material inside COBRA volume is minimized; this means that each gaps between adjacence chamber modules is also filled with helium gas. Figure 5.2 shows overviews of the drift chamber system. The helium based gas mixture, He:C_2H_6 = 50:50, is adopted as

(a) Cross-sectional view   (b) Alternative angle view
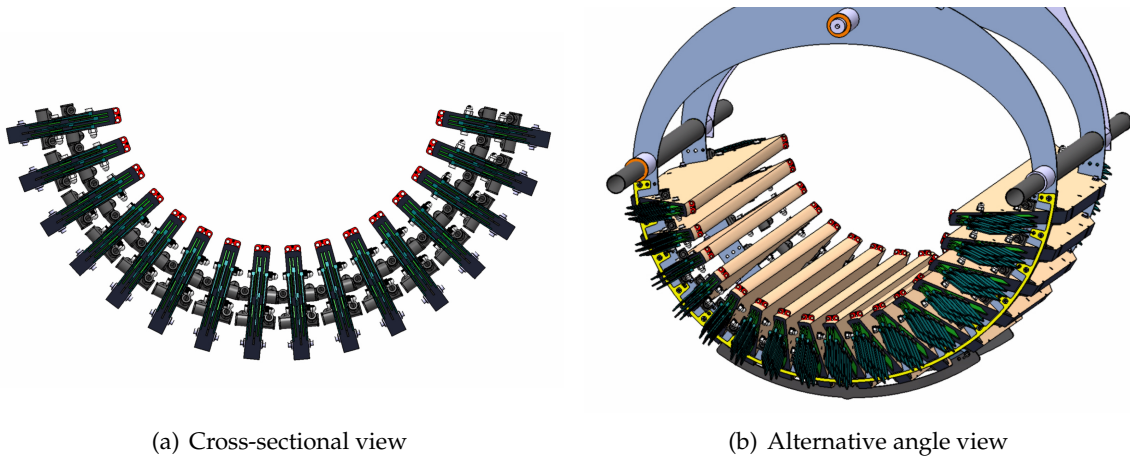
Figure 5.2: The MEG Drift Chamber Overview

the chamber active gas. For each drift chamber modules, two layers of axial sense wires and potential wires, stretched by a 4.5 mm pitch, are formed on a carbon-fibre frame. Each layer is isolated by a cathode foil and shifted by one-half cell to allow a local resolution of left-right ambiguity. The chamber wall consists of an extremely thin foil, 12.5 μm thick polyimide with aluminum deposition. Moreover, the frame of drift chamber module is formed without any structure on the target side. This *opene* frame structure makes wire-stretching more challenging but helps much to reduce unwanted background because all positrons from the target do not traverse a frame structure, as we discussed in Section 5.1.1 and shown in Figure 5.1.

5.2.2 Chamber Design

Using the helium based gas mixture is essential for the MEG drift chamber for lowering multiple scattering contributions to the momentum resolution and suppressing superfluous γ-ray generation. In general, the helium based gas has slow drift velocity (a factor 2.5 with respect to argon based gas), this can help for the spatial resolution but the capacity of operating rate is limited. Then, the small-cell design is adopted, as shown in Figure 5.3. As one can see
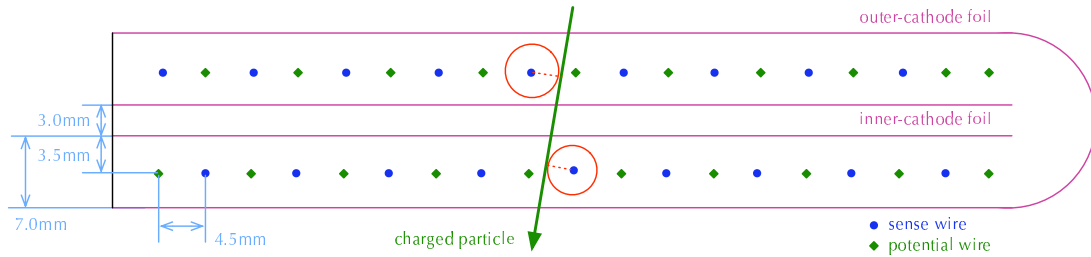
Figure 5.3: Drift Chamber Cell Design

(a) Contour plot of the potential

(b) Drift lines with isochrone map
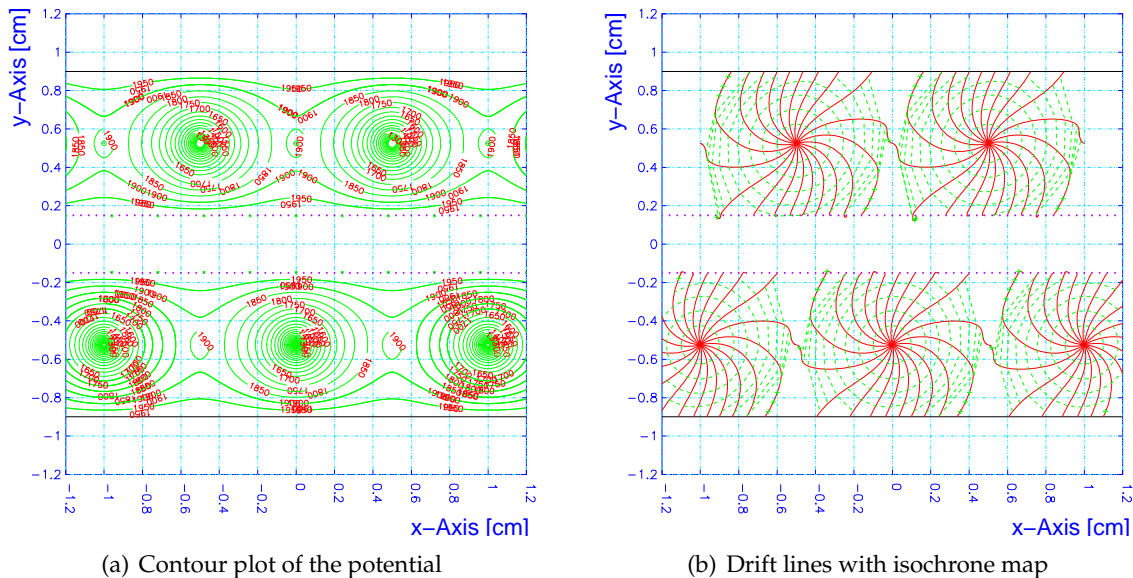
Figure 5.4: Field map and drift lines calculated by **GARFIELD** simulation incorporating the nominal condition for the MEG drift chamber. Detailed description of the simulation is given in Chapter 6.

in Figure 5.3, conventional cell configuration is adopted. Two layers of axial sense wires and potential wires are isolated by three thin-cathode foil. One cathode foil, called "outer cathode", wraps whole active gas volume, and other two cathode foils, called "inner cathode", isolate two layers with 3.0 mm gap in order to suppress a cross-talk. Each layer is staggered by half a cell to allow local resolution of left-right ambiguities. All cathodes and potential wires are

grounded and sense wires are applied positive high voltage. As shown in calculated potential contour (Figure 5.4(a)) and drift lines (Figure 5.4(b)), electric field has very simple shape and small Lorentz angle with magnetic field that can make the time-to-distance calibration easy.

Shape of the drift chamber is quite important to keep the detector acceptance. As shown in Figure 4.1, the timing counter should be placed close to the centre of magnet along the beam axis, otherwise the spectrometer loose the detection acceptance. However, putting counters near the target makes conflicts with the drift chamber. In order to put the counters close to the target with a reasonable tracking volume, the MEG drift chamber is trapezium-shaped so that counters can be involved at the bottom of trackers inferiorly and trackers can extend over the counters superiorly. Moreover, as described in the previous section, if opening the frame towards the target is possible, it is very helpful to suppress superfluous γ-ray generation. Reflecting such requirements, the MEG drift chamber is distinctive-looking, as shown in Figure 5.5. One can see the open frame structure with stretched wires in Figure 5.5(a), and Figure 5.5(b)
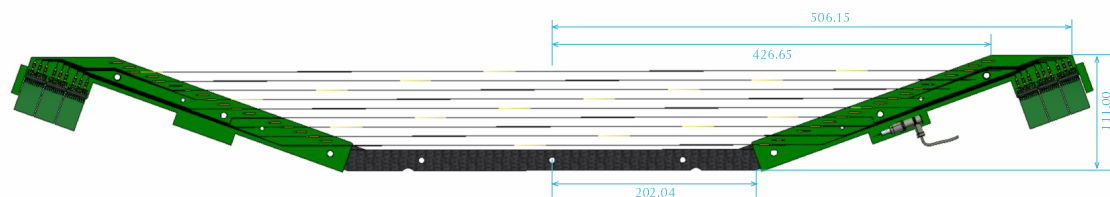
(a) Anode and Frame (unit : mm)

(b) One completed module of the drift chamber

Figure 5.5: Lateral view of the MEG Drift Chamber

shows the completed drift chamber module with outer-cathode foil. In Figure 5.5(b), the front-end electronics, pre-amplifier modules, are shown at each ends of the anode frame. Close-up view of the front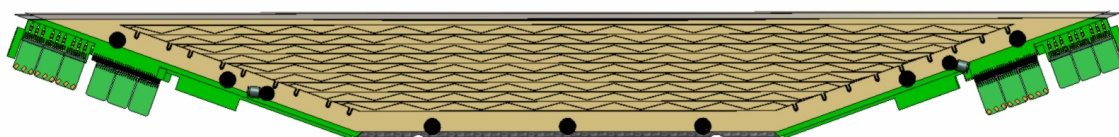-end electronics implementation is shown in Figure 5.6. The geometry of front-end electronics is restricted by several reasons. First, it should not be placed at the lower half of the anode frame, because it should avoid conflict with the PMTs of the timing counters, one can see this situation in Figure 4.1 clearly. Next, putting front-end electronics at the bottom of chambers is impossible, since the drift chamber is placed on the inner surface of the COBRA magnet directly, there is no more space. Consequently, only the end of the anode frame is allowed position to implement the front-end electronics. Thus, we have to suppress the number of readout channels, and also, consider an effect on the timing counter efficiency, because this position of front-end electronics can interrupt the positron trajectory partially. This will be discussed later in detail.

(a) Close-up view   (b) Alternative angle view
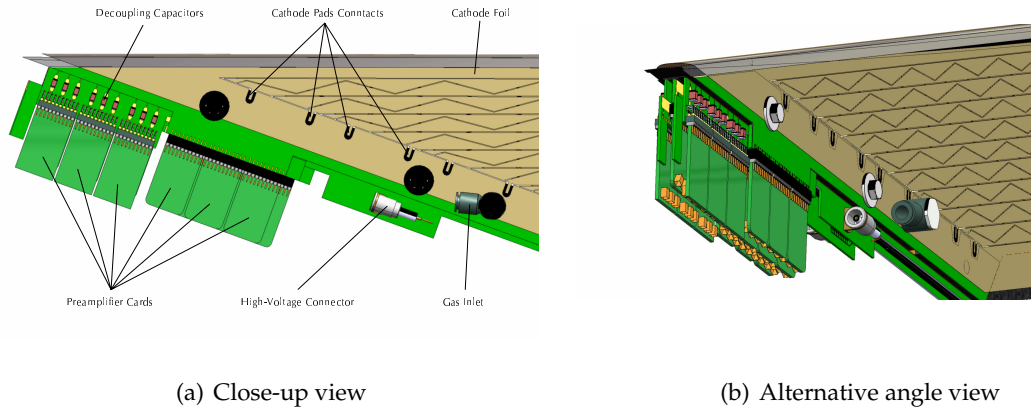
Figure 5.6: Drift Chamber Front-end Electronics Implementation

5.2.3 Chamber Gas

For many years it was believed that helium was unsuitable as a drift chamber gas because of its high ionisation potential, low primary ionisation, and large single electron diffusion. However, as we all know, helium based gas mixture is very attractive due to its long radiation length, and it is strongly required for several purposes, in particular, high luminosity B-, ϕ- and τ-factory experiments, high resolution spectrometer for lower-momentum particles below GeV level. Table 5.1 shows some important properties of some possible drift chamber active gases. Many experimental efforts have been devoted to use helium based gas mixture for a drift

Gas	Z	Density $10^{-3}(g/cm^3)$	Radiation length (m)	# of primary ion pairs per cm	Total # of ion pairs per cm
Hydrogen	1	0.089	7056	6	10
Helium	2	0.178	5299	4.8	12
Neon	10	0.901	322	12	50
Argon	18	1.782	110	29.4	90
Xenon	14	5.858	14	44	300
Methane	(10)	0.717	649	25	53
Ethane	(18)	1.356	340	41	111
Isobutane	(34)	2.590	169	84	195

Table 5.1: Properties of gases in proportional counters [64,65]

chamber. Finally, it was successfully shown that it is possible to achieve a spatial resolution of 260 μm for small drift cells with a maximum drift distance of 5 mm by adding only 6 % propane [66]. After this pioneering work, using helium as drift chamber gas came down to realistic choices, and two leading experiments for B-factory adopted helium based gases for each drift chambers; He:C_2H_6(50:50) for the Belle experiment [67,68] and He:i-C_4H_{10}(80:20) for the BaBar experiment [69,70], respectively.

For the MEG drift chamber, He:C_2H_6(50:50) is adopted same as Belle drift chamber. This gas mixture is essential for lowering the amount of material in the spectrometer. In addition, this gas mixture has another important advantage for the MEG drift chamber espetially. As described above, the MEG drift chamber is formed by the open frame structure and cathode foil is composed by the ultra-thin polyimide film with alminum deposition. In such a delicate structure, keeping cell spacings is very difficult since it can be deformed by the pressure difference between inward and outward very easily. The drift velocity of one-to-one mixture of helium and ethane saturates at roughly 4 cm/μsec for a relatively low electric field ($\sim$1.5 kV/cm) [71]. Thus, in this gas mixture, even if cell spacing is changed a bit, correction to the drift velocity is very small and not sensitive to the measurement.

5.2.4 Vernier Pad

Decreasing a number of readout channels is incompatible with achieving a good position resolution and momentum resolution. However, in order to realize an excellent sensitivity, both of them should be realized for the MEG experiment inevitably. In particular for the longitudinal spacial resolution, called "z-resolution", this issue is critical because if we consider using usual cathode-pad method to determin the z coordinate, a number of readout channels must increase drastically. Then, the **vernier-pad** method is adopted for the MEG drift chamber.

The vernier-pad method is one of the cathode-pad application using a "zig-zag" shape strip. Figure 5.7 shows a schematic view of the vernier-pad method. In this method, cathode strips
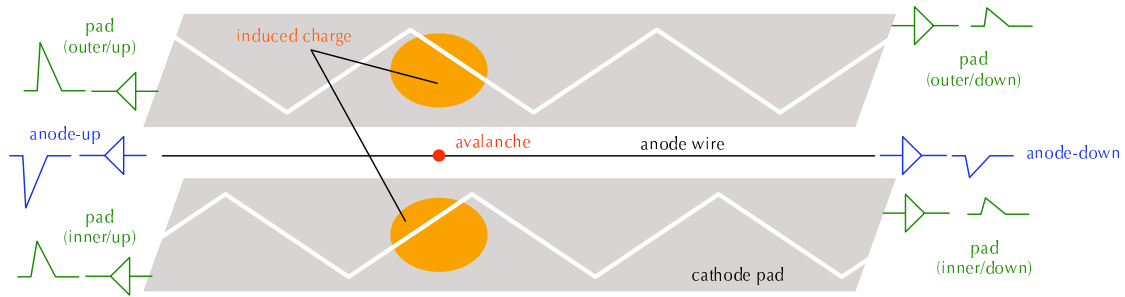
Figure 5.7: Schematic view of the vernier-pad method

are formed parallel with the anode wire when usual cathode-strip is formed perpendicular, and each strip is separated by a "zig-zag" groove into two pads. These pads are etched on both sides of the sense wire plane, so that there are four cathode pads for one sense wire. The amount of induced charge on each pad is related to the z-coordinate due to this zig-zag shape. Thus the ratios of the charges induced on the four pads can be used to accurately determine the z-coordinate. However, by using such ratios of the induced charge, one can solve this z-coodinate inside only one zig-zag period. Thus, the z-coordinate is roughly derived from the ratio of the charges measured at both ends of the hit wire with an accuracy of 1cm, then a more accurate z position is calculated by using the vernier-pad information.

(a) Drawing (unit : mm)   (b) Charge Ratio
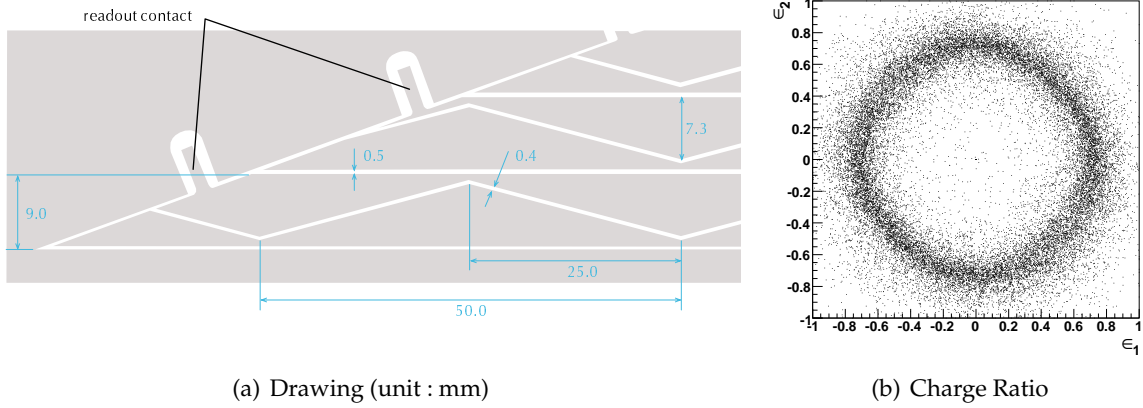
Figure 5.8: A Part of Vernier-pad Drawing and Virnier-Circle plot

For the MEG drift chamber, 5 cm zig-zag period is adopted, since the charge-division method can provide only 1cm accuracy, and a maximum error of charge division should be at most half the period of the zig-zag pad pattern in order to solve the z-coordinate uniquely over whole vernier pads. Each zig-zag pettern on both sides of the sense wire plane are staggered by quater a period so that ratios of induced charge can provide the phase in a period. One strip has two pads, and induced charge on each pads are collected at different ends of the strip, up-stream and downstream, so that it can make readout-electronics implementation symmetrically and suppress systematic error attributed any differences between both sides, as schematically shown in Figure 5.7 and a close-up pattern design, Figure 5.8(a). As mentioned above, one cell has four associated vernier-pads, outer-cathode readout at upstream/downstream; inner-cathode readout at upstream/downstream, and hence, one can define the normalized charge ratio ϵ_1 and ϵ_2 for outer-cathode pads and inner-cathode pads, respectivelly, as

$$\epsilon_1 = \frac{Q_{IU} - Q_{ID}}{Q_{IU} + Q_{ID}}, \quad \epsilon_2 = \frac{Q_{OU} - Q_{OD}}{Q_{OU} + Q_{OD}}, \tag{5.1}$$

where $Q_{IU(D)}$ denote the charges induced on the inner-upstream(downstream) pad and $Q_{OU(D)}$ denote the charges induced on the outer-upstream(downstream) pad. Figure 5.8(b) shows a scatter plot of ϵ_1 versus ϵ_2, called "vernier-circle", which was acquired by the cosmic-ray run (*cf.* chapter 8.2.1). A circuit along the round-square locus corresponds to a vernier-pad pattern period of 5 cm along the z-axis. The avalanche point of z-coordinate can be derived by comparing a measured $\epsilon_{1,2}$ with the numerically calculated values.

Origin of this method was developed as one of the cathode-pad applications, "vernier wedge technique", at CERN [72] in 1984. After this work, this method has been improved continuously for several drift chambers; *e.g.* muon trigger chamber for the D0 experiment [73], muon barrel chamber for the OPAL experiment [74], *etc*. For these experiment, this method has been developed in order to solve the economical difficulties since the number of readout channels has been ever-increasing in accordance with getting large dimension of the detector apparatus. Thus they were not necessary to achieve excellent longitudinal position resolutions,

and it was a level of a few mm for 6-10 m wire length. In succeeding years, the BESS collaboration made a new progress on this technique so that it can determine the longitudinal position with an excellent precision, 470 μm, by adopting small cell size and short wire length [75]. This work proved that there are two essential points to realize an excellent position resolution; using optimized period of the vernier pattern as short as possible and keeping good signal-to-noise ratio. The first point is limited by the wire length primarily, and thus the second point holds the key to get a good position resolution by this technique.

5.3 Drift Chamber Construction

The MEG drift chamber has been constructed with the PSI in-house engineering group, called "detector-group". As mentioned above, the design of MEG drift chamber is based on a lot of ambitious ideas, *i.e.* the available components are strongly limited and the construction must be challenging. Thus, all relevant physics researchers and the engineers belong to the detector group have collaborated to construct this challenging drift chamber. In this section, several essential parts are given in detail.

5.3.1 Wire Stretching

Wire stretching is one of the most difficult construction process due to its distinctive design. In order to minimize amount of material inside the spectrometer, as described in Section 5.2.2, the MEG drift chamber is composed by the trapezium-shaped carbon-fibre frame with missing one-side, so-called *open* frame structure (*cf.* Figure 5.5(a)). This structure makes construction very difficult; as one can suppose easily, such a structure cannot keep a mechanical stability. As well known, in the wire chamber, tension of all wires should be maintained in order to avoid any displacement due to an electrostatic force made by the high voltage, *i.e.* wire tension should be strong enough to hold against electrostatic force. But an *open* frame structure cannot keep such a strong tension stably; once wires are stretched on a frame, a frame is buckled.

At the beginning of drift-chamber development, we have been suffered from this difficulty repeatedly. Finally, we established an effectual procedure successfully as described in below. First of all, dissect the drift-chamber construction in different four components; two anode frames corresponding to two layers within one module, one cathode frame for an inner cathode foil, another cathode frame, called "hood", for an outer cathode foil. All four components must maintain a certain tension, stretching anode and potential wires, and stretching cathode foils. Next, consider the final tension when all wires and foils are stretched. For the wires, Ni/Cr (80:20) of 25μm in diameter and Be/Cu (2:98) of 50 μm in diameter are adopted for a sense and a potential wire, stretched by 50g and 120g, respectively. We can calculate the final situation of the tension, and then, it is possible to make a **pre-tension on each components in order to compensate such tensions during assembly**. Obviously, such pre-tension should be applied against a local tension by wires/foils so that each components can keep it stable; all such a pre-tension for each components should be equilibrium when assembly is completed. During the development stage, all pre-tension parameters have been modified frequently, since all pre-tensions should be changed in order to keep its equilibrium even if a tension for only one part is changed. After much trial and error, we could find an optimum setting and achieve an equilibrium.

5.3.2 Cathode Foil

A cathode foil holds the second key to minimize amount of material inside the spectrometer. As mentioned above, the drift chamber is segmented by 16 modules in the COBRA spectrometer; this feature can help us or hurt us. By separating each other, the gap between each modules is filled with pure helium gas; this can help much to reduce a mass. However, this means that all positron must pass through several cathode foils every time; signal-positron (=52.8MeV/c) track goes through four foils(two inner and two outer cathodes) × eight modules = 32 foils for a typical event. If it is constructed as the usual cylindrical drift chamber, charged particle does not have to pass through cathode foils for such many times. In fact, however, the vernier-pad technique is the most promising way to achieve excellent position resolutions for both direction, transverse and longitudinal, without increasing readout channels; it is really crucial for the experiment. Consequently, realization of the ultra-thin cathode foil which has a precise printed zig-zag pattern is absolutely necessary.

For a base material, one of the proven material verified by a lot of high energy physics experiments, polyimide,is adopted. Generally, one of the most commonly-used polyimide, **Kapton**® [*], is adopted as a base material for this kind of cathode foil, but using **UPILEX** ® [76][†] can help from the strength point of view. The tensile strength of **UPILEX**® is 2.89 times stronger than **Kapton**®; the mass of each material is almost same since the difference of composition is only one oxygen atom (**Kapton**® = $C_{22}H_{10}N_2O_5$, **UPILEX**® = $C_{22}H_{10}N_2O_4$), and thus, the largest difference is the molecular structure. The strength of base material is very important in order to suppress a deformation by stretching during the chamber assembly; this deformation can cause a serious deterioration on the z-position resolution.

Obviously, it is necessary to minimize thickness of the foil. The thinnest commercial-polyimide foil is 8μm thickness, and the second thinnest is 12.5 μm. From the cathode-patterning point of view, 8 μm polyimide is too thin; it cannot keep the strength during the cathode patterning. Then, 12.5 μm thickness of **UPILEX**® is adopted.

There are several ways to make an patterned cathode on the foil, print, lamination, physical or chemical deposition *etc.* For the MEG drift chamber, following requirements should be satisfied; (i) naturally, cathode thickness is required to be minimum, (ii) the pattern precision should be excellent, its error should be a order of 100 μm, (iii) the resistivity should be uniform. In order to guarantee an accuracy of the vernier-pad method, the requirement-(iii) is very important, since its resolution depends on the signal-to-noise ratio primarily as mentioned in Section 5.2.4, and hence, a lamination method looks the best solution. But this method needs a certain amount of metal and glue within a metalized layer, thus it cannot satisfy the requirement-(i). And then, the print method needs to be required a mass-production, because this method needs to have the master negative for the rotary duplicator; normally, such a device is extremely expensive and it is assumed to be used for the industrial purpose. Moreover, ultra-thin polyimide film can be deformed in the rotary duplicator very easily. Consequently, the most promising solution is the deposition and patterned by the chemical etching. This method needs a lot of labor hour ,and process yield must be small, if we require a excellent quality of products. However, only this method can satisfy contradicting three requirements.

Concerning the deposition metal, this should be minimized, and thus, aluminum deposition is adopted. By the contemporary technology, less than 50 nm deposition thickness is

---

[*] A brand name of the chemical corporation DuPont.
[†] A brand name of the chemical corporation UBE Industries.

possible, but this cannot guarantee the uniformity of resistivity. Because the etching process can peel the surface of aluminum deposition, the uniformity of resistivity can also be verified after the etching. Thus, it has to be compromised to have a certain thickness. Once the thickness is increased, the etching method needs to be re-optimized, and then, much trial and error have been spent. Finally, after nineteenth trial, we could achieve to establish the optimum etching procedure with the possible thinnest deposition, 400 nm. Figure 5.9(a) represents the resistivity of cathode pads as a function of the pad length for several trial steps. The first plot shows the result of the first trial, the second plot is the fifth, the third plot is the fifteenth, and the last plot is the final result, the nineteenth trial. One can see advances clearly in this series, and from the last plot, the resistivity of the final foil can be determined as 47.5 Ω/m. Figure 5.9(b) is one of the foil-production scene.

(a) Resistivity of the cathode foil during its development   (b) Cathode foil production
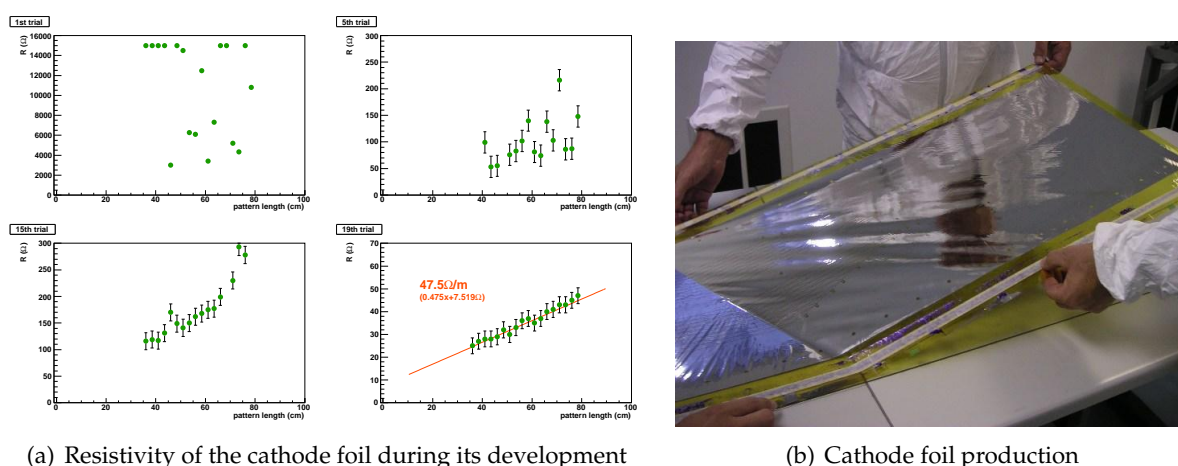
Figure 5.9: Cathode Foil

As described just before, the final specification of the cathode foil is 400 nm aluminum deposition on the 12.5 μm thickness polyimide foil. However, this deposition thickness should be measured by alternative method and converted to the "effective" thickness due to following reasons. First, this thickness, 400 nm, is converted from the number of deposition cycle, not measured by the step meter; such a conversion is not enough accurate for less than 1 μm. Second, this deposition thickness is not able to be measured by the step meter, because the base (12.5μm polyimide) is too thin for this purpose. Third, for such a ultra-thin deposition, the density of deposited metal is much less than the bulk metal, *i.e.* the effective thickness should be represented by means of so-called bulk thickness in order to estimate the amount of material. For these reasons, the effective thickness was measured by the Coulometric-Coating-Thickness-Measurement (CCTM) [77]. According to the CCTM, after all etching process, the effective thickness is 250 nm while it is presented as 400 nm of the deposition thickness. The deposition thickness has no meaning since the effective thickness by means of the bulk thickness is important. Thus, from here, we will refer the thickness of aluminum-deposition thickness as 250 nm.

The pattern contains many cross-markers for the assembly; it is possible to use these markers as the position reference for pasting foil on the frame. Such markers can be also used to estimate the patterning precision. By measuring the distances between each markers, 100 μm

of positioning accuracy is confirmed for both direction, longitudinal (1 m in total) and transverse (34 cm in total).

It is impossible to have excellent achievements for all three contradicting requirements. In order to put requirement-(iii) before (i), the BESS experiment adopted a 18 μm thickness copper-laminate on a 0.1 mm thickness of G10 plate as the vernier-cathode of the drift chamber [75]. By using this cathode, they could achieve the excellent longitudinal position resolution, 470 μm, successfully. However, this specification of the cathode is possible for them but for us, since the objective energy region is completely different. Hence, we had to compromise the level of foil resistivity, in other words, the deposition thickness; this can degrade the longitudinal position resolution a bit, but the tracking accuracy can be improved finally by reducing the multiple scattering effect.

5.3.3 Assembly

Although only two examples of the development are presented in the previous two sections, we shall move to the description of the drift-chamber assembly. As described above, after much try and error, we could achieve to satisfy the requirements for each components of the MEG drift chamber, and then, we here can complete the drift-chamber assembly. Figure

(a) Three components assembled separately   (b) Final Assembly
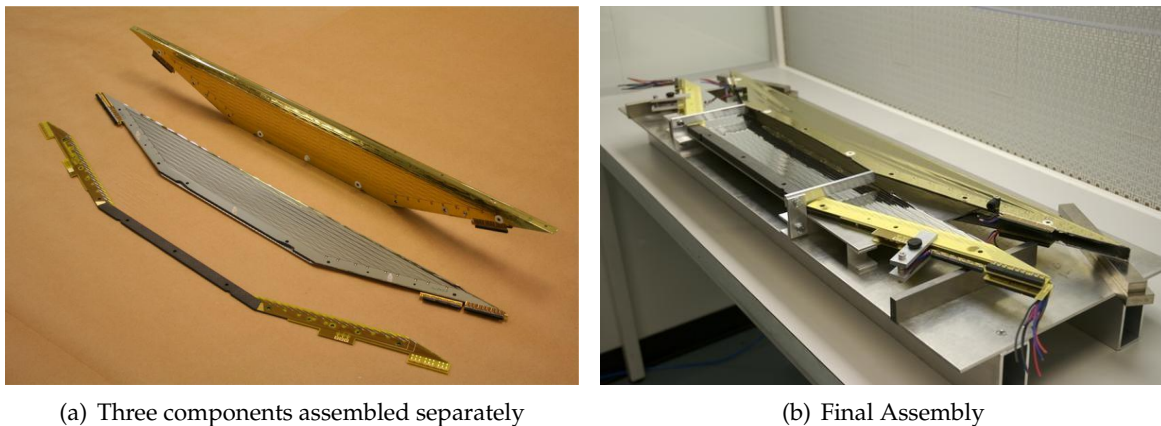
Figure 5.10: Drift Chamber Assembly

5.10(a) shows the main three components separately; from the front, the anode frame with stretched wires, the cathode frame with stretched inner cathode foils, and the cathode hood with wrapped outer cathode foil. Several completion procedures are done before the final assembly; soldering the readout line, handling the potential adjusting electrodes, power cable connection to the front-end electronics cards, molding the HV lines with epoxy resin in order to avoid discharges, putting additional insulators, putting the position-marker for optical survey, *etc.*, all components are cleaned up and mounted on the assembly jig inside a clean room, as shown in Figure 5.10(b).

And then, all components are combined and position-determining pins are driven throughout all components. The head of this pin and position-marker are used to be surveyed optically; this will be mentioned in the discussion concerning the calibration, Section 8.3.

Before the drift-chamber body is sealed off, relatively lower high-voltage (up to 500 V) is applied in order to check the all electronics connection. Finally, the drift chamber is sealed off by the silyl-based special polymer adhesive **ThreeBond 1530** [78] to keep a good gas-tight against helium gas. Figure 5.11 is a part of completed drift chamber. In this picture, the drift chamber

Figure 5.11: Completed Drift Chamber: Several parts of foils are cut to see inside chamber.

is specially assembled with the cut-foils so that we can see inside the drift chamber. One can also see the embedded readout-line partially inside the frame; this part will be mentioned in the electronics description, Section 5.4.

5.3.4 Mounting

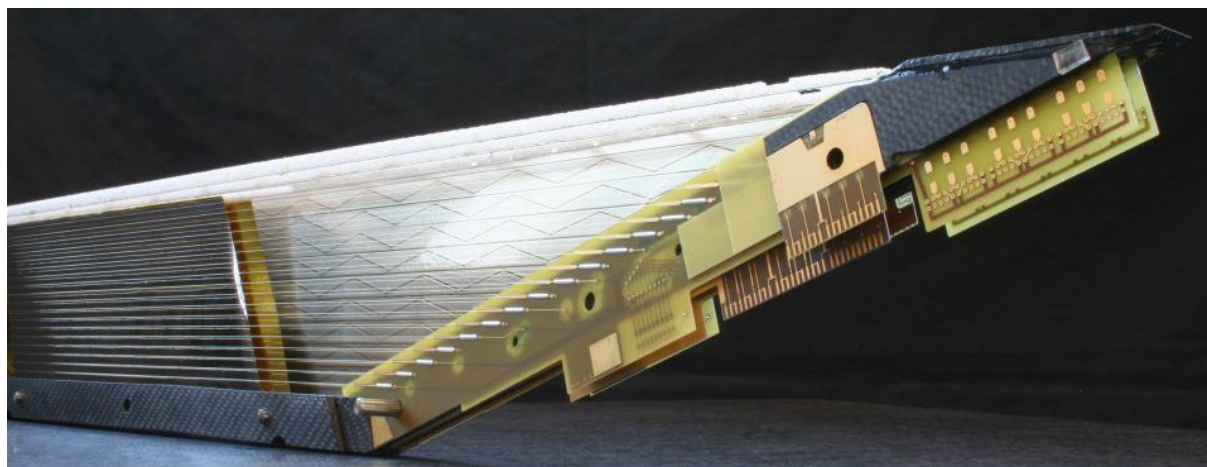The drift chambers are bench-tested individually before the installation. This test is performed in two steps separately, the first test is carried out for the fundamental activity check by irradiating β ray from the ^{90}Sr, X and γ rays from the ^{54}Mn‡ radioactive sources, and the second test is done for the electronics connection check with the final electronics by cosmic rays.

The activity of all channels, anodes and cathodes, is checked by the first test; if the chamber passes this test, the passed chamber is mounted on the support structure, as schematically shown in Figure 5.12(a). This support structure provides the platform of the drift chambers inside the COBRA magnet and determine the coordinate system of the spectrometer. This support structure also provides the cable duct which can be used by all cables, signal, high voltage, power, sensors, and gas tubes, and they are coordinated at the patch panel and connected inside/outside of the magnet via feed-through connectors, as shown in the left-part of the Figure 5.12(a). All drift chambers and accompanied items are mounted on this support structure outside the magnet, and then, installed into the magnet as an all-in-one system.

Before the final installation, all drift chambers are tested on the support structure with the final electronics. The bad channels of the pre-amplifier, cables, connectors, contacts, are found and fixed or replaced here, *i.e.* this final electronics check should be done with same electronics

---

‡ 5.4 keV soft X-ray is generated as a photopeak by 835 keV γ ray from ^{54}Mn, and this X-ray is also used for the drift-chamber waveform simulation. We will discuss this topic in Section 6.3.2.

(a) Three-dimensional drawing of the chamber mounting
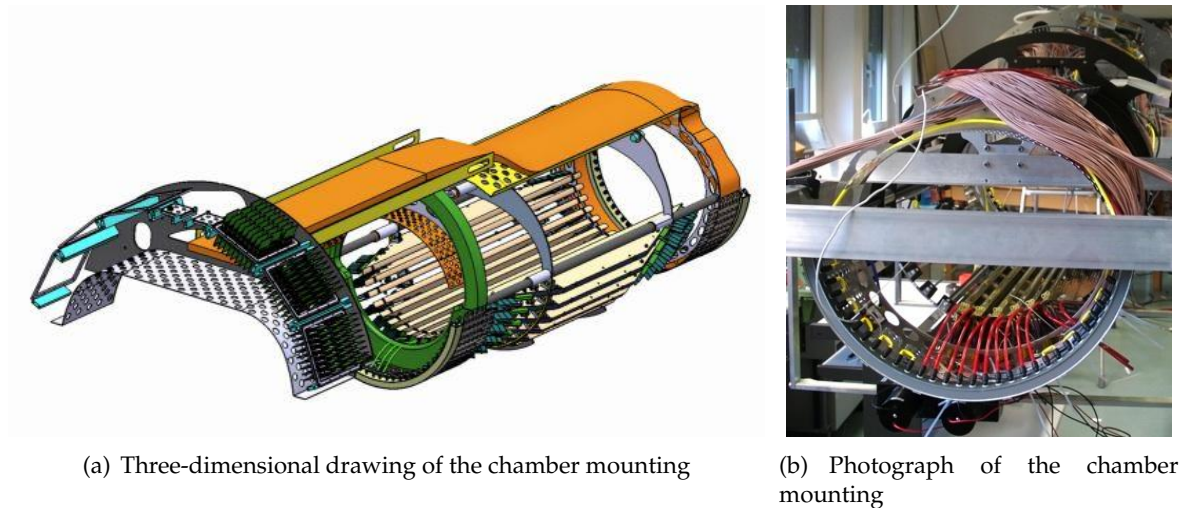

(b) Photograph of the chamber mounting

Figure 5.12: Drift Chamber Mounting

of the final experimental setup. Once this check is done, all electronics connection will not be changed during the experiment. Figure 5.12(b) shows the drift-chamber mounting progress with six chambers. In this picture, one can see two counters below the support structure, and these counters are used to make the cosmic-ray trigger for the drift-chamber final test.

After all test is performed on the support structure outside the magnet, the drift-chamber system installation is carried out. The special rail system is provided for the drift-chamber installation. This rail system has a long arm and it can drive the drift-chamber system onto the centre of magnet from the downstream end-cap. Several jigs are mounted at the step of the magnet, since the magnet is stepwise structure (see Figure 4.1), for the position determination of the installed drift-chamber system. Figure 5.13 shows the installed drift-chamber system inside the COBRA magnet. One can see sixteen drift-chamber modules as a whole system, and the drift-chamber support structure with the muon stopping target at the centre of the magnet, *i.e.* the coordinate system of the spectrometer is defined by the relations of the drift-chamber support structure and the target and the axis of the magnet.

We now have the completed drift-chamber system finally. Some parts of the drift chambers are not constructed with the primary design due to engineering difficulties, *e.g.* thickness of the aluminum deposition, *etc.* Thus, it is very important to figure out the amount of material by taking into account the final design and its materials. The Monte Carlo simulation of the MEG experiment has been developed and all the detectors are implemented very precisely; this will be discussed in section 6.2. By using this Monte Carlo simulation, it is possible to estimate the amount of material precisely.

Figure 5.14 represents the calculated amount of material. This amount of material is indicated by the total radiation length which is accumulated by the signal-positron (=52.8 MeV/c) trajectory, displayed as a function of positron-emission angle at the target, the notation of the angular coordinate is referred in Section 4.4. White rectangles indicate the spectrometer-acceptance. As one can see in these figures, if the positron is emitted close to perpendicular
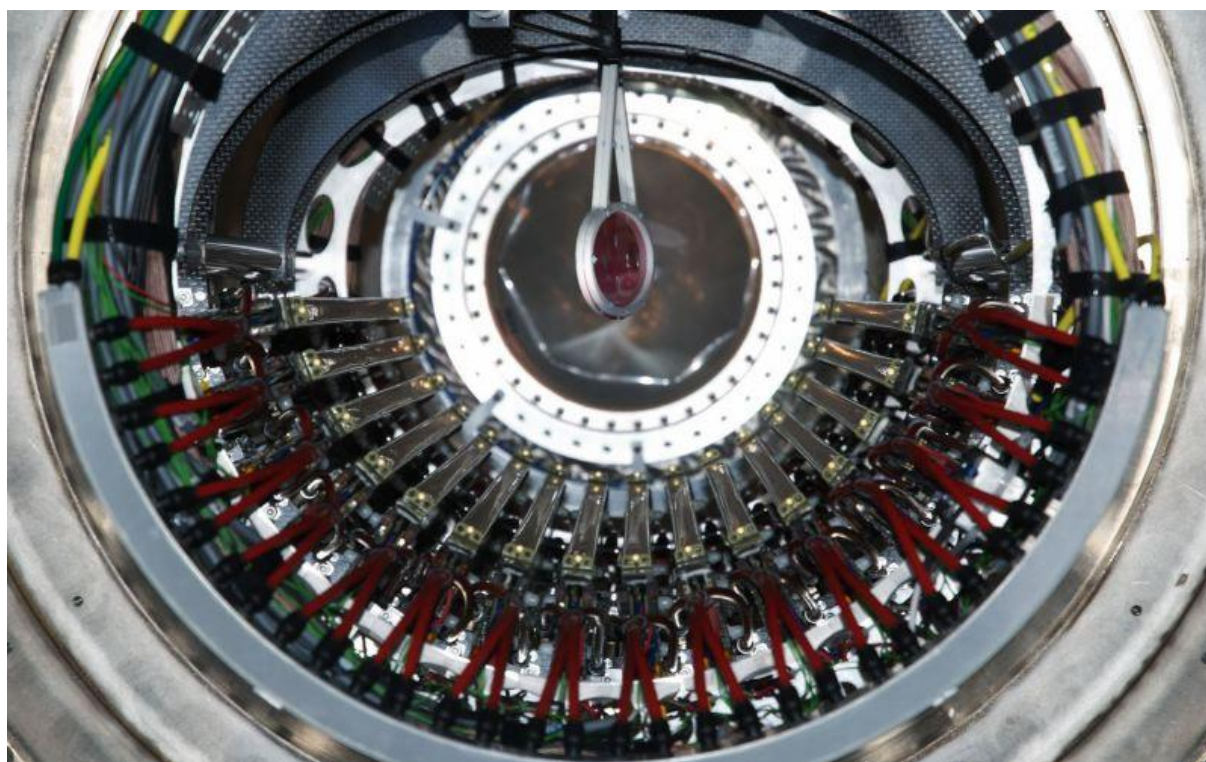
Figure 5.13: Completed Drift Chamber System inside COBRA Magnet

with respect to the beam-axis, the accumulated total radiation length increases, since such a positron curls many times inside the spectrometer even though the COBRA field sweep it out quickly. In the acceptance box, however, it is extremely small thanks to the ultimate low-mass drift chambers. The mean contribution of the gas, helium inside COBRA and helium-ethane of the drift chamber, is 0.00026 X_0; and others, cathode foil and wires, is 0.0019 X_0, *i.e.* **the total radiation length inside the tracking volume is 0.002 X_0.**

5.4   Readout Electronics

Readout lines are fabricated on a thin polychlorinated-biphenyl (PCB) base and embedded inside a carbon-fibre frame, as shown in Figure 5.11. Cathode pads are soldered on it directly and connected to the pre-amplifiers at fringe of the frame. Anode wire is connected to an embedded readout line through a decoupling capacitor (2.7 nF) and bifurcated to the high-voltage supply via a protection high-resistance (1MΩ), and applied positive 1850 V. We developed own pre-amplifier circuit with the PSI electronics group; Figure 5.15 shows a circuit diagram of one inverting-channel of the pre-amplifier. The pre-amplifier circuit is based on two-staged operational amplifiers, **OPA691** [§] [79], with an accompanied feedback circuit and protection diodes.

[§] **OPA691** is a current-feedback type fast-operational-amplifier.; operating on a very low 5.1mA supply current, using a single +5V supply, delivering a 1V to 4V output swing with over 150mA drive current and 190MHz bandwidth.

(a) Helium in the COBRA, DC gas

(b) Cathode foil, wire
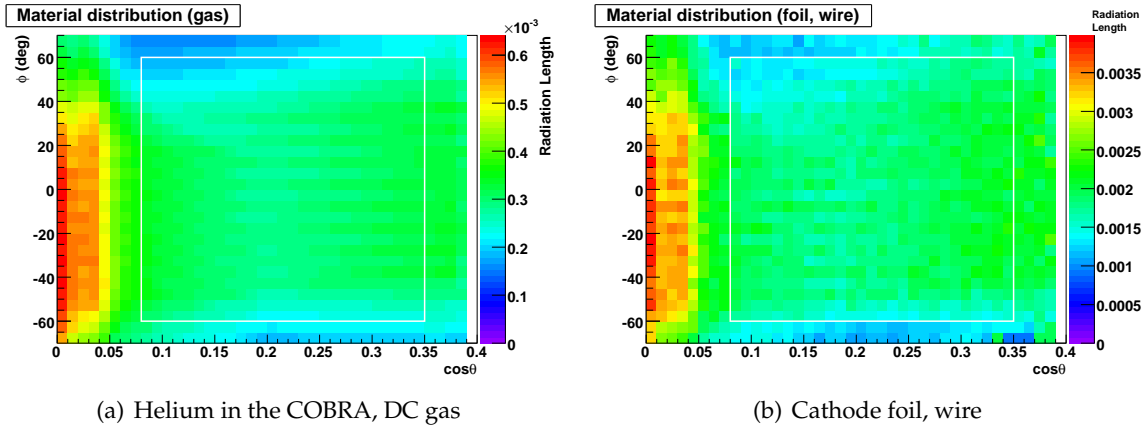
Figure 5.14: Material Distribution as a function of the e^+ emission angle
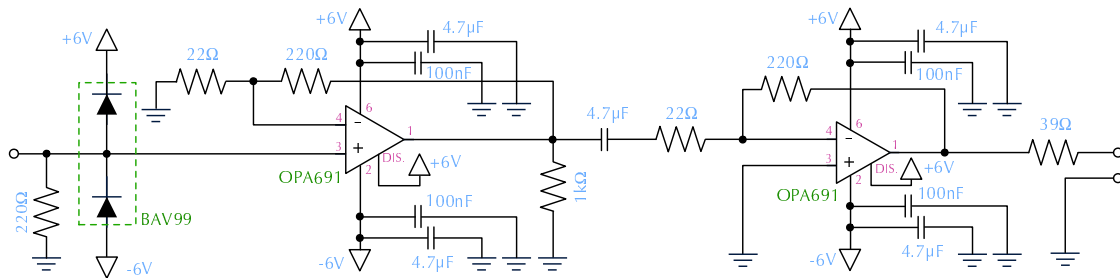
Figure 5.15: A circuit diagram of the pre-amplifier

As one can see in Figure 5.6, a pre-amplifier circuit is fabricated on a small (20.5mm × 30.5mm) glass-epoxy card, called mini-card. Two types of mini-card are provided, inverting and non-inverting, so that anode output is inverted and cathode output is not inverted, since DRS does not receive a negative input. One cell has six output channels corresponding to two anode outputs at both ends of a wire and four vernier pads of the cathode (*cf.* Section 5.2.4). Thus, 12 inverting mini-cards cover all anodes of one chamber, and 24 non-inverting mini-cards cover all cathodes; a half of them, 18 cards, are put on one-side of frame, as shown in Figure 5.6(b). The characteristics of the pre-amplifier at the standard operating condition are given in Table 5.2.

	Gain	Power (V)	Bandwidth (MHz)	Noise (mV)	Current (mA)
Invert Ch.	52	+6	140	0.53	29.7
No-Invert Ch.	52	+6	190	0.79	29.7

Table 5.2: Properties of pre-amplifier

All output signals of preamplifier are transferred by shielded-controlled-impedance coaxial

cables (**Radiall MIL-C 17/93 US** [80]) individually to the back-end electronics via feed-through patch panel at the end-cap of the COBRA magnet; only the anode signal is retouched at the patch panel due to the trigger purpose. This patch panel has resistive dividers and feedback amplifiers, and then, all anode signals are resistively-split into two outputs in the proportion of one to nine. A larger one goes to the DRS directory, and a smaller one is amplified to recover its pulse height and summed up so that several anode outputs are grouped. This grouping is done to have a specified trigger which can be used for the drift chamber self-trigger. Detailed accounts of this self-trigger mode will be given in the description of the calibration, Section 8.2.2.
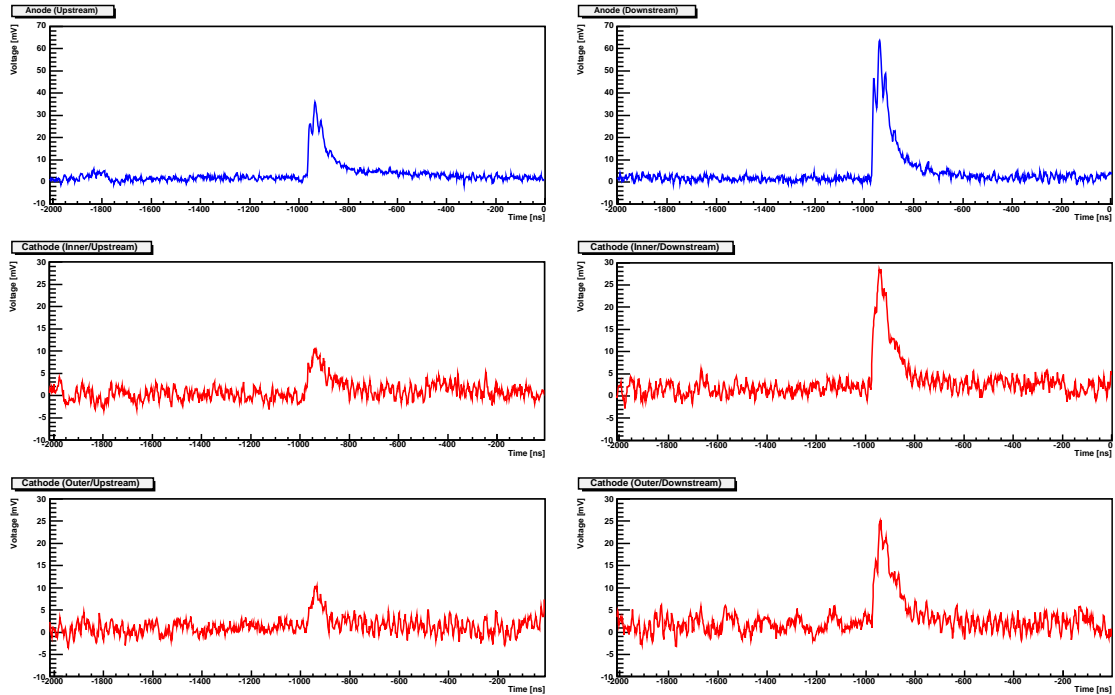
Figure 5.16: Example of output waveform associated with one wire. Upper two waveforms are anode pulses at both end of the wire, upstream and downstream, respectively. Middle and lower four waveforms are cathode pulses of four vernier pads.

As described in Section 3.5.2, all channels are recorded as a waveform format in the DRS. Figure 5.16 shows an example of six output waveforms associated with one wire. The height of vertical axes is normalized to compare pulse height so that it is arranged to be 70 mV for anode pulses and 30 mV for cathode pulses, respectively. The COBRA spectrometer consists of 16 drift chamber modules and each module has 18 sense wires, and hence the number of readout channel belong to the drift chamber system is 16(modules) × 18(wires) × 6(channels) = 1728 channels. Recording all channels into DRS evokes gigantic data size. Thus the online data-acquisition system processes several data reduction; *e.g.* a zero suppression to the non-pulse-containing channel, re-binning to aside of signal-time-window *etc.* The DRS time window for the drift chamber readout is 2 μsec (500MHz with 1024 sampling cells). The trigger latency

is arranged so that the pulse which is associated with the triggering particle appears around centre of the DRS time-window (see Section 3.5.2). The longest drift time can be roughly 250 nsec, and hence, the signal-time-window can be determined as the range of this drift time with a certain redundancy. Consequently, outside this signal-time-window can be re-binned to save a data size, because the recorded pulse in such a region is not our objective.

5.5 Drift Chamber Slow Control System

The MEG drift-chamber slow control system consists of

- Gas Control System,

- High Voltage Control System,

- Temperature/Oxygen Monitor System,

- Low Voltage Control System.

Each sub-system is controlled and monitored by individual Slow-Control-System (SCS) modules (except for the low voltage system) and integrated with the Data-Acquisition (DAQ) system using common network protocol so that the DAQ system can control it via Ethernet (or USB) network and the demanded and the monitored values can be logged. The network interface for the slow control system is provided by the MSCB bus system [81] [II]. Each SCS module has own micro-controller with analog Input/Output and programmable firmware so that module can run stand-alone without any supplementary computer. The MSCB provides a software I/O control as a C-library, and hence, one can have several possibilities to control/monitor/log SCS modules; *e.g.* it is possible to build a stand-alone slow-control application with graphical-user-interface by **LabVIEW** ® [83] since MSCB C-library is provided as a Dynamic-Link-Library on a personal computer platform. For the MEG drift-chamber slow control system, the gas-control system and the high voltage control system are implemented as individual **LabVIEW** ® programs so that these programs can control/monitor the SCS module independently from each other; the DAQ system keeps alternative access to the SCS module statistically and log all the variables that are measured by each SCS module.

The main task of the gas control system is supplying the helium-ethane mixture for the drift chamber and flushing the helium gas inside the COBRA magnet, and controlling both gas flows to equalize the drift-chamber pressure actively. On the other hand, the high-voltage control system is required to provide the automatic voltage ramp-up process, to regulate the demanded voltage stably, and to maneuver the high voltage to avoid the emergency. Additionally, the system has alternative monitoring sensor module which monitors the temperature and the fraction of the oxygen inside the spectrometer.

The most important tasks of the slow control system are the gas-pressure control and the high-voltage control system; these control systems are described in following two sections.

[II] The MSCB and SCS modules are designed, developed and maintained by the PSI electronics group, Reinhard Schmidt, and MEG collaborator, Stefan Ritt [82].

5.5.1 Gas Control

As mentioned previously, an extremely thin foil encloses the active gas volume with an open frame, and also serves as cathode pads. In consequence, an accurate gas control system is necessary to maintain the cell spacing. Our goal is to control the pressure difference between the inside and the outside of the gas volume with a stability of better than 1 Pa; this accuracy is corresponding to $\sim 100 \mu$m maximum deformation of cell-spacing. This can be realized by using extremely sensitive differential pressure transducers and flowing a large amount of gas to accelerate feedback from the pressure transducer. Figure 5.17 schematically shows the concept of the gas-pressure-equalization system. In this figure, some components are abbreviated to be a succinct view; *e.g.* alternative differential pressure transducers for the drift-chamber inlet, high-flux-helium line $^\parallel$, *etc.*
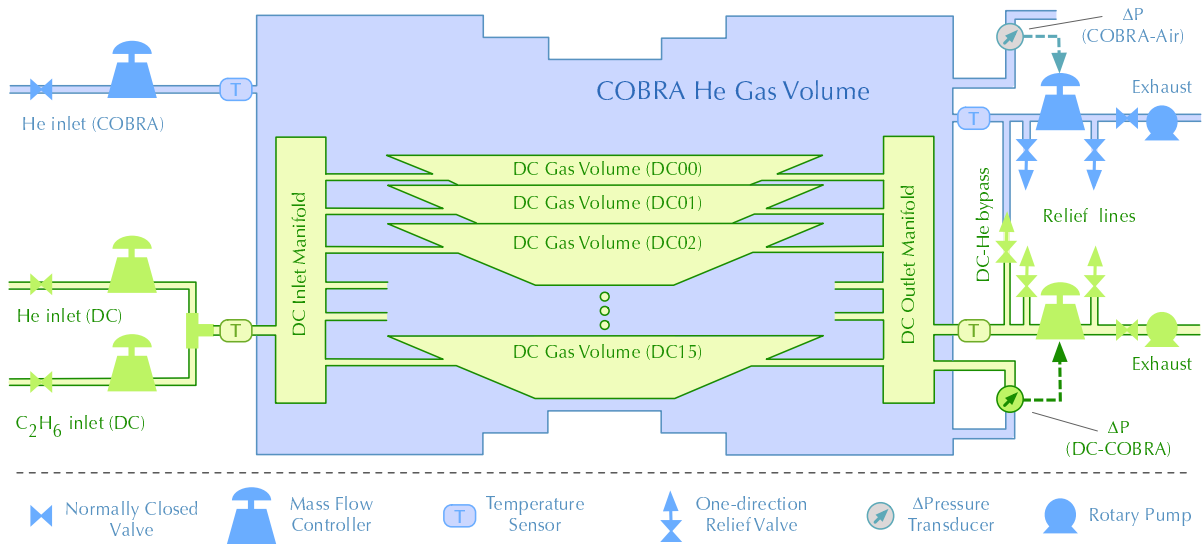
Figure 5.17: Gas-Control Flow Chart

Three inlet lines provide helium flow for the COBRA volume, helium and ethane flows for the drift-chamber volume, individually; flows are controlled by Mass-Flow-Controllers (MFC) in order to determine the gas-mixing-fraction of the drift-chamber active gas and the total flux of the COBRA-helium flow. The mixed chamber gas is buffered at the inlet manifold and derived to the each chamber volume with same gas tubing in length so that the each gas flow to all chambers is supplied uniformly and stably. The outlet of each chamber is connected to the outlet manifold together and extracted to the exhaust line by a pump actively. This exhaust flux is controlled by a MFC and this flow rate is maneuvered by the feedback from the ultra-low variable capacitance transducer, **RXLdp** [85], which monitors the pressure difference between

---

$^\parallel$ The MEG apparatus has a Cockcroft-Walton generator for a proton accelerator that is used to shoot low energy protons (kinetic energy, $T_p < 1$ MeV) upon a suitable target in order to produce high energy gamma rays to calibrate the MEG apparatus [84] . The beam line of this accelerator is parked outside the COBRA magnet normally, and then, the beam line is inserted by own bellow system into the magnet in order to transport the proton to the target. We need much more active control of the pressure equalization to avoid fast pressure change while this insertion process; alternative high-flux-helium line is provided due to this purpose.

the chamber-gas volume and the COBRA-gas volume. On the other hand, the helium flux for the COBRA-gas volume is controlled by monitoring the pressure difference between COBRA-gas volume and ambient atmosphere. Due to use of the pump in exhaust line, additional relief lines are integrated to avoid a serious accident.

The rate of gas flow that is required is set by two constraints: exchanging the gas volume fast enough to ensure good gas quality, including effects of diffusion of helium into the chamber volume, and supplying sufficiently high flow rate to ensure that the pressure control system can track increasing external atmospheric pressure. In consequence, 2000 cm^3/min helium for the COBRA-gas volume, 70 cm^3/min helium and ethane for the drift-chamber gas are adopted, respectively. The flow rate of the chamber outlet is controlled by the pressure difference to be 0.2 Pa.

For atmospheric changes, it was assumed a maximum possible rate of atmospheric pressure of 500 Pa in 10 minutes. This is conservatively large with respect to changes in atmospheric pressure when storm or cold fronts move through the area. Pressure variations due to the building are more difficult to estimate. Possible effects include those due to the air-handling system, opening of large exterior doors, *etc.* The area is partially buffered from these effects by the shielding and barrack.
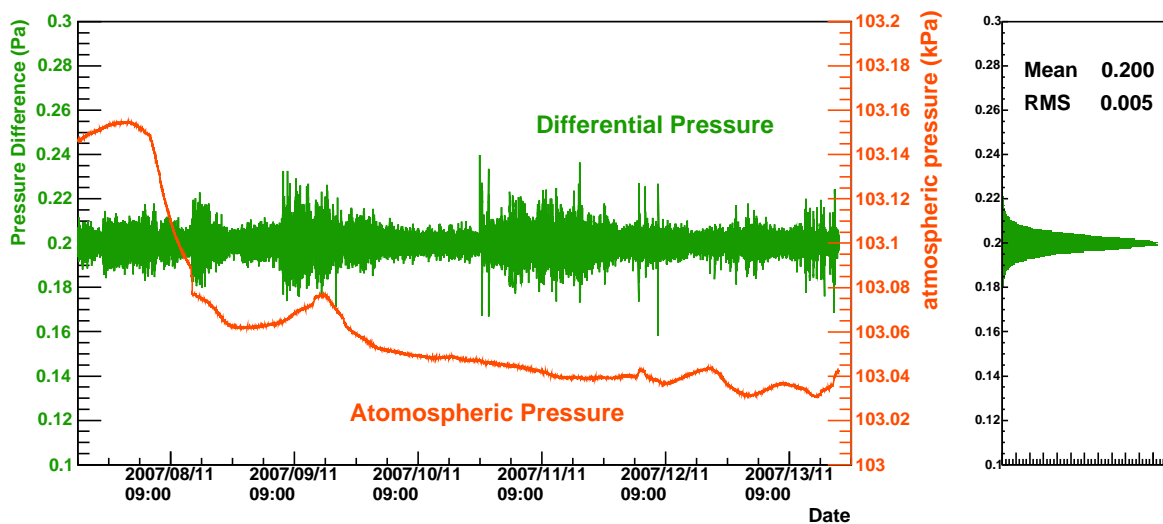
Figure 5.18: Pressure Stabilization

The developed system could manage all the pressure equalization process successfully. Figure 5.18 shows the long-term (one week) pressure equalization done by the gas control system. In this figure, two different plots are superimposed; a differential pressure between the chamber and the COBRA which should be referred to the left-side axis, and the atmospheric pressure which should be referred to the right-side axis. Even if the ambient atmosphere is varied over 130 Pa range, the pressure difference is regulated within 0.005 Pa successfully. This result satisfy the requirement very well in advance.

5.5.2 High Voltage Control

The high voltage control system provides automatic voltage ramp-up process. During the voltage ramp-up, the current can enlarge suddenly due to specification of the high-voltage regulation circuit. Additionally, if the carbon molecule of the part of carbon-fibre frame close to the wire attachment is not enough polarized, the anode current can spike instantaneously. Such current spikes can cause a serious damage on anode wire. Hence, the high-voltage ramp-up process should monitor the anode current carefully, and if system observes a certain current enlargement, ramp-up process is halted in the meantime, and then, it will be resumed after the current is enough stabilized. For the MEG drift chamber, high voltage is applied each layer individually, *i.e.* 2(layers) $\times$ 16(modules) = 32 channel of high voltage divider is necessary. In consequence, anode current is measured as a sum of nine sense wires within one layer; we set a threshold current as 40 nA for the ramp-up process.
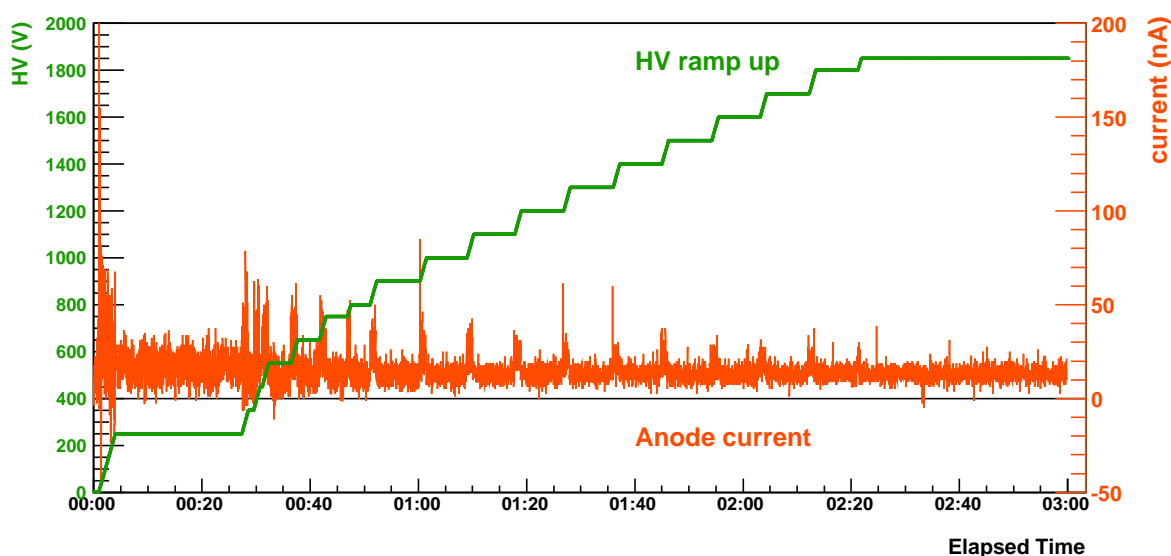
Figure 5.19: HV ramp-up process and monitored anode current

Figure 5.19 shows the high-voltage ramp-up process. In this figure, the high voltage and the current are presented as a function of elapsed time and superimposed. For a lower region of voltage, anode current is erratic, and its spike is larger than other region; this is caused by the circuit specification, since it is not easy to measure such a small current precisely within a few nano ampere at lower voltage. However, for over wide region, ramp-up process works successfully and safety.

After the high voltage achieved its demand, the system moves from "ramp-up" phase to "maintaining and monitoring" phase. Figure 5.20 presents a long term (one week) high-voltage stability; it can assure an excellent stability of 0.02 V in RMS for the 1850 V applying. The system also should have a function to avoid emergencies. If the system observes huge current, the system decreases high voltage step by step automatically and immediately until the anode current will be enough stabilized, and then, after the current is stabilized, high voltage will be recovered automatically. This situation can be considered in case of a beam intensity increases

accidentally; *e.g.* trouble on the electrostatic beam separator, accident on the beam-momentum slit, *etc.* Fortunately, such accidents did not occur during the engineering run 2007.
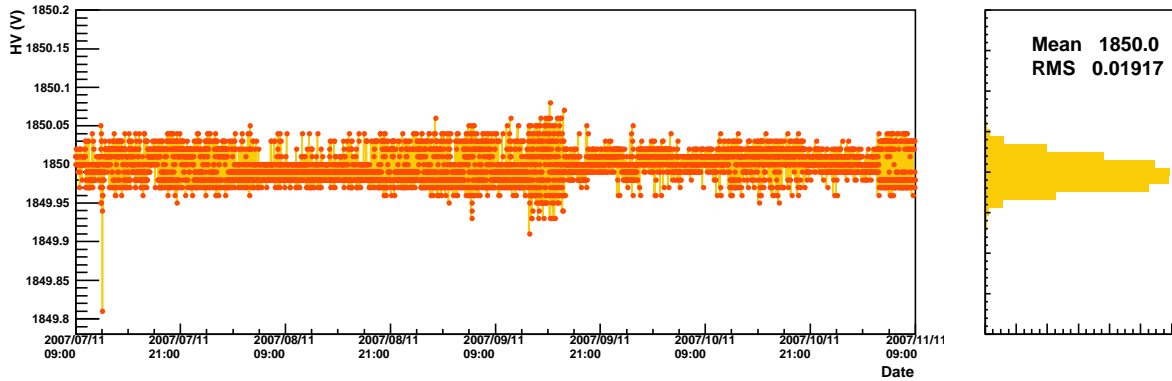
Figure 5.20: HV stability

5.5.3   Monitoring System

As mentioned above, each slow control sub-system is controlled/monitored by individual **LabVIEW** ® programs through the MSCB bus system and monitored/logged by DAQ system in a unique manner. While the gas system and the high voltage system need active control, other slow control systems keep to monitor all variables steadily; *e.g.* helium-ethane fraction inside chamber, temperature of helium gas inside COBRA close to the drift chamber [**], oxygen fraction inside COBRA to ensure the helium concentration, *etc.*.

Figure 5.21 shows one example of monitored variable, helium fraction of the drift chamber active gas. The helium-ethane fraction of the chamber active gas is measured by a helium sensor using differences of the thermal conductivity of helium-ethane mixture. This sensor can measure the helium concentration readily but it has strong temperature dependence due to its measuring principle, and hence, the temperature of this sensor is also measured by other SCS system independently in order to calibrate the output of helium sensor precisely. Upper plot of Figure 5.21(a) presents the non-calibrated helium fraction and lower plot shows the measured temperature of sensor itself; one can see strong correlation between sensor output and temperature clearly. Figure 5.21(b) is the calibrated helium fraction. From this plot, one can see the good stability of the helium-ethane fraction of chamber active gas.

On the other hand, as referred just before, oxygen fraction inside COBRA is also monitored to ensure helium concentration. During the engineering run 2007, several chambers suffered from discharge because of an exposed high voltage point on the chamber board that is in the

---

[**] The front-end electronics that is mounted directly on the chamber dissipates 300 W into the COBRA-helium volume (*cf.* Table 5.2). Thus, this heat is monitored by independent SCS system, since gain of the pre-amplifier has a small temperature coefficients. However, this heat can be removed by transfer to the flowing helium gas, and also, once thermal condition achieves its equilibrium, this heat is kept stably. Moreover, as one can suppose easily, we always take a ratio of charges measured at both ends of wire or cathode pads, *i.e.* heat changes are not so serious to the measurement sensitivity, because deviation of gain is cancelled by taking a ratio of collected charges.
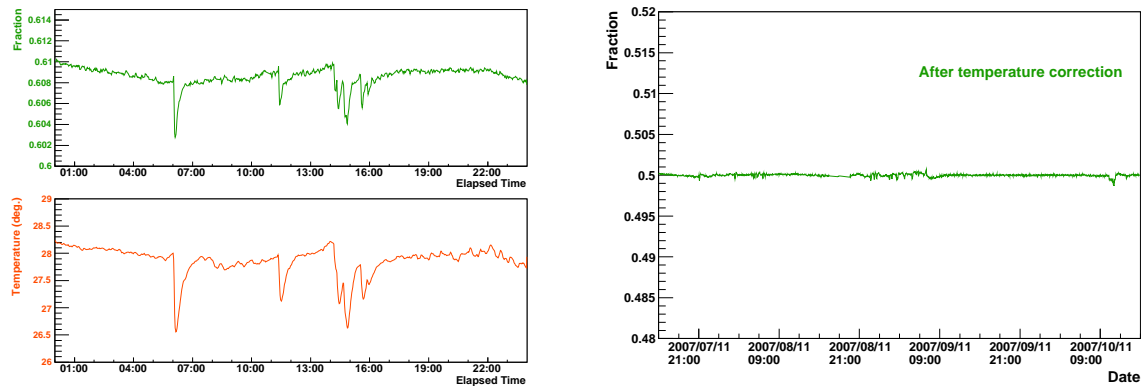
(a) non-calibrated helium fraction and temperature of the helium sensor

(b) calibrated helium fraction

Figure 5.21: Helium Fraction

helium atmosphere. In fact, such a point is molded with epoxy resin to avoid discharge. But several chambers have weakness of this mold, and then, we decided to dope small amount of air into the COBRA-helium inlet in order to control the air contamination inward COBRA; helium concentration has been controlled to be 95.75 % during the engineering run 2007. This effect will be discussed later, in Section 10.2.3.

5.6 Summary of the MEG Drift Chamber

Structure	16 modules radially aligned with $10.5°$ intervals
	Staggered 2 layers of axial wires per module
	9 cells per layer
Chamber Dimension	Trapezoidally-shaped
	R(min) = 193.38 mm, R(max) = 278.88 mm (fiducial volume)
	Z(min) = 385.66 mm, Z(max) = 827.31 mm (fiducial volume)
Cell Dimension	Conventional rectangle cell
	9.0 mm $\times$ 7.0 mm (*cf.* Figure 5.3)
	Wire Spacing : 4.5 mm
Sense Wire	Ni/Cr (80:20)
	Diameter : 25 μm
	Tension : 50 gf
	Resistance (per unit length) : 2200 Ω/m
Potential Wire	Be/Cu (2:98)
	Diameter : 50 μm
	Tension : 120 gf
Cathode Foil	Polyimide (**UPILEX** ®) with aluminum deposition
	Thickness : 12.5 μm (polyimide), 250 nm (aluminum)
Vernier Pads	4 pads per cell
	Pattern period : 50.0 mm
	Resistance (per unit length) : 47.5 Ω/m
Gas	He : C_2H_6 = 50 : 50
	Flow rate : 70+70 = 140 cm^3/min.
	Exchange time : 110 min.
	Typical drift velocity : 4 cm/μsec
	Typical electron diffusion : 140μm/cm (at 1kV/cm)
Frame	Open shape
	Carbon fibre (anode/cathode)
Voltage	Sense Wire (Anode) : + 1850 V
	Potential Wire : Ground
	Cathode : Ground
Number of Channels	Cell : 288 wires (16 modules $\times$ 2 layers $\times$ 9 cells)
	Readout : 1728 channels (288 cells $\times$ 6 channels)

Table 5.3: Characteristics and Parameters of the MEG Drift Chamber

Chapter 6

Simulation

The MEG experiment makes one's utmost efforts to minimize the number of detector component in order to suppress accidental coincidences. As mentioned above, γ ray is measured by only one detector; liquid-xenon γ-ray scintillation detector, for the energy, the timing, and the position, simultaneously. On the other hand, positron is measured by the spectrometer with low-mass tracking system. There is no vertex detector, no particle-identify detector, no muon beam monitor *etc*. In consequence, the number of physical references to the measurement is limited; the simulation of the experiment is crucially important in order to guarantee the validity of the detector responces and also the normalization of the number of events.

In this chapter, the detail of the simulation is given. First, the MEG Software Family is briefly described about not only the simulation part but also the analysis part. Next, the Monte Carlo simulation part is shown in detail, the event generation part and also the detector simulation part. Finaly, it is discussed how the electronics output is simulated.

6.1   MEG Software Family

The MEG Software Family is composed of the *online/offline* parts. The *online* part is provided by the **MIDAS** universal-data-aquisition system [86], and *offline* part consists of three parts; **megmc, megbartender**, and **meganalyzer**, as shown in Figure 6.1 schematically.

The **megmc** is the Monte Calro (MC) simulation software based on the **GEANT3** simulation tool [87] and performes **event generation** and also **detector simulation**. The event generation part is processed at the first of all, but event generation itself needs the detector information. Then, the event generation part and the detector description part is provided separatery but simulation processing is implemented as a monolithic package. The **megmc** software package provides the simulated physics event in the **ZEBRA** format [88]. Additionally, we here need two essential simulations; the **event mixture** and the **electronics simulation**. The **megmc** provides the physics simulation as a stand-alone process, however each generated events should be merged according to the high muon-beam rate. In the meantime, **megmc** can provide only the physical output, so-called "*hit*", and hence it is necessary to simulate the waveform output in the same format of the real experiment, DRS waveform format (see Section 3.5.2), through the electronics simulation. The **megbartender** provides both of them, the event mixing and the electronics simulation, simultaneously and outputs result to a **ROOT** [89] format file. After the

- Experiment -

MIDAS

.mid file

* Data Aquisition
* RAW data

- Simulation -

megmc

.rz files

megbartender

.root file

meganalyzer

.root file

* event reconstruction
* event display
* ROOT format data

* event generation
* detector simulation
* physics background
* ZEBRA format data

* event mixing
* electronics simulation
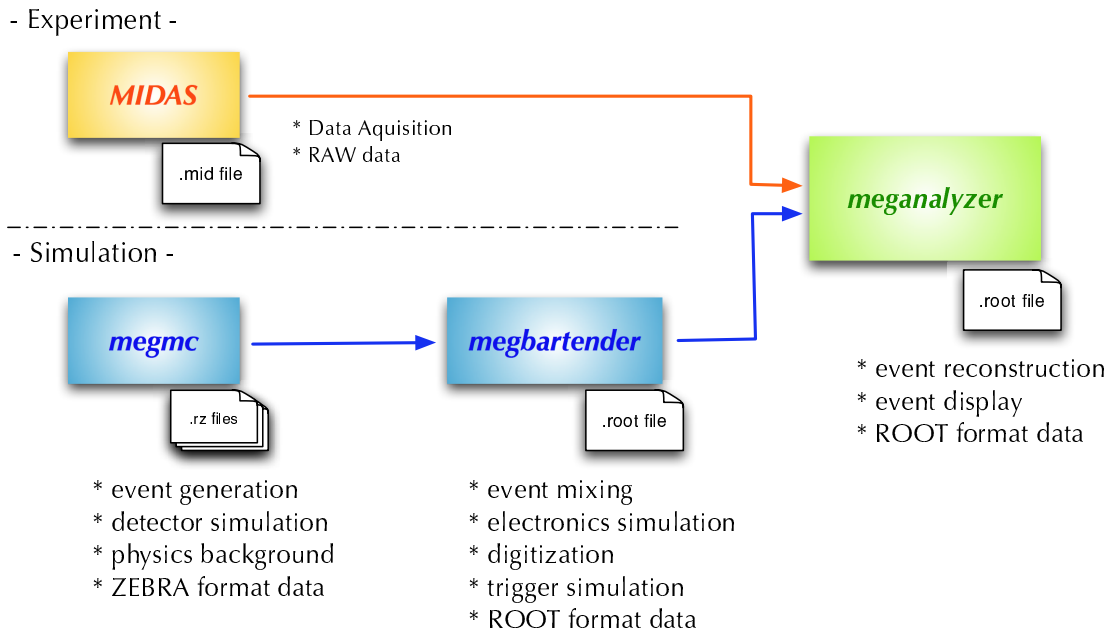* digitization
* trigger simulation
* ROOT format data

Figure 6.1: Structure of the MEG Software Family

electronics simulation process, one can step into the **event reconstruction** stage. The event reconstruction is performed by the **meganalyzer** software package, and this software provides also the **event display** for the *online/offline* both usage. In order to provide the reconstruction code for the experimental data and the simulation data universally, the **meganalyzer** is designed allowing both the input formats; **MIDAS** and **ROOT**. Finally, the **meganalyzer** gives the reconstructed variables, positron momentum, angle, and timing; and γ-ray energy, timing, incident position, *etc.* in a **ROOT** format file.

6.2 Monte Carlo Simulation

6.2.1 Event Generation

The first task of the **megmc** is the event generation. User can choose the "event mode" from 30 event types listed in Table 6.1. From ID 1 to 5, event types are assigned for the fundamental event simulation, signal event and physics background, accidental backgrounds. From ID 11 to 13, positron alone mode is assigned; mono-energetic 52.8 MeV/c positron, or Michel positron are generated for the detector studies. From ID 21 to 29, several kinds of γ-ray generation mode are concerned; mono-energetic 52.8 MeV γ, or γ-ray from the radiative decay, or γ-ray from the accidental decay, and its overlaps are generated. After event ID 50, many alternative calibration sources for each sub-detectors are implemented.

For each event type, kinematical condition (*e.g.* emission angle of signal γ, angular range for the radiative decay positron, zenith angle distribution of the cosmic ray, phase space of the muon beam, *etc.*), can be configured as user wants. As mentioned briefly, many event types

ID	event type	ID	event type
1	$\mu^+ \to e^+\gamma$ signal event	28	pile-up between flat-spectrum γ's
2	$\mu^+ \to e^+\nu_e\bar{\nu}_\mu\gamma$ radiative decay event	29	γ from AIF by using pre-computed table
3	Michel e^+ with γ from RD	30	μ^+ beam from BTS
4	Michel e^+ with γ from AIF	50	cosmic-μ in a fixed direction
5	pile-up between RD & RD	51	cosmic-μ with zenith-angle distribution
11	52.8MeV mono-enegetic e^+	61	LED light
12	Michel e^+	62	γ from thermal neutron capture on Ni
13	e^+ from flat energy spectrum	63	α from calibration radioactive source
21	52.8MeV mono-energetic γ	64	p^+ from CW accelerator
22	γ from RD	65	e^+e^- pair from 54.5/82.9 MeV γ
23	γ from AIF	66	e^+e^- pair from 129 MeV γ
24	γ from flat energy spectrum	67	γ from $\pi^0 \to \gamma\gamma$ decay
25	pile-up between RD γ's	68	p^+ from CW accelerator with LiF target
26	pile-up between AIF γ's	69	γ from $^{11}_5B(p,\gamma)^{12}_6C$ reaction
27	pile-up between RD+AIF γ's	80	Beam (configured by user)

Table 6.1: List of implemented event types in the **megmc**, (RD="Radiative Decay",AIF="Annihilation-In-Flight")

are prepared and its event kinematics can be modified flexibly. However, the **megmc** has two essential difficulties to ensure the detector response realistically, because the **megmc** can not merge events, and electronics simulation should be performed under the heavilly-overlapped situation. This is a reason that we decided to develop the MEG Software Family by three components separately.

6.2.2 Detector Simulation

In the **megmc**, all detector components are described by the standard **GEANT3** manner. Detailed geometry and material information is implemented as precisely.

Concerning the drift chamber, the detector geometry is implemented separately, listed in Table 6.2. Element-mixing ratio of the active gas, wires are written in the number of atom, but others are written in the mass ratio. In particular, since it is hard to implement real geometry of aluminum deposition on the cathode foil, each elements on the preamplifier circuit board, and coaxial cable structure, they are implemented as a blended material correctly-weighted by the mass ratio. Figure 6.2(a) shows how the drift chamber geometry is implemented, upper figure is one module view and lower picture shows the close-up view of the cross-section. Of course, all the exterior equipments are implemented precisely, cables and its duct structure is especially important since they can affect the detection efficiency of the timing counters and also generates γ rays which can be a source of accidental background. Figure 6.2(b) is an overall view of the drift chamber system. By comparing with the design view (Figure 5.12(a)), one can see that the implementation reproduces the real structure faithfully.

Each chamber module has own active gas volume, and furthermore, each gas volume is separated by "cell" that is defined by the sense wires. All the Geant-track-step passing this dummy-gas volume is recorded as a hit of the corresponding cell, if the energy loss of the

Component	Composition
Active Gas	He and C_2H_6 mixture (50:50)
Sense Wire	Ni and Cr mixture (80:20)
Potentital Wire	Be and Cu mixture (2:98)
Cathode Foil	Polyimide $(C_{22}H_{10}N_2O_4)_n$ and Al mixture
Frame	Carbon Fibre (Carbon and Epoxy resin mixture)
Support Structure	Carbon Fibre (Carbon and Epoxy resin mixture)
Pre-amplifier card	Mixture of O,C,N,H,Cu,Pb,Sn,Zn and Pd
	$\quad$ (30.1 : 24.2 : 22.0 : 2.2 : 7.3 : 2.6 : 4.0 : 4.1 : 3.5)
Cable	Mixture of C,F,Fe,Cu and Ag (11.4 : 35.9 : 5.7 : 46.2 : 0.8)
Cable Duct	Al
Gas Tube	Polyamide(Nylon6) $C_{12}H_{22}N_2O_2$
Gas Manifold	Polyvinyl Chloride (PVC) C_2H_3Cl

Table 6.2: List of implemented components for the drift chamber in **megmc**

Geant-track-step is higher than 40 eV. One can see this cell implementation and its hit determination in the lower figure of Figure 6.2(a). The **GEANT3** process has a commitment up to here, hit determination. After here, more precise simulation is provided by the alternative simulation tools in order to realize the compricated gasseous detector responses, this will be explained in the next section.

6.2.3 Geseous Detector Simulation

In order to make up the lack of the detailed behaviour simulation of the drift chamber in the **GEANT3** framework, elementary processes in the drift chamber are simulated by three alternative simulation tools, **HEED** [90]; **MAGBOLTZ** [91]; and **GARFIELD** [92].

The **HEED** program computes in detail the energy loss of fast charged particles in gases, taking delta electrons and optionally multiple scattering of the incoming particle into account. The program can also simulate the absorption of photons through photo ionisation in gaseous detectors. The **MAGBOLTZ** program provides electron transport parameters for a large variety of gases and mixtures of gases. The **GARFIELD** is one of the most famouse software to simulate the two- and three-dimensional wire chambers and to compute the field maps, electron and ion drift lines, drift time tables and arrival time distributions, signals induced on the wires by moving ions and electrons *etc.*, and also provides an interface to **HEED** and **MAGBOLTZ**.

In the **megmc**, the ionization processes inside the drift chamber active-gas region are carried out by the **GEANT** particle-tracking system, and then the drift behaviour of these generated electrons are simulated by three alternative simulation tools. The **megmc** has a charge until the drift electrons arrived close to the anode wire. After the drift electrons arrived, electron avalanche is simulated by the post-processor, **megbartender**. This procedure is complicated and not suitable from the development point of view. However, this structure has several benefits to realize required precise simulation in a reasonable way. At first, only the **GEANT3** functionality can not perform the complicated processes of the gaseous detector responce. In an analogous fashion, it is also impossible to simulate all the physics process and secondary particle generation

74

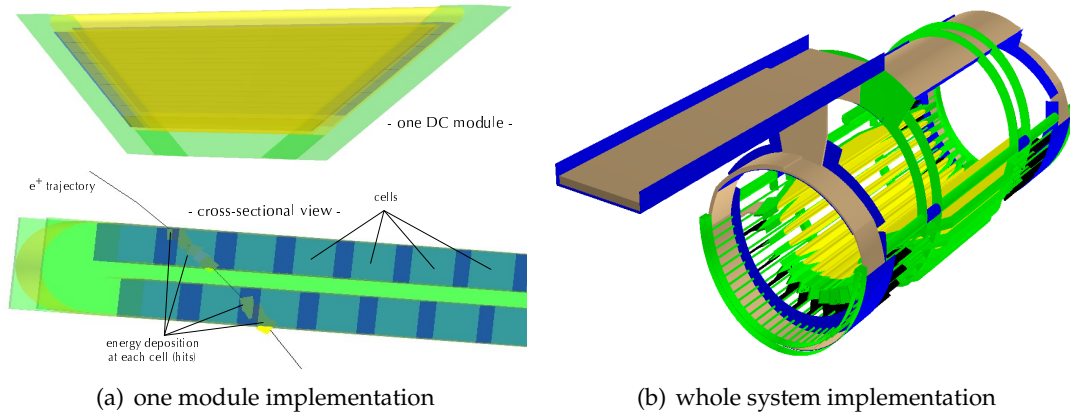(a) one module implementation   (b) whole system implementation

Figure 6.2: **GEANT** implementation for the drift chamber

only by the **GARFIELD** program. Currently, the **GARFIELD** program is generally accepted and experimentally verified by a great deal of high-energy experiments. Thus, up to the physical event process and the response simulation of the gaseous detector, the combination of **GEANT3** and **GARFIELD** can be the most encouraging simulation tool.

The most important aspects of such simulations for the MEG drift chamber are **to provide the isochrone maps for the drift electrons**; **to evaluate the uncertainty of the primary ionization**; **to estimate the effect of electron diffusion**. Creating the isochrone map is important for such a simulation purpose in general, but other two purposes are essential for the MEG drift chamber in order to reproduce the detector resolution. As mentioned in Section 5.2.3, due to
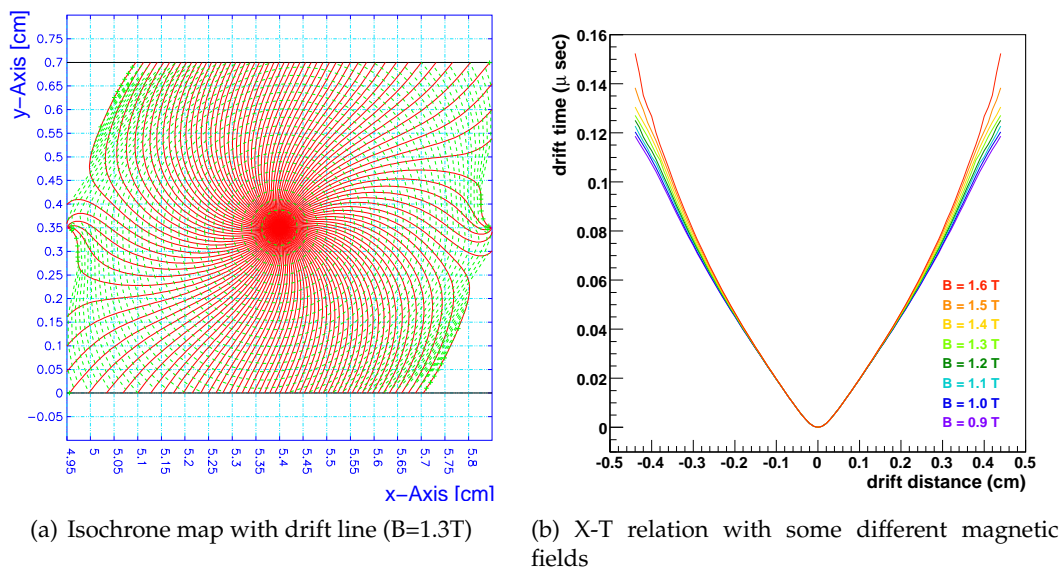

(a) Isochrone map with drift line (B=1.3T)   (b) X-T relation with some different magnetic fields

Figure 6.3: Precise isochrone map and Time-to-Distance relationship simulated by **GARFIELD**

75

the characteristics of a helium based gas, the effects of electron diffusion and fluctuation of the number of primary ionization confine the transverse spacial resolution.

Figure 6.3(a) is precisely simulated isochrone map of drift time, where the strength of magnetic field is 1.3 T. This calculated two-dimensional isochrone map is implemented in the **megmc** providing the fine drift velocity information. Here, we have to take into account the variety of the COBRA magnetic field because one can see significant difference on the Time-to-Distance, so-called "X-T" relationship, with several magnetic fields in Figure 6.3(b). In this figure, strength of the magnetic field is varied from 0.9 to 1.6 T; in the region of drift chamber in the COBRA field, field strength is distributed over this range (see Figure 4.7). From Figure 6.3(b), large discrepancy can be seen up to 35 nsec, and this is corresponding to 1.4 mm difference if we assume 4 cm/μsec of drift velocity. Thus, eight sets of the isochrone map like Figure 6.3(a) with 0.1 T intervals are provided by the **GARFIELD** and implemented into the **megmc**.

As mentioned above, the electron-diffusion effect and the fluctuation of primary ionization are essential in order to reproduce the drift-chamber resolution. Then, such fundamental effects are also simulated precisely by the **GARFIELD** as shown in Figure 6.4. Figure 6.4(a) shows the

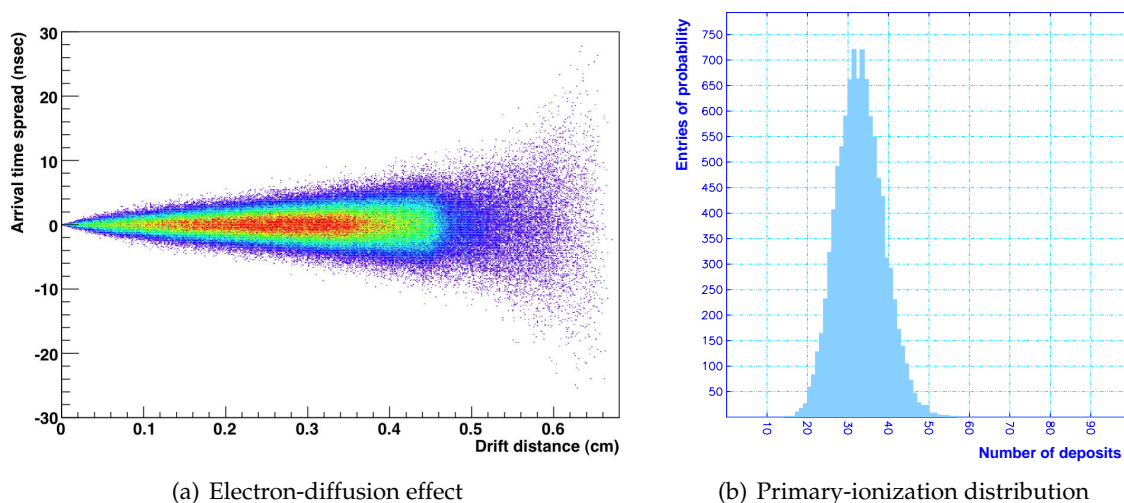| (a) Electron-diffusion effect | (b) Primary-ionization distribution |

Figure 6.4: Precise simulation of fundamental physics processes of the drift electron

arrival timing spread of the drift electron as a function of the drift distance;

Figure 6.4(a) shows the arrival timing spread caused by drift-electron diffusion. Next Figure 6.4(b) presents the number of ionization-clusters distribution. The number of created electrons per each cluster is also simulated, *i.e.* 1 to 2 electrons a cluster. Such a fundamental physics-processes simulation provides important parameters, *e.g.* diffusion coefficients, number of primary ionization, number of electrons per a cluster, attachment and dissociation coefficients, *etc.*, and such parameters are implemented into the **megmc**. Consequently, the **megmc** can simulate all the physics processes till the electron avalanche at the wire neighborhood. After the electron avalanche and electronics effects will be simulated at the postprocess, **megbartender**, because such effects should take into account the event overlaps.

6.3 Electronics Simulation

The **megbartender** program provides three important simulations; **event mixing**, **waveform simulation** and **trigger simulation**. In order to actualize the realistic high rate situation, event mixing is necessary; the naming of **megbartender** is likened to "*cocktail* of events".

After event mixing, one can simulate the electronics processes, electron avalanche at the wire neighborhood, pulse generasion on the wire and the cathode pads, pulse transportation, pre-amplifier output, and encoding to the DRS waveform format. Finally, the trigger simulation is processed.

6.3.1 Event Mixing

Event mixing should be done before waveform simulation since the waveform can be changed by how they are overlapped. In order to mix a number of diverse events, one should carry out several **megmc** processes incorporating each event types; *e.g.* $\mu \rightarrow e\gamma$ signal event, Michel positrons, *etc.*, before the **megbartender** process. It is possible to mix events in two ways; one is specifying "event rate", the other is specifying "fixed timing", and both modes work in parallel. If one wants to mix sub-events by the specified event rate, sub-events are mixed with this rate randomly in accordance with Poisson distribution, or periodically. Meanwhile, it is also possible to mix the sub-events with specified timing. Additionally, both modes are able to be merged, and hence, *e.g.* fixed signal-event interval with random background-event generation by specified muon-beam rate is a presumable example of event-mixing scheme by the **megbartender**. Figure 6.5 illustrates the result of simulated event-mixing. Figure 6.5(a) is

(a) Three-Dimensional view

(b) Two-Dimensional expansion view (Upper: $x - y$ view, Lower: $x - z$ view)
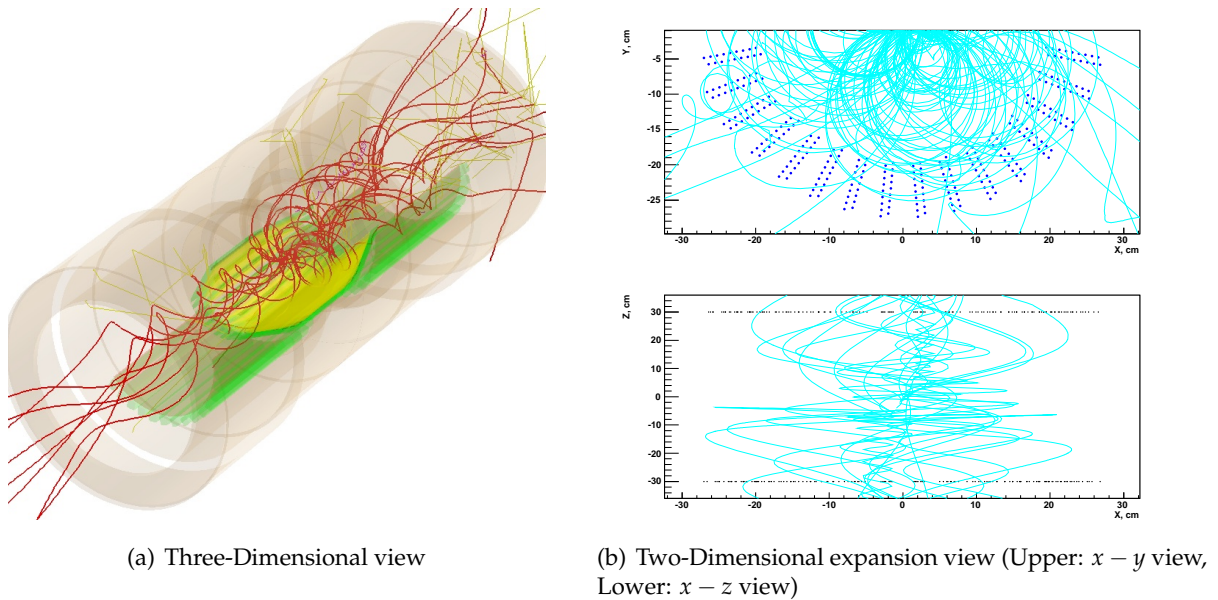
Figure 6.5: Example of event mixing processed by the **megbartender** reproducing the 3×10^7 sec^{-1} muon intensity

three-dimensional view of the event-mixing, and Figure 6.5(b) is its expansion view of two

projections; this example is simulated as 3×10^7 sec^{-1} muon beam rate, and it is expected operation rate for the MEG *live* run. We here completed the event mixing, and then, we now can perform the waveform simulation.

6.3.2 Waveform Simulation

As described in Section 3.5.2, all the detector readouts are recorded in the DRS waveform sampler. Thus, the **meganalyzer** should be able to reconstruct the event from the waveform outputs, *i.e.* the **megbartender** also should provide the same waveform format converting from the **megmc** output.

Up to here, the **megmc** produced the "physics-hit" information incorporating the "drift-electron" information for each primary ionizations individually. Hence, the remaining task is to simulate the electron avalanche at the wire nighborhood and the electronics responses including all electrical effects of "wire", "pre-amplifier", "cable", and "DRS". For more detail, the **megmc** provides the number of primary ionizations with corresponding arrival times of each drift electrons for all hit wires; this simulated arrival time is the sum of the drift time and the time-of-flight of positron from the target, and hence, this is absolute electron-avalanche timing at the wire neighborhood. Thus, all we have to do is to simulate the pulse generation weighted by the number of ionization clusters and to superimpose all generated pulses spaced by the arrival-time differences, and then, we will get the waveform output. Concerning the pulse generation, this simulation should contain the fine tuned electronics responses; this is not easy. In principle, if we could collect all parameters to simulate the electronics responces, *e.g.* absolute gas amplification, ion mobility, signal-attenuation within the wire/cable, frequency response, CR time constants, preamplifier gain/shaping, *etc.*, the pulse generation can be simulated by solving the differential equation of the equivalent circuit. However, collecting all relevant parameters is difficult, because a lot of electronics processes are correlated and reproducing several electronics properties is not enough precise. Finally, we decided to adopt the "impulse-response" method [93] in order to simulate the pulse generation for each ionization clusters instead of the standard CR-parameterization.

The impulse response of a system is its output when presented with an impulse input, *i.e.* it is a certain type of a "filter". An impulse represents the limiting case of a pulse made very short in time while maintaining its area or integral, namely something can be modeled as a Dirac δ-function. In order to characterize the output uniquely, the impulse response system has a response function, called "transfer function *". Going back to the pulse simulation for each ionization, the **megmc** provides the pairs of "number of primary ionizations (clusters)" and "arrival time of drift electrons" for each hit. Such outputs are discrete, and each pair can be characterized by

$$N_i \times \delta(x - t_i),$$

where N_i is the number of cluster of i-th ionization and t_i represents the arrival time of i-th clusters, respectively. Thus, the output of **megmc** can be considered as an input of the impulse response. If we can have the transfer function for the single drift electron, we can perform the waveform simulation by an impulse response filter.

---

* To be more accurate, a transfer function is the result of Z-transform of the difference equation which defines how the input impulse is related to the output signal.

In order to obtain the transfer function, a special measurement was carried out by irradiating 5.4 keV soft X-ray from the ^{54}Mn radioactive source. By this measurement, the output waveform provided by single electron avalanche is obtained. Figure 6.6(a) shows an example of the anode-waveform output of a 5.4 keV X-ray event, and then, the response function, so-called "template waveform", is obtained as shown in Figure 6.6(b) by averaging over a thousand events. This measurement was performed with final experimantal settings, same preamplifier,
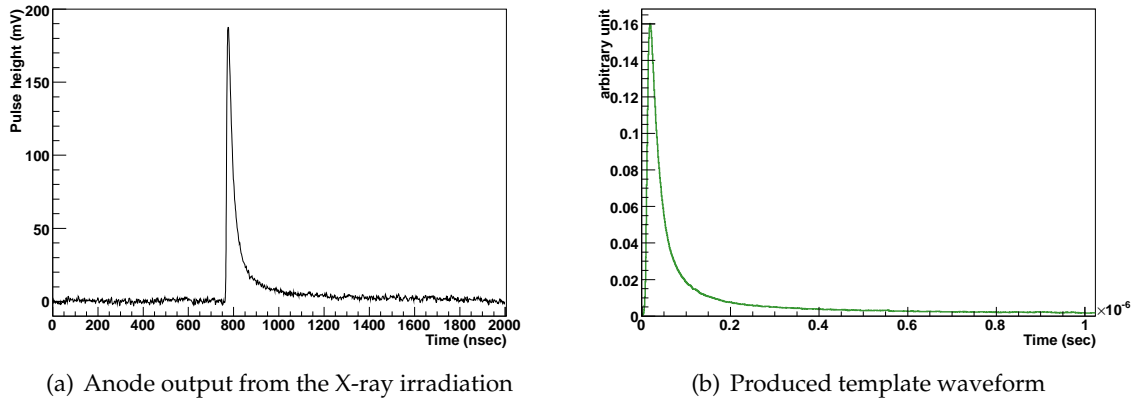

(a) Anode output from the X-ray irradiation

(b) Produced template waveform

Figure 6.6: Response function for the impulse response by ^{54}Mn radioactive source

same cable length, same DRS chip *etc.*, in order to include all the electronics effects associated with the output pulse. Thus, obtained template waveform should contain all such effects, and finally, all tools to simulate the waveform output is completed.

Now, we can simulate the output waveform by using the result of **megmc**. The left plot of Figure 6.7 illustrates the result of **megmc** corresponding to one hit wire. This histogram is the
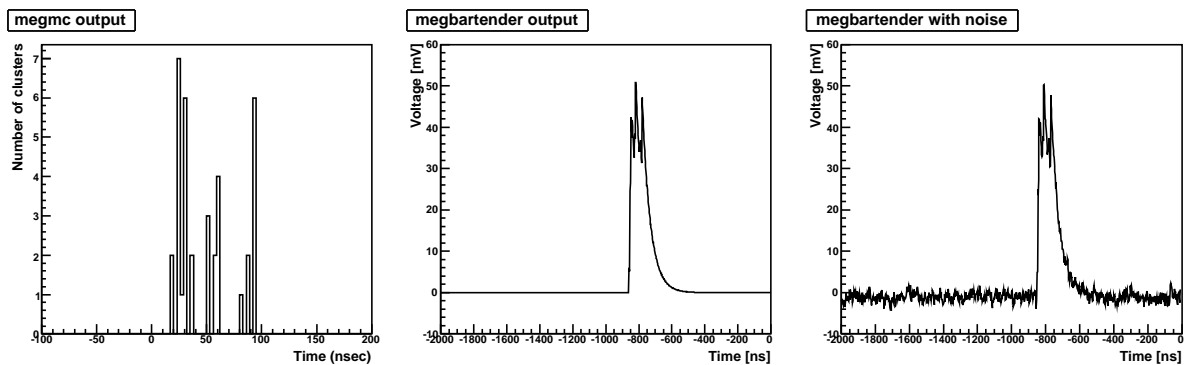

Figure 6.7: Waveform simulation; from **megmc** to **megbartender**

electron arrival time so that zero-time corresponds to the positron-start time from the target, and the entries represent the number of clusters. Then, all entries corresponding to each ion-

ization are filtered by the impulse response with obtained template waveform [†]. The centre plot of Figure 6.7 shows the result of waveform simulation by the **megbartender** incorporating the impulse-response method. Finally, the right plot of Figure 6.7 is superimposed view with the baseline noise; this should be comparable to the real output (*cf.* Figure 3.9). One can see a reasonable quality of the simulated waveform in Figure 6.7. On a final note, the quality of electronics simulation is verified by two quantities. Figure 6.8(a) shows the charge integration, pulse area, of the data and MC simulation. This data is provided by Michel positron,not X ray. One can see the excellent reproducivility even if the pulse is generated by the minimum ionizing charged particle. Figure 6.8(b) represents an alternative quantity that denotes the quality of

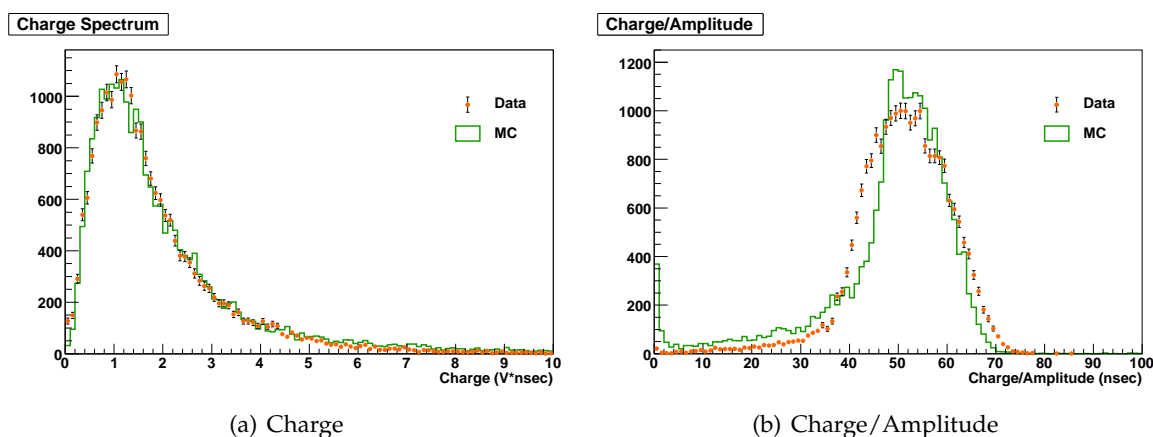
(a) Charge

(b) Charge/Amplitude

Figure 6.8: Reproducibility of Waveform Simulation

simulation, the charge divided by its amplitude. Even if the charge is reproduced successfully, shape of pulse is possibly changed. Thus, the quantity of charge over amplitude can derive a kind of shape reproducibility. From this plot, it is clearly indicated that the shape of pulse is almost reproduced successfully, but it is not perfect. There is still the possibility to improve it, *e.g.* for the small charge/amplitude region, this discrepancy may be caused by wrong number of generated ionization, this can be improved in **megmc**.

6.3.3 Trigger Simulation

The **megbartender** performs a trigger simulation in order to reproduce the data acquisition completely; *i.e.* the post-process, **meganalyzer**, can handle the MC data as well as the real data. In the current **megbartender**, several trigger modes are implemented, *e.g.* $\mu \to e\gamma$ signal trigger, $\mu \to e\gamma$ trigger by charge infomation, $\mu \to e\gamma$ trigger by timing information, calorimeter alone trigger, drift chamber alone trigger, triggerred by any sub-events *etc.* The drift chamber alone trigger mode is brought to carry out the special calibration run for the drift chamber; we will mention this trigger mode in the calibration part, Section 8.2.2. The last trigger mode, triggered by each sub-events, doesn't take into account the trigger condition so that one can see the detector response without any trigger biases.

[†] Just single impulse responce is not enough. Several shaping processes are also necessary since the real output waveform can be deviated away from the template due to attenuation.

Chapter 7

Event Reconstruction

One of the most important, almost only one, purpose of the MEG drift chamber is the track reconstruction. In this chapter, detailed explanation of the event reconstruction is expanded by following a real analysis flow.

7.1   Overview

A broad overview of the event reconstruction, from the raw data to the muon momentum and emission angle, is discussed in this section. The event reconstruction, namely e^+ track reconstruction, is carried out by the following procedure. At first, "hit" of the charged particle in the drift chamber should be reconstructed. Of course, a lot of noise hits are recorded within same integration window of the DRS waveform. There are two kinds of noise hits here, one is caused by the electronics noise, so-called white noise, and another is provided by the overlapped tracks due to high muon intensity. A certain amount of the first noise component can be rejected at this hit reconstruction stage. The rejection of the second noise component depends on topological relation with each other tracks, and hence such noise components are rejected in the next stage, namely track finding. The track finding stage is composed by two procedures, "cluster finding" and "track finding". As described above, each drift chamber module is composed by two adjacent layers of axial sence wires. Thus, each hits associated with the same track within single chamber module can be combined, so-called *clustered*, and this clustering will help track finding. The track finding is carried out by a certain ilk of the pattern recognition. In the research field of the pattern recognition, there are a lot of types of the algoritms, *e.g.* based on a neural network, cluster analysis, combinatorial optimization, topological algebra, recursive filter of a dynamic system, *etc.* The MEG tracking algorithm adopts the combination of the cluster analysis and combinatorial optimization, because the MEG drift chamber is able to measure the position of a charged particle track only in a fairly small number of measurement points so that it can not be applied any topological algebra or neural network efficiently. After all the significant hits are connected to the objective track, all the hit points are fitted to the charged trajectory. Track fitting is performed by the application of the Kalman filter [94] technique in order to take into account the multiple Coulomb scattering and the energy losses effectively.

7.2   Hit Reconstruction

All the online raw data is provided as the DRS waveform output, *i.e.* the first task of the event reconstruction is the **hit reconstruction** from the raw waveform output.

At the beggining of hit reconstruction, it is neccessary to determin the baseline of waveform. In order to keep the quality of baseline determination, a noise subtraction process is necessary. Since a carbon-fibre frame is not an ideal conductor, a certain oscillation on the waveform outputs at the both end of the wire is observed. Additional grounding between the two print-circuit bords of both end reduced such an oscillation drastically, but there is still a small oscillating component. This long-period noise component has a $180°$ phase difference between the both end of the wires, and hence, the baseline oscillation can be subtracted by applying the following steps. (1) Sum up the waveforms of both end of the wire and seach for peaks. (2) Subtract the waveform of one end of the wire from the waveform of the other end. Fit a quadratic-, or cubic-, polynomial to the differential waveform excluding the peak region. (3) Use the fitted polynomial function to subtract the noise on the original waveforms. Figure 7.1 shows an example of this noise subtraction process. In this figure, one can see the clear anti-correlation between each wire ends, and the good resulting baselines. An amplitude of this long-period noise is varying typically up to 2mV. By this procedure, the accuracy of baseline estimation can be guaranteed, and it is essential for a good pulse-timing determination.
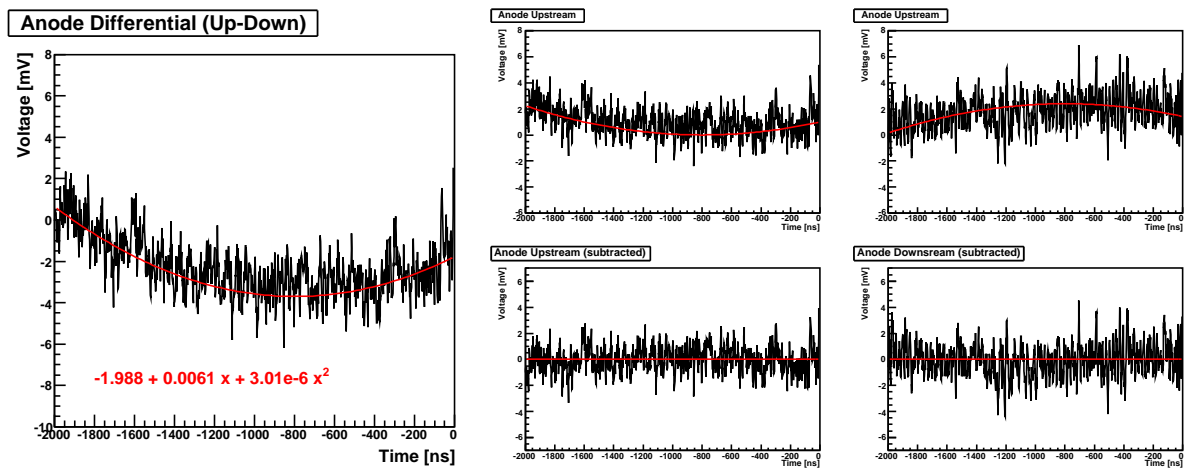

Figure 7.1: Baseline Noise Subtraction. The left plot shows the difference between upstream and downstream. Two upper plots of right side are raw waveforms and two lower plots are subtracted results. (The signal pulse is excluded in this view to simplify an expression.)

After the noise subtraction, a rough baseline determination is performed. For this purpose, the waveform amplitudes are filled in a histogram, and then, the amplitude with the maximum number of entries of the distribution is taken as a first baseline estimatation. In order to find the signal pulse on the waveform, a moving-average method [95] is adopted. The start and the end of a pulse is defined as the time when the moving average crosses a threshold. A pile-up pulses are recognized by the change of a sign of the derivative. Moreover, if the height

of found pulse is below the threshold, this candidate is rejected. This pulse-height threshold is optimized by looking the number of hit candidate as a function of various threshold, and the optimum threshold is determined to be 7 mV. After the pulse finding process the baseline calculation can be improved by using objective region of a waveform.

In order to obtain a hit timing, a leading edge of the signal pulse is fitted. In the first step, the point on rising edge, where the gradient reaches its maximum, needs to be determined. Second, the rising edge is fitted with a quadratic (or cubic) polynomial to the pulse. To optimize the rising time measurement, several fits are applied including different sets of points around the maximum gradient point. Then, out of the various fits, one result which is associated with the best fraction of χ^2 over the number of degree of freedom is adopted to determin the leading edge. Finally, the pulse timing is determined as the time of the intersection between the fitted leading edge and the fitted baseline. Figure 7.2 presents an example of leading-edge fitting

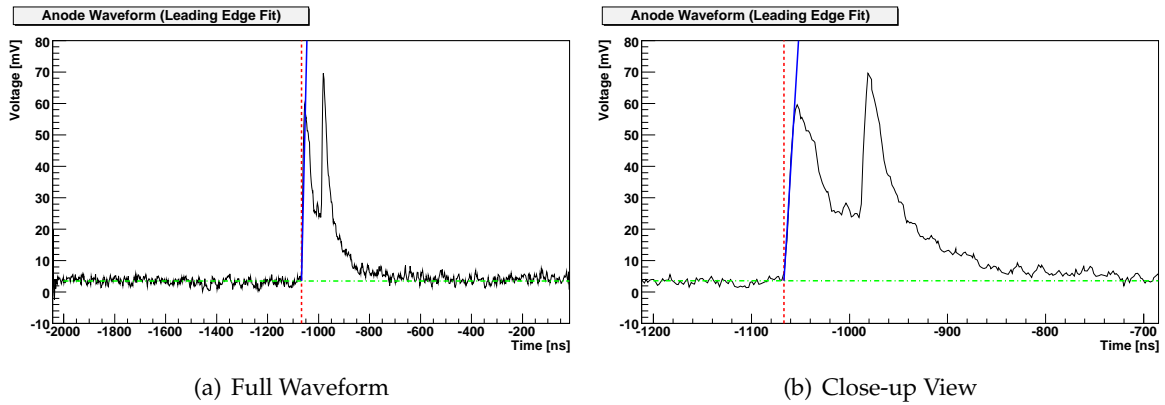(a) Full Waveform   (b) Close-up View

Figure 7.2: Leading-Edge Fitting to the signal pulse

to the signal pulse. Figure 7.2(b) is a close-up view of Figure 7.2(a). A green dot-dash-line represents the fitted baseline, a blue solid line represents the fitted leading edge, and a red dashed line represents the determined pulse time, respectively.

Once the pulse is found and its timing is determined, the pulse area is integrated and converted to another quantity, "charge" in order to obtain the hit coordinate by a charge-division method. The integration range obviously should be same for all the data-analysis including all calibrations involving charge integration, since the signal propagation on a wire depends on the frequency spectrum of the signal. The different integration ranges select different frequencies out of the total frequency spectrum of the signal pulse; the result of charge division can be different, if the integration range is changed. The integration range is optimized by looking the reconstructed z-position resolution as a function of the various integration ranges. The start point of the integration range is taken from the leading edge timing. If there is no time available from the fit (*e.g.* for small cathode signals) the avaraged anode-hit time of both ends is adopted.

At the first hit reconstruction stage, all possible pulse candidates are reconstructed even if

it is not associated with the triggering charged particle. The most important purpose of this process is to find candidates of the pulse from the waveform outputs and determine the pulse timing quickly and enough precisely. Only the obviously insignificant hit, *e.g.* one-side missing pulse, is rejected at this stage, *i.e.* a certain amount of white noise are rejected. All other noise hit is eliminated in the next stage, track finding process.

7.2.1 Hit Coordinate Reconstruction

Now, we have both informations to reconstruct the hit coordinate bidirectionally; the timing of pulse for "r" coordinate (transverse), and the charge of pulse for "z" coordinate (longitudinal). However, the r-coordinate reconstruction is not carried out at this stage due to following reason. By using a drift time, it is possible to estimate the transverse hit coordinate, but it is not enough precise because drift time-to-distance relation, so-called X-T relation, has a strong angular dependence. In Figure 7.3(a), one can see that the X-T relation has strong dependence
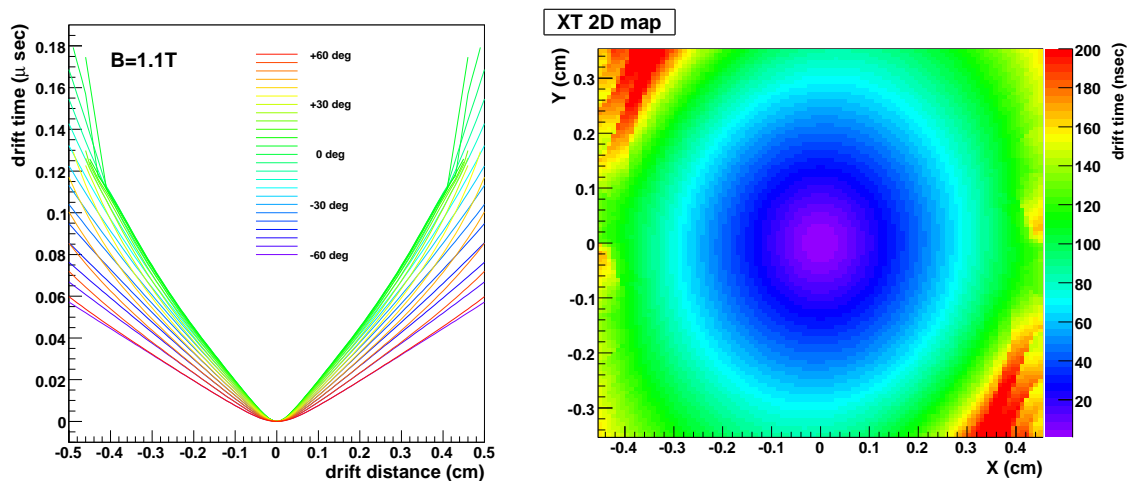
(a) Calculated X-T relation with some different incident angles with respect to the normal of DC

(b) X-T 2D map

Figure 7.3: Drift Time-to-Distance relation (B=1.1T)

on the incident angle with respect to the normal vector of drift chamber, and also in the two-dimensional X-T map, Figure 7.3(b). Additionally, before the r-coordinate determination, the left-right ambiguity of that the track passed a which side of the wire should be solved. In order to correct an angular dependence on the X-T relation and to solve the left-right ambiguity, the track-finding process should be performed. Thus, the r coordinate is reconstructed during the track-finding process, not in the hit-reconstruction process.

On the other hand, the z-coordinate reconstruction is performed here, since charge information is enough for z reconstruction. In principle, the z-coordinate reconstruction is performed in two steps; the anode charge-division method provides the rough z prediction, and then, the vernier-pad method derives the precise z coordinate, as described in section 5.2.4. Both reconstruction methods use the ratio of collected charge. In consequence, the relative gain difference between both ends of the wire, or both ends of the pad, can degrade the reconstruction

84

performance significantly; a relative gain difference is mainly caused by the fluctuation of pre-amplifier gain. Such a relative gain difference is able to be corrected at the z-calibration process that is discussed in section 8.4. Thus, the hit coordinate reconstruction in the z axis is also discussed in section 8.4 with the z-calibration procedure in detail.

Once hit reconstruction is completed, track candidate should be recognized, and we can connect hits to the candidate. In the following section, the track finding process is discussed.

7.3 Track Finding

Track finding usually means finding charged tracks in a tracking detector, *i.e.* the task of track finding is equivalent to a partition of measured coordinates into disjoint sets, allowing for the fact that some measurements are noise or belong to tracks that is not objective of the experiment. The choice of the algorithm depends on the type and on the quality of the measurement the tracking detector is able to deliver. In addition, the shape of the detector and of the magnetic field determine the mathematical model of the track; this in turn may have a decisive influence on the selection of the most suitable procedure.

Concerning the MEG tracking system, the possible number of position measurement is strongly limited due to a lot of constraints that should be satisfied by the MEG detector apparatus. In consequence, the MEG apparatus has no vertex detector; positron track must be reconstructed by drift chamber only. The MEG drift chamber is segmented in order to minimize mass in the spectrometer and to ensure precise z-coordinate measurement; this means that the number of available wire is very small. In addition, thanks to the benefit of COBRA field, it is enough to put the drift chamber on the outermost part only. This feature enables drift-chamber operation at very high muon intensity, but on the other the possible position measurement is limited to the outermost part; the trajectory must be reconstructed by coordinates in outermost region only. And also, tracker should suffer from many overlapped tracks due to high muon intensity. In such a severe circumstance, track finding and track fitting must be challenging.

Recently, in the field of high energy physics experiment, track finding has a tendency to be done with the track-fitting process, especially recursive filter of a dynamic system. A traditional track fitting based on Least-Squares-Method (LSM) is called **Global-Track-Fitting** (GTF) by contrast with that track fitting based on recursive filter is called **Sequential-Track-Fitting** (STF), or **Adaptive-Track-Fitting** [*]. While GTF handls all hit coordinates during a minimization process simultaneously, STF handls each hit coordinates individually and sequentially; *i.e.* the hit candidates can be judged by its sequential procedure of STF. Hence, track finding and track fitting can be carried out by one adaptive method all-in-one. This sounds very reasonable, however if STF is adopted as the track finding algorithm, track finding process must take a certain time since finding process will need filtering process for all of the hit candidates with each cycle. If minimization process of STF is converged rapidly, or if other algorithms than STF do not have an acceptable performance, STF is the suitable algorithm for a tracking process.

On the other hand, geometrical, or topological, pattern-recognition method can be another solution for the track-finding algorithm. If the geometrical aspect of the objective track is

---

[*] Differences between GTF and STF will be discussed in the track fitting description, section 7.4 in detail.

enough discriminative, topological pattern recognition can be much more effective and faster than STF.

As mentioned just before, algorithm adoption depends on the detector type and performances primarily. For the MEG positron spectrometer, there are several aspects as listed in following:

  (i) There is no vertex detector.

 (ii) Number of hit is strongly limited.

(iii) Only outer hit coordinate is recorded.

(iv) Only triggering particle is objective.

 (v) Objective track is only the largest radius one.

(i)-(iii) are due to ensure the tracking accuracy and background suppression, *i.e.* they are unavoidable necessity. They will affect for the track finding based on STF obviously due to lack of position measurement. Once track finding completed and all hit candidates are connected to the track, STF can work effectively even though the number of position measurement is limited. However, this can not be a solution for the track finding but track fitting. On the other hand, the MEG spectrometer has other aspects, (iv) and (v). These plays attractive roles for the track finding as described below. It is possible to mask all the hit belong to counter side of the triggering particle due to asspect (iv). In addition, the signal-time-window can be applied to eliminate noise hits. As mentioned in section 5.4, the DRS time window for the drift chamber readout is 2 μsec and the trigger latency is arranged so that the pulse which is associated with the triggering particle appears around centre of the DRS time-window. And then, the signal-time-window can be determined as the range of drift time with a certain redundancy, *i.e.* all hits that appears outside this signal-time-window can be rejected. Further more, thanks to specification of the COBRA field, asspect (v) can reject non-objective tracks, even if there are multiple track candidates within a signal-time-window. In consequense, by using such powerful asspects, geometrical pattern recognition is suitable for the MEG spectrometer.

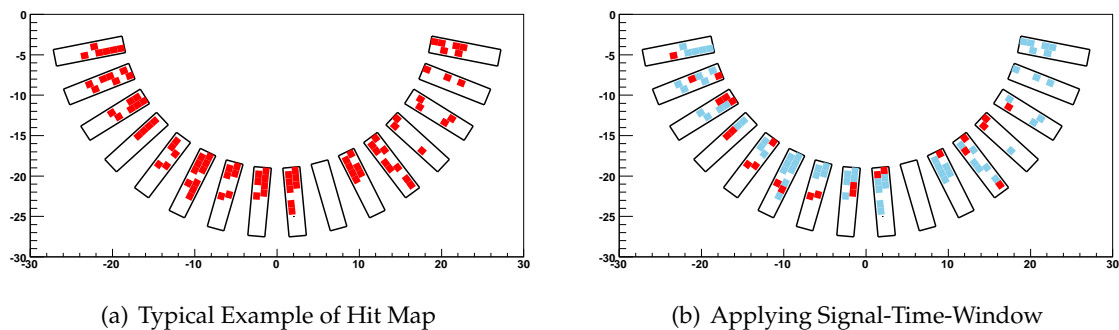(a) Typical Example of Hit Map   (b) Applying Signal-Time-Window

Figure 7.4: Two-dimensional Hit Map with The First Stage of Track Finding (Data)

Track finding is carried out by following procedure; (a) Applying signal-time-window, (b) Finding hit clusters, (c) Finding track seed, (d) Connecting clusters to the track. Figure 7.4(a)

shows an example of two-dimensional hit map (*x-y* view) of the typical event, 3×10^7/sec muon intensity, that was acquired in the engineering run 2007 [†]; red cells indicate "hit" which reconstructed by hit reconstruction process. The Signal-Time-Window is determined as 400 nsec by the maximum drift time 250 nsec with -50 and +100 nsec as forward and backward redundancy, respectively. By applying this time-window, almost 80 % of background hits can be eliminated because background pulses are lying uniformly and 1600 nsec out of 2000 nsec DRS window is rejected. Figure 7.4(b) shows the result of applying the Signal-Time-Window; light-blue cells indicate the rejected one.

7.3.1 Cluster Finding

If two hits within single chamber module are close in *z* coordinate, they are combined to a hit cluster. The left plot of Figure 7.5 shows *z*-difference distribution between neighboring two cells in the single plane; the centre plot of Figure 7.5 shows *z*-difference distribution between staggered two cells in different two planes within single chamber module, and the right plot shows its $|z|$ dependence. By investigating such relations with MC, the cluster finding criteria
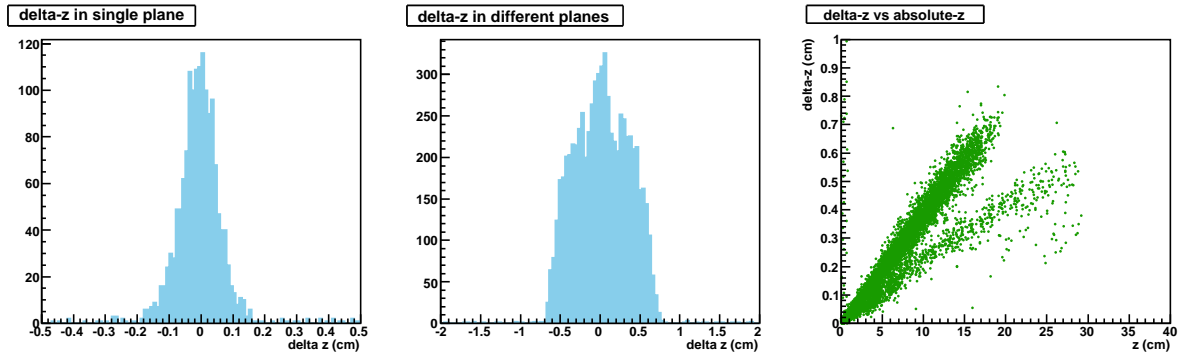
Figure 7.5: Δz distribution between two hits within single plane / different planes (MC)

are determined as listed in Table 7.1. As one can see from the plot, there is $|z|$ dependence

Two hits in single plane	Two hits in different plane
$\Delta z < 0.2$ cm + $0.02 \cdot z_1$ cm	$\Delta z < 0.6$ cm + $0.04 \cdot z_1$ cm
Two cells should be neighborhood.	Two cells allow skipping one cell.

Table 7.1: Cluster Finding Criteria

clearly, and hence, the clustering criteria are taking into account such $|z|$ dependences. In this $|z|$ dependence plot, one can see two discriminated distribution; they are corresponding to difference of the number of positron curling. These Δz distributions are simulated by MC; its reproducibility is confirmed by the data.

[†] In the engineering run 2007, several drift chambers were not operational fully, since a series of accidents occured. In this hit map, such dead (or bad) channels have a missing hit. Detailed special affairs for the engineering run 2007 is discribed in section 8.2.3; dead/bad channels are listed in Appendix B.

7.3.2 Track Seed

At first of the cluster connecting process, it is necessary to have a start point, called "track seed", connecting each clusters. There are several possible schemes to define a seed; *e.g.* the fastest hit cluster that fires trigger, number of consecutive clusters, outermost cluster, *etc.* In principle, according to the design of COBRA field, taking the outermost cluster should be an ideal track seed because the outermost track should be the signal track. However, this situation can be degraded by two reasons; the finite muon stopping distribution and missing channels of the drift chamber. In fact, muon beam had a finit spread, σ_x=9.5 mm and σ_y = 10.2 mm in the engineering run 2007, *i.e.* the outermost cluster is not necessarily connected to the signal track. On the other hand, as mentioned above, several chambers did not work fully in the engineering run 2007; starting from the outermost cluster with such missing channels is not effective. Hence, number of consecutive clusters is used as the track seed.

Finally, three consecutive clusters which satisfy the following criteria is adopted as the track seed. At first, all possible combinations of three clusters in consecutive chambers are listed. We
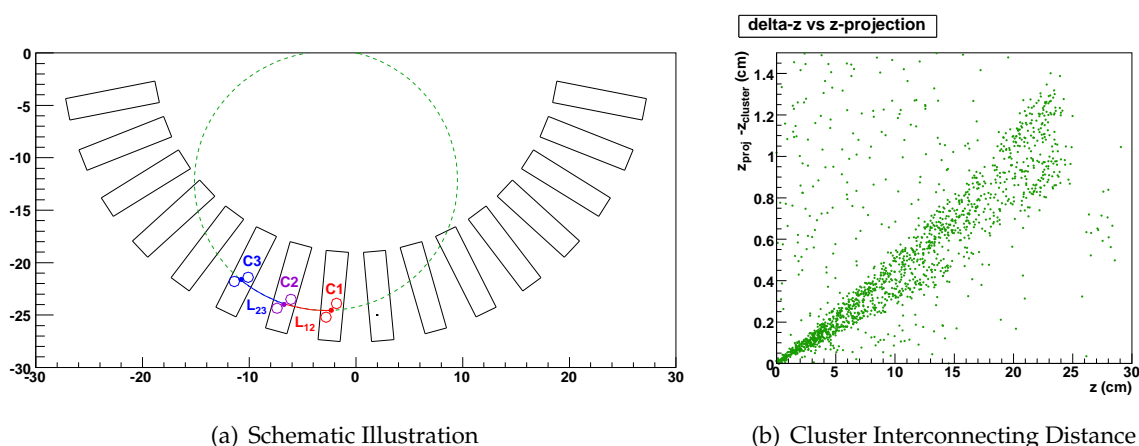

(a) Schematic Illustration

(b) Cluster Interconnecting Distance

Figure 7.6: Track Seed Finding (MC)

here introduce new parameter, "z-projection", in order to have a better constraint for track seed finding. Figure 7.6(a) can explain the definition of z-projection schematically; (1) calculate a circle in the xy-projction (green dashed-line) through the listed three clusters (C1, C2 and C3), (2) extract the arc length L_{12} of the circle and the z difference Δz_{12} between C1 and C2, (3) extract the arc length L_{23} of the circle and the z difference Δz_{23} between C2 and C3, (4) calculate the z-projection to the C3 as

$$z_{\mathrm{proj}} = z_2 + \Delta z_{12} \cdot \frac{L_{23}}{L_{12}}. \tag{7.1}$$

Figure 7.6(b) presents the difference between z_{proj} and z of next cluster as a function of $|z|$. If this difference satisfy the relation that

$$|z_{\mathrm{proj}} - z_{\mathrm{next\ cluster}}| < 0.6\,\mathrm{cm} + 0.05 \cdot |z_2|, \tag{7.2}$$

these three clusters are recognized as a track seed.

7.3.3 Cluster Connecting

We now have a track seed; we can start to extract the cluster connection from the track seed to the other chamber connecting each clusters. By looking neighboring chambers sequentially, further hits which satisfy the relation Eq.(7.2) are added to the track [‡]. If there are more than one cluster or hit within one chamber module which could be added to the track, all possible candidates are stored and ranked so that the priority of candidates are determined by means of minimizing the deviation of the hit points from the track seed. This cluster connection includes not only clusters but also single hit.

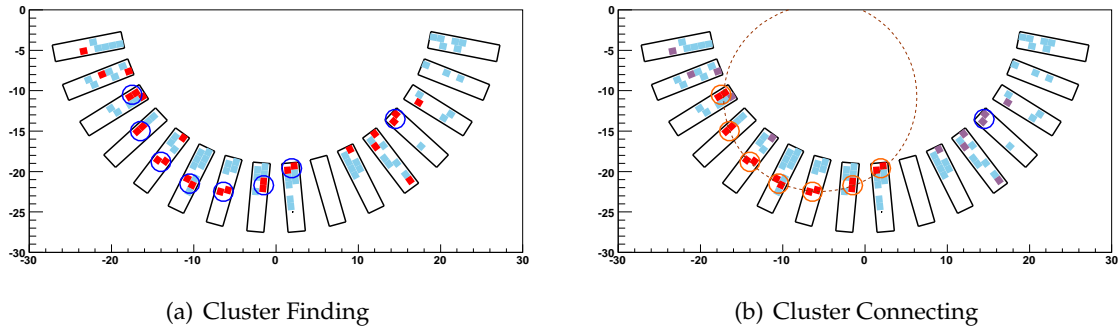(a) Cluster Finding   (b) Cluster Connecting

Figure 7.7: Track Finding (Data)

Figure 7.7 is the continuation of Figure 7.4. Only the hit was found in Figure 7.4(b), and then, Figure 7.7(a) shows applying cluster finding process to them; one can see that eight clusters are found. At this step, single hit that does not compose any cluster is not eliminated since they still have a possibility to be connected to the track; this process is just finding clusters. Next, by applying the track seed condition, Eq.(7.2), seven clusters are connected to the single track successfully; all other clusters and hits are eliminated.

As one can suppose easily, this track finding process depends on not only the topology of xy hit distribution but also the z coordinate, *i.e.* the precision of z-coordinate measurement holds the key to ensure the track-finding performance. Figure 7.8 present the final result of track finding process in $x - y$ and $z - x$ view, respectively. Red cells indicate the hit cell which belong to the found track, light blue cells indicate the eliminated hits. Green solid lines represent the reconstructed track, however this is performed by track fitting process later; we here shows it for just comparison.

During the cluster connecting process, other two important tasks are performed, "solving Left-Right ambiguity" and "timing pedestal calibration". Usually, gaseous wire chamber has Left-Right ambiguity in the location of an ionization with respect to wire *a priori*. In order to resolve this ambiguity, each wire plane is staggered by a half cell; once the track seed is found, Left-Right ambiguity is solved. However, this solution is temporary since the track seed is just one of the candidate, and thus, this resolution is revised during cluster connecting process iteratively. In addition, this process also performes the timing pedestal calibration for all readout channels. Intrinsic timing jitter of all channel with respect to the trigger is calibrated

---

[‡] Here one chamber dropping is allowed to have an acceptable efficincy for the engineering run 2007 due to missing channels.
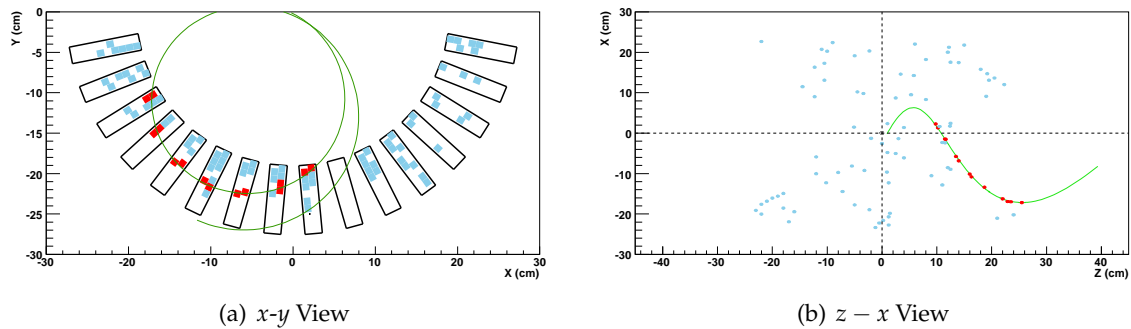
(a) *x-y* View (b) *z − x* View

Figure 7.8: Track Finding Result (Data)

by the special calibration run with the cosmic-ray trigger, however this timing jitter can be varied by another trigger, *e.g.* drift-chamber self trigger. In order to correct such timing jitter, it is necessary to perform timing pedestal correction. This correction is performed during the cluster connection, namely track finding, process, and this will be described in the discussion concerning the calibration, section 8.5.

The track finding is completed; we now can step into the track fitting stage. The performance of track finding of the spectrometer will be discussed in the analysis part, section 9.3.5, later.

7.4   Track Fitting

We here can start the final step of event reconstruction, track fitting. At first, the global descritption for track fitting in the field of high energy physics experiment is briefly given, and the special circumstances for the MEG positron spectrometer is also presented in detail. And then, the algorithm for the MEG positron track fitting can be selected. After the algorithm adoption, actual implementation to the reconstruction framework is extracted. The performances of track fitting will be discussed in the analysis description, Chapter 9 later, since the number of calibrations are necessary to guarantee a tracking accuracy.

7.4.1   Overview

Track Fitting have had a long tradition in the high energy physics experiment and also in the cosmic-ray experiment. The most popular tasks of track fitting are; **(i) to reconstruct the curl (helix) of charged trajectory in the magnetic field in order to measure its charge and momentum, and (ii) to reconstruct the vertex in order to identify the position of charged particle generated**; both (i) and (ii) are essential tasks for the MEG positron spectrometer.

In order to obtain a good tracking accuracy, the resolution of position sensitive detector has been evolved with the longstanding history. In parallel with the detector research and development, track fitting algorithms also has been investigated. Least-Squares Methods (LSM) have a long tradition in track fitting; this method is known to be optimal when the track model is linear and all probability densities involved are Gaussian. Even in homogeneous magnetic

fields the relation between track parameters and measurements is non-linear, yielding a non-quadratic cost function to be minimized. From the early bubble chamber experiments, it has been common practice to neglect effects of multiple Coulomb scattering in the procedure of estimating the track parameters. **The errors of multiple scattering were afterwards added to the covariance matrix of the track parameters all together**, *i.e.* this method is called as global fitting by contrast with another approach that is introduced below. As well known, the tracking accuracy can be enhanced by increasing the measurement points, however this introduces another difficulty due to the need of inverting a possibly very large covariance matrix of measurement uncertainties.

In the framework of the WA13 experiment at CERN, another formulation of the LSM was developed by Billoir [96], called "progressive fit". This pioneering method includes measurements recursively into the fit, updating the estimates of track parameters each time a new measurement is included, *i.e.* **one can avoid the inversion of a possibly large covariance matrix of measurement uncertainties. In addition, while material effects are afterwards added to the covariance matrix in the LSM, they are taken into account locally, as the calculation of covariance matrix terms involving multiple scattering is based on the information from all measurements included in the fit so far.** Thus this kind of sequential approach is referred as Adaptive Track Fitting (ATF). Figure 7.9 schematically shows one example of benefits of ATF by contrast with the traditional global fitting. In this example, a charged particle trajectry is fit-
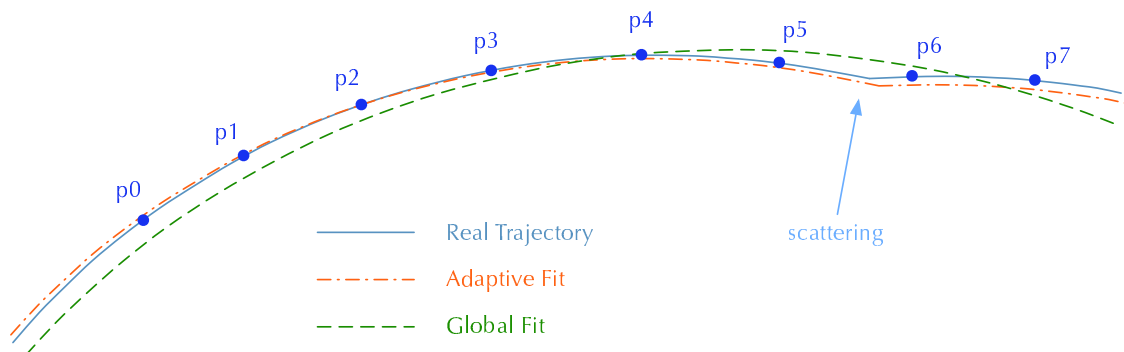

Figure 7.9: Adaptive and Global Fitting (Conceptual Rendering)

ted to eight measurement points (p0-p7) by two methods, LSM and ATF; the trajectry contains a scattring kink between p5 and p6. LSM handles all measurement points together during its minimization process, *i.e.* the reconstructed track is far from the real trajectory if the measurement contains such a hard scattering. On the other hand, ATF handles all measurement points sequentially; at the fitting step of p6, the fitter realize that the track should have a large error after p5 since the predicted position at p6 is far from real p6 by using all information of p0-p5. This also can be verified at the next fitting step of p7 by adding new position information recursively. Thanks to recursiveness of ATF, reconstructed track is in good agreement with the real track.

During the reconstruction-software development for the DELPHI experiment at CERN, it was realized that the recursive formulation of the LSM was equivalent to the Kalman filter [97].

It was then immediately known that the filter could be supplied by a *smoother* of Kalman filter, making it possible to obtain optimal estimates of track parameters anywhere along the track and not only at the end of the filter. Another important effect that needs to be treated in the estimation process is energy loss. Ionization energy loss is usually regarded as a deterministic correction to the track model when traversing a layer with material. Fluctuations can be taken into account by modifying the relevant terms in the covariance matrix of the track parameters or be neglected altogether, since they are quite small. However, there is another source of energy loss, bremsstrahlung; this kind of energy loss is dominant component for electrons with energy above ~100 MeV.

The features of Kalman filter sound attractive for the MEG positron tracking. However, as we discussed in the track finding process, the MEG positron spectrometer is strongly limited due to a lot of constraints. We here have to inspect that the Kalman filter is suitable, or not, for the MEG positron track fitting. In general, the Kalman filter technique is optimal for the following conditions:

(i) Measurements have linear relations with the objective parameters.

(ii) Number of measurements are enough large and they are discrete.

(iii) Each measurement points are enough close.

Originally, Kalman filter has been developed as a linear estimation for the state of a dynamic system from a series of incomplete and noisy measurements, *i.e.* the method assumes condition-(i) generally. However, in nature, the measurement should have a certain non-linearity with the objectives. In order to guarantee a good approximation to the linear system, condition-(ii) and -(iii) are essential. If condition-(iii) is satisfied, the "k"-th measurement point can be predicted by "$k - 1$"-th measurement linerly. Even if condition-(iii) is not enough fulfilled, condition-(ii) can guarantee the accuracy of filter with its recursiveness.

Concerning the MEG positron spectrometer, condition-(i) is not satisfied. It can be approximately satisfied with a certain precision, even it is not so accurate due to highly graded COBRA field. Condition-(ii) and -(iii) are obviously violated. However, there are definitive reasons to adopt the Kalman filter. Our target is to trace the 52.8MeV/c positron. For such a relatively low energy positron, an effect of multiple scattering is naturally critical, and it is not possible to handle such an effect by LSM efficiently. In addition, as mentioned just above, for such an energy region, bremsstrahlung is not negligible to build the covariance matrix. Moreover, the MEG apparatus does not have a vertex detector; *i.e.* the muon-decay position must be reconstructed only by the positron tracking. Even the direction of γ ray should be reconstructed from the muon-decay position. One of the feature of Kalman filter, to obtain optimal estimates of track parameters anywhere along the track and not only at the end of the filter, guarantee better vertex resolution than LSM. In consequence, the application based on the Kalman filter has been developed for the MEG positron tracking.

7.4.2 The MEG Positron Track Fitting

As discussed in the track finding process, track finder provides the found track candidates with three-dimensional cluster coordinates. As one can suppose easily, only positron is ob-

jective in the MEG spectrometer, *i.e.* the direction of track following is determined from the beginning. Thanks to this feature, **starting from the endmost cluster and following the ascending order are equivalent to follow the track natural way** except for the doubly curling event that can be judged by looking the z coordinate of clusters, since the first turn should have smaller $|z|$ than the second turn.
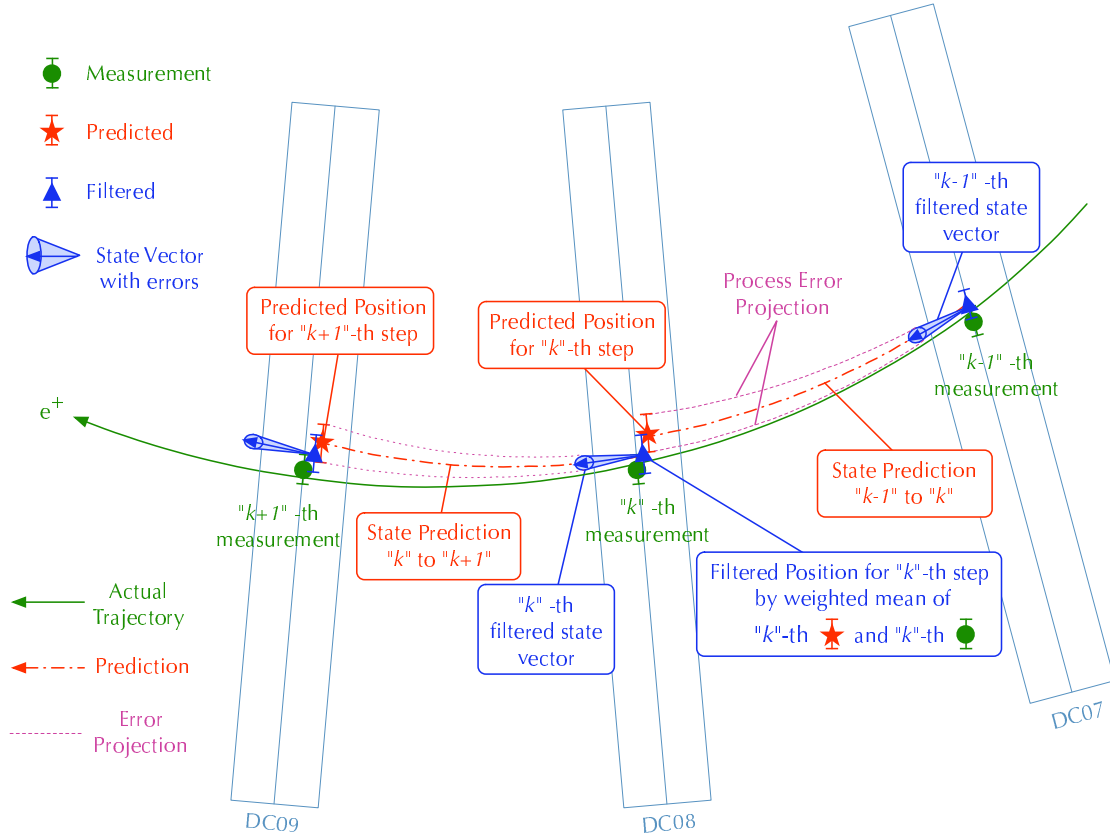

Figure 7.10: Kalman Filter Track Fit in the MEG Drift-Chamber System

In general, Kalman filter is a method of estimating the state of dynamic systems, *i.e.* the "state" is interpreted as the "track parameters" for the application of the Kalman filter to track fitting; the general formalism of the Kalman filter to the track fitting is given in Appendix C.

Track fitting by the Kalman filter is carried out by three types of operation;

- **Prediction** x_k^{k-1} : Estimation of the "future" state at "k"-th step using all the "past" measurements up to "$k-1$"-th step.

- **Filtering** x_k^k : Estimation of the "present" state at k-th step based on all the "past" measurements and including "present" measurement at "k"-th step.

- **Smoothing** x_k^n : Estimation of the "past" state at k-th step based on all "n" measurements including all the filtering.

93

To give an actual example for the MEG positron tracking, let us instantiate an example as shown in Figure 7.10. In this example, three hit coordinates with errors are measured by DC07, DC08 and DC09, and denoted as "$k-1$"-th, "k"-th, and "$k+1$"-th measurement (green circles). At the "k"-th measurement step (DC08), we can predict the "k"-th state x_k^{k-1} (red star) by using "past" state at "$k-1$"-th step (DC07) (blue triangle); this process is "Prediction".

We here can perform "Filtering" process at "k"-th step by the weighted mean of the predicted state x_k^{k-1} and the current "k"-th measurement. At this filtering process, one can calculate the filtered residuals and the covariance matrix of the filtered residuals, *i.e.* they are updated by the current measurement. In consequence, filtered state vector at the "k"-th step is reflecting the newly induced error after the "$k-1$"-th step; *e.g.* multiple scattering occuring between DC07 and DC08. In order to reflect the actual material information accounting the multiple scattering Eq.(C.14) or energy losses Eq.(C.15) to the Kalman filter, the MEG tracking software can retrieve the actual material information by using the functionality of the **g2root** [98] program; this program can handle the fine geometrical information from the **GEANT3**-base MC framework including material contents. Hence, inputing the coordinate of current step provides the actual material composition, and then, the mean angle of multiple scattering and the energy losses can be expected.

Now, we can predict the "future" state x_{k+1}^k at "$k+1$"-th step by using the newest filtered state x_k^k. By the iteration of these steps, all the track parameters at each measurement steps can be filtered. After the last (n-th) filtering, we can update the "past" state at "k"-th step by using all the filtered information; this process is "Smoothing". Finally, it is possible to have all the smoothed state vectors at each measurement steps.

One of the most important feature of the MEG positron spectrometer is adopting highly graded magnetic field. This means that it is not possible to perform "prediction" by the arc of projected trajectory onto the bending plane since it is not a circle exactly in the inhomogeneous field. In consequence, the track parameters should be extracted only by the numerical integration, namely by solving the equation of motion within the COBRA field. Because the equation of motion

$$\frac{\mathrm{d}\boldsymbol{p}}{\mathrm{d}t} = q\boldsymbol{v} \times \boldsymbol{B}$$

is second order differential equation, this should be extracted to a system of simultaneous first order differential equations

$$\frac{\mathrm{d}}{\mathrm{d}z}
\begin{bmatrix} z \\ x \\ y \\ x' \\ y' \\ \rho \end{bmatrix}
=
\begin{bmatrix}
1 \\
x' \\
y' \\
\rho\sqrt{1+x'^2+y'^2}[(\boldsymbol{r}' \times \boldsymbol{B})_x - x'(\boldsymbol{r}' \times \boldsymbol{B})_z] \\
\rho\sqrt{1+x'^2+y'^2}[(\boldsymbol{r}' \times \boldsymbol{B})_y - y'(\boldsymbol{r}' \times \boldsymbol{B})_z] \\
\rho'
\end{bmatrix}
\tag{7.3}$$

to be solved by numerical integration, where prime represents the differential with respect to z, $\rho = q/p$; this is extracted by transformation of variable from t to z. The first, second, and third components provide the track coordinate, *i.e.* they can determin the initial vertex of positron. The forth and fifth components represent the angle of track, *i.e.* they can provide positron emission angle, ϕ and θ; finally, the sixth component derives the most important result, momentum.

Now, one can solve the system Eq.(7.3) by numerical integration incorporating with the CO-BRA field map. The numerical integration is performed by the fifth order Cash-Karp [§] method, because this method can maneuver the adaptive stepsize effectively, and then, it can be converged rapidly; adaptive stepsizing for numerical integration is critical for the MEG positron tracking due to highly graded magnetic field. Figure 7.11 shows an example of the positron track fit in two directional expansions, $x - y$ and $x - z$ views. This sample data is provided by
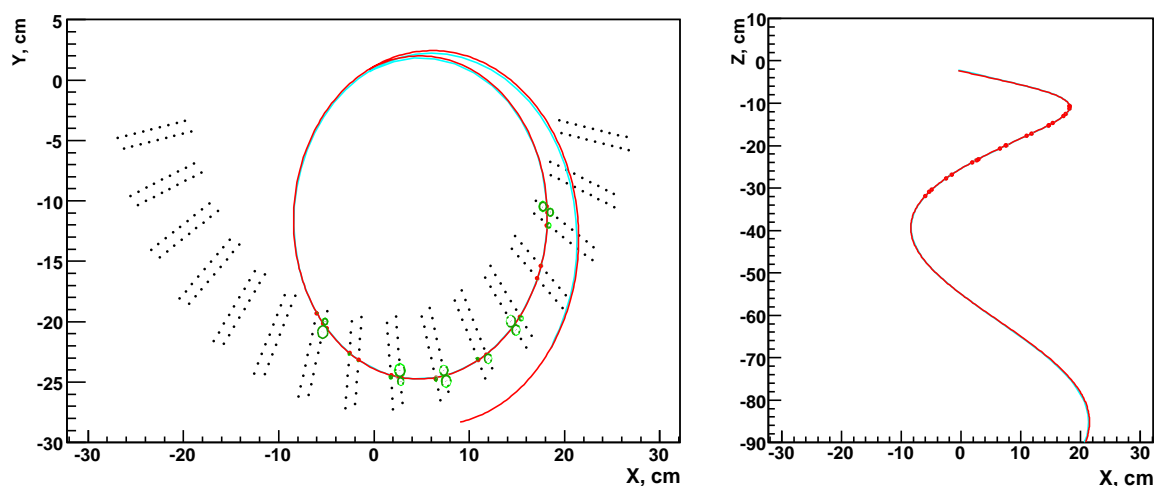

Figure 7.11: Example of the MEG Positron Track Fit (MC)

MC simulation, *i.e.* one can know the actual trajectory; red track is the reconstructed track and cyan track is the actual track. The reconstructed track is in excellent agreement with the true track. Performances of the track reconstruction will be discussed in the analysis part, section 9.3.1 and section 9.3.2.

[§] Cash-Karp [99] is one of the Runge-Kutta method. This method uses six function evaluations to calculate fourth- and fifth-order accurate solutions. The difference between these solutions is then taken to be the error of the solution. This error estimate is very convenient for adaptive stepsize integration algorithms similar with Fehlberg method or Dormand-Prince method.

Chapter 8

Calibration

In order to have a good tracking performance, it is essential to make various calibrations for the drift chamber precisely. In this chapter, calibration procedures are described in detail.

8.1   Overview

First of all, it is necessary to determine the position of the drift chambers precisely. The alignment is done by two stages; optical survey and use of cosmic-ray data. It is difficult to measure the position of each chamber directly after installation completed. In order to measure the position, the drift-chamber system is surveyed by the optical triangulation. However, we need to check the position of each individual wire. Cosmic-ray data is used for this purpose. The cosmic-ray run was carried out with a special trigger mode and without magnetic field yielding straight tracks over the whole drift-chamber system. This data is also used for the relative gain calibration between the two ends of readouts for anode and cathode, which is essential for z-coordinate determination.

After these calibrations are completed, we can step into the next calibration stage using the Michel positron data with the magnetic field. It is inevitable to perform Time-to-Distance calibration with the real COBRA field.

Finally, this Michel positron data is also usable to perform the absolute momentum calibration, because the Michel spectrum falls off rapidly at the kinematical end-point of the Michel positron, and this is *one-of-a-kind **physical*** reference for the COBRA spectrometer.

8.2   Calibration Runs

During the COBRA spectrometer engineering run 2007, we performed calibration runs for the MEG drift chamber. As discussed just before, it is necessary to have two specially triggered calibration runs for the drift chamber, namely "cosmic-ray run" and "Michel positron run". After the drift-chamber installation and electronics integration, the cosmic-ray run was carried out in September-October 2007. After the cosmic-ray run,the Michel positron data was acquired in October-December 2007.

8.2.1 Cosmic-Ray Run

Plastic-scintillation counters were equipped temporarily surrounding the COBRA magnet at beginning of the engineering run [*]. As shown in Figure 8.1, ten counters (1m length × 10cm width) that readout on both ends by PMTs were surrounding half of COBRA surface to avoid a collision with a cryostat of the liquid-xenon γ-ray detector (*cf.* Figure 3.1); this figure is simulated by MC. The cosmic-ray run was done without magnetic field to have straight track.

(a) Cosmic-ray Event (MC) (b) Another view at different angle
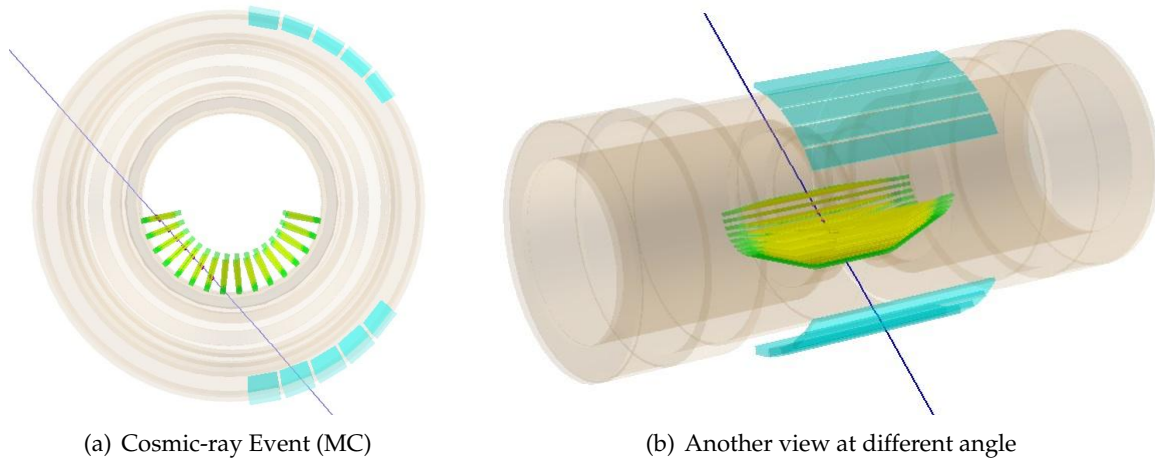
Figure 8.1: Drift-Chamber Cosmic-ray Calibration Run

In order to have long tracks through the chambers, the cosmic trigger is generated with the following logic,

"One Counter Hit" $\otimes$ "Two Consecutive Chamber Hits";

two consecutive chamber hits contain four hits, *i.e.* this is enough to guarantee a quality of straight line fitting. The MC-event example shown in Figure 8.1 is triggered by one counter hit (the second bottom counter) and seven consecutive chamber hits. Finally, 1.2M triggered events were acquired.

8.2.2 Michel Positron Run

It is inevitable to perform the Time-to-Distance calibration, so-called X-T calibration, with the COBRA field. Precise knowledge of X-T relation can give us the precise position measurement while this relation can be affected by various sources. Especially for the MEG drift chamber, the magnetic field is inhomogeneous, *i.e.* the X-T calibarion should be done for each magnetic-field strength.

---

[*] The MEG apparatus has several accompanied detectors to perform various calibrations for each sub-detector. As one of such a calibrating detector, NaI-counter array is integrated at opposite end of the liquid-xenon γ-ray detector to perform γ-ray energy calibration. In order to avoid a confliction with this NaI-counter array, the scintillation counters for the drift-chamber cosmic-ray run was available at the beginning of engineering run only, and counters had to be unmounted after cosmic-ray run completed.

Two special drift-chamber self-trigger is implemented for the Michel positron run. As described in Section 5.4, all anode signals are resistively-split into two outputs; one goes to the DRS and another is summed up with other channels so that several anode outputs are grouped. This grouping is done to have inner and outer group, as shown in Figure 8.2.

For the first mode, called "Normal Michel Trigger", in order to contain Michel tracks effectively, this trigger requires four hits in consecutive groups, as shown in Figure 8.2(a); this is blind to which end, inner or outer, is fired. In this event sample, six consecutive inner-group

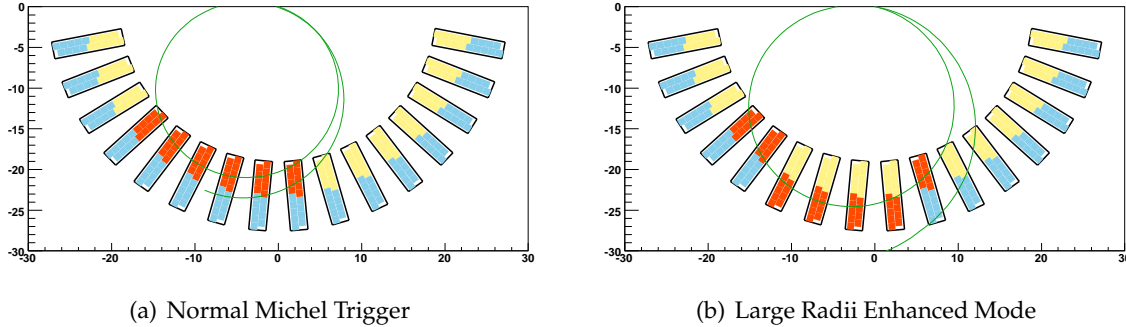(a) Normal Michel Trigger   (b) Large Radii Enhanced Mode

Figure 8.2: Michel Trigger Scheme

fire the trigger. As discussed in chapter 4, thanks to the COBRA field, only small number of high-momenta Michel positron can reach to the outer region (see Figure 4.4), *i.e.* the statistics for outer cell are much smaller than inner cell by this trigger mode. In order to collect outer cell hits effectively, the auxiliary trigger mode is implemented, called "Outer Michel Triggeer". This trigger mode requires same condition as the Normal Michel Trigger but, in addition, at least one outer group is required. In Figure 8.2(b), seven consecutive hits including four outer groups fire the trigger.

Finally, 3M and 2M events were acquired by Normal Michel Trigger and Outer Michel Trigger, respectively. The Michel positron run was carried out at low muon intensity (5×10^6 sec^{-1}) due to chamber-conditioning purposes while the real MEG experiment will be performed with 3×10^7 sec^{-1} muon intensity. In order to verify the spectrometer performances with the full intensity, additional 2M events were also taken with 3×10^7 sec^{-1} muon intensity with the Outer Michel Trigger.

Because the Michel positron run is acquired by the drift-chamber self trigger, obtained pulse timing has large ambiguity due to drift time. Thus, drift time is determined by special procedure that will be mentioned in the description of timing-pedestal calibration, Section 8.5.

8.2.3 Detector Conditions in the Engineering Run 2007

In the engineering run 2007, the drift-chamber system was not fully operational, since a series of accidents occured. Two big problems, bad connection on the patch panel and discharge,deteriorated the detector performances significantly.

The patch panel at the end-cap of the magnet, as described in Section 5.4, serves as feed-through terminal between inside and outside the magnet. The cable connectors to the panel

had no latch, and cables were strained strongly inside the magnet. In consequence, number of inner cables were disconnected. By the same token, one power cable to the pre-amplifier was also disconnected. Repair workswere not possible due to the run schedule,and then, it was determined to continue the engineering run even though it was not fully operational. The list of such missing channels are given in Appendix B.

Several chambers had high-voltage discharge outside the chamber, where is in the helium atmosphere. Although the point was molded with epoxy resin, several chambers had the weakness. These chambers were not able to be applied high voltage higher than 1600 volt stably. Finally, as mentioned in Section 5.5.3, we decided to dope small amount of air into the COBRA-helium inlet; helium concentration was controlled to be 95.8 % during the engineering run 2007. With this treatment, these chambers could be applied high voltage to 1800 volt while the default high voltage is 1850 volt.

Table 8.1 is the summary of the chamber condition. As described in Section 5.4, each plane

Chamber Plane ID	High Voltage	Pre-amplifier Power
1A	0 V	normal
1B,7AB,9AB,12AB,15AB	1800 V	normal
6AB	1850 V	disconnected
all others	1850 V	normal

Table 8.1: Drift Chamber Conditions

of chamber module is applied high voltage individually, and then, chamber-plane ID is referred in Section 4.4. The final list of the bad channels are summarized in Appendix B [†].

8.3   Wire Alignment

In order to perform the wire alignment effectively, the optical survey of drift-chamber position with respect to support structure and beam axis was done.This survey was based on the optical triangulation by using two reference markers assembled on the chamber-module body. As shown in Figure 8.3(a), each chamber has reference marker at both ends, and it has a cross mark to be observed by surveyor. And also, each chamber has position-determining pin drived throughout itself at the bottom of frame; the head of this pin is also observed by surveyor. By surverying them from the end-cap of the magnet, it is possible to calculate a vector between position-determining pin and reference marker, *i.e.* the orientation and the coordinate of each chamber module can be determined. Figure 8.3(b) shows the result of optical survey, each arrow indicates the observed chamber orientation, and the origin of arrow represents the bottom coordinate of chamber body, the arc means the surface of COBRA magnet. (**NOTICE: This is not real displacement exactly, multiplied by factor of 50 to be emphasized.**) One can see a large displacement on several chambers; this was done not by mistake, but on purpose to avoid welding parts on the cryostat of the COBRA magnet.

[†] Repair works for all problems are progressing in the winter shutdown 2007-2008 so that the real MEG experiment will run with fully operational drift chambers.

(a) Reference Marker
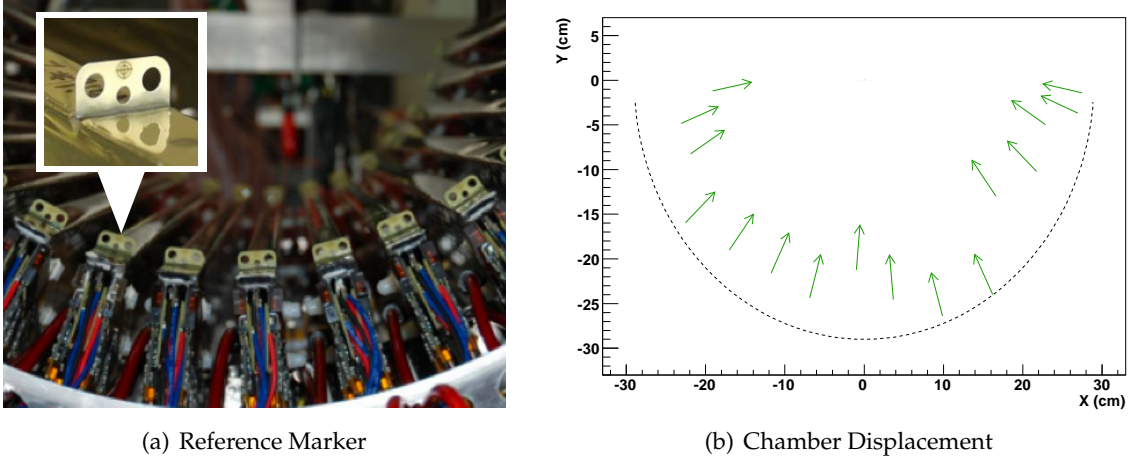

(b) Chamber Displacement

Figure 8.3: Optical Survey for Chamber-Displacement Measurement

Results from the optical survey are implemented in the database system of the MEG software family, and then, we can step into the wire-alignment analysis. Figure 8.4(a) is an example

(a) Reconstructed cosmic-ray event
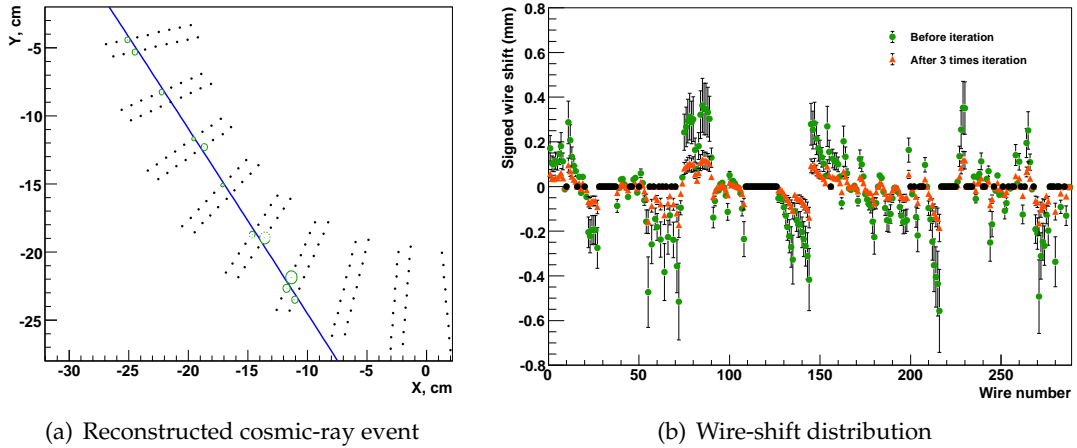

(b) Wire-shift distribution

Figure 8.4: DC Wire Alignment by Cosmic-Ray Run

of reconstructed cosmic-ray event. Masking one objective wire and performing straight track fit, and then, we can estimate a difference between fitted trajectory and predicted drift circle from the ideal wire position for the objective wire. By minimizing this residual, the wire displacement can be expected. This minimization is performed with two parameters of wire displacement, r and ϕ (distance and rotation), *i.e.* this procedure can align the wire in two-dimensional space, "$x - y$" plane. Remaining alignment in "z" direction is performed in the "z"-coordinate calibration; this will be mentioned in Section 8.4. The green circles of Figure 8.4(b) shows the signed wire shift (r) that is estimated by this way. The error bars indicate the fitting errors. The black-dot points are corresponding to the dead/bad channels. This proce-

101

dure naturally depends on shifting wire position each other, *i.e.* this procedure should be iterative. After three times iteration, this displacement is converged and the mean displacement is (47.3±38.8) μm, where the error denotes the RMS of displacement distribution; converged displacements are presented in same figure as orange triangles.

8.4 *z*-Coordinate Calibration

z coordinate is measured by combination of anode-charge-division and cathode-vernier-pad. Then, we here need a precise position reference in order to perform *z*-measurement calibration. **The MEG drift chamber has very precise *z*-coordinate reference in the chamber itself; *i.e.* it is not necessary to have an alternative position sensitive detector.**
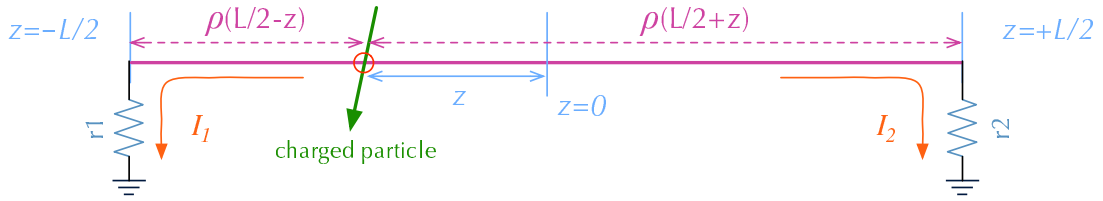

Figure 8.5: Induced currents on anode wire

At first, *z*-coordinate is roughly derived from the ratio of charges measured at both ends of the hit wire. Observable anode signal is schematically shown in Figure 8.5, where L is total wire length, ρ is wire resistance per unit length, $r_{1,2}$ are input impedances at both ends, $I_{1,2}$ are induced currents at both ends, respectively. From this picture, one can derive

$$I_1 = I_0 \frac{r_2 + \rho(\frac{L}{2} - z)}{r_1 + r_2 + \rho L}, \quad I_2 = I_0 \frac{r_1 + \rho(\frac{L}{2} + z)}{r_1 + r_2 + \rho L}, \tag{8.1}$$

where I_0 is induced current by avalanche primarily, *i.e.* these currents produce signals:

$$A_1 = \kappa_1 I_0 \frac{r_2 + \frac{R}{2} - \frac{R}{L}z}{r_1 + r_2 + R}, \quad A_2 = \kappa_2 I_0 \frac{r_1 + \frac{R}{2} + \frac{R}{L}z}{r_1 + r_2 + R}, \tag{8.2}$$

where $\kappa_{1,2}$ are gain factors of the corresponding pre-amplifier channel, and R is wire resistance ($= \rho L$). According to Eq.(8.2), the anode-charge-division ϵ_A can be written as

$$\epsilon_A = \frac{A_1 - A_2}{A_1 + A_2} = \frac{\lambda(r_2 + \frac{R}{2}) - (r_1 + \frac{R}{2}) - (\lambda + 1)\rho z}{\lambda(r_2 + \frac{R}{2}) + (r_1 + \frac{R}{2}) + (\lambda + 1)\rho z}, \tag{8.3}$$

where κ_1 / κ_2 is denoted as λ. By using Eq.(8.3), *z* coordinate can be reconstructed as

$$z = \frac{L}{R} \frac{\left[\lambda(r_2 + \frac{R}{2}) - (r_1 + \frac{R}{2})\right] - \left[\lambda(r_2 + \frac{R}{2}) + (r_1 + \frac{R}{2})\right]\epsilon_A}{(\lambda + 1) + (\lambda - 1)\epsilon_A.} \tag{8.4}$$

In general, one can assume that values of R and L are well determined while value of λ is subject for calibration. In consequence, anode *z*-coordinate calibration is equivalent to calibrate λ.

In order to calibrate λ enough precisely, it is necessary to know z much better than precision of anode-charge-division; **we here can use cathode-charge information as a precise z-coordinate reference.**

As described in Section 5.2.4, vernier pattern has periodical zig-zag strip. Thanks to geometrical period of vernier pattern, we can have a good z-coordinate reference for anode z calibration even if it is not calibrated. By using cathode-charge-ratios Eq.(5.1), we can introduce the phase of vernier pattern

$$\alpha = \tan^{-1}\frac{\epsilon_2}{\epsilon_1}, \tag{8.5}$$

as shown in Figure 8.6(a), *i.e.* one circuit of this circle, called "vernier circle", is equal to one zig-zag period, namely 5 cm. Figure 8.6(b) shows relation between α and ϵ_A; one can see stripes corresponding to each vernier periods. Each gap between ends of stripes is exactly equal to
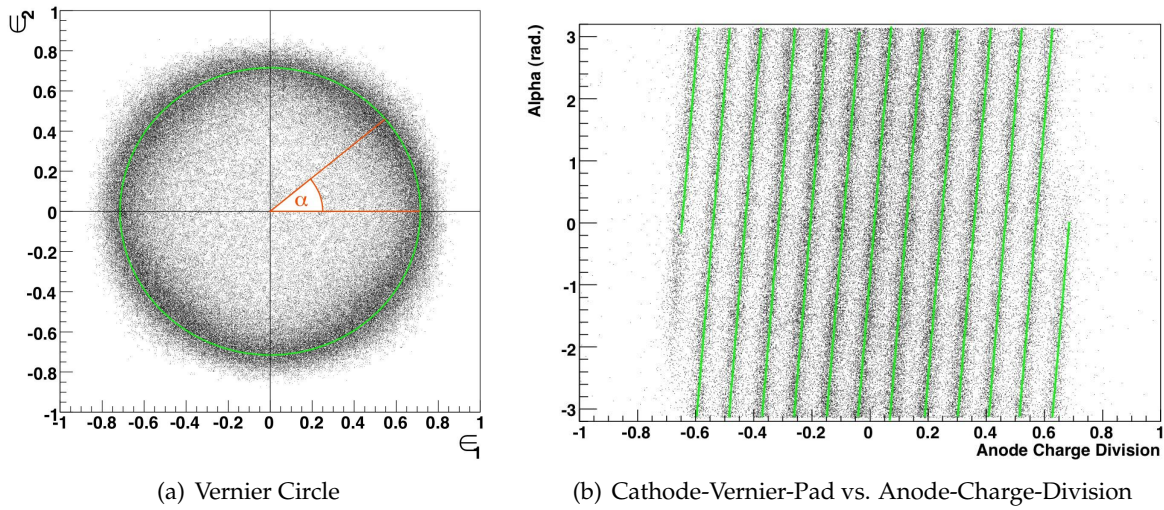

(a) Vernier Circle (b) Cathode-Vernier-Pad vs. Anode-Charge-Division

Figure 8.6: z-Coordinate Calibration

5cm, *i.e.* the precision of vernier period is guaranteed by etching accuracy; it is 100 μm (see Section 5.3.2) and much better than the charge division accuracy. By fitting these strips to Eq.(8.4), it is possible to determine λ for each wire.

In an analogous fashion, the relative gain correction λ for cathode pad is also determined due to the fact that the mean charge collected on one cathode pad should be a quarter of total charge induced on the anode. Figure 8.7(a) represents the fraction of cathode charge normalized by total anode charge as a function of α. It is fitted to a sine curve

$$C_i + A_i \cdot \sin(x - \phi_i)$$

where i represents the pad indices (i=0,1,2,3) to distinguish each pad within one cell, *i.e.* $\sum C_i$ should be 1 and each coefficient should be 0.25, the deviation from 0.25 derives a relative gain correction for each pad. In addition, fitted parameter ϕ_i gives a shift of pad pattern with respect to z direction, and then, the absolute z-coordinate calibration is enabled by comparing ϕ_i each other. After relative gain corrections λ for cathode is obtained, it is possible to perform anode z-coordinate calibration again to be ensure better resolution than the first calibration, and then,

103

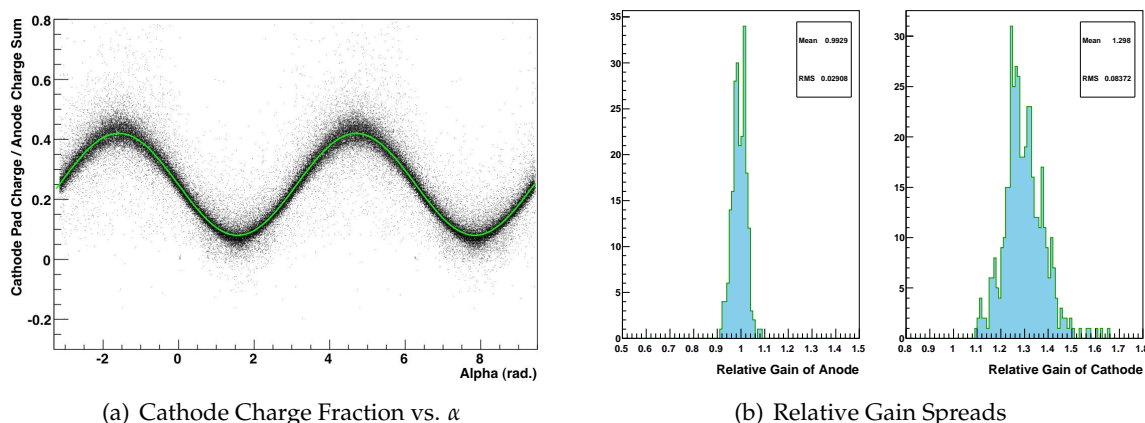(a) Cathode Charge Fraction vs. α (b) Relative Gain Spreads

Figure 8.7: Relative Gain Calibration

these procedure is carried out iteratively. Obtained variations of relative gain are 2.92 % and 6.45 % for anode and cathode, respectively, as shown in Figure 8.7(b), and then, after applying these corrections, the variations of relative gain are corrected to be 0.92 % and 1.15 % for anode and cathode, respectively. In addition, obtained z displacement, which is determined by ϕ_i, is (218 ± 119) μm, where the error denotes the RMS of displacement distribution, and then, after applying z correction, z displacement is corrected to be (101 ± 39) μm.

8.5 Timing Pedestal Calibration

It is necessary to determine the timing pedestal, or t_0, *i.e.* the "zero" time for each anode and cathode channel in order to measure the drift time enough precisely. There are several sources of difference in the pulse-propagation time among each channels; *e.g.* differences of cable length of both the signal and the trigger electronics, transition-time spread of electronics devices (pre-amplifier, DRS chips *etc.*). Such a intrinsic timing jitter for each channel can be determined by fitting of the edge of the drift-time distribution to a convolution of a step function with a Gaussian, or error function. Taking the half-height of the step as the pedestal, this allowed all channels to be aligned relative to one another; by using cosmic-ray data, intrinsic timing pedestals are determined and stored in the database system for all channels.

In particular, event reconstruction for the Michel positron run is different from others. As described in Section 8.2.2, the Michel positron data was acquired by the drift-chamber self trigger, *i.e.* the timing pedestal varies widely since the trigger timing is including the drift-time ambiguity of the triggering chamber. Then, for Michel positron run, the special t_0 determination is adopted that is carried out during track finding process. As described in Section 7.3, the track seed is built for the cluster connecting process, and then, this seed can be used to determine t_0 for the Michel positron run as following steps: (A) Calculate a circle through the cluster positions (track seed), where the cluster position is defined as the centre of two hit-wire coordinates of the cluster. (B) Extract the track angle at each hit position with respect to the normal vector of chamber module. (C) Find the smallest hit time of all hits in the track seed

and define this time as initial t_0. (D) Perform the following minimization process iteratively by that the difference between hit point and track seed converges. (D-1) Calculate two possible hit points of both side, left/right-hand of the wire, by using the X-T relation (*cf.* Figure 7.3(a)). This X-T relation is provided by **GARFIELD** program initially and calibrated by the Time-to-Distance calibration that is described in the following section. Current estimation of the drift time $t_{hit} - t_0$, track angle and the magnetic field strength at the hit position are used as input to the X-T function (D-2) Rebuild the track seed by using the calculated hit position instead of the wire positions, and then, estimate the difference between hit position and track seed for all possible combinations of hit points. (D-3) Choose the best combination with the minimal residual. After several iterations, typically three or four times, residual enough converges, and then, t_0 for each hit wire is determined, *i.e.* this timing pedestal calibration should be performed event by event for the Michel positron run analysis. Finally, the accuracy of timing-pedestal determination achieved ± 1.91 ns.

8.6 Time-to-Distance Calibration

Up to here, wire alignment, *z*-coordinate calibration and timing pedestal calibration are completed, *i.e.* wire position can be given precisely. Then, the B-field strength of hit position is also provided since wire position and *z*-coordinate are enough to know the field strength, Now, the drift time is determined by subtracting t_0 from t_{hit}. At last, we here can convert drift time to drift distance by using X-T relation which is calculated by **GARFIELD** program initially. This relation is provided as two-dimensional isochrone map as shown in Figure 7.3(b). As one can see from this figure, once we have four informations, drift time, track angle, passing side (Left-Right solution), and B-field strength, drift distance can be determined uniquely since thanks to individual cell configuration that is accompanied by potential wire both side and the small Lorentz angle; it is not necessary to measure the Lorentz angle to verify the X-T relation for this chamber. However, the calculated X-T relation should be certificated by the data; if there is a certain deviation, calculated relation should be calibrated by the data itself.

The X-T calibration is performed by simple iterative procedure as described below. (A) Calculate a difference between obtained drift distance and closest approach from the wire to the track, called "residual". (B) Put a corrective offset to the drift distance so that the residual is minimized. (C) Perform (A) to (B) for a certain statistics with similar incident angle (within $\pm 5°$) and closed field strength (within ± 0.5 T) events, and build a new X-T plot. (D) Fit a new X-T plot to the fifth- or seventh-order polynomial. (E) Re-process track fitting by using new X-T relation. The procedure (A) to (E) is repeated until convergence is achieved. It should be taken into account the field strength carefully since the COBRA field is highly graded so that the X-T relation has a strong B-field dependence (*cf.* Figure 6.3(b)). In order to reflect such a circumstance, X-T calibration is done for each B-field strength separately; *i.e.* *z* calibration should be done before X-T calibration to obtain B-field strength for each hit position. Figure 8.8 shows two examples of the result of X-T calibration. Pink-solid line present the initial X-T relation that is calculated by **GARFIELD** and light blue dots present the calibrated new X-T relation. Left plot of Figure 8.8 is corresponding to $(50\pm 5)°$ incident with (1.3 ± 0.05) Tesla of B-field strength, and right plot is corresponding to $(0\pm 5)°$ incident with (1.1 ± 0.05) Tesla, respectively. The obtained residual distributions are also shown in both plots as a function of
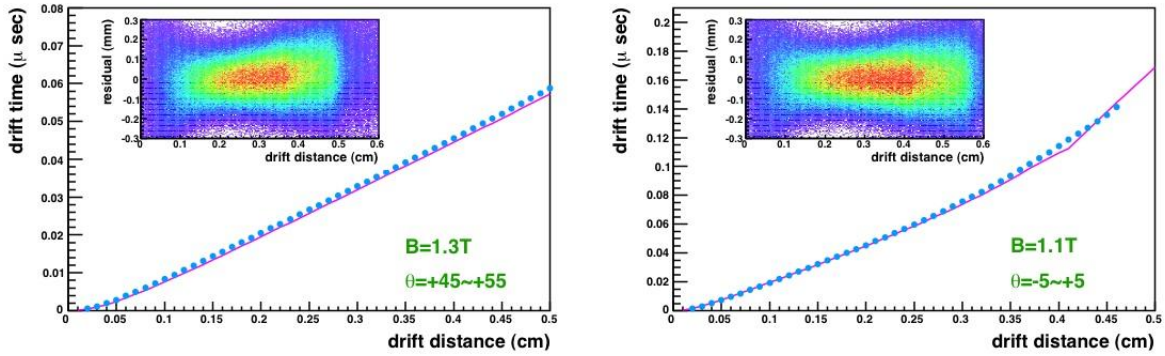
Figure 8.8: Time-to-Distance Calibration

drift distance. Now, all the calibration for drift chamber is completed.

8.7 Momentum Calibration

As mentioned above, by exploring a falling edge of the Michel spectrum, it is possible to calibrate the absolute momentum, so-called the momentum scaling calibration, since only the sharp edge of Michel spectrum at the upper kinematical endpoint provides a "*physics*" reference. However, observed edge may be smeared by the spectrometer resolution, *i.e.* the absolute momentum calibration should be done with the momentum-resolution evaluation simultaneously. Thus, all the details on the absolute momentum calibration will be given in the evaluation of spectrometer resolution, Section 9.3.1.

Chapter 9

Analysis

In this chapter, we discuss the spectrometer performances by analyzing the engineering run data.

As described in previous chapter, two calibration runs, cosmic ray run and Michel positron run, have been performed for the drift-chamber various calibrations. These calibration data can also be used to evaluate the drift-chamber intrinsic performances. Thus, first of all, we consider the single efficiency and the spacial resolutions of drift chamber by analyzing the calibration data.

After these calibration runs, spectrometer engineering run entered to next phase, "$\mu^+ \to e^+\gamma$ trigger run". As described in Section 3.5.2, the signature of $\mu^+ \to e^+\gamma$ is a back-to-back $\gamma - e^+$ pair coincident in time; $\mu^+ \to e^+\gamma$ event trigger therefore requires the presence of two high-energy particles with opposite momenta in the liquid-xenon γ-ray detector and the positron spectrometer. For the positron side, in particular, only the timing counter is used at the online-trigger level since the information from the drift chamber is too slow due to the electron drift time. In consequence, $\mu^+ \to e^+\gamma$ event trigger is fired by the coincidence of the liquid-xenon detector and the timing counter with a certain angular matching to be enhanced collecting back-to-back event *. One of the main purpose of the engineering run should be to ensure that the $\mu^+ \to e^+\gamma$ physics trigger works accurately and to evaluate the detector performances at the real DAQ condition. The later last half of engineering run was spent testing this final $\mu^+ \to e^+\gamma$ trigger. Thus, the data that was acquired by such $\mu^+ \to e^+\gamma$ event trigger can estimate the timing resolution of the timing counter.

We obtain two intrinsic performances of the drift chamber and the timing counter so far, *i.e.* we here can step into the next investigation; the spectrometer global performances, momentum, vertex and angular resolutions, efficiencies *etc.* By analyzing the data that was acquired by Michel positron run, all the tracking performances are able to be evaluated. As described in Section 8.2.2, two intensities of muon beam were tested with Michel runs; Low Rate ($5 \times 10^6 \text{sec}^{-1}$) and Normal Rate ($3 \times 10^7 \text{sec}^{-1}$), *i.e.* the rate dependences of tracking performances are also able to be investigated.

---

*PMTs of the liquid-xenon detector are grouped and the timing counters are graded by its angular coordinate equivalently in order to match the anti-direction of γ-ray and positron.

This tracking-performance evaluation contains the accuracy of tracing back to the muon decay vertex. Due to absence of the vertex detector, such an evaluation is essencial. On the other hand, positron tracing along anti-direction; towards the timing counter, is also important. In principle, the positron-impact position on the timing counter is reconstructed by the counter itself, but extrapolation from the drift chamber is also necessary to ensure the timing correction by using track-length information. In addition, there are a cartain amount of material after drift chamber before timing counter, *i.e.* positron deficit at this region is a critical issue on the spectrometer detection efficiency. Finally, such global performances of the spectrometer are estimated by analyzing all the calibration data and $\mu^+ \to e^+\gamma$ trigger run data.

9.1 Drift Chamber Performances

The intrinsic performances of the drift chamber, in particular, the efficiency and the spacial resolution, are investigated by analyzing the data sets of calibration runs; cosmic-ray run and Michel positron run.

9.1.1 Drift Chamber Efficiency

In the Cosmic-ray run, as described in section 8.2.1, no magnetic field is applied over the spectrometer. Thus, the cosmic-ray trajectory is arguably straight and it can be easily predicted that which cell should have a significant hit, if the drift chambers have enough number of hits associated with a cosmic-ray track.
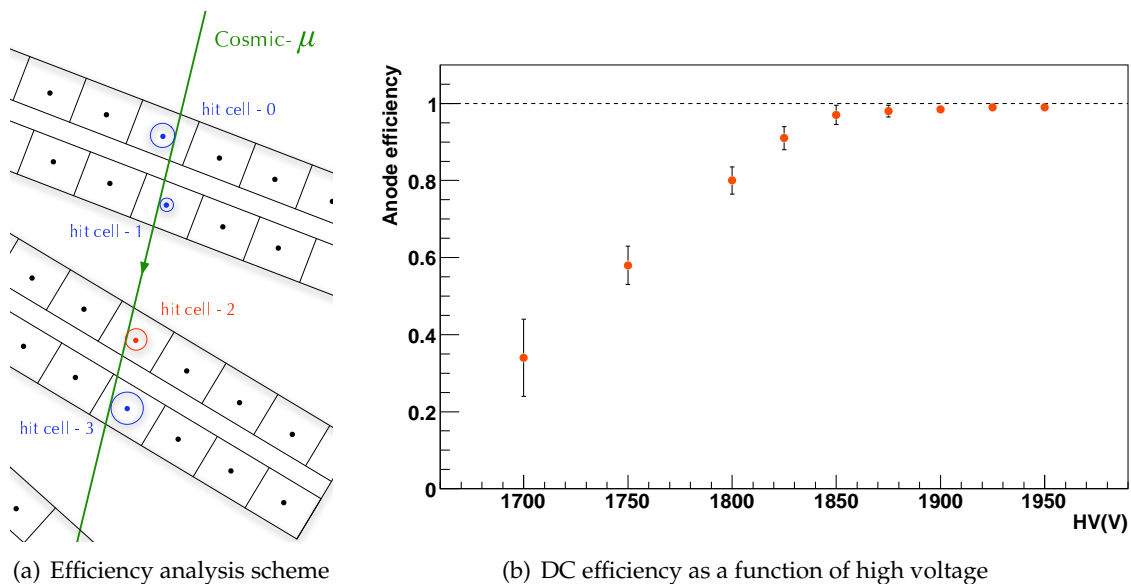

(a) Efficiency analysis scheme   (b) DC efficiency as a function of high voltage

Figure 9.1: Drift Chamber intrinsic efficiency (Data)

According to the cosmic-ray trigger condition, at least two consecutive drift chambers have siginificant hits, namely four hits. By collecting events that contains at least two more hits in addition to the triggering chamber, the single hit efficiency is evaluated. One can mask an

objective cell (other than triggering chamber) and reconstruct the cosmic-ray straight track by fitting remaining hits, as shown in Figure 9.1(a). In this sample, "hit cell 2" is objective and masked, and then, straight track is reconstructed by remaining hits; in consequence, one can predict "hit cell 2" should have a hit associating with the concerning trajectory. Adopting such a way, we can estimate a single hit efficiency for all anode wires individually. The calculated average efficiency as a function of high voltage is shown in Figure 9.1(b), where error bars represent the RMS of the efficiency distribution over all anode wires. As described in Section 5.4, applied high voltage is 1850 V. In Figure 9.1(b), one can see that this high voltage is just a beginning of fully efficient region.

9.1.2 Intrinsic Spacial Resolution

Once the track reconstruction is performed, we can estimate the intrinsic spacial resolution of drift chamber by means of the residual, closest distance between obtained hit coordinate and reconstrcucted track. The residual can be determined as two directions, transverse (r) and longitudinal (z), and then, both spacial resolutions are derived by these two residuals.

(a) Residual Distributions (b) Drift Distance Dependence
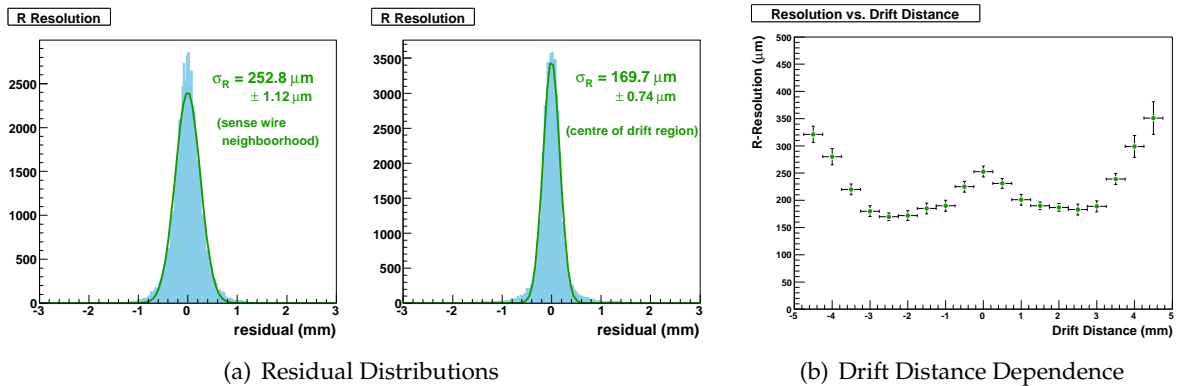
Figure 9.2: Drift Chamber Spacial Resolution in r (Data)

Figure 9.2(a) shows two examples of residual distribution of an anode. As well known, the drift-chamber spacial resolution along r direction may be suffered from the electron diffusion in the active gas and so on, *i.e.* the resolution depends on the drift distance. These two examples are collected by two drift-distance point; the left histogram is corresponding to a centre of drift distance, and the right is corresponding to a sense-wire neighborhood. Figure 9.2(b) shows the spacial resolutions in r as a function of drift distance sliced by 0.5 mm intervals, where error bars represent the error of the Gaussian fitting to the residual on the vertical axis and 0.5mm intervals in the horizontal axis, respectively. As one could expect, the resolution is degraded for a long drift distance, and also, at the wire neighborhood the resolution is deteriorated due to discrete primary ionization. For this anode wire, the best r resolution is (170 ± 0.74) μm and the worst is (351 ± 1.4) μm in σ.

On the other hand, intrinsic spacial resolution along z direction is also evaluated by means of same residual. At first, it is necessary to verify the resolution of anode-charge division in order to guarantee solving the vernier-pad relation uniquely. Figure 9.3 present the z-coordinate

109

resolution by anode-charge division methode. Figure 9.3(a) shows two examples of residual distribution in z, left histogram is corresponding to cell#8 (the shortest wire), and right histogram is corresponding to cell#0 (the longest wire), respectivery (*cf.* section 4.4). As one can
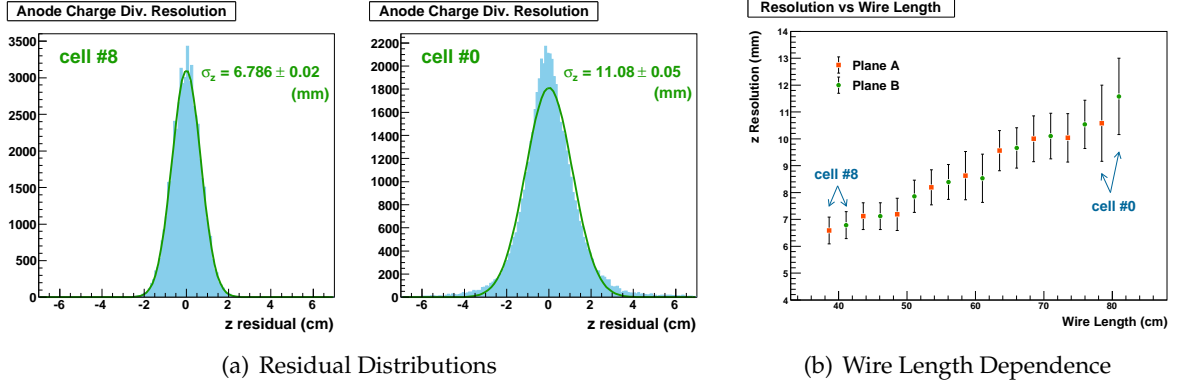

(a) Residual Distributions

(b) Wire Length Dependence

Figure 9.3: z resolutioin by Anode Charge Division (Data)

suppose easily, z spacial resolution by anode-charge division depends on the wire length due to signal attenuation; difference between these two histograms caused by this dependence. Figure 9.3(b) present the mean z resolution of charge-divition methode for all wire as a function of anode wire length, where error bar represents the RMS of resolution distribution over all chamber modules. One can see a wire-length dependence in this sequential plot. The worst resolution that is given by the longest wire is (11.50±0.05) mm, and the best resolution that is given by the shortest wire is (6.58±0.08) mm in sigma, respectivery. This is enough precise so that one can solve the vernier-pad charge-ratio relation with z coordinate uniquely since a vernier period is 5 cm.

Next, we can evaluate the spacial resolution along z-direction by the vernier-pad reconstruction. Figure 9.4(a) present two examples of residual distribution in the same cell. The
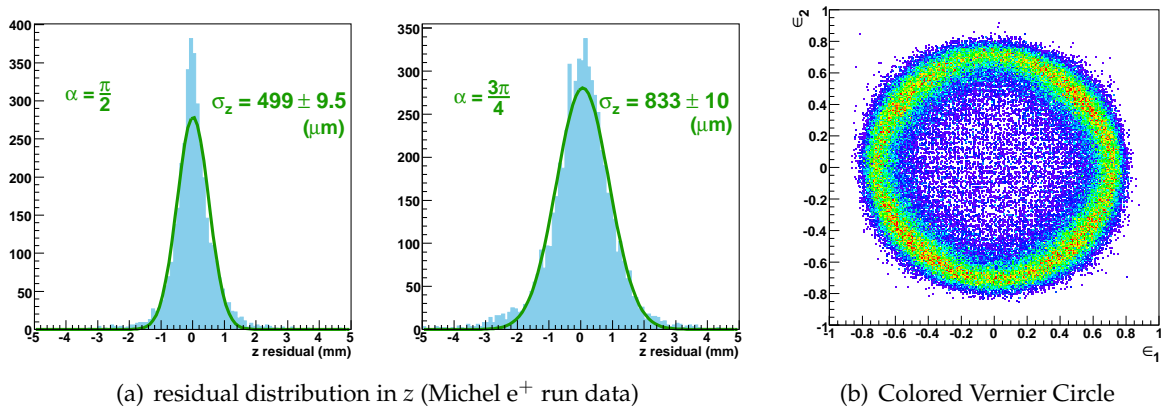

(a) residual distribution in z (Michel e$^+$ run data)

(b) Colored Vernier Circle

Figure 9.4: Drift Chamber spacial resolution in z (Data)

z-coordinate is reconstructed by measured charge of signal pulse only, *i.e.* the resolution de-

pends on the Signal-to-Noise ratio primarily; in the other words, it depends on the amount of collectable charge. At the wedge of vernier (phase of vernier circle, $\alpha = \frac{\pi}{2}n, n = 0, 1, 2, 3$), one pad has the most amount of charge and another pad has the least amount of charge. On the other hand, at the middle of wedge ($\alpha = \frac{\pi}{4}(2n + 1), n = 0, 1, 2, 3$), both pads have same amount of charge; it is almost half a maximum charge. Figure 9.4(b) shows a typical vernier circle as a color-weighted view to see the width of circle clearly; width of circle indicates the intrinsic spacial resolution without any biases by the reconstruction algorithm. As one can see in this plot, the width of circle is clearly thicker at the middle of wedge than at the wedge. Each plots of Figure 9.4(a) are corresponding to the events collected at the wedge of vernier and the middle of wedge, respectively. The best resolution of (499±9.5) μm and the worst resolution of (833±10) μm are given for this cell. The obtained z spacial resolution averaged overall this cell is (612±9.8) μm.
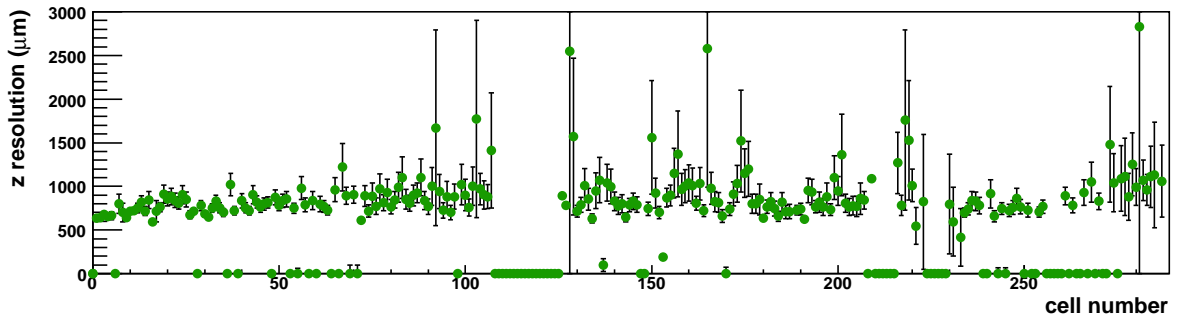

Figure 9.5: z resolution distribution for all cells (Data)

Figure 9.5 shows the z spacial resolution distribution as a function of cell number [†]. The z resolution is sensitive to many factors, *e.g.* cathode sputtering quality, electrical conntact between pad and readout-line, feed-through connection, *etc*[‡]. In consequence, the distribution of resolution is varied widely; (870±17) μm of spacial resolution is obtained on average for all cells.

9.2 Timing Counter Performances

We here discuss the intrinsic performance of another important component of the positron spectrometer, the timing counter. As described in Section 4.3, timing measurement of positron is done by a set of fast, double-layerd, orthogonally placed hodoscope arrays, positioned at both ends of the spectrometer; in particular, the timing is mainly measured by the array of plastic scintillation counters, called ϕ-counter. The scintillation fibres, called z-counter, are mainly used for the trigger purposes.

In the engineering run 2007, the ϕ-counter system was fully installed and tested with full

---

[†]Several channels have resolution of zero; they are corresponding to the bad channels.

[‡] For the engineering run 2007, the last reason, feed-through, was dominant, and it will be discussed in the bad channel lists, Appendix B in detail.

intensity muon beam same as drift chambers [§]. Here, we can investigate the intrinsic performances of ϕ-counter system, the timing resolution and the counting efficiency. In fact, it is not easy to evaluate the intrinsic counting efficiency of timing counter due to lack of operational z-counter, however it is possible to estimate the efficiency by extraporating track from the drift chamber. Thus, such a whole efficiency will be discussed as "Spectrometer Efficiency" instead of the timing-counter intrinsic effciency, in Section 9.3.5.

9.2.1 Intrinsic Timing Resolution

It is possible to evaluate the intrinsic timing resolution by analyzing the data which was acquired by $\mu^+ \to e^+\gamma$ event trigger and contained multiple hits on consecutive two ϕ counters, as shown in Figure 9.6(a). Almost always, triggering positron impacts multiple counters;

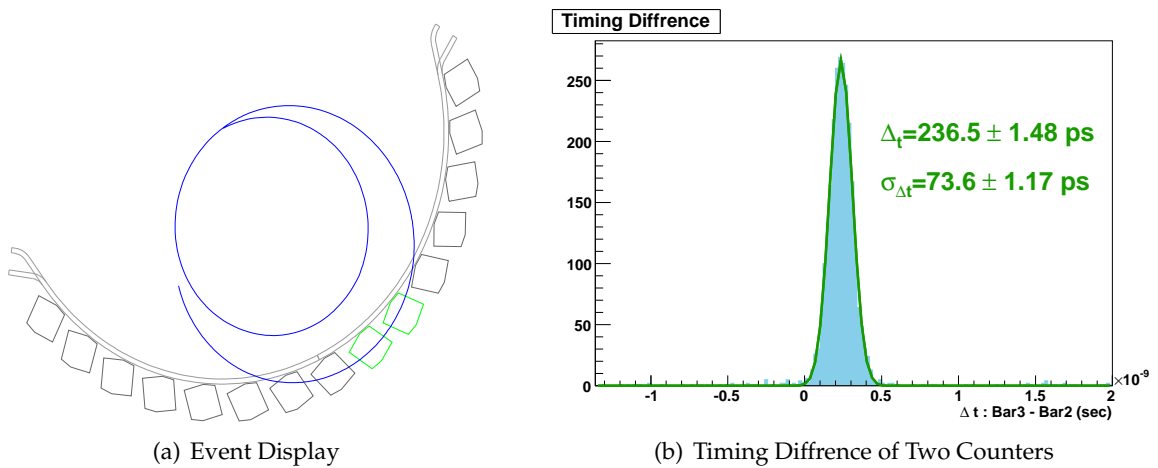(a) Event Display   (b) Timing Diffrence of Two Counters

Figure 9.6: Intrinsic Timing Resolution (Data)

e.g. positron penetrates two counters (indicated as green) and pulse that is generated within counter fires the trigger in this Figure. By subtracting the absolute hit timing of two consecutive counters, intrinsic timing resolution can be obtained. Figure 9.6(b) shows the timing difference distribution. The mean value of this distribution, $\Delta_t = 236.5$ ps, represents the mean timing gap between two consecutive counters. Obtained σ by fitting Gaussian to the distribution is (73.6 ± 1.17) ps; this obtained resolution is containing the timing uncertainty of two counters doubly, *i.e.* the intrinsic timing resolution of single counter is evaluated by

$$\sigma_t = \frac{73.6 \pm 1.17}{\sqrt{2}} = 52.0 \pm 0.83 \text{ ps.} \tag{9.1}$$

9.3 Spectrometer Performances

The individual detector performances were discussed thus far. From here, we can start to evaluate the combined performance, namely the spectrometer performances. One of the most

---

[§] *z*-counter system was also installed, however the high voltage supply was partially integrated, and thus, it was not fully tested in the run 2007.

important performance, momentum resolution, will be discussed at first. Next, vertex resolution of the muon-decay position within the stopping target will be discussed by extrapolating the reconstructed track towards the target. The vertex resolution should have a correlation with the angular resolution of the positron emission direction; both resolutions will be discussed here. On the other hand, the reconstructed track is also extrapolated towards the timing counter. Finally, the spectrometer efficiency will be given.

9.3.1 Momentum Resolution

Because a mono-energetic source of 52.8 MeV/c positron is not readily available, the momentum resolution of the spectrometer can be evaluated by only investigating the falling edge of the Michel spectrum. On the other hand, from the absolute momentum-calibration point of view, the sharp edge of the Michel spectrum at the upper kinematical endpoint provides a natural momentum calibration point. The momentum endpoint of the Michel positron is thus the most attractive nature of muon for the MEG positron spectrometer.

As given in Section 2.1.1, Michel spectrum can be described by the Michel parameters within the Standard Model. Adopting the non-polarized stopping target [¶] simplifies the differential decay rate Eq.(2.7) so that

$$\frac{d\Gamma}{dx} = \frac{m_\mu}{4\pi^3} W_{e\mu}^4 G_F^2 \sqrt{x^2 - x_0^2} \left[x(1-x) + \frac{2}{9}\rho(4x^2 - 3x - x_0^2) \right], \tag{9.2}$$

where we ignore the term involving $\mathcal{F}_{AS}$ in Eq.(2.7) by averaging over the possible polarizations involves integration of $\cos\theta_e$ over the antisymmetric interval $-1 \leq \cos\theta_e \leq 1$. An analogous argument leads to the vanishing of the term $\vec{P}_e(x, \theta_e) \cdot \hat{\xi}$. Here, it is assumed that $\eta = 0$ [‖]. Then, simplified decay rate explicitly depends on the Michel parameter ρ only, and recently, this parameter was measured ultra-precisely [102]. It is also important to remember that the radiative correction to the spectrum. In particular, the edge of Michel spectrum is deformed by the radiative correction significantly. The corrections to the first order of α is given by [103]

$$\frac{d\Gamma}{dx} = \frac{m_\mu}{24\pi^3} W_{e\mu}^4 G_F^2 x^2 \left[(3 - 2x) + \frac{\alpha}{2\pi} f(x) \right], \tag{9.3}$$

where we ignored the contribution involving muon polarization and x_0. The first term corresponds to the Eq.(9.2), the second term represents the first order radiative corrections, where $f(x)$ is given by

$$\begin{aligned} f(x) =& (6 - 4x)R(x) + 6(1-x)\ln x + \frac{1-x}{3x^2} \\ &\times \left[(5 + 17x - 34x^2)(\omega + \ln x) - 22x + 34x^2 \right], \end{aligned}$$

[¶] As described in Section 3.2, polyethylene $(CH_2)_n$ is adopted as muon stopping target. Even if the surface muon beam is fully polarized, the muon polarization is completely lost in such a polymer target [100].

[‖] Recently very precise measurement was reported by the ETHZ-PSI group [101].

where $\omega = \ln\left(m_\mu/m_e\right)$ and $R(x)$ is given by

$$R(x) = 2\sum_{n=1}^{\infty}\frac{x^n}{n^2} - \frac{\pi^2}{3} - 2 + \omega\left[\frac{3}{2} + 2\ln\left(\frac{1-x}{x}\right)\right]$$
$$- \ln x(2\ln x - 1) + \left(3\ln x - 1 - \frac{1}{x}\right)\ln\left(1 - x\right).$$

Figure 9.7(a) shows Michel spectra; "without radiative correction" and "with radiative correc-

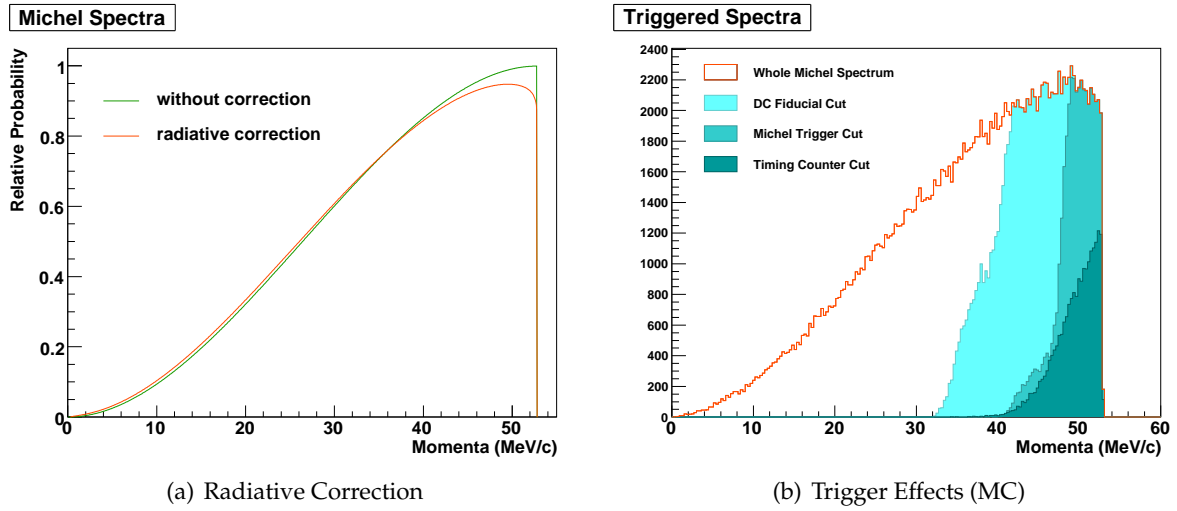(a) Radiative Correction   (b) Trigger Effects (MC)

Figure 9.7: Michel Spectrum

tion", respectively. From these two histograms, one can see the significant difference, especially at the endpoint, *i.e.* this correction is essential to guarantee good momentum calibration and resolution estimation both. In the **megmc**, Michel decay generation takes into account the radiative correction.

However, it is impossible to observe whole Michel spectrum due to restricted tracker fiducial volume and trigger effects. The MEG drift chamber can measure only the high energy part of Michel spectrum because the chamber module is placed in the large radii region, $R > 19.3$ cm. Moreover, it is also required to be enhanced for high energy part by the trigger condition of Michel positron trigger, number of consecutive hit group. Figure 9.7(b) shows such trigger effects on the observable Michel spectrum provided by MC simulation (**megmc** and **megbartender**). From this plot, one can see partially eliminated spectra of the Michel spectrum due to each trigger condition; even if it is required to have just one drift-chamber hit, the triggered spectrum is restricted, the hatched histogram labeled "DC Fiducial Cut". On the other hand, other hatched histogram labeled "Michel Trigger Cut" means that it is required to satisfy the Michel trigger condition. The last spectrum, labeled "Timing Counter Cut" can be observed by the "$\mu^+ \to e^+\gamma$ event trigger". As mentioned in the beginning of this chapter, $\mu^+ \to e^+\gamma$ event trigger requires the simultaneous presence of two high-energy particles with opposite momenta in the liquid-xenon γ-ray detector and the positron spectrometer, *i.e.* the feature of this trigger enables to reduce the trigger rate to the acceptable level. In consequence,

observable spectrum is much more restricted so that much larger bending radius is favored. Detector performances should be evaluated with the final experimental condition, *i.e.* "Michel positron trigger" and "$\mu^+ \to e^+\gamma$ trigger" both.

The shape of reconstructed edge is primarily defined by the momentum resolution of spectrometer. Thus, **absolute momentum calibration and evaluation of the momentum resolution should be performed simultaneously.** In consequence, the endpoint fitting function should be a slope with an edge convoluted with a Gaussian as illustrated in Figure 9.8. In addition, the
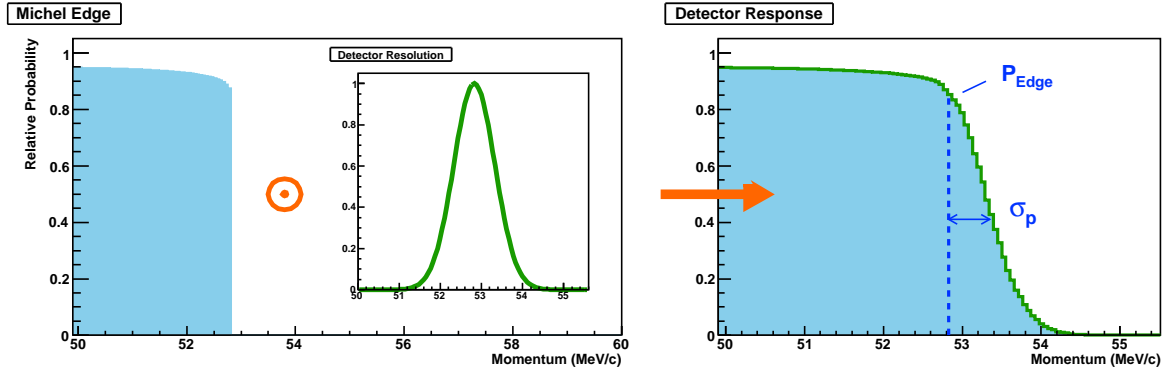

Figure 9.8: A convolution of the cut-off linear function with a Gaussian gives the shape on the right, which is used to fit the endpoint of the reconstructed spectrum.

shape of edge also depends on the trigger condition and the drift-chamber missing channel. If it is acquired by the Michel positron trigger, namely the drift-chamber self-trigger, 7% of Michel positrons can escape to outside fiducial tracking volume since they can achieve larger radii than the maximum radius of the drift-chamber region due to widely distributed muon-decay position within the target. Such positrons can skip one chamber, *i.e.* they do not satisfy the trigger condition of Michel positron run. Due to this reason, the trigger logic was eased so that dropping one chamber within consecutive series is allowed to be fired. However, as mentioned several times, there were number of missing channels for the engineering run 2007 due to discharge and cable disconnections. If the escaped channel due to large bending radius is next to the dead/bad channel, this event is not fired by the Michel positron trigger. Even if it is not taken by the self-trigger, such a track is not reconstructed by the tracking process. As one can suppose easily, such an issue occurs only for the large radius event, *i.e.* the shape of edge must be smeared. In consequence, the edge fitting should take into account the missing channels and trigger condition; the response spectra for the fitting should be provided by the MC incorporating such actual conditions.

It is observed that the momentum resolution depends on the emission angle of positron from the target. This feature can be explained clearly by the number of turns of positron curling in the fiducial tracking volume; large number of loops gives more crossing points and hence more constraints to the fit. Moreover, as well known, gaining length of the lever arm makes a significant improvement on the tracking accuracy. Thus, the edge fitting should take into account its angular dependence. Reflecting such a circumstance, fitting to the endpoint is
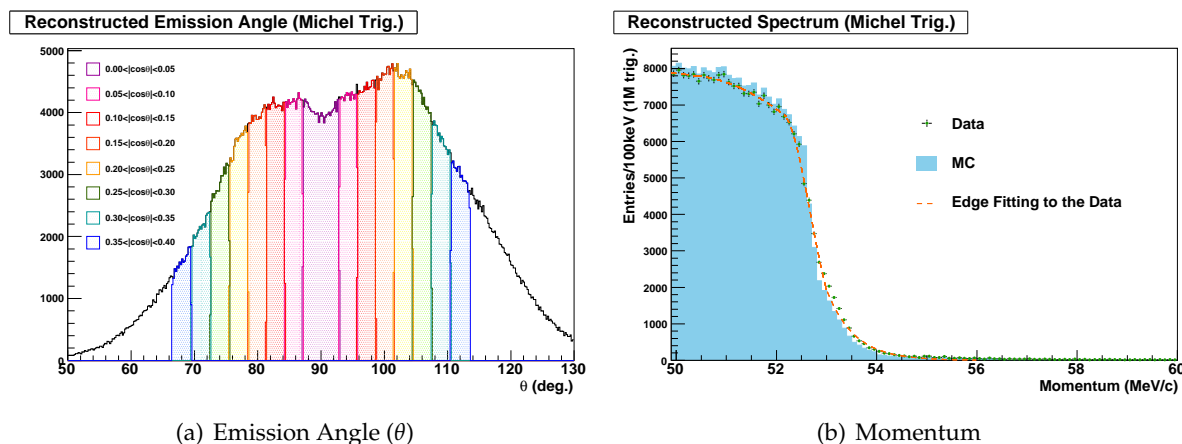
(a) Emission Angle (θ) (b) Momentum

Figure 9.9: Reconstructed Spectra (Data)

performed separately. Figure 9.9(a) shows the reconstructed emission angle with respect to the beam axis, θ. Each stripe corresponds to the angular interval of $\Delta \cos \theta = \pm 0.025$ so that it is separated into eight data sets over $0.00 < |\cos \theta| < 0.40$ while the spectrometer acceptance is $0.08 < |\cos \theta| < 0.35$ to guarantee a good tracking accuracy. For the centre of angular distribution, $0.00 < |\cos \theta| < 0.05$, statistics hollow due to the difficulty of tracking by a lot of curling. In addition, the asymmetry of distribution is due to the misalignment of target. This target misalignment is demonstrated by the target imaging using data itself; this will be discussed in the vertex reconstruction study, Section 9.3.2.

Figure 9.9(b) shows the reconstructed edge of Michel spectrum over whole acceptance of the spectrometer. In order to perform good momentum calibration and evaluation of momentum resolution, this edge of spectrum is subdivided by eight angular sets as shown in Figure 9.9(a). For the edge fitting, it is necessary to have response spectra incorporating the detector resolution and condition; the calculated spectra convoluted with a Gaussian including three parameters, kinematical edge p_{edge}, momentum resolution σ_p, and normalization N, are provided by **megbartender** with actual detector conditions. The endpoint is fitted to this response spectra with three free parameters. Once the endpoint fitting is carried out, one of the obtained parameter, p_{edge}, is used to correct the absolute scale of momentum spectrum that is possibly affected by the energy-loss of positron in the muon-stopping target and depends on the emission angle. After the momentum-scale correction, the endpoint fitting is iterated, and the momentum resolution σ_p is evaluated.

Figure 9.10 shows the endpoint of the reconstructed Michel spectrum and its fitting for several angular slices; shown spectrum is corrected by p_{edge}. The top-left plot ($0.00 < |\cos \theta| < 0.05$) and the bottom-right plot ($0.35 < |\cos \theta| < 0.40$) are outside the spectrometer acceptance, however even such positrons can be acquired by the drift-chamber self-trigger. According to the results of this edge fitting, (420 ± 23) keV/c to (544 ± 63) keV/c of momentum resolutions are obtained; (477 ± 40) keV/c is averaged resolution over spectrometer acceptance.

Same endpoint fitting with the MC simulation gains a further understanding of momen-
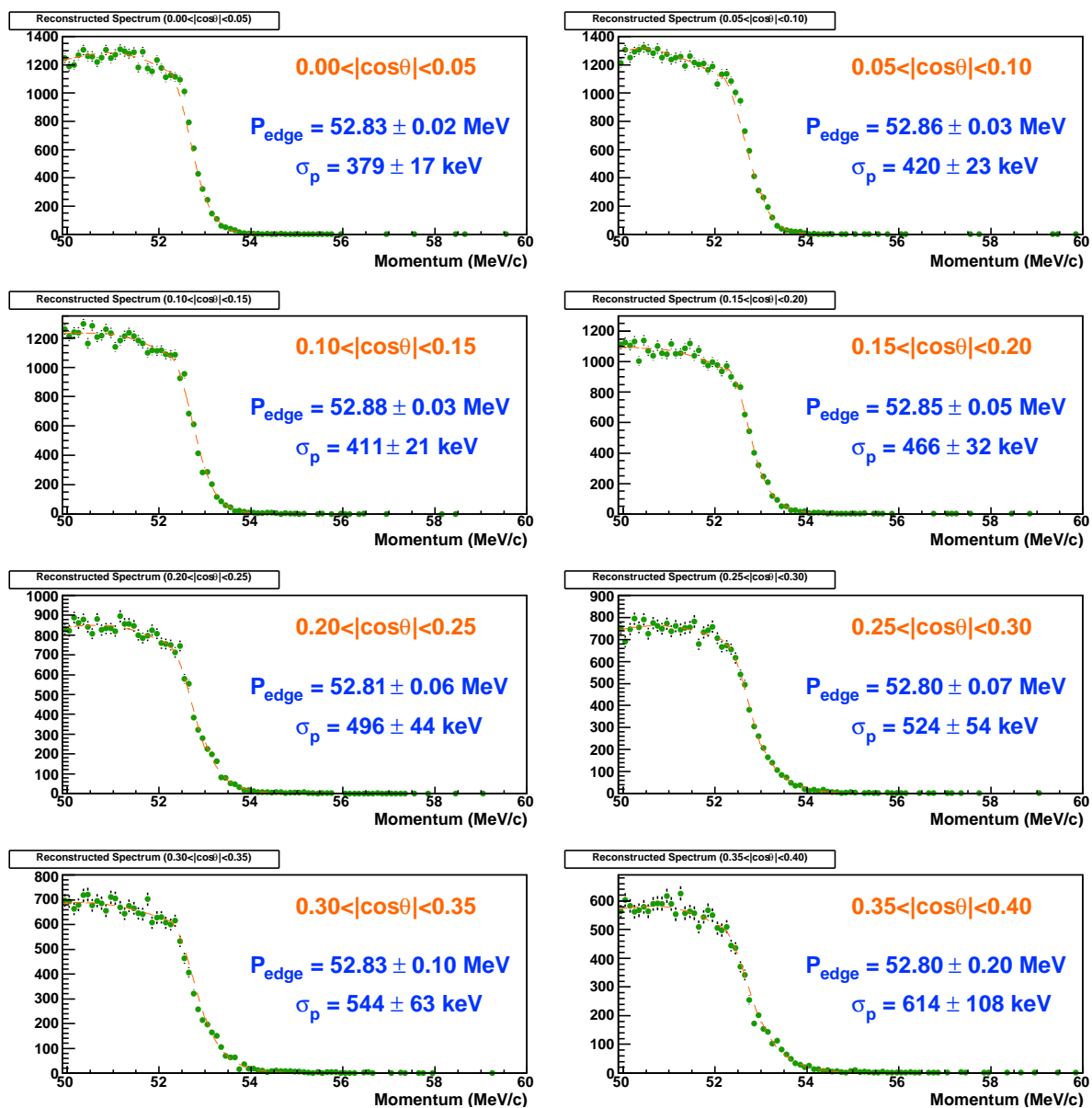
116

Figure 9.10: Endpoint fitting and Momentum Resolutions (Data)

tum resolution. In addition to the standard **megmc**, specially equipped MC simulations were developed for this purpose. As described in Chapter 6, **megmc** was developed to reproduce the complete set of drift-chamber outputs, however, this assumes all drift chamber is working correctly. All the problems for the engineering run 2007 were circumstantially taken into account in the special MC. In order to take into accout the bad chamber, missing channels, and bad spacial resolutions, the function of waveform simulation in the special MC is switched off and only the hit position is provided. The hit positions that corresponds to the missing channel are masked, and all other hit positions are smeared individually adopting the obtained resolutions that is described in Section 9.1.2. In addition, in order to reproduce the air contamination in the COBRA volume, the material description in the special MC was modified. From here, we will refere two MC simulations, standard **megmc** and specially equipped MC with actual conditions, as **MC(ideal)** and **MC(actual)** explicitly.

Figure 9.11 shows the reconstructed Michel spectrum and its endpoint fitting with MC(actual) in the same manner as Figure 9.10. Obtained resolutions are roughly same as the data, but all of them are little better than the data systematically. In the MC, it is possible to evaluate the accuracy of reconstruction purely without any bias from the response function of Michel spectrum since MC can generate monochromatic 52.8 MeV/c positron. Obtained resolution functions from the monochromatic positron are superimposed in Figure 9.11 for MC(actual) and MC(ideal) respectively. Significant deterioration due to bad condition of the engineering run 2007 is clearly shown. Average resolutions of (451±13) keV/c and (297±11) keV/c are obtained for MC(actual) and MC(ideal), respectively. From this result, it is seen that the momentum resolution obtained by the engineering run 2007 is limited by the badly conditioned chambers primarily, *i.e.* fulfillment of detector integration will possibly enhance the momentum resolution better than 300 keV/c. The sources of deterioration of the actual condition will be discussed in Section 10.2 in detail.

As described just before, the reason of angular dependence can be explained by the number of hits; large number of loops gives more crossing points and hence more constraints to the fit, and also, gaining length of the lever arm makes a significant improvement on the tracking accuracy. Once track reconstruction is completed, it is possible to investigate the track-length dependence on momentum resolution; this can show what is the dominant contribution to the momentum resolution. Figure 9.12(a) shows reconstructed momentum without scale correction as a function of reconstructed track length from the muon-stopping target to the timing counter. One can distinguish three distributions clearly; each banks are corresponding to the number of turn within drift-chamber fiducial volume. The higher tail of reconstructed momentum, the main contribution to the deterioration, is associated with the single turn event dominantly. In addition, the tail distribution looks discrete while the number of hit increases as gaining the track length linearly. In consequence, momentum resolution is determined by the number of curling, namely the lever-arm length, primarily.

On the other hand, as well known, the fitting error can be a good indicator to investigate the goodness of reconstruction indirect way. The Kalman filter process also have its error matrix as the inverse of the covariance matrix. Figure 9.12(b) represents the fitting-error distribution of the reconstructed momentum. There are two peaks; small peak is better than 0.2 MeV/c of momentum error and large peak is worth than other. These two peaks denote the number of turn; this can be confirmed by MC simulation. Figure 9.12(c) shows same error distribution provided by MC incorporating fully maintained drift chamber; only mono-energetic 52.8
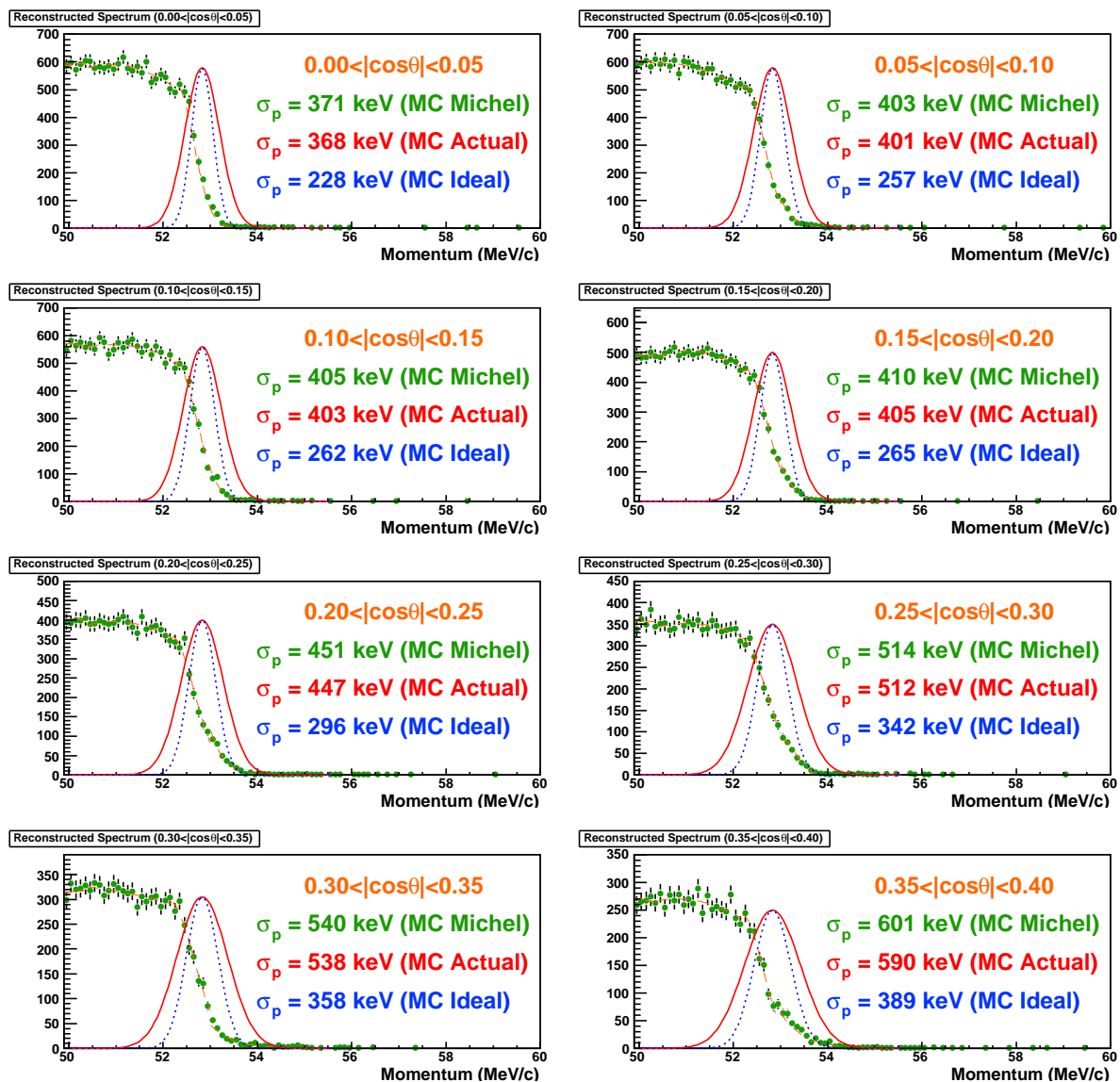
Figure 9.11: Endpoint fitting and Momentum Resolutions (MC), Green Dots : Endpoint Fitting to Michel Spectra generated by MC(actual), Red Solid Line : Resolution Function provided by MC(actual) with monochromatic e^+, Blue Dash Line : Resolution Function provided by MC(ideal) with monochromatic e^+.
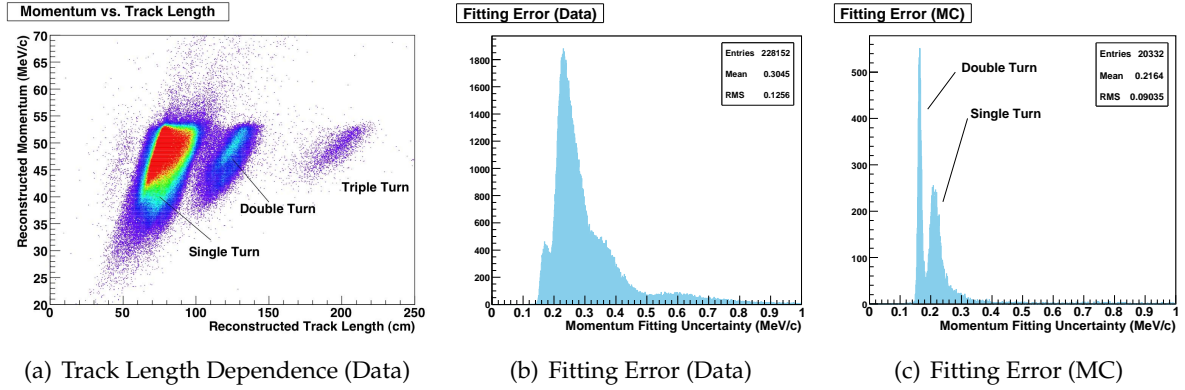
(a) Track Length Dependence (Data)   (b) Fitting Error (Data)   (c) Fitting Error (MC)

Figure 9.12: Momentum Resolution and Number of e$^+$ curling

MeV/c positron is generated in this simulation, *i.e.* low energy Michel positrons are not contained. One can see two distributions clearly. The mean fitting error of the ideal MC is better than the data by a factor of ≈1.4; this is roughly equal to the improvement that is verified by MC(ideal) and MC(actual), *i.e.* the fitting error can be useful to have a deep understanding of track fitting.

The rate and trigger dependences of momentum resolution should be studied. As described before, engineering run 2007 have been performed at several conditions; two beam intensities, Michel positron run and $\mu^+ \rightarrow e^+\gamma$ event trigger run. Figure 9.13(a) is reconstructed mo-

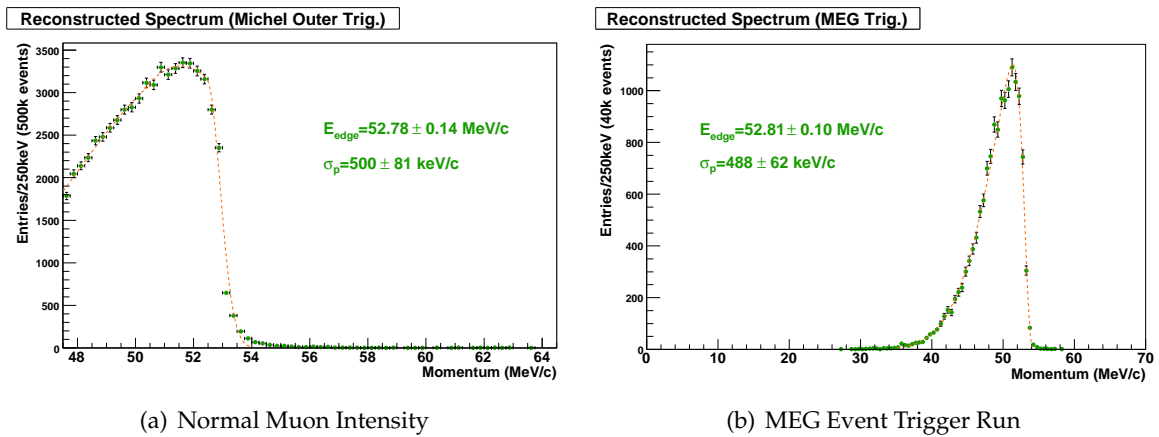(a) Normal Muon Intensity   (b) MEG Event Trigger Run

Figure 9.13: Momentum Spectra with Two Different Settings (Data)

mentum spectrum which was acquired by Michel outer trigger at the nominal muon-beam intensity, 3×10^7 sec^{-1}. In this spectrum, one can see different shape from Figure 9.9(b) at lower momentum part in particular; this is due to different trigger condition. As described in Section 8.2.2, Michel positron trigger was equipped as two different modes; "normal" and "outer". Outer trigger eliminates lower momentum region effectively. However, the shape of

120

endpoint should be same since high momentum positrons are not eliminated, *i.e.* momentum resolution can be evaluated by same way as for normal-trigger data. According to the result of endpoint fitting, obtained resolution is (500±81) keV/c on an average over whole acceptance; it is approximately equal to the resolution obtained by the Michel normal trigger data (*cf.* Figure 9.10) with low muon-beam intensity. At the same time, Figure 9.13(b) shows the reconstructed momentum spectrum which was acquired by $\mu^+ \rightarrow e^+\gamma$ event trigger at the low muon-beam intensity, 5×10^6 sec^{-1}. This time, reconstructed spectrum is shown over whole energy range; endpoint shape is determined by the detector resolution, and shape of lower tail is determined by the trigger condition. Thus, this spectrum should be speculated with simulated spectrum in Figure 9.7(b), labeled "Timing Counter Cut". For this condition, (488±81) keV/c of momentum resolution is obtained. In consequence, concerning the momentum resolution, there are no strong rate and trigger dependences.

9.3.2 Vertex Resolution

By extrapolating the reconstructed track from drift chamber to muon stopping target, target imaging can be carried out. This imaging is necessity article for several purposes. At first, it is inevitable to know the target misalignment **. As mentioned in the target description, Section 3.2, muon stopping target has several holes as shown in Figure 3.4(b). Imaging this hole by projecting the reconstructed decay coordinate onto the target plane tells the target misalignment exactly. Next, this target-hole imaging can also be used to evaluate the imaging accuracy, namely "vertex resolution". Projection of the reconstructed decay position onto one axis, x or y, should have statistical hollow corresponding to the target hall; by fitting this hollow, vertex resolution can be evaluated. Figure 9.14(a) shows the projection of reconstructed decay coordi-
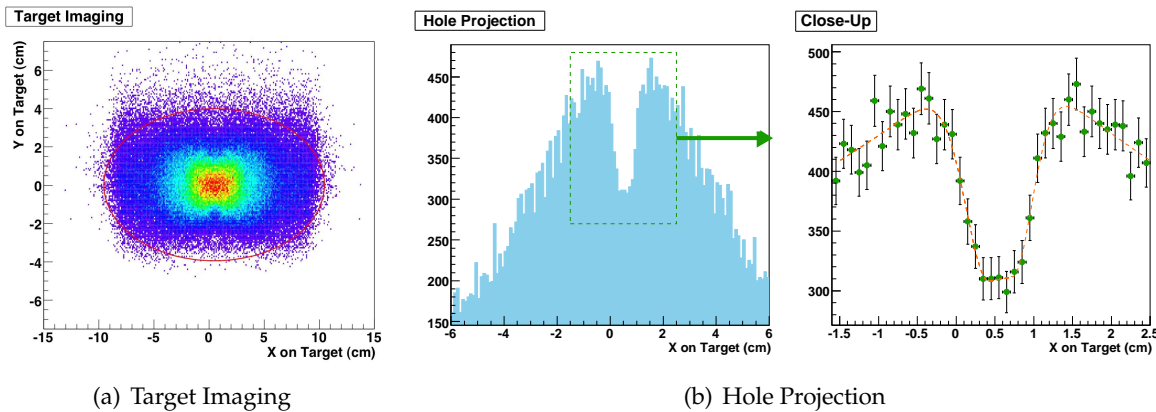

(a) Target Imaging   (b) Hole Projection

Figure 9.14: Trace-back Precision (Data)

nate onto the target plane; a red ellipse denotes the target. In this plot, one can see two holes clearly ($x \approx 0$, $y \approx \pm 1.5$), however, one cannot see other holes due to shape of beam profile and statistics; other holes are placed at the edge of beam spot. Figure 9.14(b) shows vertex

---

** The target geometry was measured by a laser level meter from the downstream end-cap. However, this was not performed by optical triangulation; the surveying accuracy should be verified by alternative measurement, *i.e.* target imaging by data itself is essential.

projection onto x axis (on the target, not global x axis) by using only strictly selected events within -2<y<-1; right plot is its close-up view. The shape of projection is determined by two characteristics; muon-beam profile and vertex resolution. These characteristics can be assumed to be Gaussian, *i.e.* the hollow can be fitted to the convolution of two Gaussian for each edge of the hole. According to the result of this fitting, (1.85±0.33) mm of vertex resolution is obtained. (1.81±0.43) mm of vertex resolution is obtained in the MC(actual) as shown in Figure 9.15(a), and MC(ideal) gives (1.10±0.13) mm of vertex resolution as shown in Figure 9.15(b).
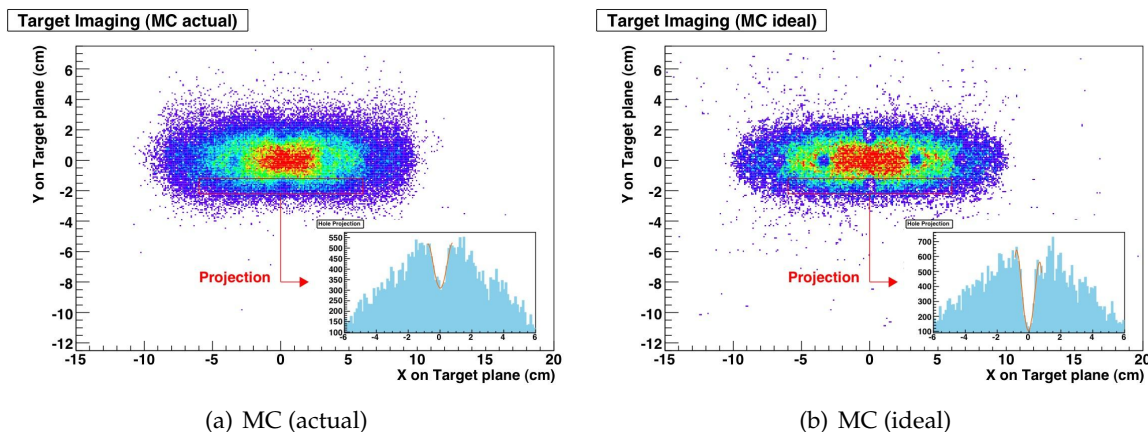

(a) MC (actual)   (b) MC (ideal)

Figure 9.15: Target Imaging and Hole Projection (MC)

From this hole fitting, it is also realized that the actual target position is off-centre by (5.25±0.05) mm with respect to the coordinate system determined by the drift chambers and its support structure. This target misalignment was demonstrated by the optical survey of the target after the engineering run 2007. The asymmetric distribution of reconstructed emission-angle (*cf.* Figure 9.9(a)) can be explained.

9.3.3 Angular Resolution

Next task is to evaluate the angular resolution of positron emission from the target. It is naturally impossible to estimate such a resolution directly due to lack of vertex detector, however this can be estimated indirectly by two methods with fine MC studies. The first possible estimation is performed by connecting with the reconstruction fitting error. As mentioned previously, the fitting error can be a good estimator of the reconstruction accuracy; *e.g.* the case of momentum resolution as shown in Figure 9.12(b) and Figure 9.12(c). If one can understand the relation between angular resolution and its fitting error in MC, the angular resolution can be evaluated by the fitting error of the obtained data. Figure 9.16(a) and Figure 9.16(b) present the error distributions of the track parameter ϕ_0 and θ_0, respectively. For the ϕ error, (0.498±0.304) degree and (0.516±0.371) degree of mean errors are obtained by the ideally conditioned MC and the actually conditioned MC, respectively, where the error denotes RMS of distribution. Then, (0.588±0.405) degree of mean error is obtained by data. On the other hand, for the θ error, (0.303±0.060) degree and (0.334±0.041) degree of mean error are obtained by ideal and actual MC, respectively, while data gives (0.344±0.077) degree. For both angle, actually con-
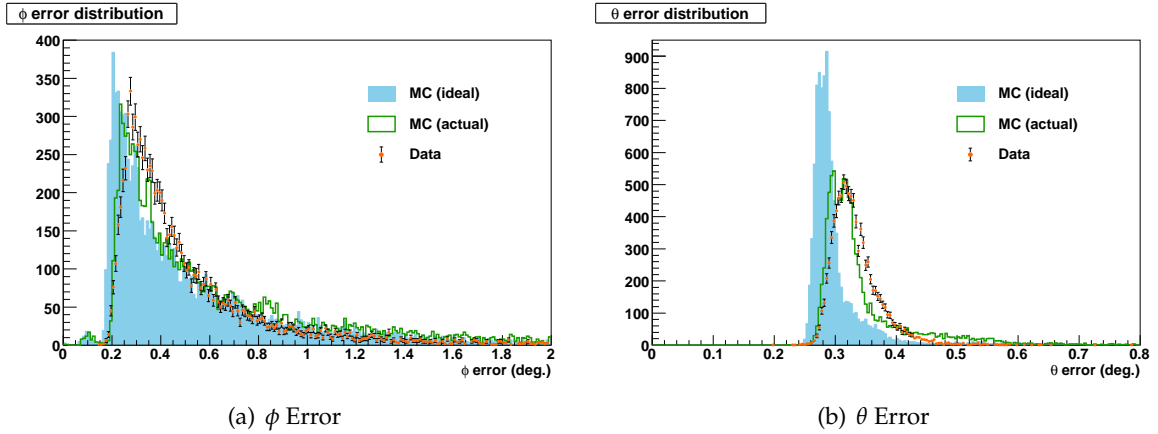
(a) ϕ Error

(b) θ Error

Figure 9.16: Error Distributions of Emission-Angle Reconstruction

ditioned MC is in agreement with data. One can see the large discrepancy between ideal MC and data in the θ-error distribution; this can be explained by that the z resolution of drift chamber is much worse than expected resolution, because θ reconstruction depends on z resolution primarily.

In the MC framework, we can estimate the angular resolution exactly by the difference between actual emission angle and reconstructed, *i.e.* by simulating several angular resolutions, relation between fitting error and angular resolution can be determined. Figure 9.17(a) and Figure 9.17(b) show the angular resolution provided by MC. For the ideal MC, (0.511 ± 0.005) and (0.297 ± 0.002) degree of ϕ- and θ-angular resolutions are obtained, and then, for the actual MC, (0.571 ± 0.006) and (0.364 ± 0.002) degree are obtained. Such an angular resolution can be con-

(a) ϕ angular resolution

(b) θ angular resolution

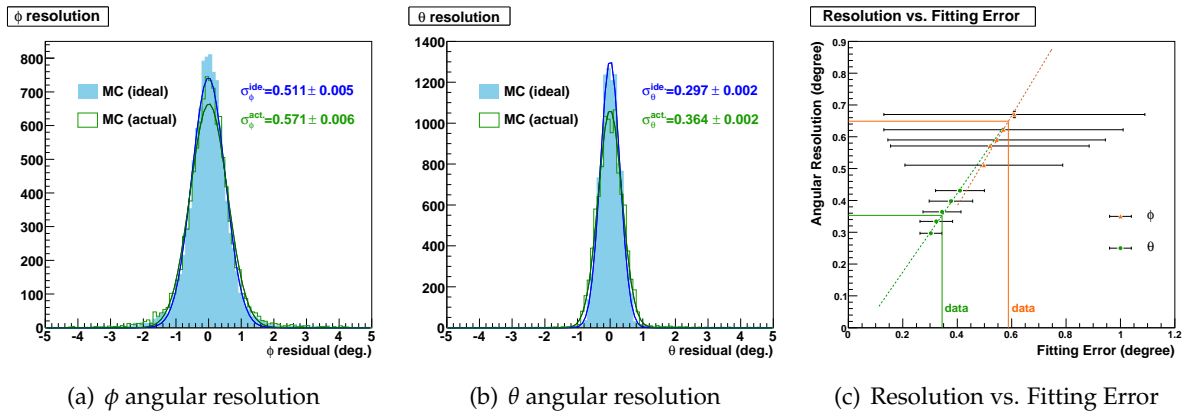(c) Resolution vs. Fitting Error

Figure 9.17: Angular Resolution Estimation (MC)

trolled by tuning the spacial resolution of drift chamber artificially in MC, *i.e.* it is possible to make an angular resolution plot as a function of fitting(reconstruction) error, as shown in Figure 9.17(c). From this figure, one can see that there is obviously linear relation between angular

123

resolution and fitting error, and thus, we can evaluate the angular resolution of the positron spectrometer for the actual condition of engineering run 2007. According to this plot and obtained mean errors from Figure 9.16(a) and Figure 9.16(b), (0.649±0.142) and (0.353±0.079) degree of angular resolution in ϕ and θ are obtained.

The second method is similar with the first method, but it uses the obtained vertex resolution instead of the fitting error. As one can suppose easily, the angular resolution is correlated with the vertex resolution. Thus, if one can know the relation between angular resolution and vertex resolution by using MC simulation, the actual angular resolution can be derived. By using obtained vertex resolution in Section 9.3.2, (1.85±0.33) mm for actual data, (0.617±0.172) and (0.341±0.129) degree of ϕ- and θ-angular resolutions are obtained. In addition, this method also expects the feasible angular resolution, (0.516±0.053) and (0.269±0.011) degree in ϕ and θ respectively, by using obtained vertex resolution of (1.10±0.13) mm from the ideally conditioned MC.

9.3.4 Timing Resolution

We have already evaluated the timing resolution in Section 9.2.1, however, the obtained resolution was estimated as an intrinsic resolution of the counter. Finally, the timing resolution should be evaluated as the spectrometer timing resolution.

Other than the intrinsic resolution, the second dominant contribution to the timing resolution is the error of track-length reconstruction since observed impact timing should be corrected by the track length, otherwise it is impossible to determine the muon-decay timing. Thus, it is necessary to evaluate the accuracy of flight-time determination after the track-length correction. In principle, track-length correction is available for the data of spectrometer alone, however, it is impossible to estimate the accuracy of flight-time determination since we do not have any timing reference with respect to the positron flight. Due to this reason, we evaluated the intrinsic timing resolution by subtracting hit timing between two adjacent counters. Thus, we here estimate the accuracy of timing determination by combination of data and MC.

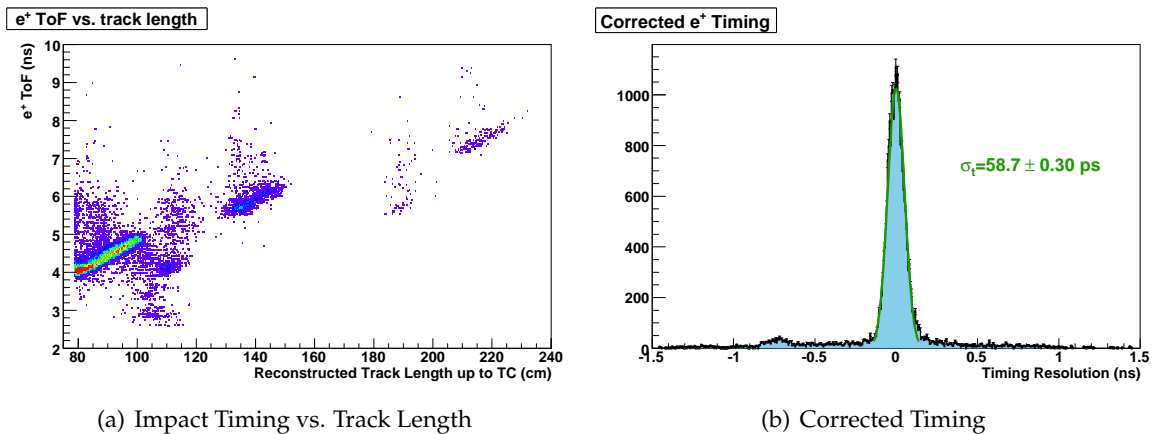(a) Impact Timing vs. Track Length   (b) Corrected Timing

Figure 9.18: e^+ Timing Correction by Track Length (MC)

Figure 9.18(a) shows the relation between positron time of flight and reconstructed track length from target to timing counter. This plot is provided by special MC simulation incorporating the intrinsic timing resolution that is obtained in Section 9.2.1. Three discrete distributions are shown similar with Figure 9.12(a), *i.e.* it denotes the number of positron turn. In between the single and double turn, there is small number of events out of the linear series. They are caused by the scattering at the drift-chamber frame or at the preamplifier cards. This scattering occurs after the drift chamber but before the timing counter, *i.e.* it causes a serious deterioration on the timing resolution. By using this relation, the impact timing can be corrected by the reconstructed track length. Figure 9.18(b) shows the timing residual and its Gaussian fitting; obtained timing resolution is (58.7±0.30) ps. By employing quadratic summation to distinguish the uncertainty caused by track-length error, σ_t^{corr},

$$\sigma_t^{\text{corr}} = \sqrt{58.7^2 - 52.0^2} = 27.2 \text{ ps}$$

is obtained as the timing uncertainty associated with track-length error. In Figure 9.18(b), there is a long tail component due to positron scattering after the drift chamber. As shown in this figure, such events are rejected from the evaluation of timing resolution, *i.e.* this results a deterioration on efficiency. This issue will be mentioned in the spectrometer-efficiency description, Section 9.3.5.

9.3.5 Spectrometer Efficiency

Momentum, Vertex, Angular, and Timing resolutions were evaluated as the spectrometer performances, and thus, we here have to evaluate another performance, efficiency, quantitatively. From the spectrometer point of view, efficiency can be considered by two quantities, track reconstruction efficiency from the target to the drift chamber, and from the drift chamber to the timing counter. The former should be considered as the track-reconstruction capability of the tracking system, and the latter should be referred as the total efficiency of the spectrometer. In fact, the latter is dominant due to the positron scattering after fiducial tracking volume.

Track Finding Efficiency

As discussed in Section 7.3, we have a powerful track finding tool with the time-window elimination and three-dimensional clustering. We here summarize the track finding efficiency by following each finding steps as a comparison with data and MC, as listed in Table 9.1. In or-

Low Rate	(5×10^{6}sec^{-1})		Normal Rate	(3×10^{7}sec^{-1})	
	Cluster Finder	Track Finder		Cluster Finder	Track Finder
Data (2007)	99.9 %	97.9 %	Data (2007)	99.9 %	97.1 %
MC (actual)	99.9 %	98.1 %	MC (actual)	99.9 %	98.0 %
MC (ideal)	100 %	99.9 %	MC (ideal)	100 %	99.7 %

Table 9.1: Track Finding Efficiency

der to verify the detector deterioration, MC simulation is performed including actual missing channels and fully operational condition, respectively. It is also necessary to evaluate the efficiency for two muon-beam rates both, low and normal, to certificate it at the real experimental

condition. In Table 9.1, the former item, Cluster Finder, means the cluster finding efficiency by using the time-window elimination and the clustering condition with z coordinate, and then, the latter item, Track Finder, means the efficiency of retrieving the track seed with two additional hit from all clusters. This estimation is performed for the data acquired by Michel trigger, *i.e.* data must contain small radius events. Such low momenta events should be rejected from the finding efficiency since they do not contain enough number of hits, and also, they are not our objective. Hence, only large radius events that achieve at least cell#6 are included into the efficiency estimation; all other events with small radii are excluded from this estimation. From this table, one can see the good finding power and the good agreement with the MC including missing channels, *i.e.* it can be expected to have a fully operational finder for the ideal spectrometer condition.

Next, we have to evaluate the track reconstruction efficiency, since even if the track seed could be found successfully, the track is not necessarily reconstructed to be guaranteed the reconstruction accuracy. The track reconstruction efficiency is summarized in Table 9.2. The

Low Rate $(5\times10^6\mathrm{sec}^{-1})$			Normal Rate $(3\times10^7\mathrm{sec}^{-1})$		
	Track Fitting	χ^2 cut		Track Fitting	χ^2 cut
Data (2007)	77.8 %	66.1 %	Data (2007)	75.1 %	65.3 %
MC (actual)	80.4 %	67.2 %	MC (actual)	80.2 %	66.9 %
MC (ideal)	99.5 %	97.9 %	MC (ideal)	99.2 %	97.5 %

Table 9.2: Track Reconstruction Efficiency

former item, Track Fitting, means the efficiency of successful fitting. The track fitting process requires several conditions during its process; three consecutive clusters, three additional hits (not necessarily cluster) to the track seed, individual χ^2 at each hit point is smaller than 50 (5σ equivalent) for the first fitting, individual χ^2 at each hit point is smaller than 18 except for the first fitting, total χ^2/ndf is smaller than 20. Hence, the efficiency of successful fitting means the efficiency satisfying such conditions. The latter item, χ^2 cut, means alternative event selection to have a good momentum and angular resolutions; total χ^2 is smaller than 50, reconstructed vertex is inside the target, covariance matrix element of the track parameter $\rho(= q/p)$ is smaller than 0.1. After applying this condition, final track-reconstruction efficiency is obtained. From this table, one can see that the final efficiency for the data is obviously smaller than the efficiency of ideal spectrometer condition; *i.e.* poor reconstruction efficiency for the engineering run 2007 is caused by missing channels of drift chamber primarily. In addition, we have an equally good agreement with MC including missing channels for the study of track finding efficiency.

Track Extrapolation Efficiency

Figure 9.19 schematically shows that a positron is scattered by the materials after passing the drift chambers; this is provided by MC simulation. There are several electrical parts between the drift chamber and the timing counter; *e.g.* carbon-fibre frame, preamplifier, cable, and cable duct *etc*. Even though the geometrical configuration of such electrical parts is optimized, and the amount of material is minimized to avoid the interaction with positrons, some of positrons

are scattered by such electrical parts inevitably, *i.e.* they may cause a serious deterioration on the counting efficiency. In Figure 9.19(a), one can see that a positron is scattered at the cable just
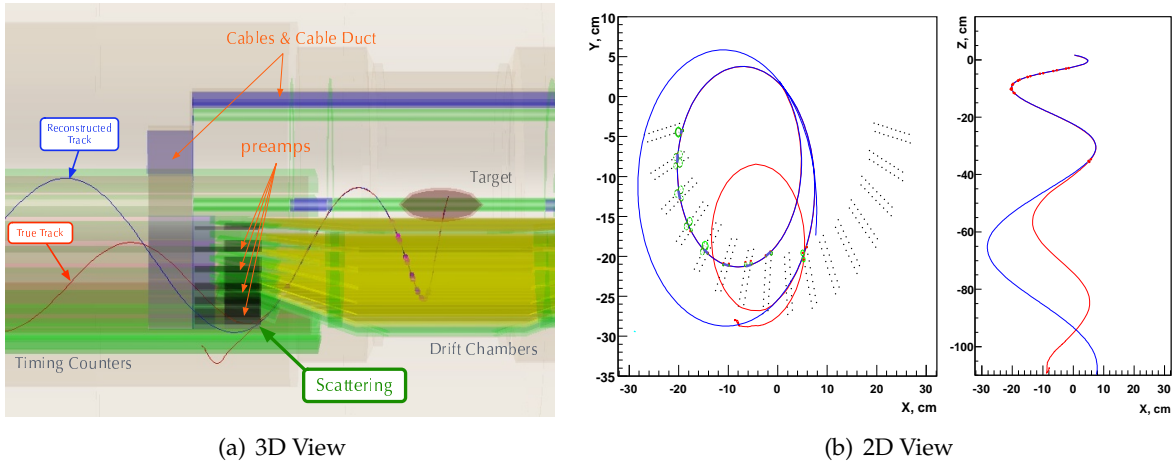

(a) 3D View

(b) 2D View

Figure 9.19: Positron Scattering After the Tracking Volume

after the preamplifiers; red line illustrates the true track and blue line presents the reconstructed track by the drift chamber. Figure 9.19(b) shows two-dimensional $x - y$ and $x - z$ view of the track reconstruction for the same event which presented in Figure 9.19(a). From these figures, one can see that the reconstructed track is in excellent agreement with the true track before the scattering. In consequence, the hit on timing counter can be expected by the drift-chamber tracking precisely, *i.e.* this allows to calculate the efficiency of track extrapolation from the drift chamber to the timing counter; in other words, the timing-counter efficiency as a whole spectrometer.

This effect obviously depends on the positron emission angle primarily because the material distribution is not homogeneous, *i.e.* spectrometer counting efficiency should be evaluated as a function of positron-emission angle. This inefficiency can be measured by analyzing the data which was acquired by the MEG event trigger; such data contain the significant hits in the drift chamber and the timing counter both. Dividing the number of hit in timing counter by the number of expecting hit provided by the track reconstruction derives such inefficiency. Figure 9.20(a) is a two-dimensional timing counter inefficiency map as a function of positron emission angle where a white rectangle represents the spectrometer acceptance. From this plot, one can see that there are clearly inefficient regions, *e.g.* $\cos\theta \approx 0.18$. It naturally depends on the material distribution between the drift chamber and the timing counter. Figure 9.20(b) gives the material distribution as a function of positron emission angle that is calculated by the MC simulation; it is indicated by the total radiation length so that is accumulated by the positron from the target to the timing counter. One can see that the inefficiency is obviously correlated with the material distribution. There is one exception in the region of $\cos\theta > 0.38$; inefficiency is very high in this region, however the amount of material is small. This inefficiency is caused by the edge of timing counter; *i.e.* here is not a fiducial volume of timing counter. This region is excluded from the detector acceptance anyway. From Figure 9.20(a), one can conclude that

(a) Timing Counter Inefficiency Map   (b) Material Distribution
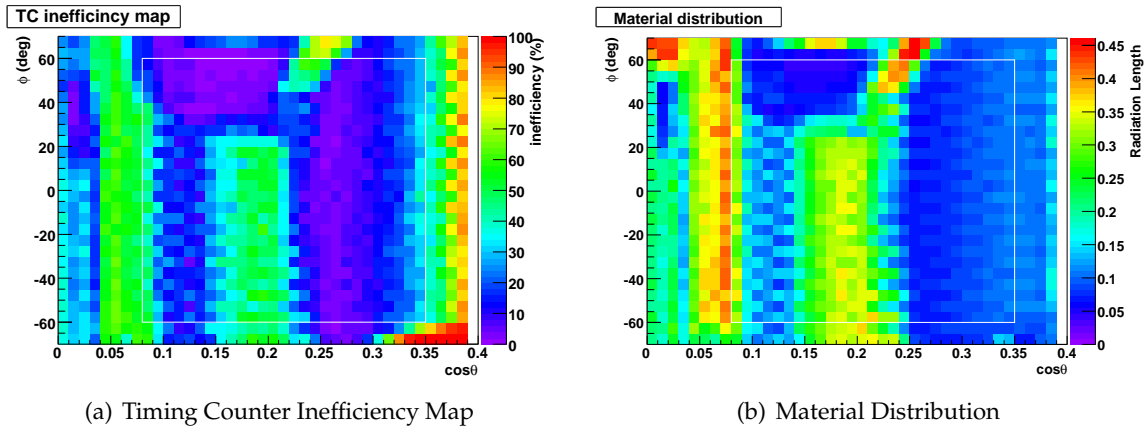
Figure 9.20: Spectrometer Inefficiency

the timing counter inefficiency is 34.5 % on an averaged over the spectrometer acceptance, and this effect is caused by the material outside the drift chamber mainly.

Let us subdivide Figure 9.20(b) into each component of the drift chamber in order to understand the source of inefficiency and consider the possible improvements for the MEG detector apparatus. Figure 9.21 shows five material-distribution plots as a function of positron emission angle for each components individually. The first plot, shown in top-left, present the contribution from gas, cathode foil, and wires, so-called drift-chamber fiducial. The second plot, shown in top-right, present the contribution from the carbon-fibre frame. The third plot, shown in middle-left, present the contribution from the drift-chamber preamplifier cards. The fourth plot, shown in middle-right, present the contribution from the drift-chamber cables. The fifth plot, shown in bottom-left, present the contribution from the cable duct. The last plot, shown in bottom-right, shows the material budget as a function of emission angle in $\cos \theta$, averaged over ϕ, by stacks of each contribution. For the material contribution of drift-chamber fiducial is negligible; it is less than others by two orders of magnitude. By comparing each contributions with measured inefficiency Figure 9.20(a), we can conclude that all components have a certain contributions to the timing counter inefficiency even though the cable has much larger amount of material than others. This can be explained by the following consideration; if positron scattered by the frame or preamplifiers, this positron goes out of ideal orbit largely since the gap between drift chamber and timing counter is not short, while the gap between cable duct and timing counter is very short, *i.e.* even if positron is scattered by the cable or cable duct, many of them can impact the timing counter with ideal orbit.

Finally, we here obtain the timing counter inefficiency that is caused by the materials accompanied by the drift-chamber system. As we discussed in previous subsection, the drift-chamber system has an individual efficiency, so-called tracking efficiency. Thus, the spectrometer efficiency should be referred as the product of tracking efficiency and the counting efficiency. In consequence, for the engineering run 2007, spectrometer efficiency is 42.8 %. It is also possible to estimate the spectrometer efficiency by using same logic with the MC simulation incorpo-
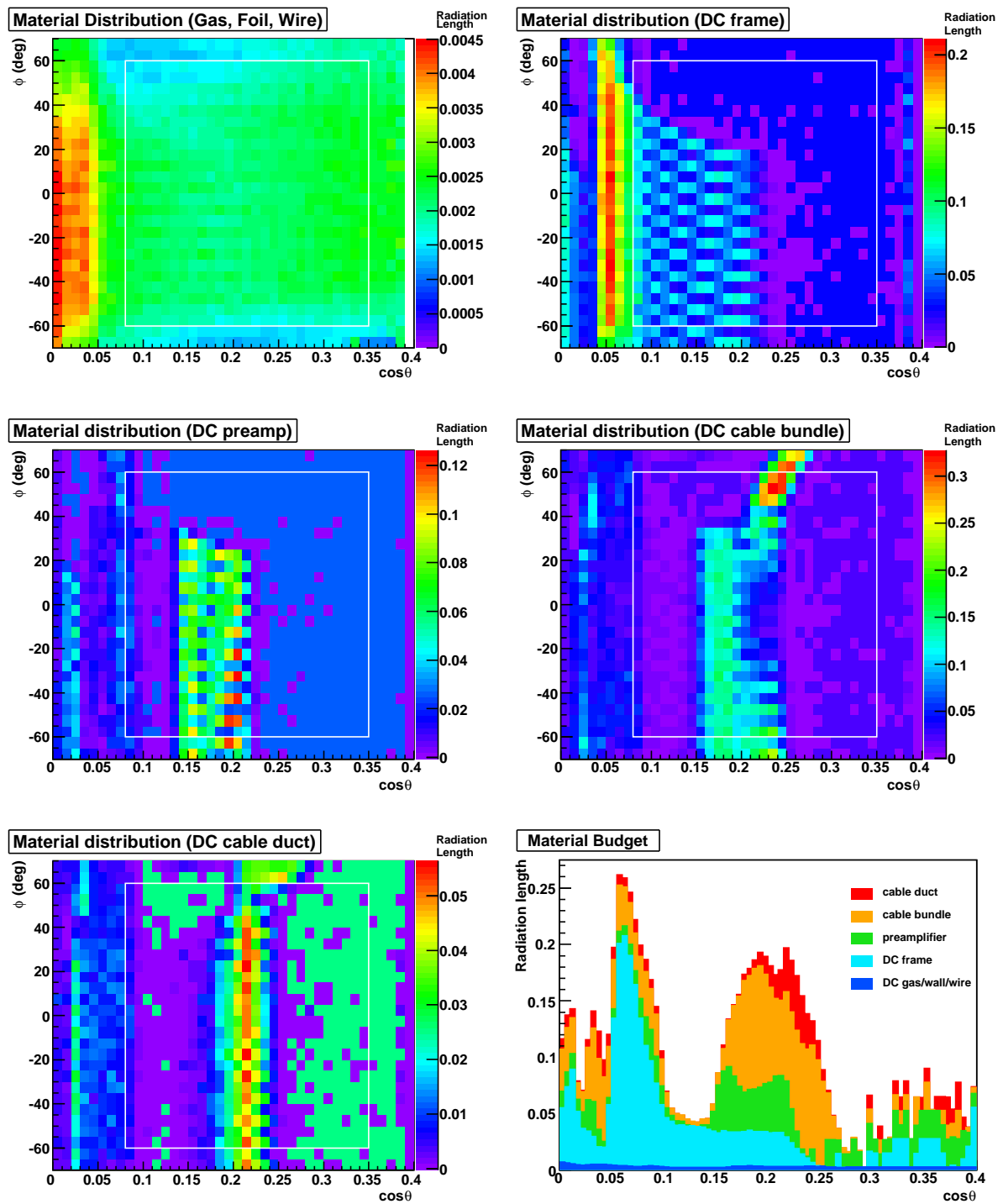
Figure 9.21: Material Distribution of Individual Composition, Material Budget

rating actual situation; it is 43.8 %. It is good agreement with the data, *i.e.* we can evaluate the feasible spectrometer efficiency by MC with fully equipped drift chambers; it is 63.9 %.

Chapter 10

Discussion

All the spectrometer performances are obtained by analyzing the data of engineering run 2007. Now is a time to discuss the spectrometer performances in detail and the feasible sensitivity of the MEG experiment. At first, all the systematic uncertainty which can affect on the drift-chamber performances are summarized and estimated its contributions. This estimation is essential to consider the feasibility of MEG and also to find the possible improvements. Next, the systematic uncertainty to the spectrometer performances is discussed. Finally, we discuss the MEG feasible sensitivity.

10.1   Limiting Factors to Drift-Chamber Performances

As the first discussion, let us consider the limiting factors to the drift-chamber intrinsic performances.

10.1.1   High Voltage

In general, the systematic uncertainty is frequently contributed by a slow control system. First of all, we therefore consider the stability of slow control system, in particular concerning the high voltage.

The instability of high voltage can affect the drift-chamber spacial resolutions directly via changing the drift velocity. As shown in Figure 5.20, we succeeded to control the high voltage better than 0.02 volt (RMS) for 1850 volt applying over the engineering period of 2007; **the stability of high voltage is 0.0011 %.** In addition, as described in Section 5.2.3, thanks to well-known property of He-C_2H_6 gas mixture, electron drift velocity saturates for a relatively low electric field [71]. In consequence, calculated systematic uncertainty to the drift-chamber transverse spacial resolution caused by the high-voltage instability is ± 0.40 μm; the maximum deviation is ± 1.08 μm. On the other hand, the longitudinal spacial resolution is not affected by the high-voltage instability since z coordinate is derived by taking the ratio of collected charge at both ends of wire and cathodes, *i.e.* always such instability gets balanced out in the z-coordinate reconstruction.

For the engineering run 2007, as described in Section 8.2.3 and listed in Table 8.1, nine planes out of thirty-two planes have been applied only 1800 volt due to discharge problem

131

while the nominal high voltage is 1850 volt. Thus, the spacial resolutions and the efficiency of such planes were degraded.

As shown in Figure 9.1(b), applying 1800 volt provides 80.1 % of single efficiency. By applying same analytical treatment with that described in Section 9.1.2, (177$\pm$0.89) to (450$\pm$1.02) μm of transverse spacial resolutions for such lower-voltage planes are obtained at the best and worst region of drift distance, respectively. Then, the longitudinal spacial resolution is also studied; (909$\pm$10.9) μm to (1.51$\pm$0.21) mm are obtained at the best and worst region of vernier circle, respectively.

They are not referred to the systematic uncertainty to drift-chamber intrinsic spacial resolution, however, they should be taken into account in the systematic uncertainty to the spectrometer global performances; they will be mentioned in Section 10.2 again.

10.1.2 Gas Condition

Another important component of the slow control system, gas contorol, is also usually referred as a source of systematic uncertainty.

As described in Section 5.5.1 and shown in Figure 5.18, the pressure difference between interior and exterior of the chamber has been maintained better than 0.005 Pa in RMS, even if the ambient atmosphere is varied over 130 Pa range. This is corresponding to 0.5 μm of maximum difference of the cell spacing. The wire spacing is 4.5 mm, *i.e.* possible deviation of the drift distance caused by pressure changing is only 0.0111 % of the maximum drift distance. This number is referred to the limiting factor to the transverse spacial resolution. In consequence, the systematic uncertainty to the transverse spacial resolution caused by pressure instability is $\pm$0.25 μm.

10.1.3 Gas Characteristics

We here summarize the possible limiting factors due to properties of the drift-chamber active gas.

As shown in Figure 6.4(a), the effect of drift-electron diffusion can be calculated precisely. Then, the systematic uncertainty to the transverse spacial resolution can be evaluated to be $\pm$90.1 μm.

In general, helium-based gas mixture has another disadvantage due to large fluctuation of number of primary ionization. Then, the accuracy of charge collection may be degraded, *i.e.* ionization-loss dE/dx measurement is worse than other gas-mixture. However, this does not affect to the MEG drift chamber since we are not requested to measure the quantity of dE/dx, and also charge fluctuation gets balanced out in the z-coordinate reconstruction always. In consequence, we here do not count the fluctuation of primary ionization as a source of systematic uncertainty.

10.1.4 Electronics

In the engineering run 2007, readout electronics have been not conditioned very well. Following three items mainly contribute to the systematic uncertainty;

- Cable disconnection at the feed-through connector

- Bad conntact at the feed-through connector

- DRS fake pulse

- Baseline noise

Other than them, there are still several items, *e.g.* baseline fluctuation, cross-talk, *etc.*, however, they are not main components to the systematic uncertainty.

Concerning the first item, cable disconnection, if the cable is disconnected at the feed-through, corresponding channel is not usable, *i.e.* this affects to the spectrometer performances, not the drift-chamber spacial resolution. Thus, we here do not treat this item as a source of systematic uncertainty; this will be discussed in Section 10.2 later.

For the second item, bad conntact, several channels are affected by the bad conntact at the feed-through connector; they are listed in Appendix B and labeled "bad contact". They nearly lost the contact but still connected, and then, signals of such channels are very noisy or not efficiently observed. This problem happened only for the cathode readout, *i.e.* only the z reconstruction was suffered from this issue. For such channels, (798±0.91) μm to (2.03±0.36) mm of longitudinal resolutions are obtained at the best and worst region of vernier circle, respectively. This contribution is referred to the systematic uncertainty to the spectrometer global performances.

Meanwhile, the DRS contains a problem which cause the fake pulse. Details of this problem are given in Appendix A. As shown in Figure A.1(a), DRS2 sometimes has an unreal pulse at the end of Domino cycle of DRS. If this fake pulse is overlapped with the signal pulse as shown in Figure A.1(b), the z reconstruction must be screwed up. It is not easy to evaluate this effect quantitatively. We here estimate this effect by following steps; (i) evaluate the frequency of this problem, (ii) evaluate the amount of charge which is induced by this fake, (iii) evaluate the deviation of z coordinate which is calculated from (ii).
As described in Appendix A, the fake pulse does not occur always, *i.e.* the frequency of fake pulse can be evaluated only by counting the fake pulse from all the recorded pulses. According to this analysis, (28.3±11.9) % of events contain the fake pulse; the evaluated error is very large because this effect depends on many items, *e.g.* instantaneous rate, temperature, and individual characteristics of the chip. The fake pulse has a fixed width corresponding to 64 sampling cells (*cf.* Appendix A), *i.e.* the fake-pulse overlapping occurs within (2.83±1.19) % events, where we assumed that the typical signal time-window is 200 ns out of 2 μsec DRS range. Secondary, the evaluated amount of charge induced by the fake pulse is (383±129) mV·ns; we here adopt the area of pulse (volt×sec) as a charge for simple discussion. By adding this amount of charge into the signal cathode pulse, it is possible to evaluate the deviation of the cathode charge; charge deviation is evaluated to be (15.3±5.2) %. Finally, it is turned out that the systematic uncertainty to the transverse spacial resolution caused by the DRS fake pulse is (138±42) μm.

The baseline noise was measured by the pedestal trigger, *i.e.* random trigger by the clock. Obtained baseline fluctuation is 0.2 mV in average; it denotes RMS of all DRS cells over 2 μsec integration. However, for the bad contact channels, they have large fluctuations on the baseline, 1.2-5.9 mV. This noise level is enough small for the transverse spacial resolution, but

not enough for the longitudinal spacial resolution. By putting such baseline fluctuations into the **megbartender**, systematic uncertainty due to baseline noise is evaluated to be (109 ± 10) μm on the longitudinal spacial resolution.

10.1.5 Timing Determination

As described in Section 8.5, in order to guarantee the accuracy of timing determination for the drift chamber, timing pedestal calibration has been performed. Then, the obtained accuracy is ±1.91 ns. This is corresponding to (76.4 ± 5.2) μm as the uncertainty of transverse spacial resolution.

10.1.6 Alignment

In general, one of the most significant contribution to the systematic uncertainty of the drift-chamber resolution is misalignment of detectors. In principle, the global coordinate system of the MEG positron spectrometer is determined by the drift chamber and its support structure themselves, *i.e.* misalignment of other components, target, timing counter *etc.*, does not contribute to the systematic uncertainty of drift-chamber resolutions. However, internal misalignment of each chamber, namely wire misalignment, contributes to the systematic uncertainty at a certain level. In order to minimize such an uncertainty, the cosmic-ray run has been carried out, as described in Section 8.2.1. However of course, it is not perfect.

As discussed in Section 8.3 and shown in Figure 8.4(b), all the wire coordinates are relatively aligned with an accuracy of (47.3 ± 38.8) μm. This is indirectly connected to the systematic uncertainty of drift-chamber transverse spacial resolution. By adding this wire-position deviation to the tracking software randomly, amount of deteriolation can be evaluated; it is determined to be ±33.5 μm as the uncertainty of transverse spacial resolution.

As described in Section 8.4, z coordinate alignment has also been carried out at the analysis of cosmic-ray run data. After z correction, obtained relative deviation of z coordinate is (101 ± 39) μm. This deviation is corresponding to $\pm$ 92 μm as the uncertainty of longitudinal spacial resolution.

10.1.7 Relative Gain Fluctuation

As described in Section 8.4, z-coordinate calibration is equivalent to the relative gain correction between both ends of the wire for not only the anode but also the cathode. After the z-coordinate calibration, finite fluctuation of relative gain is remained; this fluctuation has a certain contribution to the longitudinal spacial resolution. By putting obtained relative gain distribution (*cf.* Figure 8.7(b)) into the **megbartender**, (199 ± 13) μm of systematic uncertainty is evaluated for the longitudinal spacial resolution.

10.1.8 Spacial Fluctuation of Induced Charge

For the longitudinal spacial resolution, spacial fluctuation of the induced charge has a large contribution to the systematic uncertainty. Positrons deposit each ionization along an oblique track, *i.e.* the positive charge is induced on the vernier pad widely and inhomogeneously by z-direction. This effect can be evaluated by the **GARFIELD** program; it is $\pm354\mu$m.

10.1.9   Accuracy of Reference Position

The accuracy of the reference position is refered as the source of systematic uncertainties since the spacial resolutions are evaluated by the difference between reconstructed and its reference position. Main contribution to such an accuracy is the effect of multiple Coulomb scattering. By the well-known expression [104], ambiguities of the reference-position determination are evaluated to be $\pm 125 \mu$m and $\pm 175 \mu$m for r- and z-direction.

10.1.10   Summary of Contributions to the Spacial Resolutions

We here summarize the sources of systematic uncertainty to the drift-chamber spacial resolutions.

Resolutions	Effect	Uncertainty
Transverse Spacial Resolution:	High Voltage	± 0.40
169.7 to 351.2 μm	Gas Pressure	± 0.25
are obtained (Data)	Timing Determination	± 76.4
	Alignment (r)	± 33.5
	Electron Diffusion	± 90.1
	Multiple Coulomb Scattering (r)	± 125
	(Total in quadrature	± 175)
Longitudinal Spacial Resolution:	DRS Fake Pulse	± 138
499 to 833 μm is obtained (Data)	Alignment (z)	± 92
	Relative Gain Fluctuation	± 199
	Baseline Noise	± 109
	Charge Distribution	± 354
	Multiple Coulomb Scattering (z)	± 175
	(Total in quadrature	± 485)

Table 10.1: Contributions to systematic uncertainty in Spacial Resolutions

10.2   Limiting Factors to Spectrometer Performances

Limiting factors to the drift-chamber spacial resolutions are summarized so far. Thus, we here step into the next stage; limiting factors to the spectrometer global resolutions.

10.2.1   Missing Channels

As mentioned several times, we had many dead/bad channels of drift chamber in the engineering run 2007; the description of dead/bad channels is given in Appendix B in detail. These missing channels naturally cause a serious deterioration on the tracking accuracy and efficiency. In order to evaluate such deteriorations, specially equipped MC, called MC(actual), was developped as mentioned in Section 9.3.1. Thus, it is possible to distinguish the contributions from each effects by turning it on in MC(actual) one by one.

By turning on only the mask of missing channel in MC(actual), 388 keV/c of momentum resolution is obtained. In Section 9.3.1, 297 keV/c of momentum resolution was obtained by MC(ideal), *i.e.* 249 keV/c of uncertainty is caused by the effect of missing channels.

10.2.2 Spacial Resolutions

The uncertainty caused by the spacial resolution is described here. Figure 10.1(a) and Figure 10.1(b) present the transverse and longitudinal spacial resolution dependence on the momentum resolution, respectively, as a function of spacial resolution. Each dots are obtained by

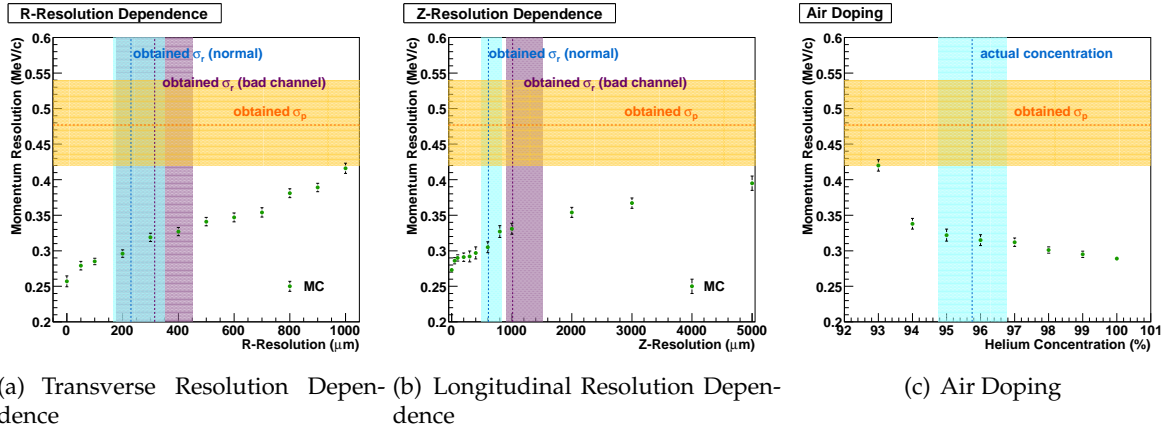(a) Transverse Resolution Dependence (b) Longitudinal Resolution Dependence (c) Air Doping

Figure 10.1: Limiting Factors to Momentum Resolution

specially equipped MC so that the drift chamber is fully operational but the spacial resolution is artificially controlled. From these figures, one can see that bad resolution chamber causes a certain deterioration. For example, if all chambers are degraded like hatched region which is corresponding to 1800 volt planes, momentum resolution will degrade to 331 keV/c.

For the transverse resolution dependence, by assuming the mean transverse resolution which is obtained in 2007, 322 keV/c of momentum resolution is obtained. On the other hand, for the longitudinal resolution dependence, by employing same manner, 335 keV/c is obtained. In consequence, ± 135 and ± 164 keV/c of systematic uncertainty associated with transverse and longitudinal resolutions are included in the deterioration on momemtum resolution.

10.2.3 Air Doping

Finally, let us consider the effect of the air doping. As mentioned in Section 5.5.3, during the engineering run 2007, a small amount of air has been doped into the COBRA-helium volume in order to avoid discharge on the drift-chamber high voltage point. It obviously causes a certain deterioration on the tracking accuracy. Figure 10.1(c) shows the momentum resolution as a function of helium concentration inside COBRA. In the run 2007, it was controlled to be 95.75 %; hatched region in this plot represents the variation of helium concentration during the engineering run.

Accoring to the result of this study, the momentum resolution is degraded to be 318 keV/c due to air contamination, *i.e.* ± 125 keV/c of uncertainty is included in the deterioration on

momemtum resolution.

10.2.4 Feasible Spectrometer Resolution

As shown in previous sections, sources of each systematic uncertainty are investigated. We here estimate the feasible resolution of the spectrometer.

MC(actual) successfully reproduced the degraded momentum resolution of 451 keV/c. This is roughly comparable with obtained resolution of 477 keV/c. However there is still a certain discrepancy, *i.e.* the quadratic difference, $477^2 - 451^2 = 155^2$, is outstanding uncertainty that may be caused by still missing something in MC.

In consequence, the feasible resolutions can be expected with two situations. First, if all the problems will be fixed, it can be conservatively expected to be "MC(ideal)" + "outstanding uncertainty", $\sqrt{297^2 + 155^2} = 335$ keV/c.

Second, if only the easy problems, cable connection and discharge, will be fixed, it can be pessimistically expected to be $\sqrt{477^2 - 249^2 - 125^2} = 387$ keV/c.

10.3 Possible Improvements

As described previously, if it is possible to improve the drift-chamber condition, better momentum resolution is available. In fact, it is really possible by fixing three main problems.

First of all, concerning the discharge problem, this discharge was caused at an exposed high voltage point on the chamber board that is in the helium atmosphere. In fact, such a point is molded with epoxy resin to avoid discharge. However, several chambers have weakness of this mold. By putting more resin comprehensively, this problem can be fixed [*]. Then, all the missing channels and bad channels associated with this problem will be cleared up.

Next, concerning the cable disconnecting problem, the most of such channels were caused by disconnection at the feed-through connector. This feed-through provides the interface between inward and outward of the COBRA magnet; all the signal, high voltage, power, and sensor cables are connected to this feed-through. In fact, for the signal and power cable connectors, they do not have a latch; connected cables are self-maintained. In the laboratory test, it worked without problem since it was not connected with whole cables and not tested for extended period. However, after we closed the end-cap flange of COBRA, some of them have been disconnected by own weight. Thus, this can be fixed by the modification of the feed-through connectors and cable handling.

Finally, concerning the DRS fake pulse, as described in Appendix A, fake pulse will vanish away in DRS4.

In consequence, ideally condition of the spectrometer will be available in the MEG physics run 2008.

---

[*]This was already confirmed in 2007-2008 winter shutdown.

10.4 The MEG Sensitivity

In the final Section of the Discussion Chapter, we here discuss the feasible sensitivity of the MEG experiment by using obtained performances and expected possible improvements for the MEG positron spectrometer.

10.4.1 Detector Performances

In order to evaluate the background, it should be listed the detector performances, resolutions and efficiencies. Table 10.2 summarize the obtained performences by the engineering run 2007 and the expected resolutions for the MEG physics run 2008. All resolutions are converted

Quantity	Enginering Run 2007	Physics Run 2008
e^+ Momentum Resolution (%)	2.2	1.5
e^+ Angular Resolution (mrad)	14.5	11.5
e^+ Timing Resolution (ps)	127	103
γ Energy Resolution (%)	-	5.0
γ Spacial Resolution (mm)	-	9.0
γ Timing Resolution (ps)	-	150
Acceptance (%)	9	9
e^+ Detection Efficiency (%)	43.8	63.9
γ Detection Efficiency (%)	-	>40
Muon Rate (sec^{-1})	3×10^7	3×10^7

Table 10.2: Detector Peformances (Obtained and Expected)

to Full-Width-at-Half-Maximum (FWHM), an momentum resolution is represented in the percentage, and then, angular resoultion is converted from degree to radian. The values of the positron spectrometer for the Engineering Run 2007 are obtained values, and its prospects for the Physics Run 2008 are derived from the MC investigation incorporating actual situation of the engineering run 2007 and the ideal condition of the physics run 2008. For the γ-ray detector, listed resolutions are expected by using engineering run data and results from the MC studies.

10.4.2 Backgrounds

Physics Background

The differential decay width of radiative muon dacay is calculated as a function of x, y, and z which is defined in Section 2.4.1. Given the detector resolutions, the sensitivity limitation from $\mu \to e\nu\nu\gamma$ decay can be evaluated by integrating the differential decay width over the resolutions, or more precisely, over the kinematic box region of the signal which is determined by the detecter resolutions. Let us take δx,δy, and δz to be the kinematic range of the signal region for positron energy ($1-\delta x \leq x \leq 1$), that for photon enegy ($1-\delta y \leq y \leq 1$), and that for the opening angle ($0 \leq z \leq \delta z$), respectively. The integration is done with consideration of the kinematics constraints among x, y, and z are small, the allowed range of z is therefore

138

determined to be $0 \leq z \leq 2\sqrt{(1-x)(1-y)}$, instead of δz. The partial branching ratio after the integration is given by [105]

$$
\begin{aligned}
\mathrm{d}\mathcal{B}(\mu \to \mathrm{e}\nu\bar{\nu}\gamma) &= \frac{1}{\Gamma(\mu \to \mathrm{e}\nu\bar{\nu})} \int_{1-\delta x}^{1} \mathrm{d}x \int_{1-\delta y}^{1} \mathrm{d}y \int_{0}^{\min\left[\delta z, 2\sqrt{(1-x)(1-y)}\right]} \mathrm{d}z \frac{\mathrm{d}\Gamma(\mu \to \mathrm{e}\nu\bar{\nu}\gamma)}{\mathrm{d}x\mathrm{d}y\mathrm{d}z} \\
&= \frac{\alpha}{16\pi} \Big[J_1(1 - P_\mu \cos\theta_\mathrm{e}) + J_2(1 + P_\mu \cos\theta_\mathrm{e}) \Big] \mathrm{d}(\cos\theta_\mathrm{e}),
\end{aligned}
\tag{10.1}
$$

where δx, δy and δz are a half width of the $\mu \to \mathrm{e}\gamma$ signal region for x, y and z, respectively, θ_e is the angle between the muon spin and the positron momentum direction, and $\Gamma(\mu \to \mathrm{e}\nu\bar{\nu})$ is the total muon decay width. J_1 and J_2 are given as the sixth power of a combination of δx and δy.

For the case of $\delta z > 2\sqrt{\delta x \delta y}$, where the upper bound of the z integration range is simply reduced to $2\sqrt{(1-x)(1-y)}$, J_1 and J_2 are given by

$$
J_1 = (\delta x)^4 (\delta y)^2, \quad J_2 = \frac{8}{3}(\delta x)^3 (\delta y)^3.
\tag{10.2}
$$

Figure 10.2(a) shows a sensitivity limitation of the branching ratio of $\mu \to \mathrm{e}\gamma$ imposed by $\mu \to$

(a) $\delta z > 2\sqrt{\delta x \delta y}$ (b) $\delta z < 2\sqrt{\delta x \delta y}$
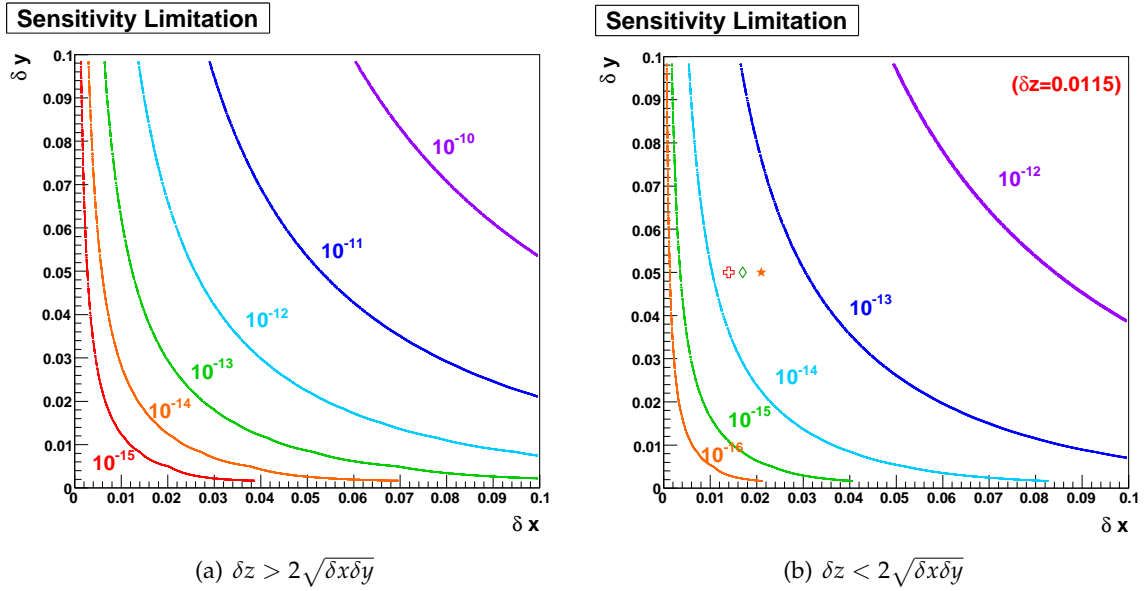
Figure 10.2: Sensitivity limitation of the branching ratio of $\mu \to \mathrm{e}\gamma$ imposed by $\mu \to \mathrm{e}\nu\nu\gamma$ decay

$\mathrm{e}\nu\nu\gamma$ decay as a function of δx and δy, for the case of unpolarized muons and $\delta z > 2\sqrt{\delta x \delta y}$.

If one could get a good angular resolution of δz, better than the kinematic ally allowed angle of $2\sqrt{\delta x \delta y}$, the z integration range should be properly taken into account. In such a case, the

distribution in Eq.(10.1) is given by

$$J_1 = \frac{8}{3}(\delta x)^3(\delta y)\left(\frac{\delta z}{2}\right)^2 - 2(\delta x)^2\left(\frac{\delta z}{2}\right)^4 + \frac{1}{3}\frac{1}{(\delta y)^2}\left(\frac{\delta z}{2}\right)^8,$$

$$J_2 = 8(\delta x)^2(\delta y)^2\left(\frac{\delta z}{2}\right)^2 - 8(\delta x)(\delta y)\left(\frac{\delta z}{2}\right)^4 + \frac{8}{3}\left(\frac{\delta z}{2}\right)^6. \tag{10.3}$$

Figure 10.2(b) shows a sensitivity limitation for the case of unpolarized muons and $\delta z < 2\sqrt{\delta x \delta y}$. This plot is calculated with the angular resolution of $\delta z = 0.0115$ which is listed in Table 10.2.

From Figure 10.2(b), one can see that, in order to achieve a sensitivity limit of a level of 10^{-15}, both δx and δy should be better than 0.02 even if one can have an excellent angular resolution.

Let us return from digression to our subject, MEG sensitivity. It is clear that the MEG apparatus satisfies the condition $\delta z \leq 2\sqrt{\delta x \delta y}$, i.e. by using values listed in Table 10.2 with Figure 10.2(b), or with Eq.(10.1) and Eq.(10.3), one can conclude that the contribution of **the physics background to the branching ratio is $< 1.4 \times 10^{-14}$ for the MEG physics run 2008**; plotted as a cross-mark in Figure 10.2(b). If only the easy problem will be fixed in the drift chamber, the physics background to the branching ratio is $< 2.9 \times 10^{-14}$; plotted as a diamond-mark. Same contribution can be calculated by the obtained resolution in the engineering run 2007, the physics background to the branching ratio is $< 4.5 \times 10^{-14}$; plotted as a star-mark. Even if all the problem will be not fixed, the physics background to the branching ratio can be eliminated successufully.

Accidental Background

Given the sizes of the signal region, the effective branching ratio of the accidental background $\mathcal{B}_{\text{acc}}$ Let us take δx, δy, $\delta\theta_{e\gamma}$ and $\delta t_{e\gamma}$ to be the half-width of the signal region for positron, γ energy, angle $\theta_{e\gamma}$, and relative timing between positron and γ, respectively. (Eq.(2.12)) can also be evaluated. We here are requested to estimate the partial branching ratio f_e^0 and f_γ^0. Then f_e^0 can be estimated by integrating the Michel spectrum of normal muon decay Eq.(9.2), which is the case of using unpolarized target of Eq.(2.7), over $1 - \delta x \leq x \leq 1$,

$$f_e^0 = \int_{1-\delta x}^1 dx \frac{d\Gamma}{dx} = \int_{1-\delta x}^1 dx\,(x^2(3-2x)) \approx 2(\delta x). \tag{10.4}$$

This evaluation integrates the theoretical Michel spectrum, however the Michel spectrum is smeared by finite resolutions of the detector. Thus, it is required to take into account the resolution effect to this evaluation. In Section 9.3.1, the response functions of the detector resolution are obtained for Data and MC, respectively. By using the obtained response functions, it is possible to count the number of event that is swept out from the signal region [1-δx;1] and is swept in from the background region [0,1-δx]. The fraction of these two numbers is evaluated to be 1.09, i.e. this effect is negligible.

On the other hand, given the angular resolution, $\delta\theta_{e\gamma}$, the back-to-back resolution $\Delta\omega_{e\gamma}/4\pi$ is given by $\Delta\omega_{e\gamma}/4\pi = \delta\theta_{e\gamma}^2/4$. As for f_γ^0, if the radiative muon decay $\mu \to e\nu\nu\gamma$ is considered as a source of the 52.8 MeV photon, it can be given by integrating the photon energy spectrum

within the width of the signal region $(1 - \delta y \leq y \leq 1)$. For unpolarized muons, it is given by [105]

$$f_\gamma^0 = \int_{1-\delta y}^{1} \mathrm{d}y \int \mathrm{d}(\cos\theta_\gamma) \frac{\mathrm{d}\mathcal{B}(\mu \to \mathrm{e}\nu\nu\gamma)}{\mathrm{d}y\,\mathrm{d}(\cos\theta_\gamma)} \approx \left(\frac{\alpha}{2\pi}\right)(\delta y)^2 \Big[\ln(\delta y) + 7.33\Big]. \qquad (10.5)$$

From Eq.(10.5), it is shown that f_γ^0 for $\mu^+ \to \mathrm{e}^+ \nu_e \bar{\nu}_\mu \gamma$ decay is roughly proportional to $(\delta y)^2$.

The other sources of high-energy photons are annihilation in flight of positron from the Michel decay and external bremsstrahlung. The contribution from annihilation of positron in flight depends on the materials along the positron track path; this is estimated by **megmc** incorporating all the material information. And then, it is confirmed that the contribution from annihilation in flight is less than the radiative muon decay.

From the above discussion, (Eq.(2.12), Eq.(10.4), and Eq.(10.5)), the effective branching ratio of accidental background is given by

$$\mathcal{B}_{acc} = \mathcal{R}_\mu \cdot (2\delta x) \cdot \left[\frac{\alpha}{2\pi}(\delta y)^2 \big(\ln(\delta y) + 7.33\big)\right] \times \left(\frac{\delta\theta^2}{4}\right) \cdot (2\delta t). \qquad (10.6)$$

Figure 10.3(a) shows the effective branching ratio of accidental background as a function of

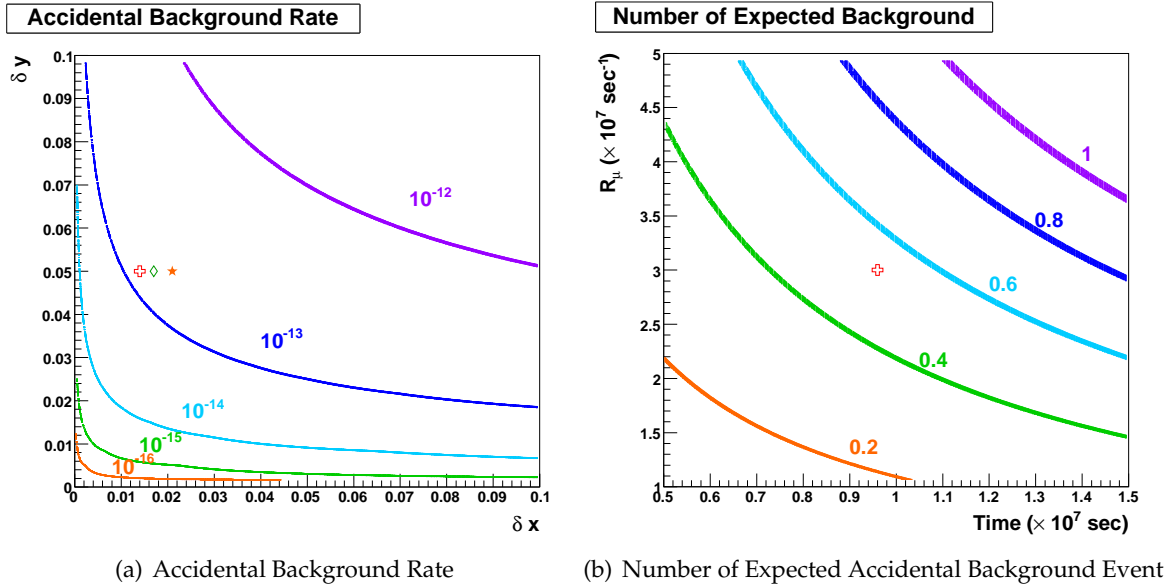(a) Accidental Background Rate   (b) Number of Expected Accidental Background Event

Figure 10.3: Accidental Background Estimation

δx and δy. By employing the expected performance that is quoted in Table 10.2, **accidental background rate for the MEG physics run 2008 can be evaluated to be 1.3×10^{-13}**, as plotted as a cross-mark in Figure 10.3(a). If only the easy problem will be fixed in the drift chamber, the accidental background is evaluated to be 1.6×10^{-13}; plotted as a diamond-mark. It is also possible to calculate the accidental background by the obtained resolution in the engineering run 2007, it is evaluated to be 2.0×10^{-13}; plotted as a star-mark.

Obtained background rate is larger than the radiative muon decay, and it is close to the aiming sensitivity. Then, let us evaluate the number of background event. As shown in next section, by assuming other two parameters, experiment-running time T and muon-beam intensity $\mathcal{R}_\mu$, the single event sensitivity can be evaluated. By using this single event sensitivity with obtained background rate, we can estimate the number of background; Figure 10.3(b) shows the number of expected background event as a function of T and $\mathcal{R}_\mu$.

We are planning to have 24-weeks of beamtime in 2008; according to the PSI proton-accelerator operation procedure, 24-weeks beamtime is corresponding to 9.6×10^6 sec. By employing these numbers with expected beam intensity, 3×10^7 sec^{-1}, as plotted as a cross-mark in Figure 10.3(b), **the number of background event for the MEG physics run 2008 is expected to be 0.59 .** If only the easy problem will be fixed in the drift chamber, the number of background event is evaluated to be 0.73. It is also possible to calculate the accidental background by the obtained resolution in the engineering run 2007, it is evaluated to be 0.90.

10.4.3 Sensitivity

Finally, let us evaluate the single event sensitivity and the feasible upper limit that will be determined by physics run 2008. The single event sensitivity for the MEG experiment is given by

$$\mathcal{B}(\mu^+ \to e^+\gamma) = \frac{1}{\mathcal{R}_\mu \cdot T \cdot (\Omega/4\pi)} \times \frac{1}{\epsilon_e \cdot \epsilon_\gamma \cdot \epsilon_{\text{sel}}}, \tag{10.7}$$

where $\Omega/4\pi$ is detector solid angle, ϵ_e, ϵ_γ are detection efficiencies for positron and γ ray while ϵ_{sel} denotes the efficiency of event selection. By putting expected positron-detection efficiency $\epsilon_e = 63.9$ % , expected γ-ray detection efficiency $\epsilon_\gamma = 40$ %, possible selection efficiency $\epsilon_{\text{sel}} = 70$ %, muon-beam intensity $\mathcal{R}_\mu = 3 \times 10^7$, experiment-running time $T = 9.6 \times 10^6$, and detector solid angle $\Omega/4\pi = 0.09$ that is calculated from the detector geometrical acceptance, **the single event sensitivity for the MEG physics run 2008 can be evaluated as**

$$\mathcal{B}^{2008}(\mu^+ \to e^+\gamma) = 2.2 \times 10^{-13}.$$

Finally, we now have all parameters to calculate the confidence interval by adopting the unified Feldman-Cousins approach [106], for a Poisson-distributed signal over an expected background of 0.5 events. In case of no candidate observed, 2.2×10^{-13} single event sensitivity implies **the upper limit on $\mathcal{B}^{2008}(\mu^+ \to e^+\gamma)$ at the 90 % Confidence Level as**

$$\mathcal{B}^{2008}(\mu^+ \to e^+\gamma) < 6.5 \times 10^{-13} \ (90\% \ C.L.)$$

for the MEG physics run 2008. If only the easy problem will be fixed in the drift chamber, expected upper limit is 7.4×10^{-13}. It is also possible to calculate the upper limit by the obtained resolution in the engineering run 2007, it is evaluated to be 9.8×10^{-13}.

Chapter 11

Conclusion

In the MEG experiment, in order to achieve unprecedented sensitivity, we have developed an innovative positron spectrometer comprising a highly graded magnetic field, ultimate low-mass drift chambers and fast timing counters. This positron spectrometer is required to be operational with high intensity muon beam without losing the detector resolutions. Furthermore, this spectrometer necessarily consists of only light material in order to avoid the background generation to the γ-ray detector. In consequence, the detector design and constcution have been very challenging.

Assembly, Construction, and Installation of the spectrometer have been completed in the summer 2007, and the engineering run has been performed in late 2007.

The drift chamber and the timing counter have been operated in the COBRA field and controlled successfully. The drift chamber has been operational with 3×10^7 sec^{-1} muon-beam intensity thanks to the COBRA field.

We established all the calibration procedure for the spectrometer and completed it, and then, we collected more than 5 M Michel decay events. After all the calibration run, the MEG event trigger has been tested. And then, by employing this trigger, the radiative muon decay events has been acquired. By analyzing engineering run data, we conclude that the positron spectrometer could achieve 0.9 % of momentum resolution and 6 mrad of angular resolution in σ for 52.8MeV/c positron at the maximum muon-beam intensity, even though the spectrometer has been not conditioned well.

We have developed fully-equipped Monte Calro simulation and event reconstruction program within the single software package. And then, we performed precise Monte Calro simulation incorporating actual detector conditions for the engineering run; all obtained resolutions in run 2007 are reproduced successfully. Finally, by incorporating ideally conditioned spectrometer with this MC simulation, 0.5 % of momentum resolution and 4 mrad of angular resolution are obtained.

We verified that this innovative positron spectrometer can provide excellent performances for the MEG experiment to explore the $\mu \rightarrow e\gamma$ decay with an unprecedented sensitivity. Even only 24-weeks physics run in 2008, it can achieve the upper limit of 6.5 $\times 10^{-13}$(90%C.L.) improved by two orders of magnitude over the current best limit. Even the bad conditioned chambers in the engineering run 2007 can reach a sensitivity below 10^{-12}.

Appendix A

DRS Fake Pulse

For the engineering run 2007, we used DRS2 as the waveform sampler (*cf.* Section 3.5.2). In fact, this version of DRS has a problem so that the recorded waveform sometimes contains an unreal pulse, called "fake pulse" [58].

This phenomenon is caused by the architectural reason of the DRS2, *i.e.* this fake pulse is inevitable. Figure A.1(a) shows a typical example of the fake pulse. As one can see in this figure, the pulse height is not so high (2-3 mV), *i.e.* the anode pulse is not affected so much since the anode pulse height is much higher than it. However, the cathode pulse height is sometimes comparable with the fake pulse since the cathode pulse possibly decreases much due to vernier pattern. Figure A.1(b) is an example that the cathode pulse is overlapped with

(a) Fake Pulse Example (b) Fake Pulse with a Cathode Signal Pulse
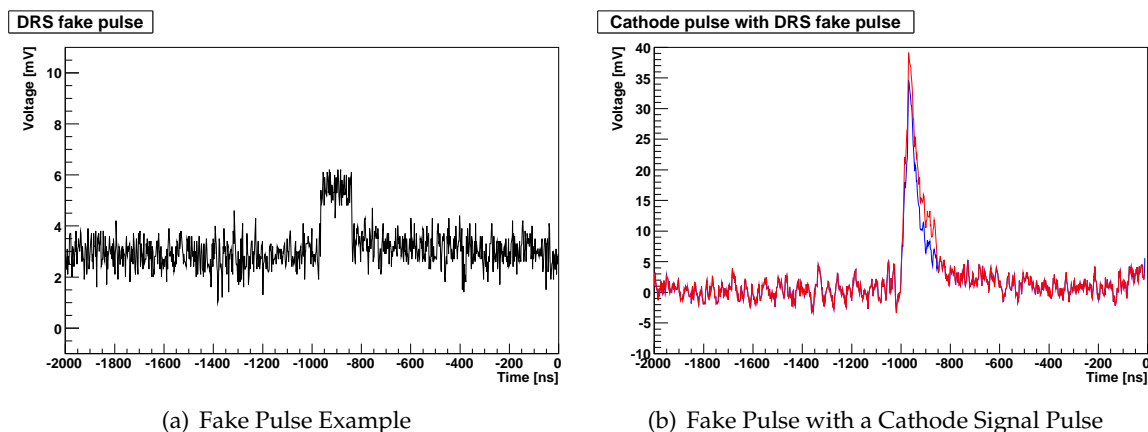
Figure A.1: DRS Fake Pulse

the fake pulse; the blue pulse shows the cathode pulse without fake, and the red pulse contains the fake. As one can see in this display, the fake-pulse effect to the z reconstruction by the vernier-pad method is indispensable.

This fake pulse is caused by a temperature dependence of the DRS2 chip. When the DRS2 chip is heated up, the response function is deviated from the ideal response. This is due to

the fact that the current passing through the individual transistors in the Domino cells has a strong temperature dependence. Due to this issue, the response calibration is required to be performed at frequent intervals, and then, the deterioration can be suppressed at a certain level. Even though such a calibration applied frequently, another problem still remains. If the chip is triggered with a different frequency from the one used to calibrate the chip, the response function is deviated again. The change of voltage level is almost uniform over all 1024 sampling cells except for the last 64 cells. Due to architectural circumstanse of the DRS2, these 64 cells have a strong frequency dependence, and then, these cells cause the fake pulse, as shown in Figure A.1(a). Thus, this square pulse has a fixed width corresponding to 64 cells.

This fake pulse can be solved by replacing the transistor by a differential pair of transistors; this modification is done on the head version of DRS, "DRS4". The DRS4 will be supplied in the summer 2008 and integrated with the MEG DAQ system immediately.

Appendix B

Bad Channels (2007)

B.1 List of Bad Channels

Module	Description	Channel Identification	Comment
DC00A	cell 0 : 1 anode lost	dc00Aa0u	disconnection
	cell 6 : 1 cathode lost	dc00Ac6uh	disconnection
DC00B	all OK		
DC01A	all off		HV off (discharge)
DC01B	cell 1 : both anode lost	dc01Ba1u/d	disconnection
DC02A	cell 0 : 1 cathode lost	dc02Ac0dc	disconnection
	cell 3 : 1 cathode low gain	dc02Ac3uc	preamp malfunction
DC02B	cell 0 : 1 cathode lost	dc02Bc0uc	disconnection
	cell 8 : 1 cathode lost	dc02Bc8dh	disconnection
DC03A	cell 1 : 1 cathode lost	dc03Ac1dh	disconnection
	cell 4 : low efficiency	dc03Aa4u/d	bad contact
	cell 6 : 1 anode lost	dc03Aa6u	disconnection
DC04A	all OK		
DC04B	all OK		
DC05A	all OK		
DC05B	all OK		
DC06A/B	all off		LV disconnection
DC07A	all OK		
DC07B	all OK		
DC08A	cell 3 : 1 cathode low gain	dc08Ac3dh	preamp malfunction
DC08B	all OK		

Table B.1: List of Dead/Bad Channels in 2007 (DC00-DC08)

Module	Description	Channel Identification	Comment
DC09A	all OK		
DC09B	all OK		
DC10A	all OK		
DC10B	all OK		
DC11A	all OK		
DC11B	cell 1 : 1 cathode lost	dc11Bc1uh	disconnection
	cell 3 : 1 cathode lost	dc11Bc3uh	disconnection
	cell 6 : 1 cathode lost	dc11Bc6dc	disconnection
	cell 7 : 1 cathode lost	dc11Bc7dc	disconnection
	cell 8 : all cathode noisy	dc11Bc8a/c	bad contact
DC12A	cell[5-8] low efficiency	-	bad contact
DC12B	cell 0 : anode huge pulse	dc12Ba0u	preamp malfunction
	cell[1-8] :very low efficiency	-	bad contact
DC13A	cell 5 : 1 cathode lost	dc13Ac5uh	disconnection
	cell 6 : 1 cathode lost	dc13Ac6dh	disconnection
DC13B	cell 0 : 1 cathode lost	dc13Bc0dh	disconnection
	cell 2 : all cathode noisy	-	bad contact
	cell 7 : 2 cathodes lost	dc13Bc7uh/dh	disconnection
DC14A	cell 1 : 1 cathode lost	dc14Ac1dh	disconnection
	cell 6 : 1 cathode lost	dc14Ac6dh	disconnection
DC14B	cell 1 : 1 cathode lost	dc14Bc1uc	disconnection
	cell 3 : 1 cathode lost	dc14Bc3uh	disconnection
	cell 4 : 1 cathode lost	dc14Bc4dc	disconnection
	cell 6 : 1 cathode lost	dc14Bc6dc	disconnection
	cell 8 : 1 cathode lost	dc14Bc8uh	disconnection
DC15A	cell 1 : 1 cathode lost	dc15Ac1uh	disconnection
	cell 2 : all cathode noisy	-	bad contact
	cell 5 : 1 cathode lost	dc15Ac5uh	disconnection
DC15B	cell 6 : noisy baseline	dc15Bc6dc	preamp malfunction
	cell 7 : noisy baseline	dc15Bc7dc	preamp malfunction
	cell 8 : noisy baseline	dc15Bc8dc	preamp malfunction

Table B.2: List of Dead/Bad Channels in 2007 (DC09-DC15)

If one cell lost an anode channel, this cell was disabled since only one side of anode wire can not provide z measurement with a reasonable accuracy. Such cells are referred as "dead channel" in this thesis. DC01A, DC06A and DC06B were completely turned off due to discharge problem and disconnecting power cable. They are also referred as "dead channel". Several cells lost a cathode channel out of four pads associated with one cell. In principle, such cells can reconstruct the hit position along z, however the spacial resolution must be bad. Such cells are referred as "bad channel" in this thesis. In addition, other several cells had bad contacts or bad preamplifier channels. Such channels are also referred as "bad channel" in this thesis.

B.2   Map of Bad Channels

Figure B.1(a) shows the map of bad channels for the engineering run 2007. Figure B.1(b) shows same map with real hits of the data which was acquired by the Michel trigger with $3 \times 10^7 \, \text{sec}^{-1}$ muon intensity.

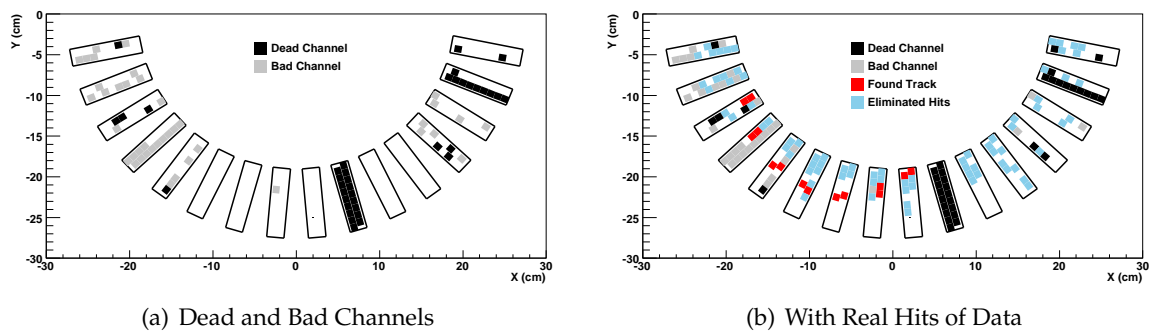
(a) Dead and Bad Channels   (b) With Real Hits of Data

Figure B.1: Map of Dead/Bad Channels (2007)

From Figure B.1(b), one can see that the track finding and track fitting are affected by missing channels seriously.

Appendix C

Kalman Filter and Its Application to the Track Fitting

C.1 Overview

The Kalman filter is an algorithm that processes measurements to deduce an optimum estimate of the past, present, or future state of a dynamic system by using a time sequence of measurements of the system behaviour, plus a statistical model that characterizes the system and measurements errors, plus initial condition information.

The Kalman filter addresses the general problem of trying to estimate at different points ($1 \leq k \leq n$) the state x_k of a discrete process that is governed by the linear stochastic difference equation

$$x_k = \mathbf{F}_{k-1} x_{k-1} + w_{k-1} \tag{C.1}$$

with a measurement m_k that is given by

$$m_k = \mathbf{H} x_k + \epsilon_k. \tag{C.2}$$

where $\mathbf{F_k}$ is a transport matrix from "$k-1$"-th measurement to "k"-th measurement with a process noise w_k, and $\mathbf{H_k}$ is a transport matrix between the measurement m_k and state x_k with a measurement error ϵ_k.

The system equation (C.1) is not deterministic since the track experiences stochastic processes such as multiple scattering, bremsstrahlung, *etc.* These processes are taken into account by the process noise w_k. w_k and ϵ_k are assumed to be independent of each other with zero expectation values:

$$E\{w_k\} = 0, \quad \text{cov}\{w_k\} = \mathbf{Q}_k, \quad 1 \leq k \leq n,$$
$$E\{\epsilon_k\} = 0, \quad \text{cov}\{\epsilon_k\} = \mathbf{V}_k, \quad 1 \leq k \leq n,$$

where $\mathbf{Q}_k$ and $\mathbf{V}_k$ are process noise and measurement noise covariances, respectively.

Eq.(C.1) in the absence of the last term is the standard equation of motion with a propagator $\mathbf{F}_{k-1}$ (transport matrix). Note that at the moment $\mathbf{F}_{k-1}$ is assumed to be constant.

Regarding a track in space as a dynamic system the filtering technique is applied to the track fitting. For example, in the case of a particle moving in magnetic field this can be done

naturally by identifying the state vector x_k of the dynamic system with a vector

$$x_k = (x, y, \tan\theta_x, \tan\theta_y, 1/p_L)$$

of five parameters uniquely describing the track at each point of the trajectory. The **F** matrix propagates the state vector on one plane to the state vector on the next plane combining position information with directional information. The transport matrix implicitly contains information about a gap between planes.

In general the set of parameters x_k is not measured directly; only a function of x_k, $\mathbf{H}x_k$, is observed. For example, in the case of the transverse tracker one does not measure x_k but $x\prime = x\cos\alpha + y\sin\alpha$ in the chamber coordinate system which corresponds to

$$\mathbf{H} = (\cos\alpha, \sin\alpha, 0, 0, 0). \tag{C.3}$$

There are three types of operations to be performed in the analysis of a track fitting by Kalman Filter.

- **Prediction** is the estimation of the "future" state vector at position "k" using all the "past" measurements up to and including "$k-1$". State x_k^{k-1} is a prediction (*a priori* state estimation).

- **Filtering** is the estimation of the state vector at position "k" based upon all "past" and "present" measurements up to and including "k". x_k^k is a filtered state vector (*a posteriori* state estimation).

- **Smoothing** is the estimation of the "past" state vector at position "k" based on all "n" measurements taken up to the present time. x_k^n is a smoothed state vector.

C.2   Prediction

The first step to estimate x_k is the prediction (time update):

$$x_k^{k-1} = \mathbf{F}_{k-1} x_{k-1}^{k-1}, \tag{C.4}$$

$$\mathbf{C}_k^{k-1} = \mathbf{F}_{k-1}\mathbf{C}_{k-1}^{k-1}\mathbf{F}_{k-1}^T + \mathbf{Q}_{k-1}, \tag{C.5}$$

where Eq.(C.4) projects the state ahead and Eq.(C.5) projects the error covariance ahead, $\mathbf{C}_k^{k-1}$ is covariance matrix at "k"-th position predicted by "$k-1$"-th state.

C.3   Filtering

The filtered estimate (measurement update) x_k^k is calculated as a weighted mean of the prediction and the observation:

$$\mathbf{K}_k = \mathbf{C}_k^{k-1}\mathbf{H}_k^T[\mathbf{H}_k\mathbf{C}_k^{k-1}\mathbf{H}_k^T + \mathbf{V}_k]^{-1}. \tag{C.6}$$

This matrix is called the **Kalman Gain Matrix** defining the correction to the predicted state due to the current observation. By using this Kalman Gain Matrix, the prediction Eq.(C.4) can be updated as

$$x_k^k = x_k^{k-1} + \mathbf{K}_k[m_k - \mathbf{H}_k x_k^{k-1}], \tag{C.7}$$

and the error covariance is also updated by

$$\mathbf{C}_k^k = [\mathbf{I} - \mathbf{K}_k \mathbf{H}_k]\mathbf{C}_k^{k-1}. \tag{C.8}$$

The error covariance may be also expressed in a computationally superior form

$$\mathbf{C}_k^k = [\mathbf{I} - \mathbf{K}_k \mathbf{H}_k]\mathbf{C}_k^{k-1}[\mathbf{I} - \mathbf{K}_k \mathbf{H}_k]^T + \mathbf{K}_k \mathbf{V}_k \mathbf{K}_k^T. \tag{C.9}$$

The filtering is a recursive operation. The prediction step and the filtering step are repeated for the next plane proceeding progressively from plane "1" to plane "n". The state vector at the last filtered point contains always the full information from all points.

At each step one can calculate the filtered residuals r_k^k, the covariance matrix of the filtered residuals $\mathbf{R}_k^k$ and the filtered χ^2:

$$r_k^k = m_k - \mathbf{H}_k x_k^k,$$

$$\mathbf{R}_k^k = \mathbf{V}_k - \mathbf{H}_k \mathbf{C}_k^k \mathbf{H}_k^T,$$

$$\chi_k^2 = r_k^{kT}(\mathbf{R}_k^k)^{-1}r_k^k,$$

where χ_k^2 is χ^2 - distributed with dim(m_k) degrees of freedom. The total χ^2 of the track is given by the sum of the χ_k^2 contributions for each plane.

The system of equations defining the Kalman filter represents an asymptotically stable system, and thus, the estimate of the state vector x_k^k becomes independent on the starting point x_0^0, $\mathbf{C}_0^0$ as k is increased.

C.4   Smoothing

When the last plane (n-th) is taken into account the Kalman filter performs the final step, called smoothing. The filter runs backward in time updating all filtered state vectors on the basis of information from all n planes. The equations describing **smoothing** are given by

$$\mathbf{A}_k = \mathbf{C}_k^k \mathbf{F}_k^T (\mathbf{C}_{k+1}^k)^{-1}.$$

Thus $\mathbf{A}_k$ represents "smoother" for the "k"-th state, and by using this smoother, smoothed "k"-th state is described by

$$x_k^n = x_k^k + \mathbf{A}_k(x_{k+1}^n - x_{k+1}^k),$$

where superscript n indicates that it is smoothed by using all measurements 1 to n. By the same token, smoothed covariances and residuals are given by

$$\mathbf{C}_k^n = \mathbf{C}_k^k + \mathbf{A}_k(\mathbf{C}_{k+1}^n - \mathbf{C}_{k+1}^k)\mathbf{A}_k^T,$$

$$r_k^n = m_k - \mathbf{H}_k x_k^n,$$

$$\mathbf{R}_k^n = \mathbf{V}_k - \mathbf{H}_k \mathbf{C}_k^n \mathbf{H}_k^T.$$

So far it was assumed that the problem of estimation of a discrete-time process is described by a linear stochastic differential equation. For example, however, in the presence of a magnetic field the track propagator $\mathbf{F}$ is non-linear. Let's assume that the process of a particle propagation is governed by the non-linear stochastic differential equation

$$x_k = f(x_{k-1}) + w_{k-1} \tag{C.10}$$

with a measurement m in the form Eq.(C.2); f is a non-linear function. The Kalman filter can be applied to this system by linearizing the system, *e.g.* about the estimated trajectory. If deviations between the estimated trajectory and the actual trajectory remain sufficiently small the linear approximation is valid. The non-linear equation (C.10) can be written down in the linearized form as

$$x_k = \mathbf{f}(x_{k-1}^{k-1}) + \mathbf{F} \cdot (x_{k-1} - x_{k-1}^{k-1}) + w_{k-1} \tag{C.11}$$

where as before x_k, m_k are the actual state and measurement vectors, x_k^k is a filtered estimate of the state at step k. $\mathbf{F}$ is Jacobian matrix

$$\mathbf{F} = \frac{\partial \mathbf{f}_i(x_{k-1}^{k-1})}{\partial x_j}. \tag{C.12}$$

Therefore the complete set of extended Kalman filter equations is given by Eqs.(C.5)-(C.8),(C.11) by using $\mathbf{F}$ in the form (C.12).

In order to apply the extended Kalman filter to a track fitting for a particle moving in the magnetic field (the magnetic field is in z direction) one has to choose the state vector parameters, define the initial state vector and calculate the transport matrix $\mathbf{F}$, the projection matrix $\mathbf{H}$, and the noise matrix $\mathbf{Q}$. As it was mentioned above in this case the state vector can be chosen in the form $x_k = (x, y, t_x, t_y, 1/p_L)$ where x, y are the track coordinates in the tracker system, $t_x = p_x/p_L$, $t_y = p_y/p_L$ define the track direction. The projection matrix $\mathbf{H}$ is given by Eq.(C.3). Due to multiple scattering the absolute value of electron momentum remains unaffected, while the direction is changed. This deflection can be described using two orthogonal scattering angles, which are also orthogonal to the particle momentum. In terms of these variables the noise matrix is given by

$$\mathbf{Q}_k = \langle \theta^2 \rangle (t_x^2 + t_y^2 + 1) \begin{pmatrix} 0 & 0 & 0 & 0 & 0 \\ 0 & 0 & 0 & 0 & 0 \\ 0 & 0 & t_x^2+1 & t_x t_y & t_x/p_L \\ 0 & 0 & t_x t_y & t_y^2+1 & t_y/p_L \\ 0 & 0 & t_x/p_L & t_y/p_L & \frac{(t_x^2+t_y^2)}{p_L^2(t_x^2+t_y^2+1)} \end{pmatrix}. \tag{C.13}$$

For the variance of the multiple scattering angle the well-known expression [104]

$$\langle \theta^2 \rangle = (13.6 MeV/p)^2 \frac{[1 + 0.038 \ln(t/X_0)]t}{X_0} \tag{C.14}$$

is used, where X_0 is a radiation length, t is a distance traveled by the particle inside a scattering medium. In addition, energy losses are taken into account by

$$p\prime = p - \left\langle \frac{\mathrm{d}E}{\mathrm{d}x} \right\rangle t. \tag{C.15}$$

Bibliography

[1] T. Mori *et.al.* (MEG Collaboration). Search for $\mu^+ \rightarrow e^+ \gamma$ down to 10^{-14} branching ratio, 1999. (Research Proposal to Paul Scherrer Institut, R-99-05).

[2] M. L. Brooks *et.al.* (MEGA Collaboration). New limit for the family-number non-conservating decay $\mu^+ \rightarrow e^+ \gamma$. *Phys. Rev. Lett.*, Vol. 83, pp. 1521–1524, 1999. [arXiv:hep-ex/9905013].

[3] L. Calibbi *et.al.* Lepton flavor violation from supersymmetric grand unified tehories: Where do we stand for MEG, PRISM/PRIME, and a super flavor factory. *Phys. Rev. D*, Vol. 74, p. 116002, 2006.

[4] S. Neddermeyer and C. Andeerson. Note on the Nature of Cosmic-Ray Particles . *Phys. Rev.*, Vol. 51, pp. 884–886, 1937.

[5] C. S. Wu. *Muon Physics*. Academic Press Inc., 1975.

[6] W. Fetscher and H. J. Gerber. *Precision Tests of The Standard Electroweak Model*, Vol. 14 of *Advanced Series on Directions in High Energy Physics*, chapter 5: A. Precision Measurements in Muon and Tau Decays, pp. 657–705. World Scientific Publishing Co. Ltd., 1995.

[7] R. R. Crittenden *et.al.* Radiative Decay Modes of the Muon. *Phys. Rev.*, Vol. 121, pp. 1823–1832, 1961.

[8] W. Bertl *et.al.* Search for the decay $\mu^+ \rightarrow e^+ e^+ e^-$. *Nucl. Phys. B*, Vol. 260, pp. 1–31, 1985.

[9] S. Freedman *et.al.* Limits on neutrino oscillations from $\overline{\nu_e}$ appearance. *Phys. Rev. D*, Vol. 47, pp. 811–829, 1993.

[10] U. Bellgardt *et.al.* Search for the decay $\mu^+ \rightarrow e^+ e^+ e^-$. *Nucl. Phys. B*, Vol. 299, pp. 1–6, 1988.

[11] D. R. Bolton *et.al.* Search for rare muon decays with the Crystal Box detector. *Phys. Rev. D*, Vol. 38, pp. 2077–2101, 1985.

[12] Particle Data Group. Review of Particle Physics. `http://pdg.lbl.gov`.

[13] D. Počanić. Study of pion structure through precise measurements of the $\pi^+ \rightarrow e^+ \nu \gamma$ decay. Presented at 5th International Workshop on Chiral Dynamics (CD2006), Durham, USA, September 2006; Proceedings will be published by World Scientific Co., Ltd.

[14] L. Michel. Interaction between Four Half-Spin Particles and the Decay of the μ-Meson. *Proc. Phys. Soc. A*, Vol. 63, pp. 514–531, 1950.

[15] A. Lenard. Inner Bremsstrahlung in μ-Meson Decay. *Phys. Rev.*, Vol. 90, pp. 968–973, 1953.

[16] C. Fronsdal and H. Überall. μ-Meson Decay with Inner Bremsstrahlung. *Phys. Rev.*, Vol. 113, pp. 654–657, 1959.

[17] T. Kinoshita and A. Sirlin. Radiative Decay of the Muon. *Phys. Rev. Lett.*, Vol. 2, pp. 177–178, 1959.

[18] S. Eckstein and R. Pratt. Radiative muon decay. *Ann. Phys.*, Vol. 8, pp. 297–309, 1959.

[19] W. Eichenberger *et.al.* Measurement of the parameter $\bar{\eta}$ in the radiative decay of the muon as a test of the V-A structure of the weak interaction. *Nucl. Phys. A*, Vol. 412, pp. 523–533, 1984.

[20] S. Bilenky *et.al.* Lepton mixing, $\mu \to e\gamma$ decay and neutrino oscillations. *Phys. Lett. B*, Vol. 67, pp. 309–312, 1977.

[21] E.W. Kolb and M.S. Turner. *The Early Universe*. Addison Wesley, 1990.

[22] T.P. Cheng and L.F. Li. $\mu \to e\gamma$ in Theories with Dirac and Majorana Neutrino-Mass Terms. *Phys. Rev. Lett.*, Vol. 45, pp. 1908–1911, 1980.

[23] J. L. Hall *et.al.* New flavor violations in supergravity models. *Nucl. Phys.*, Vol. B 267, pp. 415–432, 1986.

[24] F. Gabbiani *et.al.* A Complete analysis of FCNC and CP constraints in general SUSY extensions of the standard model. *Nucl. Phys. B*, Vol. 477, pp. 321–352, 1996. [arXiv:hep-ph/9604387].

[25] R. Barbieri and L.J. Hall. Signals for supersymmetric unification. *Phys. Lett. B*, Vol. 338, pp. 212–218, 1994.

[26] R. Barbieri, L.J. Hall and A. Strumia. Violations of lepton flavour and CP in supersymmetric unified theories. *Nucl. Phys. B*, Vol. 445, pp. 219–251, 1995.

[27] J. Hisano *et.al.* Lepton-flavor violation in the supersymmetric standard model with seesaw-induced neutrino masses. *Phys. Lett. B*, Vol. 357, pp. 579–587, 1995.

[28] J. Hisano *et.al.* Lepton-flavor violation via right-handed neutrino Yukawa couplings in the supersymmetric standard model. *Nucl. Phys. B*, Vol. 445, pp. 219–251, 1996.

[29] J. Hisano *et.al.* Enhancement of $\mu \to e\gamma$ in the supersymmetric SU(5) GUT at large $\tan \beta$. *Phys. Rev. D*, Vol. 58, p. 116010, 1998.

[30] J. Hisano *et.al.* Atmospheric neutrino oscillation and large lepton-flavour violation in the SUSY SU(5) GUT. *Phys. Lett. B*, Vol. 437, pp. 351–358, 1998. [arXiv:hep-ph/9711348].

[31] L. Wolfenstein. Neutrino oscillations in matter. *Phys. Rev. D*, Vol. 17, pp. 2369–2374, 1977.

[32] J. N. Bahcall. *Neutrino Astrophysics*. Cambridge University Press, 1988.

[33] S. Fukuda *et.al.* (Super-Kamiokande Collaboration). Solar ^{8}B and hep Neutrino Measurements from 1258 Days of Super-Kamiokande Data. *Phys. Rev. Lett.*, Vol. 86, pp. 5651–5655, 2001. [arXiv:hep-ex/0103032].

[34] K. Eguchi *et.al.* (KamLAND Collaboration). First Results from KamLAND: Evidence for Reactor Antineutrino Disappearance. *Phys. Rev. Lett.*, Vol. 90, p. 021802, 2003. [arXiv:hep-ex/0212021].

[35] Q. R. Ahmad *et.al.* (SNO Collaboration). Measurement of day and night neutrino energy spectra at SNO and constraints on neutrino mixing parameters. *Phys. Rev. Lett.*, Vol. 89, p. 011302, 2002. [arXiv:nucl-ex/0204009].

[36] J. N. Bahcall and C. Peña-Garay. A road map to solar neutrino fluxes, neutrino oscillation parameters, and tests for new physics. *JHEP*, Vol. 11, p. 004, 2003. [arXiv:hep-ph/0305159].

[37] Y. Kuno and Y. Okada. Muon decay and physics beyond the standard model. *Rev. Mod. Phys.*, Vol. 73, pp. 151–202, 2001. [arXiv:hep-ph/9909265].

[38] G. Feinberg. Decays of the μ Meson in the Intermediate-Meson Theory. *Phys. Rev.*, Vol. 110, pp. 1482–1483, 1958.

[39] E. Hincks and B. Pontecorvo. Search for Gamma-Radiation in the 2.2-Microsecond Meson Decay Process . *Phys. Rev.*, Vol. 73, pp. 257–258, 1948.

[40] G. Danby *et.al.* Observation of High-Energy Neutrino Reactions and the Existence of Two Kinds of Neutrinos. *Phys. Rev. Lett.*, Vol. 9, pp. 36–44, 1962.

[41] A. van der Schaaf *et.al.* A search for the decay $\mu^+ \rightarrow e^+\gamma$. *Nucl. Phys. A*, Vol. 340, pp. 249–270, 1980.

[42] P. Depommier *et.al.* New Limit on the Decay $\mu^+ \rightarrow e^+\gamma$. *Phys. Rev. Lett.*, Vol. 39, pp. 1113–1116, 1977.

[43] W. W. Kinnison *et.al.* Search for $\mu^+ \rightarrow e^+\gamma$. *Phys. Rev. D*, Vol. 25, pp. 2846–2868, 1982.

[44] C. J. Oram *et.al.* Commissioning of a new low energy $\pi - \mu$ channel at TRIUMF. *Nucl. Instr. Meth.*, Vol. 179, pp. 95–103, 1980.

[45] J. H. Brewer. μ^+ SR with surface muon beams. *Hyperfine Interactions*, Vol. 8, pp. 831–834, 1981.

[46] Beam Line Studies for the MEG Experiment. PSI-Scientific Report 2002.

[47] Beam Line Development for the MEG Experiment. PSI-Scientific Report 2003.

[48] Evonik Degussa GmbH. `http://www.degussa.com`.

[49] S. Mihara. R&D work on a liquid-xenon photon detector for MEG experiment at PSI. *Nucl. Instr. Meth. A*, Vol. 518, pp. 45–48, 2004.

[50] A. Baldini *et.al.* Liquid xenon scintillation calorimetry and Xe optical properties. *IEEE trans. on Dielect. and Electr. Insul.*, Vol. 13, pp. 547–555, 2006. [arXiv:physics/0401072].

[51] S. Mihara *et.al.* Development of a liquid-xenon photon detector – towards the search for a muon rare decay mode at Paul Scherrer Institute. *Cryogenics*, Vol. 44, pp. 223–228, 2004.

[52] T. Doke *et.al.* Development of a Liquid xenon scintillation detector for a new experiment to search for $\mu \rightarrow e\gamma$ decay. *Nucl. Instr. Meth. A*, Vol. 505, pp. 199–202, 2003.

[53] A. Baldini *et.al.* Absorption of scintillation light in a 100 ℓ liquid xenon γ-ray detector and expected detector performance. *Nucl. Instr. Meth. A*, Vol. 545, pp. 753–764, 2005. [arXiv:physics/0407033].

[54] S. Mihara *et.al.* Development of a method for liquid xenon purification using a cryogenic centrifugal pump. *Cryogenics*, Vol. 46, pp. 688–693, 2006.

[55] R. Sawada. Liquid xenon gamma ray detector for MEG. *Nucl. Instr. Meth. A*, Vol. 581, pp. 522–525, 2007.

[56] S. Ritt. The DRS chip: cheap waveform digitizing in the GHz range. *Nucl. Instr. Meth. A*, Vol. 518, pp. 470–471, 2004.

[57] S. Ritt. The DRS2 chip: a 4.5 GHz waveform digitizing chip for the MEG experiment. *Nucl. Sci. Symp. Conf. Rec. 2004 IEEE*, Vol. 2, pp. 974–976, 2004.

[58] M. Schneebeli. The Drift Chamber of the MEG Experiment and Measurement of the ρ-parameter in the Michel Spectrum of the Muon Decay. *Ph.D. Thesis*, ETH Zürich, 2008.

[59] W. Ootani *et.al.* Development of a Thin-wall Superconducting Magnet for the Positron Spectrometer in the MEG Experiment. *IEEE Trans. on Applied Superconductivity*, Vol. 14, pp. 568–571, 2005.

[60] S. Dussoni. Search for Lepton Flavour Violation: The MEG experiment. *Ph.D. Thesis*, Università degli Studi di Genova, 2006.

[61] R. Valle. Development of the Timing Counter for the MEG experiment. *Ph.D. Thesis*, Università degli Studi di Genova, 2006.

[62] Saint Gobain. `http://www.saint-gobain.com`.

[63] Hamamatsu Photonics. `http://www.hamamatsu.com`.

[64] F. Sauli. Principles of Operation of Multiwire Proportional and Drift Chambers. CERN 77-07 (1977).

[65] F. Sauli. *Experimental techniques in high energy nuclear and particle physics*, chapter 2; Principles of Operation of Multiwire Proportional and Drift Chambers, pp. 79–188. World Scientific Publishing Co. Ltd., 1987.

[66] W. Zimmermann *et.al.* Helium-Propane as Drift Chamber Gas. *Nucl. Instr. Meth. A*, Vol. 243, pp. 86–90, 1986.

[67] S. Uno *et.al.* Study of a drift chamber filled with a helium-ethane mixture. *Nucl. Instr. Meth. A*, Vol. 330, pp. 55–63, 1993.

[68] H. Hirano *et.al.* A high-resolution cylindrical drift chamber for the KEK B-factory. *Nucl. Instr. Meth. A*, Vol. 455, pp. 294–304, 2000.

[69] G. Sciolla *et.al.* (BaBar Drift Chamber Collaboration). The BaBar drift chamber. *Nucl. Instr. Meth. A*, Vol. 419, pp. 310–314, 1998.

[70] M. H. Kelsey. Performance and aging of the BaBar Drift Chamber. *Nucl. Instr. Meth. A*, Vol. 535, pp. 206–211, 2004.

[71] O. Nitoh *et.al.* Drift Velocity of Electrons in Helium-Based Gas Mixtures Measured with a UV Laser. *Jpn. J. Appl. Phys.*, Vol. 33, pp. 5929–5932, 1994.

[72] D. F. Anderson *et.al.* A Simple "Vernier" Method for Improving the Accuracy of Coordinate Readout in Large Wire Chambers. *Nucl. Instr. Meth.*, Vol. 224, pp. 315–317, 1984.

[73] D. Green *et.al.* Acurate Two-Dimensional Drift Tube Readout Using Time Division and Vernier Pads. *Nucl. Instr. Meth. A*, Vol. 256, pp. 305–312, 1987.

[74] J. Allison *et.al.* The diamond shaped cathode pads of the OPAL muon barrel drift chambers. *Nucl. Instr. Meth. A*, Vol. 310, pp. 527–534, 1991.

[75] Y. Ajima *et.al.*(BESS Collaboration). A Superconducting Solenoidal Spectrometer for a Balloon-Borne Experiment. *Nucl. Instr. Meth. A*, Vol. 443, pp. 71–100, 2000.

[76] UBE Industries Ltd. `http://www.upilex.jp/e_index.html`.

[77] Helmut Fischer AG. `http://www.helmut-fischer.com`.

[78] ThreeBond Co. Ltd. `http://www.threebond.co.jp/en/`.

[79] Texas Instruments Inc., OPA691. `http://www.ti.com`.

[80] Radiall S. A. `http://www.radiall.com`.

[81] MIDAS Slow Control Bus. `http://midas.psi.ch/mscb/`.

[82] S. Ritt and R. Schmidt. The MSCB bus - A Field Bus Tailored to Particle Physics Experiments. PSI-Scientific Report 2001.

[83] National Instruments Co. LabVIEW, `http://www.ni.com/labview/`.

[84] A. Baldini *et.al.* The Boron Way, 2007. MEG Technical Notes, vol. 43.

[85] ASHCROFT Inc. `http://www.ashcroft.com`.

[86] MIDAS Data Acquisition System. `http://midas.psi.ch/`.

[87] GEANT, Detector Description and Simulation Tool Version 3.21/14. `http://wwwasd.web.cern.ch/wwwasd/geant/`.

[88] ZEBRA, A data structure management package. CERN Program Library Long Writeups Q100/Q101.

[89] R. Brun and F. Rademakers. ROOT, An Object-Oriented Data Analysis Framework. `http://root.cern.ch`.

[90] I. Smirnov. HEED, Interactions of particles with gases Version 1.01. `http://consult.cern.ch/writeup/heed`.

[91] S. Biagi. Magboltz, Transport of electrons in gas mixture Version 7.1. `http://consult.cern.ch/writeup/magboltz`.

[92] R. Veenhof. Garfield, Simulation of gaseous detectors Version 8.01. `http://garfield.web.cern.ch/garfield`.

[93] E. C. Ifeachor and B. W. Jervis. *Digital Signal Processing*, chapter 7; Finite Impulse Response (FIR) Filter Design. Prentice Hall, Inc., 2nd edition, 2002.

[94] R. E. Kalman. A New Approach to Linear Filtering and Prediction Problems. *Trans. ASME J. Basic Engineering*, Vol. D 82, pp. 35–45, 1960.

[95] S. M. Ross. *Introduction to Probability and Statistics for Engineers and Scientists*, chapter 13; Quality Control, pp. 545–580. Academic Press Inc., 3rd edition, 2004.

[96] P. Billoir. Track fitting with multiple scattering: A new method. *Nucl. Instr. Meth.*, Vol. 225, pp. 352–366, 1984.

[97] Frühwirth. Application of Kalman filtering to track and vertex fitting. *Nucl. Instr. Meth. A*, Vol. 262, pp. 444–450, 1987.

[98] C. H. Christensen. Convert GEANT geometry to ROOT. `http://swoolley.org/man.cgi/1/g2root`.

[99] J. R. Cash and A. H. Karp. A variable order Runge-Kutta method for initial value problems with rapidly varying righ-hand sides. *ACM Trans. Math. Software*, Vol. 16, pp. 201–222, 1990.

[100] R. A. Swanson. Depolarization of Positive Muons in Condensed Matter. *Phys. Rev.*, Vol. 112, pp. 580–586, 1958.

[101] N. Danneberg *et.al.* Muon Decay: Measurement of the Transverse Polarization of the Decay Positrons and its Implications for the Fermi Coupling Constant and Time Reversal Invariance. *Phys. Rev. Lett.*, Vol. 94, p. 021802, 2005.

[102] J.R. Musser *et.al.* (TWIST Collaboration). Measurement of the Michel Parameter ρ in Muon Decay. *Phys. Rev. Lett.*, Vol. 94, p. 101805, 2005. [arXiv:hep-ex/0409063].

[103] T. Kinoshita and A. Sirlin. Radiative Corrections to Fermi Interactions. *Phys. Rev.*, Vol. 113, pp. 1652–1660, 1959.

[104] W. T. Scott. The Theory of Small-Angle Multiple Scattering of Fast Charged Particles. *Rev. Mod. Phys.*, Vol. 35, pp. 231–313, 1963.

[105] Y. Kuno and Y. Okada. Proposed $\mu \to e\gamma$ Search with Polarized Muons. *Phys. Rev. Lett.*, Vol. 77, pp. 434–437, 1996. [arXiv:hep-ph/9604296].

[106] G. J. Feldman and R. D. Cousins. Unified approach to the classical statistical analysis of small signals. *Phys. Rev. D*, Vol. 57, pp. 3873–3889, 1998. [arXiv:physics/9711021].

Acknowledgement

For the Pisa and Genova collaborators, I am thankful to Dr. Giovanni Signorelli and Dr. Donato Nicolo. They are my oldest Italian friends and collaborators. And also, I would like to thank Dr. Simeone Dussoni and Dr. Riccardo Valle. Thanks to them, I could really enjoy working with a lot of Italian colleagues, including food and wine, of course.

For the Russian collaborators, I am profoundly grateful to Mr. Andrey Korenchenko and Mr. Nicholai Kravchuk of Dubna for their devoted collaborations. For another Russian institute, Budker's colleagues, I would like to acknowledge Dr. Dimitri Grigoriev, Dr. Boris Khazin, and Dr. Fedor Ignatov. Indeed I could not complete my tracking business without Fedor. Discussions with Boris helped me to establish the calibration procedures. Dima, he has encouraged me at any time.

For the former collaborators, I express cordial gratitude to Dr. Kenji Ozone of KEK. He was a senior member of our laboratory, and I have learned many things from him at the beginning of my PhD.

For the KEK collaborators, Prof. Akihiro Maki and Prof. Tomiyoshi Haruyama have given me constructive comments and warm encouragement. Special thanks to Mr. Katsuyuu Kasami; I really enjoyed working and traveling with him together.

For the REPIC corporation, I want to express my appreciation for Mr. Kazuo Konno and Mr. Sada-aki Kudo. Thanks to their strenuous efforts, the excellent cathode foil was completed.

I would like to take this opportunity to thank all the collaborators of MEG again.

———————————————————————————

In the final paragraph, I want to express my heartfelt appreciation to Dr. Matthias Schneebeli, Dr. Malte Hildebrandt and Dr. Johny Egger. Thanks to them, I could enjoy my Swiss-Life not only scientific but also my backstage life.

Working and Discussing with Matthias helped me a lot of things that is described in this thesis. I absolutely could not finish my thesis without him.

I always have had the support and encouragement from Malte. Many-many times, I disturbed his job due to my trouble, however he always have supported me without lowering looks. I am very grateful for his kind assistance.

My deepest appreciation goes to Dr. Johny Egger. I got really lucky that he was my advisor in PSI. However, he was not advisor only in PSI but also in anywhere. I have learned a lot of things from him. And also, I could enjoy Swiss-Life thanks to his kind help. I really thank Johny most sincerely for his invaluable help. I dedicate this thesis to him.

Finally, I sincerely thank my parents, Hisako and Nobuzou, for their support for many years. I learned so much from my parents, and I am so grateful to them.

March 2008, Tokyo,
Hajime Nishiguchi